Biophysical characterization and computational modeling of phase separation of immune adapter proteins

Dissertation
to acquire the doctoral degree in mathematics and natural science
'Doctor of Philosophy'
at the Georg-August-Universität Göttingen

in the doctoral degree program of Biology
at the Georg-August University School of Science

Submitted by

Joachim Maier

from Bad Saulgau

Göttingen, May 2021

Thesis Committee

Prof. Christian Griesinger
Department of NMR-based Structural Biology
Max Planck Institute for Biophysical Chemistry, Göttingen

Prof. Dirk Görlich
Department of Cellular Logistics
Max Planck Institute for Biophysical Chemistry, Göttingen

Prof. Jürgen Wienands
Department of Cellular and Molecular Immunology
University Medical Center Göttingen

Members of the Examination Board

Reviewer: Prof. Christian Griesinger
Department of NMR-based Structural Biology
Max Planck Institute for Biophysical Chemistry, Göttingen

Second Reviewer: Prof. Jürgen Wienands
Department of Cellular and Molecular Immunology
University Medical Center Göttingen

Further members of the Examination Board:

Prof. Dr. Rubén Fernández-Busnadiego
Institute of Neuropathology,
University Medical Center Göttingen

Prof. Dr. Kai Tittmann
Department of Molecular Enzymology
Göttingen Center of Molecular Biosciences
Georg-August University Göttingen

Prof. Dr. Ramin Golestanian
Department of Living Matter Physics
Max Planck Institute for Dynamics and Self-Organization

Date of the oral examination: 09.07.2021.

Affidavit

Herewith I declare that I prepared the doctoral thesis titled “Biophysical characterization and computational modeling of phase separation of immune adapter proteins” on my own and with no other sources and aids than indicated.

_____

Göttingen, 31.05.2021

Related publications

Parts of the work presented in this thesis led to the following publications:

1. Wong, L. E., Bhatt, A., Erdmann, P. S., Hou, Z., Maier, J., Pirkuliyeva, S., Engelke, M., Becker, S., Plitzko, J., Wienands, J., & Griesinger, C. (2020). **Tripartite phase separation of two signal effectors with vesicles priming B cell responsiveness.** Nature communications, 11(1), 848. https://doi.org/10.1038/s41467-020-14544-1

2. Wong, L. E., Maier, J., Wienands, J., Becker, S., & Griesinger, C. (2018). **Sensitivity-Enhanced Four-Dimensional Amide-Amide Correlation NMR Experiments for Sequential Assignment of Proline-Rich Disordered Proteins.** *Journal of the American Chemical Society*, *140*(10), 3518–3522. https://doi.org/10.1021/jacs.8b00215

Abstract

The processes of B cell activation and development are stimulated by antigen binding to the B cell receptor. Pre-signaling clusters are present in unstimulated, resting B cells and assemble by tripartite phase separation of two signaling adapter proteins, SLP65 and CIN85, and intracellular VAMP7-positive vesicles. The pre-signaling clusters of the B cell receptor signaling pathway are required for the adaptive immune response. A compromised humoral immune response has been reported in patients where SLP65 or CIN85 malfunction. Also, B cell culture studies show that pre-signaling clusters are required for an intracellular Ca^{2+} response. Thus, phase separation of these proteins in B cells seems to be functionally relevant.

In order to dissect the thermodynamics of phase separation of SLP65 and CIN85, we determined the affinities of the binding modules, i.e. the proline rich motifs (PRMs) and the SH3 domains individually and modelled it with an appropriate program.

Before this study, the binding preferences and number of relevant binding modules were unknown. Three SH3 domains of each CIN85 monomer that forms a trimer bind to a number of PRMs of SLP65. First, the promiscuous binding of the three SH3 domains of CIN85 to seven potential PRMs of SLP65 was disentangled on the modular level. Therefore, monovalent binding affinities of the individual SH3 domains to the individual PRM peptides were determined. This revealed one particular strong binding motif, PRM4, with dissociation constants of ~200 µM, 6 µM and 35 µM for SH3A, SH3B and SH3C, respectively. The promiscuous interaction further comprises four medium affine binding motifs (PRM1, PRM3, PRM5 and PRM6) with dissociation constants in the range of ~60 µM to 1 mM, and two weakly binding motifs (PRM2 and PRM*) with dissociation constants above 1 mM.

Next, the question was addressed whether PRM4 or SH3B are main drivers for phase separation. Therefore, mutant constructs were designed. Weak (inactivated PRM4) and strong (3xPRM4) binding constructs of SLP65, and a strong binding construct of CIN85-3SH3 (3SH3B) were expressed. Pre-signaling clusters can be reconstituted *in vitro* with SLP65- and CIN85 protein constructs together with small unilamellar vesicles (SUVs). The critical concentration of phase separation was measured for mixtures in presence or absence of SUVs, and for mixtures with different combinations of mutant constructs. The binding entities

3xPRM4, 3SH3B and SUVs promoted phase separation to a different extent. Comparative analysis showed that phase separation is promoted by SUVs very effectively. The artificially designed strong binding construct 3SH3B showed a similar strong effect. The inactivation of PRM4 by single point mutation increases the critical concentration, indicating that PRM4 has a substantial effect, but to a lesser extent than SUVs. The artificially designed binding entity 3xPRM4 had the smallest effect in promoting phase separation among the mutant constructs designed for strong binding.

Furthermore, we focused on the aspect of the structural arrangement of vesicles inside the condensed phase. The vesicle distribution was visualized in collaboration with Prof. Plitzko's group by cryo-electron tomography, highlighting that SUVs condense in droplets.

Subsequently, after the detailed characterization of tripartite phase separation *in vitro* experimentally, an early-stage model was developed to describe the SLP65-CIN85 interaction network beyond the schematic representation. The sticker-spacer lattice modelling program LASSI was phenomenologically parameterized and used to simulate phase separation of the SLP65-CIN85 interaction network. For simulation purposes, SLP65, CIN85-3SH3 and their strong and weak binding mutant constructs shared the same sticker-spacer architecture, but differed in the strength of the interaction terms according to the modular design. Interaction of hexavalent SLP65 (6 x PRMs) with trivalent CIN85 (3 x SH3) constructs were simulated. Initially simulated and experimentally-determined critical concentrations did not agree well. However, the agreement was improved when the energy terms of the C-terminal SH3 module were set to zero in the *wildtype*-like 3SH3 construct referred to as 2SH3 construct. The validity of this approach is based on experimental evidence ([174] and unpublished results of my colleague Daniel Sieme.)

Finally, the view was shifted towards the biological relevance by correlating the binding affinities to previous *ex vivo* experiments. We found that the binding affinities determined *in vitro* are correlated to the partly reconstituted Ca^{2+} signals in $SLP65^{-/-}$ cells transfected with SLP65-PRM single point mutants.

Moreover, the phase separation properties of mutant constructs were correlated to two readouts, namely the Ca^{2+} signal capacity and the number of pre-signaling clusters. The wildtype-SLP65 reconstituted cells showed most droplets and highest Ca^{2+} signal. The

abolishment of vesicle interactions showed the most pronounced effect *in vitro* and *in vivo*. In vesicle-binding deficient ΔN-SLP65 transformed cells, droplets were absent and the Ca^{2+} signal was abolished. For SLP65-3xPRM4 reconstituted cells, droplets were still present but reduced, and the Ca^{2+} signal was decreased, but not abolished. Thus, the SLP65-3xPRM4 reconstituted cells showed the least pronounced effect among the mutant constructs, which is in line with the *in vitro* observations. The outcomes of the *in vitro* phase separation assays and the *in vivo* readouts correlate and indicate that phase separated pre-signal clusters rely on the contribution of individual PRMs. In this work, a comprehensive description of SLP65-CIN85 phase separation is given.

Acknowledgements

The development of this project was not an act by a single person. From the project's outline to the final conclusion, there are connections to many people. And each indifferent, nonchalant move and each tiny event of progress determined the projects outcome. The small, but significant contribution of many people is not printed here.

I am grateful to my family for their constant support, cheers and ray of hopes.

I am very thankful to Prof. Christian Griesinger for providing an outstanding research environment, funding and lots of opportunities to present, exchange and discuss the ongoing research.

I am grateful to the Thesis Advisory Committee members Prof. Jürgen Wienands and Prof. Dirk Görlich for valuable input at the meetings, the curiosity-driven suggestions and guidance.

I thank Stefan Becker for his proactive suggestions and valuable discussions, and for his efforts in keeping the laboratory equipment running for everyone. I appreciate the contributions from Claudia Schwiegk, Kerstin Overkamp, Melanie Wegstroth and Karin Giller of providing samples and tips & tricks for sample handling and preparation.

Special thanks are for Leo Wong for introducing me into the project, his valuable suggestions, the fruitful discussions of experiments and science in general, the exchange of experience, showing me how to operate and maintain NMR spectrometers and the conversation about topics outside the work environment. I thank Daniel Sieme for the valuable discussions. I thank Ángel Perez Lara from the Laboratory of Neurobiology for the introduction to isothermal calorimetry and the following productive discussions.

I'd like to thank our collaborators Michael Engelke and Arshiya Bhatt from the Institute for Cellular and Molecular Immunology for open discussions and new perspectives. I'd like to thank Dr. Philipp Erdmann, Zhen Hou and Prof. Jürgen Plitzko from the Department of Molecular Structural Biology at the MPI of Biochemistry for the great collaboration of the cryo-ET studies of SLP65-CIN85-SUV droplets.

My thanks goes to Juan Carlos Fuentes for the help in daily challenges, the scientific discussions and for the conversations outside the topic of my project. I thank Nasrollah Rezaie-Ghaleh for valuable suggestions in setting up NMR experiments and for the discussions about the project. I'd like to thank Kris Runge for the explanations about spectrometer maintainance, for many conversations about various topics, and for enjoyable self-made cakes. I'd like to give thanks to Filippo Favretto for the joint care about the 800 MHz spectrometer and the conversations revolving around spins and other things. I thank Dirk Bockelmann for the support in technical issues and Petra Breiner for her assistance to the department. I'd like to thank Peter Lenart and Antonio Politi for granting me access to the Live-cell Imaging facility and Dirk Kamin for access to the Facility for Innovative Light Microscopy. I'd like to acknowledge Prof. Rohit Pappu and Furqan Dar for the fruitful discussions about modeling phase separation with LASSI. I acknowledge Thomas Burg for valuable discussions and for providing me access to the microfluidics lab. I thank Marie Fuest and Giovanni Marco Nocera for the introduction in microfluidic-based cell experiments, sharing their expertise and the support in the experimental set-up.

A big thanks goes to the former and present department members for good company, enlightening discussions during the seminars, the conversations during the daily breaks and joint sport activities.

Table of Contents

Introduction:

1.1 The principle of biocondensation in cellular organization

1.1.1 The question about cellular organization

The physicochemical properties of biomolecules translates miraculously to a higher stage of a single cell, which would not function without cellular organization. Traditionally, a cell is depicted with membrane-enclosed organelles such as the nucleus, the endoplasmic reticulum and mitochondria altogether surrounded by a lipid bilayer. The view on macromolecular complexes deduces that cells operate through specific and selective interactions mediated by well defined, tight binding events, which also conveys a rather static picture of cellular organization. Explaining complex spatio-temporal interaction networks inside a living cell by solely relying on constitutive binding raises difficulties. Is there another way to describe molecular arrangements in a molecular crowded cell?

1.1.2 Spherical bodies inside a cell - from the past till now

Most textbook illustrations of a cell dismiss spherical shaped bodies although they are known for more than 100 years [1, 2]. Among such bodies are nucleoli, Cajal bodies [3, 4], promyelocytic leukemia (PML) nuclear bodies [5-7], germ granules [7], stress granules [8] and signaling clusters [9]. Microscopy and fluorescence recovery after photobleaching was applied to investigate the structural and dynamic nature of such bodies, and these studies reported e.g. the fusion and fission of Cajal bodies and their high velocity relative to diffusion [10, 11]. Cajal bodies indeed diffuse at a speed of approximately 0.3 μm/min which is faster than expected for a cytoplasmic particle of that size. Furthermore, rapid exchange rates of paraspeckle with the nucleoplasm [12], highly mobile nucleosome proteins [13], rapid exchange rates of PML and Nuclear autoantigen Sp-100 and de novo assembly of PML nuclear bodies [14-16], the transport and assembly of P bodies [17, 18] and stress granules [19, 20] was observed. In contrast to membrane-enclosed organelles, these structures revealed increased dynamics in terms of fusion

events or rapid exchange of molecules between their interior and the exterior cytoplasm or nucleoplasm. Thus, these spherical shaped bodies have been described as dynamic clusters, hubs, spots, foci, puncta, assemblies or granules. It became obvious that a cell has plenty of dynamic, higher-order structures, however, a possible general process of assembly had to be revealed. Eventually, in pioneering studies on germline P-granules (2–4 µm diameter), the pattern of P-granule formation and their common liquid behavior were investigated [7]. Fusion and surface wetting of P-granules were directly observed and viscosity and surface tension of P-granules had been directly compared to colloidal liquids realizing that the physical process of phase separation could explain liquid-like properties and concentration dependent assembly. These findings brought back the principle of phase separation in the field of cellular organization [7].

1.1.3 The dynamic nature of cellular bodies

Phase separation is the transition from a single, homogeneous mixture to a binary or multicomponent mixture (Figure 1).

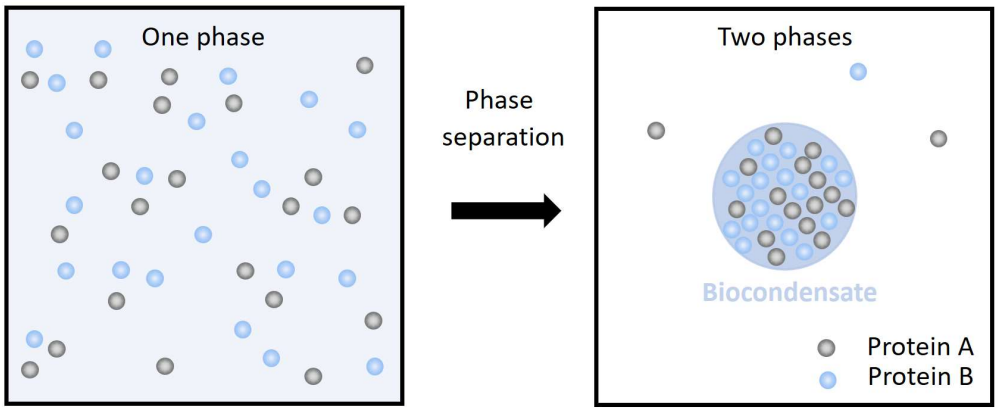

Figure 1: Illustration of phase separation: Phase separation is the demixing process of a homogenous mixture into two or more phases. In the simplest case, a dilute and condensed phase originates from a single, homogenous mixture.

In pioneering studies on frog oocytes nucleoli, Brangwynne *et al.* exhibited an example of a dynamically organized condensate versus an ordered, well defined assembly [21]. The size and shape of spherically appearing nucleoli were measured. Also, nucleoli were manipulated by a needle to probe fusion characteristics. The spherical shape, the fusion behavior and the power law-governed size distribution were attributed to liquid-like droplets. Consequently, the existence of dynamic structure in contrast to well-defined assembly relaunched the idea of phase separation of cytoplasm [22] as a conceptual framework for subcellular organization [23].

More and more cellular membrane-less organelles, recently termed biomolecular condensates or biocondensates [24], were discovered. Numerous examples show their great diversity in material states, sizes, cellular localizations and cell types as illustrated by selected examples in the next section below.

1.1.4 Localization and possible significance of biocondensates

The perception of the dynamics of cellular bodies may have foreshadowed the new perspective of the material properties of biocondensates [25], which can be grouped in three categories: liquid-, gel- or solid-like [26]. Their liquid properties are certainly tunable [27], and the material state can be related to interactions of particular amino acid residues [28]. Remarkably, biocondensates can alter their state with time, the so called “aging”, e.g. from a liquid state towards a solid or aggregate state [29].

The localization of biocondensate seems not to be restricted to any cellular environment. It appears that biocondensates can be associated with any cellular structure, and versatile localization have been reported (Figure 2). Phase separation occurs in the nucleus [30], the cytosol [31], the Golgi matrix [32, 33], the pyrenoid organelle of algae [34], as metabolic granules [35] or stress granules [36, 37]. Biocondensation is associated to the endoplasmatic reticulum [38], the nuclear pore complex [39], ribonucleoproteins [40], and to extracellular galectin-3 [41] or is proposed to drive myelin membrane assembly [42]. Moreover phase separation plays an important role in viral infection when viral proteins undergo phase separation in viral factories [43].

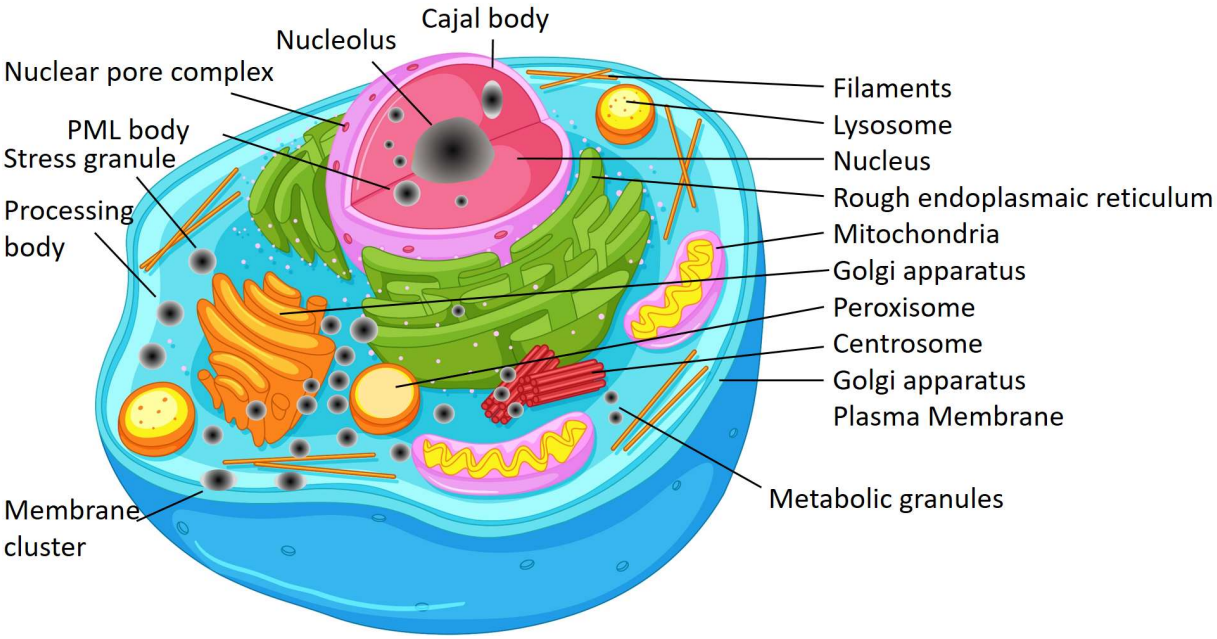

Figure 2: Cellular organization by membrane-bound and membrane-less organelles. The interior of a cell is a crowded environment, including different biocondensates of versatile composition. However, multiphasic condensates are not considered in this illustration [Figure adapted from Freepik.com]. Membrane-less bodies are color-coded black.

While revealing that biocondensates are widespread among eukaryotic organisms, concomitantly functional implications were proposed; e.g. for nuclear bodies [44], stress granules [45] and signaling clusters [46, 47], heterochromatin [48], centrosome-localized proteins [49] and proteasome-containing nuclear bodies [50]. These reports highlight the functional significance of biocondensates (Figure 3). Primarily, biocondensates may serve as organizational hubs, reaction cubicle [51] and sequestration loci [52, 53]. Biocondensates can be compositionally regulated [54] and reaction kinetics can be tuned by modulated effective concentrations [24]. The most prominent example of an organizational hub is the nucleus, which is free of membrane-bound compartments and has a multiphase nature [55].

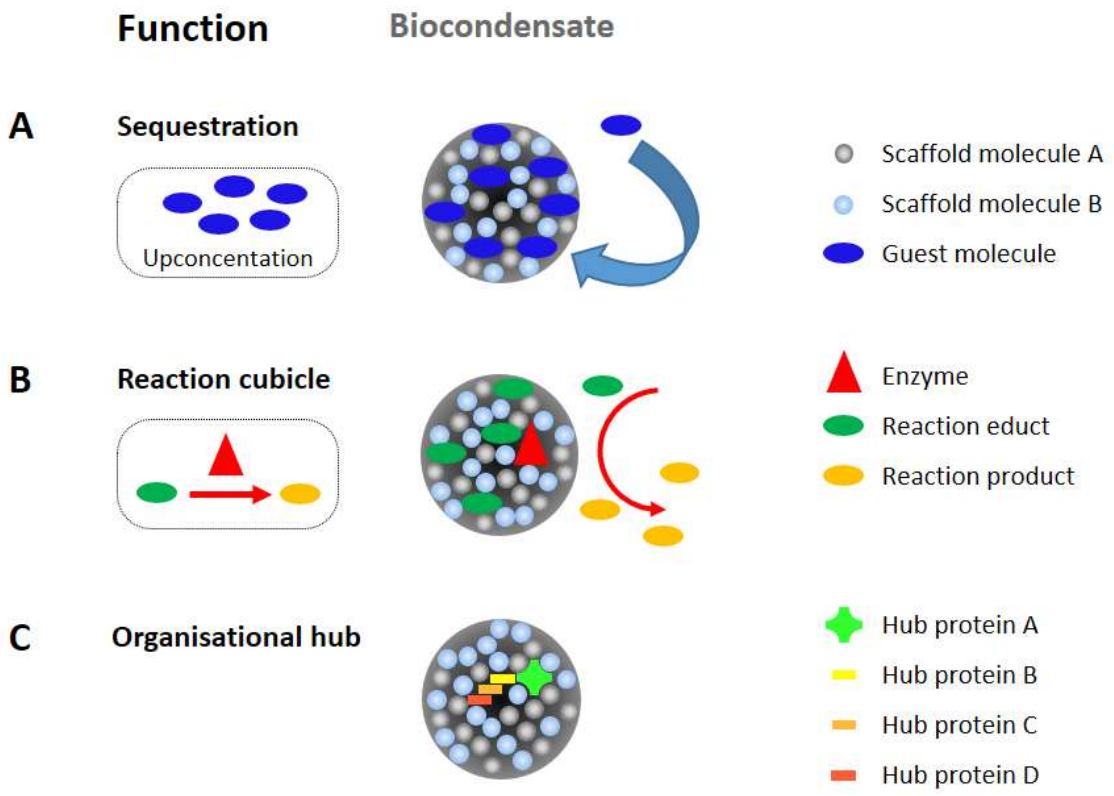

Figure 3: Possible functions of biocondensates. (A) Sequestration of molecules can serve to regulate the availability of signaling molecules and can interrupt signaling pathways by withdrawing signaling molecules. (B) The function as reaction cubicle implies the tuning of reaction kinetics by increased effective concentration of enzymes or educts. (C) Scaffold proteins can configure a network of molecules for the purpose of organization.

On the one hand physiological function is significant, on the other hand disease imposes relevance as well [43, 56], e.g. phase separation of Fused in Sarcoma (FUS) is correlated to neurodegenerative disease [57, 58]. Moreover, phase separation is related to coacervation and is speculated to be a selection mechanism [59-62]. The evolution and function of phase separation is likely manifested in the genome and proteome. Hence, phase separation is an interesting topic in different research areas.

1.1.5 Driving forces and sequence determinants of phase separation

The capability of phase separation extends to all classes of biomolecules. What are the driving forces of phase separation? Bimolecular condensation can involve protein-protein, RNA-protein, RNA-RNA interactions as well as interactions with DNA and lipids [63, 64]. Non-covalent electrostatic [65, 66], hydrophobic [67-69], π-π, cation-π interactions, and conformational entropy are driving forces of phase separation [70]. Multivalence [71] and low-affinity binding [31, 46, 63, 72-74] are hallmarks of liquid-liquid phase separation in biology. But biomolecular condensation does not simply rely on chemical properties alone; the linker length, the pattern or distribution of interaction sites, the orientation, virtually the molecular architecture has positive or negative cooperative effects. It is of interest to pinpoint relevant protein and nucleic acid sequences and identify sequence determinants of phase separation.

Intrinsically disordered protein (IDP) or intrinsically disordered region (IDR) within proteins are prone to phase separation [75-77]. One prominent example is the protein FUS of ribonucleoprotein granules [57], which phase separates by its low complexity domain driven by cation-π interactions. Another prominent example is the intrinsically disordered N terminus of Ddx4 in germ granules, which drives phase separation by electrostatic interactions [31].

Besides IDPs, RNA is very prone to phase separation. RNA-RNA interaction driven phase separation is mediated by unspecific Watson-Crick base-pairing, non-canonical base-pairing, and helical stacking [78].

Yet another class of phase-separation-prone proteins contains low-complexity aromatic-rich kinked segments, which form kinked beta-sheets and are associated to biocondensates [79]. Low complexity domains can interact with polyanionic RNA, e.g. by RNA-binding domain [80, 81], cationic protein residues [65, 82] or RNA binding motif RRG/RG [83].

Adapter proteins are also prone to phase separation. Similar to multiple-charged, polyanionic RNA or DNA, they possess multiple domains, which bind to several short linear motifs (SLiM) [84]. The phase separation of modular proteins with structured domains connected by intrinsically disordered linkers [85] was first demonstrated for the Nck/N-WASP system involving multiple SH3 domains [46]. The diversity of biocondensates poses a challenge on finding a general model to understand and describe common characteristics of biomolecular phase separation.

1.2 Theory and simulation of biocondensation

1.2.1 The need for simulations

Phase separation is a very general principle and extends to all kinds of biomolecules and many organisms. It seems not to be restricted to any geometry, since there are condensates of long stranded DNA or RNA [86], plasma membrane associated condensates [87], intrinsically disordered proteins and modular domain proteins. Is it possible to set up a mathematical framework to describe common features of phase separation? Is there a common model for transient interactions of biopolymers? The literature about the physics of phase separation, reviewed by Weber et al. [88], is comprehensive, but limited in the applicability to biological questions. Lin et al. [89] reviews the applicability of analytical polymer theories to characterize sequence dependency [89]. Analytical theories, e.g. the Flory–Huggins solution theory [90], can be applied to elucidate basic biophysical principles, although its basic approach leaves a gap for more details. Analytical theories can be regarded as extremely coarse-grained [89] and may not reproduce experiments well. Computer simulations could bridge the gap. The insights of molecular simulations can connect theory with experiments, since conclusions from simulations can encourage the design and development of new experiments. V*ice versa* experimental results are a stimulus to develop or improve simulations.

1.2.1 Finding a simulation method for a desired model

Until now, phase separation has been simulated by several methods or combination of methods, each with their advantages and disadvantages (Table 1). The choice of an approach is linked to the focus of the investigation. Langevin dynamics simulation was used to study phase separation, but was restricted in this study to small timescales [91]. Also, field-theoretic simulation was evaluated to simulate phase separation [92].

Many molecular dynamics (MD) simulations have been performed with a different focus. The focus had been set on the residue-level resolution in a slab-geometry MD simulations to determine phase diagrams [93], the molecular environment in a macromolecule-resolution MD

simulation [94] or the energetic driving forces using a coarse-grained dissipative particle MD simulation [27]. Due to limited computational power, often a tradeoff needs to be found between resolution and simulation time. In several simulations the desirable resolution is considered, e.g. in the all-atom MD simulation [95] or the minimal coarse-grained model for >1000 proteins [96]. Furthermore, coarse-grained MD simulations were applied in approaches which emphasize on the sequence dependency [97], the experimental parameterization [98] or the multivalency using a coarse-grained, Brownian Dynamics simulation with reactive binding that mimics specific interactions [99]. Phase separation has also been investigated for a system of active particles [100]. An active particle is defined to produce or consume a chemical. In the studied system, the concentration is dependent on both diffusion and the production or consumption of chemicals. Another promising approach is the Monte Carlo simulation. In contrast to MD, where trajectories are calculated by solving Newton's equations of motion, Monte Carlo simulations probe the configurational space by specially designed move set and select for the lowest energy configuration. A patchy-particle Monte Carlo simulation was implemented to study the tuning of phase separation by regulators [101]. A coarse-grained Monte Carlo simulation for a sticker-spacer model was implemented to study the effects of disordered linkers in multivalent proteins [102] or to calculate phase diagrams of modular domain proteins [103]. The latter model is called LAttice simulation engine for Sticker and Spacer Interactions (LASSI) and allows to simulate phase separation based on defined molecular interactions, concentrations and architecture. Martin *et al.* developed a predictive LASSI model for prion-like domains (PLDs) to investigate the phase separation behavior based on the sequence features. This model is specifically parameterized for the amino acid composition of PLDs, which are enriched in polar amino acids and contain singly distributed aromatic residues [104]. The model received its predictive power by fitting the experimentally-determined binodals to the simulation data, such that the temperature and concentration were calibrated into standard units. Thus LASSI is suitable to simulate phase separation behavior of IDPs, however the applicability to multidomain proteins is not straightforward. LASSI allows to define molecular architectures of stickers and spacers with predefined interaction energies and is capable to simulate phase separation concentrations of IDPs and also multivalent proteins [103], however there is yet no reported example of an

experimentally parameterized natural system of multidomain proteins undergoing phase separation.

Table 1: Computational studies about phase-separation simulations and their advantages and limitations. Most methods apply coarse-grained MD or Monte Carlo methods to simulate phase separation of a finite-sized number of biomolecules.

Study	Method	Advantages	Disadvantages
Ranganathan *et al.* [91]	Langevin dynamics	Dynamics by implementation of harmonic-spring and Lennard-Jones-potential force fields	2D-lattice; small timescale
Zheng *et al. [95]*	All-atom MD simulation	High resolution; tacks diffusion of water and ions	Simulation was restricted to 40 chains of one protein
Dignon *et al.* [93]	Coarse-grained MD simulation	Residue-level resolution	Simulations of IDPs, but not protein domains
Dutagaci *et al.* [94]	Coarse-grained MD simulation	Novel approach to address size and charge effects	Macromolecule-level resolution
Bartolini *et al.* [27]	Dissipative particle dynamics	Captures morphology	Simulations of polymers, but not protein domains
Statt *et al.* [97]	Coarse-grained MD simulation	Reveals impact of sequence pattern	Simulations of polymers, but not protein domains
Espinosa *et al.* [96]	MD simulation	Minimal coarse grained set up	No sequence dependence
Zumbro *et al.* [99]	Brownian dynamics simulation	Captures multivalency and diffusion effects	Simple, coarse-grained model
Agudo-Canalejo, Golestanian nn [100]	Brownian dynamics simulation	Minimal model to investigate phase separation mediated by chemical interactions	No implementation of linkers
Benayad *et al.* [98]	Coarse-grained MD simulation	Strategy to fine-tune the potential energy	Simulations of IDPs, but not protein domains
Ghosh *et al.* [101]	Patchy-particle Monte Carlo simulation	Prediction of partition constants	No implementation of linkers
Harmon *et al.* [102]	Coarse-grained Monte Carlo simulation	Model adapted for architecture of multivalent systems	Low resolution
Choi *et al.* [103]	Coarse-grained Monte Carlo simulation	Model adapted for architecture of multivalent systems	Low resolution

1.3 Tripartite phase separation of pre-signaling cluster in B cells

1.3.1 B and T cell receptor signal transduction

The immune system provides several layers of defense, relying on the crosstalk of various immune cells. The immune system is generally described by two categories, the innate and the adaptive immunity. In principle, the innate immune system's mechanism of defense is non-specific, but immediate. In contrast, the adaptive immune system establishes a specific defense against new threats, but requires days to weeks to be effective [105]. B and T lymphocytes have a key role in mediating adaptive immunity [106]. T cells communicate with other immune cells and stimulate cytokine production [107]. B cells recognize antigens, develop into plasma B cells, produce antibodies and can develop into memory B cells [108, 109]. B and T cells take advantage of somatic recombination [110, 111] to create a diverse set of unique antibody genes, which are integrated into surface-expressed receptor complexes, the B cell receptor (BCR) and the T cell receptor (TCR), respectively. These antigen receptors mainly trigger the adaptive immune response. SLP65 [112] and SLP75 [113] are crucial signaling proteins involved in BCR and TCR signal transduction, respectively. In principle, signaling is achieved by complex protein networks [114], however BCR and TCR signaling are now seen in the light of phase separation [115]. Phase separation of adapter proteins in immune cells has been demonstrated in T cells [46, 53, 87] and in B cells [116].

1.3.2 Adapter proteins involved in BCR signaling

SLP65 and CIN85 are the proteins of interest in this project. They are adapter and signaling proteins in B cell receptor signaling. In B cells, SLP65 and CIN85 together with vesicles assemble by tripartite phase separation and constitute a pre-signaling cluster [116]. Both proteins are essential for a proper Immunoglobulin G response. SLP65 is required for proper function in mice [117] and humans [118]. Also, gene deficiency of CIN85 causes B cell malfunction related malignancies [119].

It has been recognized that phase separation can implement a switch-like behavior [120]. The project's cell biological focus on the CIN85-SLP65 phase separation primed Ca^{2+} signaling capacity. In resting B cells, pre-signaling clusters resides in the cytosol, in which SLP65 is associated to VAMP7 (vesicle associated membrane protein 7)-positive vesicles [121] (Figure 4: A, B). The SLP65-interaction partner CIN85 is essential for pre-signaling cluster assembly [122] and B-cell responsiveness [116].

SLP65 function within the BCR signaling pathway is briefly outlined below (Figure 4 D). After the BCR signaling is stimulated by antigen binding, the downstream signaling cascade is initiated [123]. The BCR's immunoreceptor tyrosine-based activation motifs (ITAMs) are phosphorylated [124, 125], recruit and activate spleen tyrosine kinase (Syk) [126-130]. In parallel, SLP65-CIN85 clusters are translocated to the plasma membrane [131] (Figure 4 C), where Syk phosphorylates SLP65 [112, 132]. Phosphorylated SLP65 recruits both Bruton's tyrosine kinase (BTK) and its substrate phospholipase Cγ2 (PLCγ2) via interactions with the effector's SH2 domains [133, 134]. Phosphorylation-activated PLCγ2 produces second messengers inositol biisphosphate (IP_2) and diacylglycerol (DAG) spreading the signal further within the cell [134].

In this work, the molecular requirements of pre-signaling cluster formation is further investigated *in vitro* and correlated to *ex vivo* experiments to corroborate the physiological relevance of tripartite phase separation.

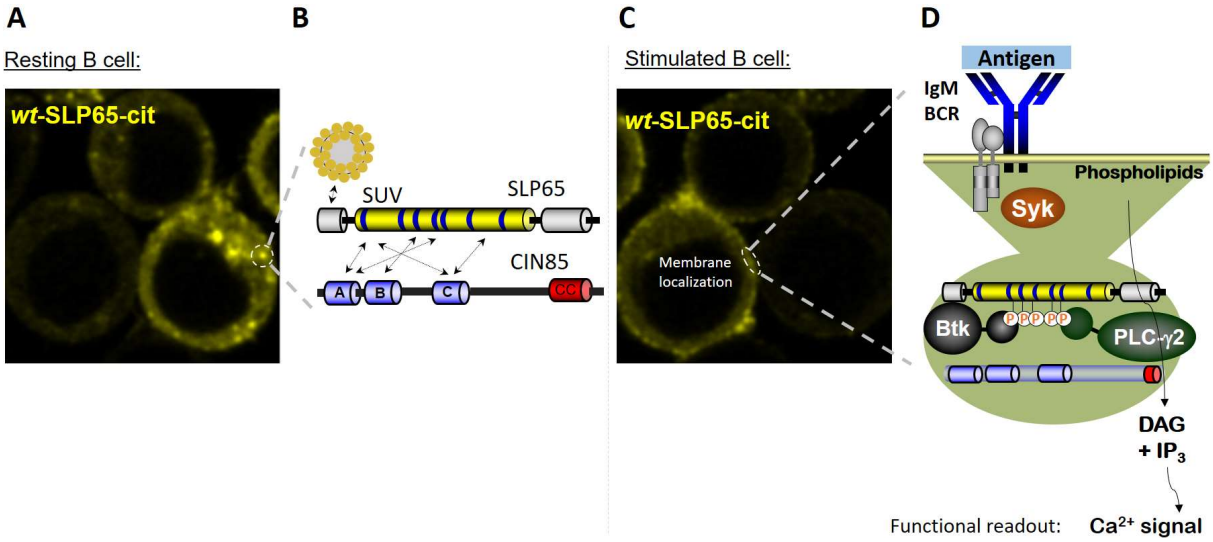

Figure 4: Pre-signaling clusters of SLP65, CIN85 and VAMP7-positive vesicles prime Ca2+ signaling. A) Confocal fluorescence microscopy of SLP65-deficient DT40 B cells reconstituted with a citrine-tagged SLP65 showing *wildtype* citrine-tagged SLP65 (*wt*-SLP65-cit) localization in condensates and the cytosol of resting B cells (adapted from Engelke *et al.* [121]) B) Schematic representation of SLP65 and CIN85 constructs, indicating SUV binding to SLP65's N-terminus [121] and promiscuous binding of SLP65 to CIN85 [122]. C) Confocal fluorescence microscopy of SLP65-deficient DT40 B cells reconstituted with *wt*-SLP65-cit after B cell stimulation: *Wt*-SLP65-cit translocates to the plasma membrane, where it co-localizes with antigen and CIN85 [122]. D) Schematic representation of SLP65's involvement in BCR signaling: Antigen-bound BCR activates Syk, which in turn phosphorylates SLP65. Phosphorylated SLP65 recruits effector proteins Btk and PLC-γ2, which induces an intracellular Ca^{2+} signal via second messengers.

1.4 The SH3 – PRM interaction

The promiscuous interaction of CIN85's three SH3 domains with PRMs of SLP65 is necessary for phase separation [116] and the structural elements of these proteins are introduced here. The SH3 domain family is one of the most abundant domains in the eukaryotic genome [135]. It specifically recognizes PRMs [136]. Both PRMs and SH3 domains are present in SLP65 and CIN85. SLP65 is an intrinsically disordered protein except for the C-terminal SH2 domain. It binds to vesicles via its intrinsically disordered, positively charged N terminus. It has seven potential proline-rich motifs (PRMs) within the intrinsically disordered region (Figure 5). CIN85 has three SH3 domains, a proline-rich region (PRR) and a coiled-coil domain (CC). The CIN85's SH3 domains preferentially recognize the amino acid sequence PxxxPR, an atypical PRM [137]. The three SH3

domains of CIN85 bind multiple PRMs of SLP65 in a promiscuous manner as shown by paramagnetic relaxation enhancements experiments [116].

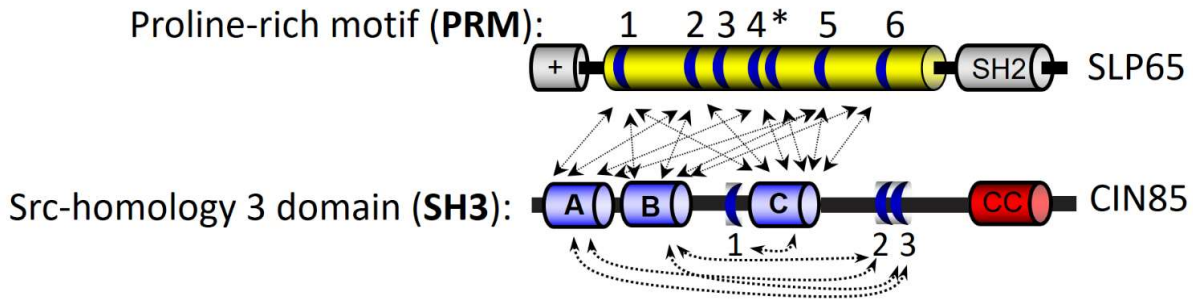

Figure 5: Schematic secondary structure representation of SLP65 and CIN85 indicating promiscuous binding. SLP65 has a vesicle-binding, positively charged N-terminus, an IDR harboring seven potential PRMs (1,2,3,4,*,5,6) according to Wong *et al.* [116] and a C-terminal SH2 domain. "*" is used for one PRM since it partially overlaps with PRM4. CIN85 has three SH3 domains, a proline-rich region (PRR), a trimerization coiled-coil domain (CC), and three PRMs (CIN85-PRM1,2,3). The linker between SH3B and SH3C harbors the recently identified CIN85-PRM1 (D. Sieme, unpublished results). CIN85 binds to SLP65 via promiscuous SH3-PRM interactions.

The SH3 domain is a ~60 amino acid long globally folded protein module, composed of a core of five β-strands linked by the RT loop, the N-Src loop, the distal loop and a 3_{10} helix (Figure **6**). The SH3 domains of CIN85 share 38% sequence identity and have 66% sequence similarity.

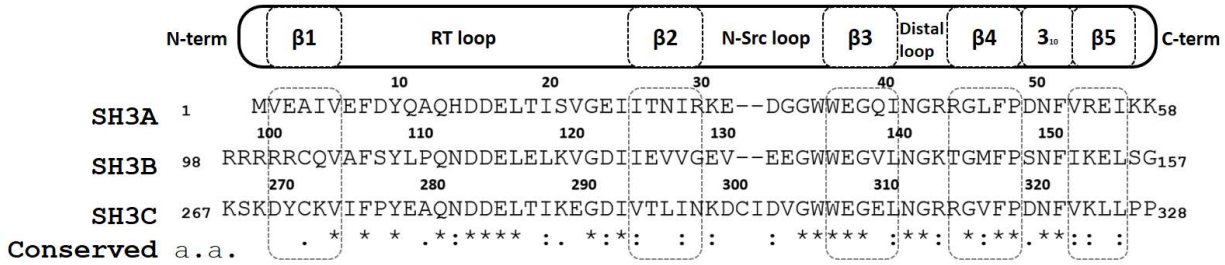

Figure 6: Secondary structure representation and alignment of CIN85 SH3 domains. Schematic representation of a SH3 domain secondary structure from CIN85; beta-sheets, loops and the 3_{10}-helix are indicated. Conserved amino acids of SH3A, SH3B and SH3C are shown as obtained by multiple sequence alignment (Clustal Omega). β-strands are indicated by a dashed box. Residue numbers represent amino acid positions within the CIN85 protein sequence.

1.5 NMR spectroscopy

1.5.1 Concept of NMR spectroscopy

The promiscuous binding of CIN85's SH3 domains to SLP65's PRMs is weak. Nuclear magnetic resonance (NMR) is a broadly applied method in many fields and also excellently suited to determine binding parameters of weak interactions ($K_A < 10^5$, $K_D > 10$ µM). A comprehensive introduction to NMR is given in the textbooks by Cavanagh [138] and Levitt [139]. A brief overview about its historic development and the basic concepts is given below, in order to give the reader an understanding for the measurement principle. The introduction also includes a section about chemical exchange, which will be encountered in this thesis.

In quantum mechanics, a spin is a mathematical concept to express the quantum nature of the magnetic moment of a particle. Electrons and certain nuclei have a spin. For nuclei with spin, protons and neutrons act like a gyroscope inducing a tiny magnetic moment. The spin is an angular momentum originating from the intrinsic spins of the elementary particles of which a nucleus is composed of. Nuclei with an odd mass number, like ^{1}H, ^{13}C and ^{15}N, always have an angular momentum. Nuclei with an even mass number and an odd charge, like ^{2}H and ^{14}N, have an angular momentum, too. The angular momentum has an associated magnetic momentum, which precesses about an external magnetic field B_0. This movement is called Larmor precession. The Larmor frequency v_0 is given by:

$$v_0 = \frac{\gamma}{2\pi} * B_0 \quad \text{(frequency in Hz)} \qquad \text{(eq. 1)}$$

$$\omega_0 = \gamma * B_0 \quad \text{(angular frequency in radians per second)} \qquad \text{(eq. 2)}$$

where γ is the gyromagnetic ratio. The magnetic energy E_{mag} is the dot product of the magnetic momentum **µ** and the magnetic field **B**:

$$E_{mag} = -\vec{\mu} * \vec{B} \qquad \text{(eq. 3)}$$

Similar to any magnetic material, the nuclear magnetic momentum will prefer a low energy alignment to the external magnetic field.

The macroscopic measurement of nuclear magnetization of a spin ensemble of molecules in a solution was a decades-long journey starting with Zeeman's discovery. Zeeman described in 1896, that the spectral lines of light were splitting in a high magnetic field [140]. In 1922, the quantized nature of a nuclear spin was first discovered by Stern and Gerlach [141-143]. In the Stern-Gerlach experiment, a beam of silver atoms was deflected by a spatially varying magnetic field and detected on a glass slide. The detected spot pattern was counterintuitively spread in two directions, corresponding to the two spin states α and β of the single paramagnetic electron, in contrast to a continuous spot as it would be expected from a non-quantized spin. We note that this pattern indicates the existence of two states. The theory of quantum mechanics can explain these two states due the spin ½ of the electron.

The total angular momentum S can be expressed in quantized form as the absolute value of $\vec{S}$ and is described by the spin quantum number S:

$$\left|\vec{S}\right| = \sqrt{S * (S+1)} * \hbar \qquad \text{(eq. 4)}$$

where $\vec{S}$ is the spin angular momentum vector and ħ is the reduced Planck constant. As mentioned above, a spin aligns in a particular orientation in the presence of an external, applied magnetic field. We are interested in the z-component of $\vec{S}$, since an external magnetic field B_z (also written as B_0) is commonly used in NMR. So, spins have a preferred orientation in an external magnetic field and the magnetic quantum number m_I is so to speak a description of the rotational direction. The magnetic quantum number m_S can have discrete values depending on the spin quantum number S:

$$m_S = -S, -S+1, \ldots, +S\text{ - }1\text{ , }+S \qquad \text{with } S = 0, \frac{1}{2}, 1, \frac{3}{2}, \ldots, \frac{9}{2} \qquad \text{(eq. 5)}$$

For a nuclei with a particular spin quantum number S, the number of "rotational" states is given by the z-direction components of $\vec{S}$:

$$S_z = m_S * \hbar \qquad \text{(eq. 6)}$$

For example,

$S_z = -\frac{1}{2}\hbar$ and $S_z = +\frac{1}{2}\hbar$, corresponding to $m_S = \pm\frac{1}{2}$.

Each spin ½ has two states, a low energy α-spin state (+½) and a high energy β-spin state (-½), aligned with (up) or against (down) the magnetic field, respectively. The angular momentum is associated with the magnetic momentum:

$$\mu_z = \gamma * S_z \qquad \text{(eq. 7)}$$

where γ is the gyromagnetic ratio of a nucleus (Table 2). ^{1}H, ^{13}C, ^{15}N and ^{31}P have S = ½, and these ½-spins are commonly used in NMR spectroscopy. Since ^{13}C and ^{15}N have low natural abundance, isotope labeling is applied to enrich NMR sensitive nuclei in samples.

In the previously mentioned Stern-Gerlach experiment, the splitting of the beam can be explained by the existence of two states with opposite magnetic moments. The silver isotopes ^{107}Ag and ^{109}Ag have spin ½. They have two possible values of S_z.

Table 2: Gyromagnetic ratio γ, spin quantum number S and natural abundance of nuclei commonly used in NMR.

Nucleus	γ [rad * sec^{-1} * gauss^{-1}]	S	Natural abundance [%]
^{1}H	26.753	½	99.980
^{2}H	4.106	1	0.016
^{13}C	6.728	½	1.108
^{15}N	-2.712	½	0.37
^{31}P	10.841	½	100.00

The next step of the journey towards biomolecular NMR was the demonstration of nuclear magnetic resonance. The energy difference between two nuclear states is:

$$\Delta E = E_\beta - E_\alpha \qquad \text{(eq. 8)}$$

However, nuclear spin states are only degenerate in the presence of an external magnetic field, such that the two spins have different orientation and energy. According to the Zeeman effect,

the energy difference increases with increasing external magnetic field strength as can be seen by applying equation 3 and equation 7 to equation 8:

$$\Delta E = \left(\overrightarrow{\mu_\beta} * \vec{B}\right) - \left(\overrightarrow{\mu_\alpha} * \vec{B}\right) = \left(-\frac{1}{2}\hbar\right) - \left(+\frac{1}{2}\hbar\right) * (\gamma * B_0)$$

$$= -(\hbar * \gamma * B_0) \qquad \text{(eq. 9)}$$

Transitions between the two states can be excited by radiofrequency at resonance condition (Figure 7), where h is Planck's constant, and v is the frequency of the radiation:

$$\Delta E = h * v \qquad \text{(eq. 10)}$$

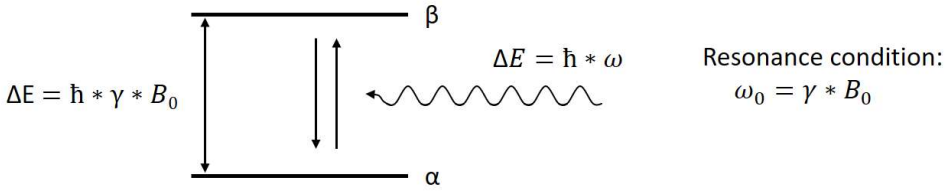

Figure 7: Resonance transitions by electromagnetic radiation at Larmor frequency. The nuclear spin states are flipped if the irradiation frequency matches the resonance condition. Equilibration of nuclear spin populations is reached by saturating irradiation.

Nuclear magnetic resonance was first experimentally demonstrated in a lithium chloride beam by Rabi *et al.* in 1938 [144]. The set up included an applied B_0 to degenerate the spins according to the Zeeman splitting. A second oscillating, time dependent B_1 field was applied to excite the resonance while sweeping the B_0 field. The experiment was successful, when an absorption peak was detected as the resonance condition was matched. In 1945, Bloch [145] and also Purcell [146] reported NMR in liquids and solids, respectively, each using a different type of experimental set up. In both set ups the B_0 was swept, while Purcell detected the absorption, Bloch detected via the nuclear induction effect. The latter conveyed the measurement principle for further developments. The continuous wave method demanded long measurement times. Eventually, this was succeeded by the pulse/Fourier transform method pioneered by Ernst and Anderson [147]. Fourier Transform NMR allowed the realization of 2D and higher dimensional experiments.

To illustrate signal detection, the magnetization transfer is described for the simplest NMR experiment, which includes an excitation pulse, followed by detection. In thermal equilibrium, the ratio of the populations of the two states is given by the Boltzmann factor according to the principles of statistical mechanics.

$$\frac{N_\alpha}{N_\beta} = \frac{e^{\left(\frac{+\frac{1}{2}*\hbar*\gamma*B_0}{k_b*T}\right)}}{e^{\left(\frac{-\frac{1}{2}*\hbar*\gamma*B_0}{k_b*T}\right)}} = e^{\left(\frac{\Delta E}{k_b*T}\right)} \qquad \text{(eq. 11)}$$

with the number of nuclei N in state α/β, the Boltzmann constant k_b and the absolute temperature T. This small but significant population difference results in a macroscopically excitable net magnetization M_z. The magnetization $\vec{M}$ is described by its components $\vec{M} = M_x + M_y + M_z$. A transmitter coil, perpendicular to the static B_0 field enables the application of radio frequency pulses. This corresponds to the application of a second magnetic field B_1. In the simplest 1D experiment, a y-pulse of chosen duration rotates the z-polarized magnetization M_z by 90° into the perpendicular orientation M_x.

A spin precesses according to the Bloch equations that have the same expression as a classical oscillation with the magnetization: $Mx, y(0)$ being the values of the x and y magnetization at time 0.

$$M_x\,(t) = M_x(0) * \cos(\omega_0 * t) - M_y(0) * \sin(\omega_0 * t) \qquad \text{(eq. 12)}$$

$$M_y\,(t) = My(0) * \sin(\omega_0 * t) + M_x(0) * \cos(\omega_0 * t) \qquad \text{(eq. 13)}$$

The magnetization components in the transverse plane induce a voltage in the receiver coil. During detection, the signal is exponentially decaying due to spin relaxation. The spin-lattice relaxation T_1 restores the net magnetization. Note that ω_0 has different values for spins in different chemical environments. This free induction decay (FID) is a superposition of all the frequencies of all excited spins. For analysis, the FID is Fourier Transformed to obtain a NMR spectrum. In more sophisticated experiments, an evolution period with additional pulses and delays is included, in order to manipulate the magnetization and gain the desired information.

NMR is able to probe the chemical environment of molecules since the electron shell around a nucleus interact with the external B_0 field. In principle, the electron shell generates an own field opposing or enhancing the external magnetic field, which is described as shielding or deshielding. With the shielding constant σ (deshielding: δ), the resulting B_0' is given by:

$$B_0' = (1 - \sigma)\, B_0 = (1 - \delta)\, B_0 \qquad \text{(eq. 14)}$$

The electron density determines the resulting B_0' at the nuclear spin. If the electron density is larger, then the B_0' gets smaller. A lower magnetic field results in a reduced resonance frequency, or simply called resonance. The resonance frequency is field dependent and thus not characteristic *per se*. Thus, the chemical shift scale is used to have a comparable, field-independent experimental value. The chemical shift δ of a resonance ω is given as a dimensionless value in *parts per million* (ppm, 10^{-6}) referenced to resonance ω_{ref} of a standard substance:

$$\delta = \frac{\omega - \omega_{ref}}{\omega_{ref}} * 10^{-6} \qquad \text{(eq. 15)}$$

In case of deshielding, a higher resonance frequency is observed in a spectrum at larger chemical shift (downfield). The resonance frequency differs largely between different types of nuclei (^{1}H, ^{13}C, etc.) due to the gyromagnetic ratio. However, for a distinct type of nucleus the chemical shift range is narrow. In proteins, ^{1}H chemical shifts are typically in a range between -1 to 14 ppm and ^{13}C chemical shifts are in a range between 0 and 220 ppm for diamagnetic molecules.

The study of proteins by 1D experiments is limited by the overlap of resonances. The 2D NMR experiment, heteronuclear single-quantum correlation (HSQC) experiment, is commonly used to monitor chemical shift changes upon protein-ligand binding. In a ^{1}H-^{15}N HSQC experiment the proton and nitrogen spins of the amide group are coupled via their chemical bond, which is called J-coupling. The correlation of ^{1}H and ^{15}N chemical shifts are recorded as cross peaks in a 2D spectrum, which can resolve overlapping resonance. The simplest HSQC version and the exchange-regime dependent appearance of the spectrum is briefly outlined in the following section. A more detailed description is given in the reference to the commonly used notations [148, 149]. The HSQC pulse sequence contains the 'Insensitive nuclei enhancement by

polarization transfer' (INEPT) pulse sequence, which is integrated in many pulse sequences as a heteronuclear polarization transfer element [150].

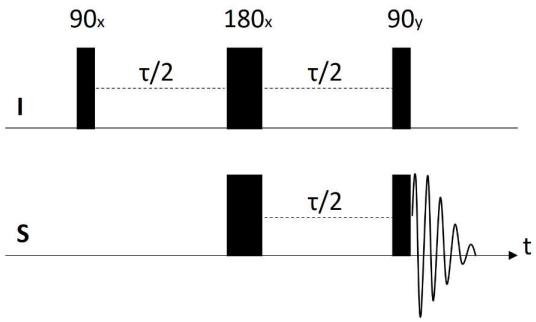

Figure 8: Pulse sequence of an INEPT. The INEPT pulse element is used to transfer magnetization from nuclei I to nuclei S via J_{IS} coupling. The first pulse creates transverse magnetization I_y. The period τ has to be adjusted according to $1/2J_{IS}$ to obtain antiphase magnetization $2I_xS_z$, while the 180° pulses on I and S nuclei refocus chemical shift evolution. Narrow and wide rectangular bars represent 90° and 180° pulses, respectively.

In the INEPT sequence, the proton spin is represented by I, and the nitrogen spin by S (Figure 8). First, the initial proton magnetization I_z is polarized by a 90_x pulse to in-phase proton magnetization $-I_y$. This is followed by magnetization transfer involving a period τ/2, two 180_x pulses on the proton and the heteronucleus, and again a period τ/2. After the period τ the magnetization $-I_y$ is refocused and converted to anti-phase coherence $-2I_xS_z$ by the influence of the proton-nitrogen J_{HN} coupling. The last two 90_x pulses convert the $-2I_xS_z$ coherence to$-2I_zS_y$, which converts after refocusing of the coupling to a detectable magnetization of the nitrogen.

In the HSQC experiment, two INEPT sequence elements are integrated. In the first one, the excited proton magnetization is transferred to the nitrogen, and in the second one, the nitrogen magnetization is transferred back to proton for detection. In between, the nitrogen chemical shift ω_s evolves during the evolution period t_1 according to $2I_zS_y \cos(\omega_s t_1) - 2I_zS_x \sin(\omega_s t_1)$. During the reverse INEPT period the detectable magnetization $I_x \cos(\omega_s t_1)$ is obtained. Proton chemical shift ω_I evolves during the detection period. With heteronuclear decoupling and quadrature detection a single resonance is detected for each proton-nitrogen spin system. The time-domain signal is expressed as:

$$S(t_1, t_2) = \cos(\omega_S * t_1) * e^{i*\omega_I*t_2} \qquad \text{(eq. 16)}$$

The dispersive signal $-\mathrm{i}\sin(\omega_S * t_1)$ is obtained analogously. Eventually, the 2D spectrum is obtained by sequential Fourier transformations of the time domain t_1 and t_2 to the frequency domains ω_S and ω_I.

1.5.2 Concept of chemical exchange

The influence of exchange processes, e.g. protonation, water-exchange or ligand binding affect the appearance of the NMR spectrum [151]. The reaction that describes binding of a monovalent ligand L to a single site on a protein P is:

$$[P] + [L] \underset{k_{-1}}{\overset{k_1}{\rightleftarrows}} [PL] \qquad \text{(eq. 17)}$$

Where k_1 is the forward rate constant for ligand binding, and k_{-1} is the reverse rate constant for unbinding. Regarding this reaction as a chemical exchange process, the protein has two states, the free state P and the bound state PL. Nuclei can experience a change of their chemical environment upon binding, which results in a difference of the resonance frequency of the bound and the unbound state $\Delta\nu = \nu_P - \nu_{PL}$. The chemical shift of the unbound and bound state differs, and consequently two populations of the spin are manifested.

The equilibrium populations of the two states $[L]_{eq}$ and $[PL]_{eq}$ are given by the equilibrium constant K_{eq}:

$$\mathrm{K_{eq}} = \frac{\mathrm{k_1}}{\mathrm{k_{-1}}} = \frac{[\mathrm{PL}]_{\mathrm{eq}}}{[\mathrm{L}]_{\mathrm{eq}} * [\mathrm{P}]_{\mathrm{eq}}} \qquad \text{(eq. 18)}$$

$$[PL] * k_{-1} = [P] * [L] * k_1 \qquad \text{(eq. 19)}$$

Exchange effects in the spectrum are perceived depending on the exchange rate $k_{ex} = k_1 + k_{-1}$ relative to the frequency difference of the NMR parameter (chemical shift, relaxation rates, etc.) being measured.

In the slow exchange regime k_{ex} << $\Delta\nu$, the rate of exchange is slower than the $\Delta\nu$. Two resonances are observed originating from the unbound and the bound state. The peak integral is

proportional to the population. The chemical shift is not affected by the exchange, however, an increased exchange rate reduces the lifetime, which is observed as a broader peak.

In the fast exchange regime k_{ex} >> Δν, both states are observed as a single resonance with a population averaged resonance frequency ν_{obs}. Due to fast exchange an individual nucleus may change several times its state, such that the observed precession is a combination of the precessions of the unbound and bound states. Fast exchange with averaged resonance occurs more often when a small chemical shift change Δν or a large exchange rate k_{ex} characterizes the reaction.

1.6 Isothermal titration calorimetry

Isothermal titration calorimetry (ITC) is a widespread technique used to analyze molecular interaction. The measurement principle relies on the change in heat, which is released or absorbed by the binding event [152, 153]. It allows to measure the thermodynamic parameters enthalpy ΔH and entropy ΔS, the equilibrium association constant K_A and the stoichiometry n. At constant temperature and pressure the Gibbs free energy is given as

$$\Delta G = -RT\, ln(K_A) = \Delta H - T\Delta S \qquad \text{(eq. 20)}$$

and the dissociation constant given as $K_D = 1/ K_A$.

1.7 Scope of the thesis

A compromised humoral immune response has been reported for malfunctioning SLP65 or CIN85 adapter proteins. Multivalent SLP65 and CIN85 interact with each other and form phase-separated pre-signaling clusters in resting B cells. The pre-signaling clusters are involved in B cell activation and B cell development via the B-cell receptor (BCR) signaling pathway. Tripartite phase separation is driven by promiscuous interaction of PRMs with SH3 domains, SLP65 binding to vesicles and CIN85's trimerization by its coiled-coil domain.

There is no predictive theory that describes phase separation on grounds of molecular interactions and molecular sequence-determinants. In this thesis, I focused on the SH3-PRM interaction of CIN85 and SLP65 and aimed to improve the understanding of phase separation regarding the range of affinity and the modular pattern.

Therefore I pursued the following tasks:

- Measure the range of affinities of PRMs and SH3 domains with NMR spectroscopy and isothermal calorimetry
- Classify distinct binding elements according to their contribution to phase separation using a fluorescence microscopy assay to determine the critical concentrations.
- Simulate phase separation of SLP65 and 3SH3 by the LAttice simulation engine for Sticker and Spacer Interactions in order to find parameter sets that agree with the experimental critical threshold concentrations.
- Correlate *in vitro* determined monovalent binding affinities with *ex vivo* Ca^{2+} signaling capacity
- Correlate effects of designer constructs from *in vitro* phase separation experiments with *ex vivo* readouts of the Ca^{2+} signaling capacity and number of cytosolic droplets.

Materials and methods

2.1 Consumables

Buffer reagents and chemicals were purchased from Merck, Sigma or Roth if not stated otherwise.

List of reagents and chemicals:

Additive of lysis buffer: Complete™-EDTA (Roche, Basel, Switzerland)
Atto 430LS, ATTO-TEC GmbH, Siegen
Deuteriumoxid, Deutero GmbH, 56288 Kastellaun
DOPC, Avanti Polar Lipids, Alabaster, Alabama, USA
DOPE, Avanti Polar Lipids, Alabaster, Alabama, USA
DOPS, Avanti Polar Lipids, Alabaster, Alabama, USA
DURAN test tube, 14 x 130 mm, 16 ml (Schott) DWK Life Sciences GmbH, Wertheim
Eppendorf UVette, 20-200 µl, Eppendorf AG, Hamburg
Eppendorf reaction tube, 1.5 ml, 2 ml, 5 ml, Eppendorf AG, Hamburg
HiLoad 26/60 Superdex 200 prep grade, GE Healthcare, Chicago, Illinois, USA
PCR-based mutagenesis (Quikchange II kit, Agilent, Santa Clara, California, USA)
Pefabloc - protease inhibitor Merck KGaA, Darmstadt
Polycarbonate membrane, pore diameter = 50 nm, diameter = 0.75" (19 mm), Avestin
PTFE tubing, 1/16" AD, 1.0 mm ID, CS-Chromatographie Service GmbH, Langerwehe
Superdex 75 10/300 GL, GE Healthcare, Chicago, Illinois, USA
Superdex 30 10/300 GL, GE Healthcare, Chicago, Illinois, USA
Uncoated µ-Slide 8 Well, ibidi GmbH, Gräfelfing
Vivascience concentrators, Sartorius, Göttingen

2.2 Plasmids

For protein expression of $SLP65_{1-330}$-3xPRM4 (in the following referred to as SLP65-3xPRM4) and CIN85-3SH3B commercial plasmids were purchased (Invitrogen) and the coding sequences were cloned into *Escherichia coli* expression vectors. The SLP65-3xPRM4 coding sequence was cloned into a pET16b/TEV via BamH1/Ndel restriction sites. For fluorophore labeling a C-terminal cysteine was introduced by site-directed mutagenesis using primers SLP37 and SLP38 (see section 2.3). The coding sequence for CIN85-3SH3B was cloned via BamH1/HindIII restriction sites into a modified pET28a vector (Novagen) encoding for an N-terminal Z2 fusion domain with TEV cleavage site and an His7-tag. The $SLP65_{1-330}$-R247A (in the following referred to as SLP65-R247A) plasmid was generated by site-directed PCR mutagenesis on the $SLP65_{1-330}$ plasmid described previously [116] using primers SLP21 and SLP22. For expression of PFN1, the pfn1 gene was cloned from the pCMV SPORT6-PFN1 [154] (provided by the Harvard Medical School) into pET32a vector (Novagen) [155].

2.3 Primers

SLP21: $SLP65_{1-330}$-R247A forw., into C271A, S236C

$^{5'}$cac cat ccc cgt tgc caG Cgg ccg gga aaa aac caa c$^{3'}$

SLP22: $SLP65_{1-330}$-R247A rev., into C271A, S236C

$^{5'}$GTT GGT TTT TTC CCG GCC GCT GGC AAC GGG GAT GGT G$^{3'}$

SLP37: $SLP65_{1-330}$-3xPRM4 (mutant C-terminal cysteine) forw.

$^{5'}$CCT CTG CCG AGC TTT AGC AGC TGC taa AGG ATC CGG CTG CTA AC$^{3'}$

SLP38: $SLP65_{1-330}$-3xPRM (mutant C-terminal cysteine) rev.

$^{5'}$GTT AGC AGC CGG ATC CTT TAG CAG CTG CTA AAG CTC GGC AGA GG$^{3'}$

2.4 Instruments

Analytical balance MC1, Sartorius Lab Instruments GmbH, Göttingen

Agilent 8453 UV-visible spectrophotometer, Agilent Technologies Deutschland GmbH, Waldbronn

Äkta Purifier (900), GE Healthcare, Chicago, Illinois, USA

Bruker Avance 600 MHz equipped with a QCI 600S3 H-P/C/N-D-05 Z probe

Bruker Avance 700 MHz equipped with a CPTCI 1H-13C/15N/D Z probe

Bruker Avance NEO 700 MHz equipped with a CPP TCI 1H/19F-13C/15N/D Z probe

Bruker Neo 800 MHz equipped with a CP TCI 800S7 H-C/N-D-03 Z probe

Bruker Avance 800 MHz equipped with a CP2.1 TCI 800S6 H-C/N-D-05 Z probe

Bruker AVANCE III HD 900 MHz equipped with a CP TCI 900S6 H-C/N-D-05 Z probe

Cold centrifuge, Avanti J-20, Beckman Coulter, Brea, California, USA

Cold centrifuge, Avanti J-30I, Beckman Coulter, Brea, California, USA

Confocal Laser scanning microscope Zeiss LSM780, Plan-Apochromat 40x/1.4 Oil DIC M27 objective

Confocal Laser scanning microscope Zeiss LSM880, LCI Plan-Neofluar 63x/1.3 Imm Korr DIC M27 objective

Confocal Laser scanning microscope TCS SP5 Leica

Confocal Laser scanning microscope TCS SP8 Leica

Drying cabinet, EED72, BINDER GmbH, Tuttlingen

Dynamic light scattering, DynaPro Titan Batch System s/N: 218-DPTH, Wyatt Technologies Corporation, Goleta, California, USA

Emulsiflex homogenizer C3, Avestin

Freeze dryer, Alpha 2-4 LD plus, Martin Christ Gefriertrocknungsanlagen GmbH, Osterode am Harz

Freezer, VIP series -86 °C, SANYO Electric Biomedical Co., Osaka, Japan

HPLC system (PU-2080Plus, MD-2010, DG-2080-54, LG-2080-04, AS-2055), JASCO Deutschland GmbH, Pfungstadt

ITC calorimeter: VP-ITC System, MicroCal, Northampton, Massachusetts, USA

LC-MS system, Waters Corporation, Milford, MA, USA

Microcentrifuge 5415R, Eppendorf AG, Hamburg

Mini Extruder, Avanti Polar Lipids, Alabaster, Alabama

Seveneasy pH-meter S20, Mettler Toledo, Gießen

Ultrasonic homogenizers, Sonoplus HD 3100, BANDELIN, Berlin

Vortex Genie 2, Scientific Industries Inc., Bohemia, New York, USA

Water Purification System, Milli-Q Reference A, Sartorius, Göttingen

2.5 Software

Cara.1.8.4.2 [156]

CcpNmr Analysis 2.4.2, The Collaborative Computing Project for NMR (CCPN) [157]

CLUSTAL 2.1 multiple sequence alignment [158]

Dynamic light scattering: Dynamics v6.12.0.3, Wyatt Technology Corp., Goleta, California, USA

LASSI v0.1.0 [103]

MATLAB R2019b, The MathWorks Inc., Natick, Massachusetts, USA

Microsoft Excel 2016, Microsoft, Redmond, Washington, USA

Molecular visualization: VMD 1.9.v1 [159]

NMR acquisition and processing: Topspin 4.08, Bruker, Billerica, Massachusetts, USA

NMR binding analysis: TITAN v1.5-3-g3566 [160]

ITC analysis: Origin 7 SR2 v7, Origin Lab Corporation, Massachusetts, USA

ITC measurement: VP Viewer 2000, MicroCal, Northampton, Massachusetts, USA

PyMOL Molecular graphics system v.2.3.3, Schrödinger Inc., USA

Scientific Python Development Environment: Spyder 3.3.6

Secondary structure propensity prediction: δ2D v2.0.0 [161]

UV-vis spectrometer: ChemStation B.04.02, Agilent Technologies, Santa Clara, California, USA

2.6 Protein expression, purification and labeling

Purified and fluorophore-labeled proteins were provided by Claudia Schwiegk or (Max Planck Institute for Biophysical Chemistry, Department of NMR-based Structural Biology). Purified profilin-1 was provided by Melanie Wegstroth (Max Planck Institute for Biophysical Chemistry, Department of NMR-based Structural Biology).

The three individual SH3 domains of CIN85 SH3A, SH3B and SH3C were expressed in *Escherichia coli* BL21 (DE3) (New England Biolabs). The sequence of SH3A and SH3B were cloned into a pGEX4-T, encoding Glutathione-S-transferase (GST) fusion proteins, expressed and purified by affinity chromatography (resin: Pierce™ Glutathione Agarose). The proteins were dialyzed at 23 °C against 20 mM HEPES (pH 7.2), 150 mM NaCl, 1 mM DTT. Thrombin was added during dialysis to cleave off the GST fusion tag. The second purification step was a size exclusion chromatography (Superdex 75 16/60 GL, GE Healthcare). Fractions were pooled and dialysed for >12 at 4° C against 20 mM HEPES (pH 7.2), 100 mM NaCl buffer, 1 mM DTT and 0.5 mM PMSF. The coding sequence of SH3C was cloned into a modified pET16b vector including a TEV-protease cleavage site and a His_7-tag for affinity purification. After expression and affinity purification, the

SH3C protein was dialyzed for > 12 h at 23 °C against 20 mM Tris/HCl (pH 8.0), 200 mM NaCl, 0.5 mM EDTA, 1 mM DTT, 0.5 mM PMSF buffer including TEV-protease (TEV-Protease:SH3C 1:50) to cleave the His_7-tag. To remove the cleaved His_7-tag a reverse affinity purification (Ni-NTA Protino resin, Macherey-Nagel) was done. Then protein was dialyzed against 20 mM HEPES (pH 7.2), 100 mM NaCl, 1mM DTT, 0.5 mM PMSF and afterwards purified by size exclusion chromatoraphy in the same buffer.

$SLP65_{1-330}$, CIN85-3SH3 and CIN85Δ57 were expressed as described previously [116].

SLP65-R247A, SLP65-3xPRM4 and CIN85-3SH3B were expressed in strain BL21 (DE3) (New England Biolabs) and purified by Ni-NTA affinity chromatography. The His_7-tag was removed by TEV-cleavage (1:50 mass ratio, protease:protein) during dialysis against 20 mM Tris/HCl (pH 8.0), 200 mM NaCl, 0.5 mM EDTA, 1 mM DTT and 0.5 mM PMSF. The cleaved off His_7-tag was removed by reverse affinity chromatography and the flow through was dialyzed against 20 mM HEPES (pH 7.2), 200 mM NaCl, 1 mM DTT and 0.5 mM PMSF. As last purification step, the protein was applied to a gel filtration column (HiLoad 16/60 SD 75 gel filtration column, GE Healthcare).

Finally, all proteins were dialyzed against 20 mM HEPES (pH 7.2), 100 mM NaCl, 1 mM TCEP, 0.5 mM Pefabloc and their final concentration was adjusted with Vivascience concentrators (Sartorius) of appropriate molecular weight cutoffs.

For fluorescence labeling, atto 430LS dye (Atto-Tec) was conjugated by a maleimide thiol reaction (according to the manufacturer´s protocol). $SLP65_{1-330}$, SLP65-R247A and SLP65-3xPRM were atto 430LS-labeled at residues C271 or the mutant S236C and also the introduced C331, respectively. The reaction product was always purified by size exclusion chromatography (Superdex 75 10/300 GL, GE Healthcare).

PFN1 was expressed in BL21(DE3) *E. coli* cells, which were lyzed on an Emulsiflex homogenizer (Avestin), followed by centrifugation (20 min, 20 000 rpmi, Avanti J-30I, Beckman Coulter). The supernatant was loaded on a poly-L-proline column (packed with NBr-activated Sepharose 4B resin coupled to poly-L-proline, GE Healthcare) followed by an elution of the purified protein with 8 M urea. The protein was refolded while the urea was removed by stepwise dialysis in 20mM

TRIS (pH 7.5), 0.5mM EDTA, 0.5mM EGTA, 1.5mM magnesium-acetate and 2 mM DTT. The protein was further purified on by anion exchange chromatography on a DEAE FF column (GE Healthcare) and finally concentrated to 3mM PFN1 in 20mM TRIS (pH 7.5), 0.5mM EDTA, 0.5mM EGTA, 1.5mM Mg-acetate and 2 mM DTT buffer.

Protein concentration was determined by UV-vis absorbance using the molar extinction coefficient at 280 nm. Protein concentrations were corrected for atto 430LS absorption, which has its maximum absorption peak at 430 nm. Thus, the concentration of atto 430LS-tagged protein constructs was determined by the molar extinction coefficient at 280 nm taking into account the absorbance ratio 280 nm / 430 nm of atto 430LS.

2.7 Peptide ligands

The amino acid sequences of the peptide ligands were derived from a 14 amino acid long region around PRMs comprising SLP65-PRM1, SLP65-PRM2, SLP65-PRM3, SLP65-PRM4, SLP65-PRM*, SLP65-PRM5, SLP65-PRM6, SLP65-PRM4-R247A and a 24 amino acid long region comprising two potential motifs SLP65-PRM4+PRM* (Table Table **3**).

Table 3: SLP65-derived peptides: The peptides derived from the SLP65 sequence were synthesized to measure the binding affinities to SH3A, SH3B and SH3C.

SLP65-PRM1	K_{40}VKAPPSVPRRDYA_{53}
SLP65-PRM2	T_{105}RPVH-PALPFARGE_{118}
SLP65-PRM3	A_{158}LQKPQVPPKPKGL_{171}
SLP65-PRM4	P_{238}PAAPSPLPRAGKK_{251}
SLP65-PRM*	A_{248}GKKPTTPLKTTPV_{261}
SLP65-PRM5	C_{271}EEKPIPAERHRGS_{284}
SLP65-PRM6	I_{303}HQKPIPLPRFTEG_{316}
SLP65-PRM4-R247A	P_{238}PAAPSPLPAAGKK_{251}
SLP65-PRM4+PRM*	P_{238}PAAPSPLPRAGKKPTTPLKTTPV_{261}

To study CIN85's proline-rich region 366-425, first, two peptides were synthesized from the sequences CIN85-S1 and CIN85-S2 (Table 4). CIN85-S2 was further split and the two peptides CIN85-PRM2 and CIN85-PRM3 were synthesized.

Table 4: CIN85-derived peptides: The peptides derived from the CIN85 sequence were synthesized to measure the binding affinities to SH3A, SH3B and SH3C.

CIN85-S1	E_{366}RPEMLPNRTEEKERPEREPKLDL$_{389}$
CIN85-S2	L_{390}QKPSVPAIPPKKPRPPKTNSLSRPGALPPRRPERP$_{425}$
CIN85-PRM2	L_{390}QKPSVPAIPPKKPRPPKTNS$_{410}$
CIN85-PRM3	L_{411}SRPGALPPRRPERP$_{425}$

The peptides derived from SLP65-PRM 1-6 were designed by Leo Wong (Max Planck Institute for Biophysical Chemistry, Department of NMR-based Structural Biology). All peptides were provided by Kerstin Overkamp (Max Planck Institute for Biophysical Chemistry, Department of NMR-based Structural Biology). The peptides were synthesized by solid-phase peptide synthesis with acetylated and amidated at the N- and C- termini, respectively. The terminal modified peptides were purified on a RP18 column. For injection on the column, the peptides were dissolved in H_2O with 0.1 % TFA as running buffer. For elution, an acetonitrile solution with 0.1% TFA was used. Molecular mass/charge ratio was measured by HPLC-mass spectrometry. Peptides with correct molecular weight and > 95% purity were further used. Peptides were lyophilized and a stock solution was prepared by weighting in the peptide powder.

2.8 Isothermal titration calorimetry

The interactions between single SH3 domains and single peptides and the interactions of SLP65 constructs to CIN85 constructs were measured by isothermal ITC on a VP-ITC MicroCalorimeter (MicroCal). Titrations were done at 37 °C with 60 s initial delay, a stirring speed of 307 rpm and a

reference power of 10 µCal/second. The injection scheme is shown in table 5. For the measurement of monovalent interactions, 500 µM peptide was titrated to 20 µM SH3 domain with a spacing (Time between injection points) of 400 s. For titration of multivalent designer constructs, the spacing was increased to 600 s to reach equilibration after each injection. For smoothening the data, the filter period over which the data channel conversions are averaged was set to 2 s. Peptides and protein samples of SLP65 constructs dissolved in 20 mM HEPES (pH 7.2) buffer with 100 mM NaCl were degassed before titration.

Table 5: Injection scheme for ITC titrations on the VP-ITC MicroCalorimeter (MicroCal). SLP65-peptides derived from PRM1 to PRM6 and CIN85-peptides derived from CIN85's proline-rich region were titrated to SH3A, SH3B and SH3C domains. *Wildetype*, weak- and strong-binding $SLP65_{1-330}$ constructs were titrated to CIN85-3SH3/3SH3B constructs. Total injection volume was 284 µl.

Injection number	Injection volume [µl]	Duration of injection [ms]	Time between injection points: Spacing [s]	Filter Period [s]
1	4.0	8.0	400 / 600	2
2	20.0	40.0	400 / 600	2
3	20.0	40.0	400 / 600	2
4	20.0	40.0	400 / 600	2
5	20.0	40.0	400 / 600	2
6	20.0	40.0	400 / 600	2
7	20.0	40.0	400 / 600	2
8	20.0	40.0	400 / 600	2
9	20.0	40.0	400 / 600	2
10	20.0	40.0	400 / 600	2
11	20.0	40.0	400 / 600	2
12	20.0	40.0	400 / 600	2
13	20.0	40.0	400 / 600	2
14	20.0	40.0	400 / 600	2
15	20.0	40.0	400 / 600	2

Binding isotherms of multivalent protein constructs were fitted with the single-site model (Origin 7) due to the lack of complete data set for global analysis [162, 163] (Appendix I). Binding isotherms of peptide titrations were fitted with the single-site model (Origin 7) fixing the n-value = 1 (no floating n value) (Appendix J).

2.9 Vesicle preparation

SUVs were prepared as briefly described previously [116]. Lipids were weighed in separately in glass vials (Duran) and completely resuspended in chloroform to obtain DOPC, DOPE and DOPS stock solutions. A mixture with a total volume of 1 ml and a final total lipid concentration of 5 mM with a lipid composition of 65:25:10 (DOPC: DOPE: DOPS *%w/w*) was prepared. To prepare a lipid film, the lipid composition was dried from chloroform by a nitrogen stream. The lipid film was either stored for later use or lyophilized for >12 hours. To generate vesicles, the lipid film was resuspended in 20 mM HEPES (pH 7.2) buffer with 100 mM NaCl and rigorously shaken for complete resuspension. The final lipid suspension was transferred to a 15 ml plastic tube (Falcon) for high power tip sonication on ice for 2 x 20 min (Sonoplus HD 3100). Tip sonication settings were a 60% amplitude power and pulsation switching between 3 sec on and 2 sec off (or a pulsation switching cycle of 2 sec on / 2 sec off). After sonication, the suspension was diluted 1:10 for the measurement of the vesicle hydrodynamic radius distribution by dynamic light scattering (DLS). The solution was checked for clarity and then further extruded 25 times (Mini Extruder, Avanti Polar Lipids) using a 50 nm polycarbonate membrane filter (Avestin) to achieve a more homogenous vesicle size distribution. To check the extrusion process, the SUV hydrodynamic radius distribution of a 1:10 dilution was measured by DLS. The 5-mM-lipid SUV preparation was diluted 1:2 to a final 2.5-mM-lipid SUV solution to be used in the microscopy assay.

2.10 In vitro droplet reconstitution

For *in vitro* reconstitution of SLP65/CIN85/SUV droplets, components were mixed in a 1.5 ml Eppendorf tube in the following order. Buffer was pipetted first. The tube containing SUVs stock solution (2 mM lipid stock) was flipped 2-3 times, SUV solution was added and homogeneously mixed. Then, the SLP65 stock solution was rigorously shaken for 1 second (Vortex), added and homogenously mixed by resuspending the solution 5 x. Next, the CIN85 stock solution was rigorously shaken for 1 second (Vortex), added to the SLP65/SUV suspension and homogenously mixed by resuspending the solution 5 – 10 x. The total volume of the mixture was 25 µl. The

mixture was transferred to a microscope slide (uncoated µ-Slide 8 Well, ibidi GmbH, Gräfelfing) and incubated for 50 – 70 minutes at 23 °C.

Note that poor, inhomogeneous mixing yields a few large droplets and a minor number of regular-sized droplets, such that in the worst case, droplets can be overlook if not the whole region is examined under the microscope. Also note that replicability is achieved if protein stock concentrations for pipetting are considered and dilutions are made accordingly. Dilution stocks of 8 µM, 25 µM, 80 µM and 125 µM protein concentration were prepared and used in fluorescence microscopy assay mixtures requiring concentrations below 60 µM. The highest available SLP65-R247A stock concentration of 640 µM was used for the "SLP65-R247A – 3SH3" assays. Protein stock concentrations of 25 µM and 125 µM were used for "SLP65-3xPRM4 – 3SH3" and "SLP65-R247A – 3SH3 – SUVs" fluorescence microscopy assay mixtures. 25 µM and 80 µM protein stock concentrations were used for "SLP65-3xPRM4 – 3SH3B" and "SLP65-R247A – 3SH3 - SUVs" fluorescence microscopy assay mixtures. 8 µM and 25 µM protein stock concentrations were used for the remaining seven fluorescence microscopy assay mixtures, with "$SLP65_{1\text{-}330}$ – 3SH3", "SLP65-3xPRM4 – 3SH3", "$SLP65_{1\text{-}330}$ – 3SH3 - SUVs", "SLP65-3xPRM4 – 3SH3 - SUVs", "SLP65-R247A – 3SH3B - SUVs", "$SLP65_{1\text{-}330}$ – 3SH3B - SUVs" and "SLP65-3xPRM4 – 3SH3B - SUVs"

Fluorophore-labeled and unlabeled SLP65 constructs were mixed in order to ease microscopy and keep the same laser excitation power and camera detection settings. Fluorescence-labeled SLP65 protein stock was used up to a concentration of 10 µM, and mixed with unlabeled SLP65 constructs, if a concentration above 10 µM was required.

2.11 In vitro droplet reconstitution for cryo-electron tomography

Cryo-electron tomography was performed in collaboration with Prof. Plitzko's lab (Department of Molecular Structural Biology, MPI of Biochemistry, Martinsried). 1 µM $SLP65_{1–330}$, 1 µM CIN85Δ57 and SUVs (1 mM lipid concentration) were mixed as described above and incubated in an Eppendorf tube for 45 min. 3.4 µl of the mixture were transferred to a carbon grid (R2/1 copper TEM grids, Quantifoil) and blotted between filter paper and a teflon membrane on a Vitrobot Mark IV (FEI) using the following settings: blot force = 10, blot time =10 s,

temperature = 21 °C, humidity = 90%, immediately afterwards the blot was plunge-frozen in liquid ethane.

The samples were kept vitreous, mounted on a Polara cryo-transmission electron microscope and screened at low magnification for sample features and desired thickness for suitable cryo-electron tomography locations. Tomograms were acquired on a transmission electron microscope (Titan Krios, FEG 300 kV, FEI) [116].

Sample preparation was done by Zhen Hou (Department of Molecular Structural Biology, Max Planck Institute of Biochemistry) and myself. Data acquisition and processing was done by Philipp Erdmann (Department of Molecular Structural Biology, MPI of Biochemistry) and Zhen Hou.

2.12 NMR spectroscopy

For the NMR titration experiments, the ^{15}N-labeled proteins were expressed in M9 minimal medium [164] supplemented with ^{15}N-NH_4Cl and expressed as described above. Samples were prepared in 1.5 ml reaction tubes and transferred with a PTFE tubing into 3-mm NMR tubes (Hilgenberg). 0.5 mM DSS was added as chemical shift reference and 4% D_2O was added for locking. The NMR titrations were performed at 37 °C on 600 MHz, 700 MHz, 800 MHz or 900 MHz spectrometers equipped with a z-gradient cryoprobe. Table 6 lists the protein and peptide concentrations of the two CIN85 fragments (CIN85-S1 and CIN85-S2) comprising the proline-rich region of CIN85, which were titrated the 3SH3 construct, and the concentrations of the titration of PFN1 to SLP65. The receptor concentration of the CIN85's SH3 domains and the titration ratios (ligand:protein) are listed in Table 7.

Table 6: Concentrations of NMR titrations of CIN85-S1, -S2 and PFN1 to 3SH3 or SLP65. Receptor concentration and ligand/protein ratios for the NMR titrations of and CIN85-derived peptides (ligand) to the 3SH3 construct (receptor), and for the titration of PFN1 to SLP65.

Ligand: Peptide X	Receptor: CIN85-SH3 domain	Receptor concentration [µM]	Molar ligand/receptor ratios
CIN85-S1	3SH3	100	0.4, 0.9, 1.3, 1.7, 2.5, 5.0
CIN85-S2	3SH3	100	0.4, 0.9, 1.3, 1.7, 2.5, 5.0
PFN1	$SLP65_{1-330}$	100	0.02, 0.09, 0.4, 1.7, 3.0

Table 7: Concentrations of NMR titration experiments of peptides to the SH3 domains. NMR titration of SLP65- and CIN85-derived peptides (ligand) to the SH3A, SH3B or SH3C domain (receptor) was performed at the indicated receptor concentration and ligand/protein ratios.

Ligand: Peptide X	Receptor: CIN85-SH3 domain	Receptor concentration [µM]	Molar ligand/receptor ratios
SLP65-PRM1	SH3A	200	0.2, 0.5, 0.7 , 0.9, 1.1, 1.4 , 1.6, 1.8, 2.0, 2.6, 3.3
SLP65-PRM2	SH3A	200	0.6, 1.2, 1.8, 2.4, 3.2, 4.7
SLP65-PRM3	SH3A	200	0.5, 0.9, 1.4, 1.8, 2.3, 2.7, 3.5, 4.3
SLP65-PRM4	SH3A	200	0.3, 0.6, 0.9, 1.2, 1.5, 2.4, 4.1, 7.1, 10.2, 10.7
SLP65-PRM*	SH3A	200	0.3, 0.6, 0.9, 1.2, 1.8, 2.4, 3.3, 4.7
SLP65-PRM5	SH3A	200	0.5, 0.9, 1.5, 1.8, 1.9, 2.2, 2.6, 3.8, 5.7, 9.0
SLP65-PRM6	SH3A	200	0.3, 0.6, 0.9, 1.2, 1.5, 2.4, 3.3, 4.7, 9.0
CIN85-PRM2	SH3A	200	0.2, 0.5 , 0.9, 1.9, 2.7, 4.0, 6.9, 9.9
CIN85-PRM3	SH3A	200	0.7, 1.1 , 1.6, 2.4, 3.7, 6.8
SLP65-PRM1	SH3B	260	0.2, 0.5, 0.8, 1.1, 1.3, 1.6, 2.2, 2.8, 3.4, 4.0
SLP65-PRM2	SH3B	200	0.3, 0.6, 0.9, 1.2, 1.8, 2.7, 4.7, 7.4, 10.0
SLP65-PRM3	SH3B	260	0.5, 0.9, 1.4, 1.8, 2.3, 2.7, 3.5, 4.3, 5.6
SLP65-PRM4	SH3B	200	0.6, 1.3, 1.6, 2.5, 3.4, 4.1, 5.0, 10.0
SLP65-PRM*	SH3B	200	0.6, 1.2, 1.5, 2.1, 2.9, 3.4, 4.2, 8.0, 11.6
SLP65-PRM5	SH3B	200	0.3, 0.9, 1.2, 1.5, 2.1, 3.0, 3.4, 4.2, 8.0
SLP65-PRM6	SH3B	200	0.6, 0.9, 1.2, 1.5, 2.4, 3.3, 4.7
CIN85-PRM2	SH3B	200	0.2, 0.5, 0.9, 1.4, 2.3, 3.6, 6.9, 10.7, 11.2
CIN85-PRM3	SH3B	200	0.2, 0.5, 0.9, 1.3, 2.2, 3.5, 6.6
SLP65-PRM1	SH3C	200	0.3, 0.6, 0.9, 1.2, 1.5, 2.4, 3.3, 4.7, 9.0
SLP65-PRM2	SH3C	200	0.6, 1.2, 1.8, 2.4, 3.3, 4.7, 8.9, 12.8
SLP65-PRM3	SH3C	200	0.9, 1.2, 1.5, 2.4, 3.3, 4.7, 9.0
SLP65-PRM4	SH3C	200	0.3, 0.6, 0.9, 1.2, 1.5, 2.4, 3.3, 4.7, 9.0
SLP65-PRM*	SH3C	200	0.3, 1.2, 1.5, 2.4, 3.3, 4.7, 9.0
SLP65-PRM5	SH3C	200	0.3, 0.6, 0.9, 1.2, 1.5, 2.4, 3.3, 4.7, 9.0
SLP65-PRM6	SH3C	200	0.9, 1.2, 1.5, 2.4, 3.3, 4.7, 9.0
CIN85-PRM2	SH3C	150	0.2, 0.3, 0.8, 1.3, 2.1, 3.4, 6.8, 9.8
CIN85-PRM3	SH3C	150	0.2, 0.3, 0.8, 1.3, 2.1, 3.4, 6.8, 9.8

The sensitivity-enhanced ^{15}N-HSQC experiment was measured with the standard pulse program (hsqcetf3gpsi, see Appendix A for transcript of the pulse program) or an adapted version (hsqc15N.leo, in house pulse program) with 2048 complex points in the direct dimension, 256 complex points in the indirect dimension, 4-12 scans and a recycle delay in the range of 1.2 – 1.5 s. A water-flipback pulse for water suppression and waltz16 decoupling was applied. Spectra were processed in Topspin 4.06 (Bruker) applying a cosine-squared window function in both dimensions and if required a 0th or 1st order phase correction. Spectra were analyzed by 1D chemical shift or 2D lineshape analysis (Appendix E and H).

The NMR triple resonance assignment experiments HNCACB (hncacbgp3d, [165, 166]) and CBCA(CO)NH (cbcaconhgp3d [166, 167] were acquired of both 1 mM ^{13}C,^{15}N-labeled SH3A domain and 0.5 mM ^{13}C,^{15}N-labeled SH3C domain at 700 MHz and 800 MHz spectrometers, respectively in 20mM HEPES (pH 7.2), 50 mM NaCl buffer at 298 K. For SH3B assignment, the HNCA (hncagpwg3d [168-170]) NMR experiments was recorded in 20mM HEPES, pH 7.2, 50 mM NaCl buffer at 600 MHz at 298 K. The triple resonance experiments were recorded by L. Wong. In order to analyze ^{15}N-HSQC titration experiments, a ^{15}N-HSQC experiment at 30 °C was recorded, and the ^{1}H and ^{15}N assignment were transferred from 25 °C to 37 °C by following the chemical shift with increasing temperature.

2.13 Fluorescence microscopy

The presence of reconstituted droplets was imaged by confocal fluorescence microscopy using a Zeiss LSM780 or LSM880 confocal microscope, an MBS 458 beam splitter and a Plan-Apochromat 40x/1.4 Oil DIC M27 objective or an LCI Plan-Neofluar 63x/1.3 immersion corrected DIC M27 objective. After 45 min incubation time, nearly all large droplets, and after 60 min incubation time, nearly all small droplets settled on the surface of the sample well (uncoated µ-Slide 8 Well, ibidi GmbH, Gräfelfing). The focus was set 1-2 µm below the surface and a z-stack of 4 – 12 images with a step size of 1 µm was acquired. Atto 430LS-tagged SLP65 was excited by an argon laser at 458 nm. Emission was detected in the 520-600 nm range. Laser settings and representative acquisition parameters were chosen depending on the fluorophore concentration (Table 8). In

parallel, bright field images were recorded (detector gain BF: 400). Images of the surface (z-position at ~0 µm) were selected and analyzed with the ImageJ software (NIH, Bethesda, MD, USA).

Table 8: Acquisition scheme of fluorescence microscopy parameters. Representative Laser settings and representative acquisition parameters were chosen to adapt to varying atto 430LS-tagged SLP65 concentrations.

Atto 430LS concentration [µM]	Argon laser attenuation	Detector Gain of ChS1	Format [pixel] and zoom factor	Speed factor	Number of sum average
10	0.4	800	1k x 1k 1	4	1
10	0.4	800	2k x 2k 3	6	1
8	0.5	800	1k x 1k 1	3	1
8	0.5	800	2k x 2k 3	5	1
6	"	800	1k x 1k 1	3	1
6	"	800	2k x 2k 3	5	1
5	"	800	1k x 1k 1	4	1
5	"	800	2k x 2k 3	6	1
4	0.6	800	1k x 1k 1	4	1
4	"	800	2k x 2k 3	6	1
3	"	800	1k x 1k 1	4	1
3	"	800	2k x 2k 3	6	1
2.5	"	800	1k x 1k 1	4	1
2.5	"	800	2k x 2k 3	6	1
2	0.7	800	1k x 1k 1	3	1
2	0.7	800	2k x 2k 3	5	1
1.5	"	800	1k x 1k 1	4	1
1.5	"	800	2k x 2k 3	6	1
1	0.8	800	1k x 1k 1	4	1
1	0.8	800	2k x 2k 3	6	1
0.5	"	1050	1k x 1k 1	3	2
0.5	"	1050	2k x 2k 3	3	2
0.25	0.9	1050	1k x 1k 1	3	4
0.25	0.9	1050	2k x 2k 3	3	4
0.18	1.0	1050	1k x 1k 1	3	4
0.18	1.0	1050	2k x 2k 3	3	4
0.13	1.0	1050	1k x 1k 1	4	8
0.13	1.0	1050	2k x 2k 3	4	8

2.14 Lattice-based Monte Carlo simulations of phase separation:

2.14.1 Simulation parameter settings and structure of the molecular architecture

A sticker-spacer lattice model for the system of SLP65 and the 3SH3 fragment of CIN85 ($CIN85_{1-333}$) was designed to simulate phase separation by a Monte Carlo approach using the software LASSI. The molecule architecture is defined by stickers and spacers. The architecture of SLP65 comprises 6 stickers representing 6 PRMs and the architecture of 3SH3 comprises 3 stickers (Figure 9). In the simulations, each sticker occupies one lattice point, while the spacers are implicitly modeled by a distance restraint without occupying a lattice point. The number of a.a. in SLP65's and CIN85's linkers were scaled considering the fact that 6 amino acids of the PRM form 1 bead interacting with one SH3 domain represented also by 1 bead. Thus, we represent also in the linkers 6 amino acids by 1 bead introducing the linker scaling by 1/6. . Further linker scalings (2/3, 1/2, 1/3, 1/8, 1/9 and 1/11) are used and discussed.

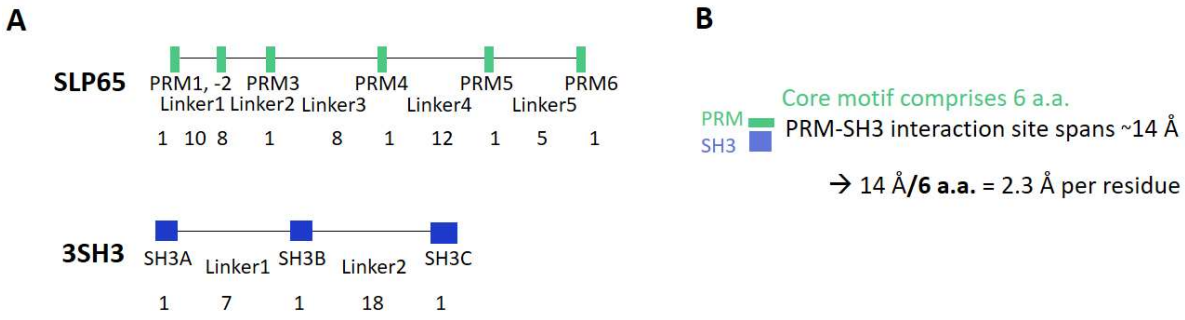

Figure 9: Molecular architecture design in LASSI. A) The design of the SLP65 and CIN85 structures in LASSI is based on stickers and spacers/linkers. The SLP65's PRMs and CIN85's SH3 domains are stickers, which are defined as a single bead on one lattice position. The linkers are modeled by a distance restraint, whose length is defined by an integer number in lattice units. B) The scaling of linker by 1/6 implies a reasonable length of the inter-residue distance (14 Å/6 = 2.3 Å per residue). The diameter of the SH3 domain is around 14 Å = 1 bead and is covered by 6 interacting amino acids of the respective PRM. Therefore the 60 a.a. of Linker 1 in SLP65 are represented by 60/6 = 10 linker beads (see also Table 10**Table 9**).

Table 9: Parameter settings for the linkers of CIN85. CIN85's linkers were scaled for the purpose of parameterization. Both PRM and SH3 stickers have to be modeled as single beads (length of a PRM/SH3 sticker = 1). The factor 1/6 scales the length of a linker residue to the ~14 Å long binding site of a SH3-PRM interaction, with a 6 a.a. long motif (14 Å / 6 a.a. = 2.3 Å).

CIN85:	# of aa in Linker 1 42	# of aa in Linker 2 108
Scaling factor	**Linker length**	
4/6	28	72
3/6	21	54
2/6	14	36
1/6	7	18
1/8	5	14
1/9	4	12
1/11	4	10

Table 10: Parameter settings for the linkers of SLP65. Modeled linker length were set by scaling the sequence length of the five linkers of SLP65.

SLP65:	# of aa in Linker 1 60	# of aa in Linker 2 45	# of aa in Linker 3 74	# of aa in Linker 4 27	# of aa in Linker 5 26
Scaling factor:			**Linker length**		
4/6	40	32	48	20	16
3/6	30	24	36	15	12
2/6	20	16	24	10	8
1/6	10	8	12	5	4
1/8	8	6	9	3	3
1/9	7	5	8	3	3
1/11	5	4	7	2	2

In the Monte-Carlo simulation of LASSI, several move sets are predefined algorithms used to displace stickers and spacers of a chain and change the networking states of stickers applying a Markov Chain Monte Carlo move [103]. There is one move per step and a particular move takes place at a chosen frequency within a chosen number of steps. The number of total step was set to $2*10^9$ in order to approach convergence of the simulation. Rotational, local, co-local, shake, translation, small cluster translation, cluster translation, pivot and double pivot moves were

applied at frequencies of 0.25, 0.13, 0.25, 0.04, 0.04, 0.04, 0.04, 0.13, 0.10 per step considering the suggestions for the settings from the authors of the program [103]. The simulations included in total 2000 molecules (1000 for each SLP65 and 3SH3) in order to avoid finite-size effects [103].

The isotropic and anisotropic pairwise interaction energy matrices define all sticker-sticker interactions (Figure 10). A positive interaction energy term leads to a repulsion. A negative interaction energy term is used to model the attraction of an interaction of single PRM-stickers to single SH3 stickers. All isotropic interaction energy terms were set to 0 (Table 11 A) to allow for simulations with short linker lengths as suggested by the authors of LASSI (personal correspondence). The anisotropic interaction energy terms were experimentally parametrized by the Gibbs free energy ΔG.

The PRM-SH3 energy terms of the anisotropic pairwise interaction matrix were derived from experimentally determined dissociation constants. For illustration, the anisotropic pairwise interaction energy matrix of $SLP65_{1-330}$ – 3SH3 is shown in Table 11 B. Models were generated for $SLP65_{1-330}$, for SLP65-R247A, for SLP65-3xPRM4, 3SH3 and 3SH3B considering the individual energy terms of the mutated motif or SH3 domain. The R247A mutation was defined by setting the PRM4 energy terms to 0. The 3xPRM4 mutation was considered by replacing the energy terms of PRM5 and PRM6 with the energy terms of PRM4. And the 3SH3B design was defined by replacing 3SH3's energy terms of SH3A and SH3C by the energy terms of SH3B. 2SH3 was defined by setting the energy terms of SH3C to 0. For illustration, the design of the anisotropic pairwise interaction matrix of SLP65-3xPRM4 - SH3B is shown in Table 8 C.

- Energy terms of the isotropic pairwise interaction energy matrix were set to 0.
- Energy terms E of the anisotropic pairwise interaction energy matrix were set equal to the ΔG, which were derived from the binding constant:

K_D [µM]	PRM1	PRM2	PRM3	PRM4	PRM5	PRM6	SH3A	SH3B	SH3C
PRM1	0	0	0	0	0	0	175	241	630
PRM2	…	0	0	0	0	0	3770	2712	4169
PRM3	…	…	0	0	0	0	342	501	3036
PRM4	…	…	…	0	0	0	159	6	35
PRM5	…	…	…	…	0	0	107	54	209
PRM6	…	…	…	…	…	0	149	96	89
SH3A	…	…	…	…	…	…	0	0	0
SH3B	…	…	…	…	…	…	…	0	0
SH3C	…	…	…	…	…	…	…	…	0

$$\Delta G = RT \ln(K)$$

ΔG in units of [kCal/mol]
NMR experiments at 37 °C → T = 310 K
R = 1.987 cal/K

$$E = \Delta G$$

Anisotropic pairwise interaction energy matrix E_{ij}:

#SC_SC_POT	PRM1	PRM2	PRM3	PRM4	PRM5	PRM6	SH3A	SH3B	SH3C
PRM1	0	0	0	0	0	0	-5.33	-5.13	-4.54
PRM2	…	0	0	0	0	0	-3.44	-3.64	-3.38
PRM3	…	…	0	0	0	0	-4.92	-4.68	-3.57
PRM4	…	…	…	0	0	0	-5.39	-7.38	-6.32
PRM5	…	…	…	…	0	0	-5.63	-6.06	-5.22
PRM6	…	…	…	…	…	0	-5.43	-5.70	-5.74
SH3A	…	…	…	…	…	…	0	0	0
SH3B	…	…	…	…	…	…	…	0	0
SH3C	…	…	…	…	…	…	…	…	0

Figure 10: Scheme for setting the pairwise interaction energy matrices. The isotropic interaction energy terms were set to 0 to allow for simulations with short linker lengths. The anisotropic interaction energy terms were experimentally parametrized by the Gibbs free energy ΔG.

Table 11: Representation of the symmetric, pairwise interaction matrices. A value of the matrix refers to the interaction energy of a distinct sticker-sticker pair. The terms define the interaction energy E, which is used to calculate the interaction's equilibrium probability $p \propto \exp(-\beta * k_B * E)$, where β is the inverse simulation temperature `MC_Temp`, and the Boltzmann constant is defined as k_B = 1 energy units / temperature units. A) Isotropic interaction matrix including positive terms for consideration of repulsion. B) The pairwise interaction matrices of $SLP65_{1\text{-}330}$ – 3SH3. C) The pairwise interaction matrices of SLP65-3xPRM4 – 3SH3B.

A)	**PRM1**	**PRM2**	**PRM3**	**PRM4**	**PRM5**	**PRM6**	**SH3A**	**SH3B**	**SH3C**
PRM1	0.000	0.000	0.000	0.000	0.000	0.000	0.000	0.000	0.000
PRM2	0.000	0.000	0.000	0.000	0.000	0.000	0.000	0.000	0.000
PRM3	0.000	0.000	0.000	0.000	0.000	0.000	0.000	0.000	0.000
PRM4	0.000	0.000	0.000	0.000	0.000	0.000	0.000	0.000	0.000
PRM5	0.000	0.000	0.000	0.000	0.000	0.000	0.000	0.000	0.000
PRM6	0.000	0.000	0.000	0.000	0.000	0.000	0.000	0.000	0.000
SH3A	0.000	0.000	0.000	0.000	0.000	0.000	0.000	0.000	0.000
SH3B	0.000	0.000	0.000	0.000	0.000	0.000	0.000	0.000	0.000
SH3C	0.000	0.000	0.000	0.000	0.000	0.000	0.000	0.000	0.000

B)	**PRM1**	**PRM2**	**PRM3**	**PRM4**	**PRM5**	**PRM6**	**SH3A**	**SH3B**	**SH3C**
PRM1	0.000	0.000	0.000	0.000	0.000	0.000	-5.33	-5.13	-4.54
PRM2	0.000	0.000	0.000	0.000	0.000	0.000	-3.44	-3.64	-3.38
PRM3	0.000	0.000	0.000	0.000	0.000	0.000	-4.92	-4.68	-3.57
PRM4	0.000	0.000	0.000	0.000	0.000	0.000	-5.39	-7.38	-6.32
PRM5	0.000	0.000	0.000	0.000	0.000	0.000	-5.63	-6.06	-5.22
PRM6	0.000	0.000	0.000	0.000	0.000	0.000	-5.43	-5.70	-5.74
SH3A	-5.33	-3.44	-4.92	-5.39	-5.63	-5.43	0.000	0.000	0.000
SH3B	-5.13	-3.64	-4.68	-7.38	-6.06	-5.70	0.000	0.000	0.000
SH3C	-4.54	-3.38	-3.57	-6.32	-5.22	-5.74	0.000	0.000	0.000

C)	**PRM1**	**PRM2**	**PRM3**	**PRM4**	**PRM4**	**PRM4**	**SH3B**	**SH3B**	**SH3B**
PRM1	0.000	0.000	0.000	0.000	0.000	0.000	-5.33	-5.13	-4.54
PRM2	0.000	0.000	0.000	0.000	0.000	0.000	-3.44	-3.64	-3.38
PRM3	0.000	0.000	0.000	0.000	0.000	0.000	-4.92	-4.68	-3.57
PRM4	0.000	0.000	0.000	0.000	0.000	0.000	-7.38	-7.38	-7.38
PRM4	0.000	0.000	0.000	0.000	0.000	0.000	-7.38	-7.38	-7.38
PRM4	0.000	0.000	0.000	0.000	0.000	0.000	-7.38	-7.38	-7.38
SH3B	-5.33	-3.44	-4.92	-7.38	-7.38	-7.38	0.000	0.000	0.000
SH3B	-5.13	-3.64	-4.68	-7.38	-7.38	-7.38	0.000	0.000	0.000
SH3B	-4.54	-3.38	-3.57	-7.38	-7.38	-7.38	0.000	0.000	0.000

First, the simulation temperature `MC_Temp` was varied to observe phase separation for both SLP65-3xPRM4 & 2SH3 and SLP65-R247A & 3SH3B. Next, the linker length was varied aiming to match the ratios of experimental critical concentrations with the ratios of simulation critical concentrations.

2.14.2 Determination of the simulated critical concentration of phase separation

The percolation value reports about the extent, how much the cluster-network is spanning the simulation cell, and is defined as a number between 0 and 1 [171]. The value 0 indicates that no network of molecules is present, whereas a value of 1 means that the one site of the simulation box is connected to the other site by a large cluster of molecules. The global density inhomogeneity parameter (GDIP) is a quantitative measure of the inhomogeneity and is established in LASSI in order to distinguish a homogeneous system from a phase separated system. A negative GDIP means that the system has not phase separated. A GDIP above 0.025 means that the system phase separated. In order to simulate the critical concentration, the box size was varied in steps of 10 until the simulation resulted in a GDIP > 0.025. The percolation value can correlate well with the critical concentration defined by the GDIP, if cooperativity drives the network formation [104].

In test simulations, the percolation value was used as a proxy of the phase separation in order to avoid time-consuming calculations of the GDIP. The percolation threshold was determined by decreasing the box size. Simulated critical concentrations were calculated from the number of molecules per voxel in units [number of molecules / voxel].

In order to check the correlation between the experimentally observed critical concentrations for phase separation and the predictions from LASSI different constructs were compared to each other. They are R247A-3SH3B *vs* $SLP65_{1-330}$-3SH3B, $SLP65_{1-330}$-3SH3B *vs* 3xPRM4-3SH3B, $SLP65_{1-330}$-3SH3 *vs* $SLP65_{1-330}$-3SH3B, $SLP65_{1-330}$-2SH3 *vs* $SLP65_{1-330}$-3SH3B, 3xPRM4-3SH3 vs 3xPRM4-3SH3B, 3xPRM4-2SH3 vs 3xPRM4-3SH3B and $SLP65_{1-330}$-2SH3 *vs* 3xPRM4-2SH3. To measure the agreement between experiment and LASSI simulation, an error factor is introduced, which

reports about the agreement of experimental and simulated factors of phase separation. The linker length scale, the simulation temperature or specific energy terms were varied in order to find simulation parameters resulting in minimal error factors. In order to analyze the agreement of experimental data with simulations involving either the 3SH3 construct or the 2SH3 construct, the set of simulations including 3SH3 and the other set of simulations including 2SH3 were analyzed separately. The error factor takes into account the phase separation factors f of the five pairs p: R247A-3SH3B *vs* SLP65$_{1\text{-}330}$-3SH3B, SLP65$_{1\text{-}330}$-3SH3B *vs* 3xPRM4-3SH3B, SLP65$_{1\text{-}330}$-2SH3 *vs* SLP65$_{1\text{-}330}$-3SH3B and 3xPRM4-2SH3 vs 3xPRM4-3SH3B.

$$f_{p,3SH3} = \left[\frac{\varphi_{SLP65(1-330)-3SH3}}{\varphi_{SLP65-3xPRM4-3SH3}}, \frac{\varphi_{SLP65-R247A-3SH3}}{\varphi_{SLP65(1-330)-3SH3}}, \frac{\varphi_{SLP65(1-330)-3SH3B}}{\varphi_{SLP65-3xPRM4-3SH}}, \frac{\varphi_{SLP65(1-330)-3SH3}}{\varphi_{SLP65(1-330)-3SH3}}, \frac{\varphi_{SLP65-3xPRM4-}}{\varphi_{SLP65-3xPR\quad-3SH3B}}\right] \qquad \text{(eq. 21)}$$

with φ as the critical concentration for phase separation for a particular pair p.

The phase separation factors f involving the 2SH3 construct is calculated analogously.

$$f_{p,2SH3} = \left[\frac{\varphi_{SLP65(1-330)-2SH3}}{\varphi_{SLP65-3xPRM4-2SH3}}, \frac{\varphi_{SLP65-R247A-3SH3}}{\varphi_{SLP65(1-330)-3SH3}}, \frac{\varphi_{SLP65(1-330)-3SH3}}{\varphi_{SLP65-3xPRM4-3}}, \frac{\varphi_{SLP65(1-330)-2SH3}}{\varphi_{SLP65(1-330)-3SH3B}}, \frac{\varphi_{SLP65-3xPRM4-2SH3}}{\varphi_{SLP65-3xPRM4\ -3SH3}}\right] \qquad \text{(eq. 22)}$$

The mean of the deviation of the simulated phase separation factors from the experimental phase separation factor yields the error factor. In particular, the error factor was calculated by selecting the quotient which is greater than 1, either $\frac{f_{p,experiment}}{f_{p,2SH3/3SH3,simulation}}$ or its inverse $\frac{f_{p,2SH3/3SH3,simulation}}{f_{p,experiment}}$ and taking the mean of the selected terms.

$$Error\ factor = \frac{1}{5} * \left(\sum_p \frac{f_{p,experiment}}{f_{p,2SH3/3SH3,simulation}}\ or\ \frac{f_{p,2SH3/3SH3,simulation}}{f_{p,experiment}}\right)\% \qquad \text{(eq. 23)}$$

Since phase separation of SLP65-R247A could not be detected (Figure 27), the factors from SLP65-R247A-2SH3 vs SLP65$_{1\text{-}330}$-2SH3 (3.2x) and SLP65-R247A-2SH3 vs SLP65-R247A-3SH3B (> 32x) were not considered (Figure 28).

Results

3.1 Disentangling of promiscuous CIN85 - SLP65 interaction on the modular level

3.1.1 SLP65 IDR has partly polyproline II secondary structure propensity

The promiscuous interactions of PRMs with CIN85's SH3 domains drives phase separation. Aiming to identify all phase-separation relevant PRMs, the SLP65 sequence was inspected at a closer look (Figure 11). Four reported PRMs of SLP65 bind to CIN85 [131]. However, the protein sequence contains similar motifs suggesting that there could be more binding motifs. The secondary structure can be a predictor of binding. Since the total number of PRMs within SLP65 is unknown, the secondary structure propensity of SLP65 was further investigated. Secondary structure propensity analysis is a sensitive tool to study IDPs. It has been applied to study fibrillation of synuclein paralogs indicating that β-sheet propensities drive oligomerization in contrast to α-helix propensity, which favor a monomeric state [172].

```
        10         20         30         40         50
MDKLNKITVP ASQKLRQLQK MVHDIKNNEG GIMNKIKKLK VKAPPSVPRR
        60         70         80         90        100
DYASESPADE EEQWSDDFDS DYENPDEHSD SEMYVMPAEE NADDSYEPPP
       110        120        130        140        150
VEQETRPVHP ALPFARGEYI DNRSSQRHSP PFSKTLPSKP SWPSEKARLT
       160        170        180        190        200
STLPALTALQ KPQVPPKPKG LLEDEADYVV PVEDNDENYI HPTESSSPPP
       210        220        230        240        250
EKAPMVNRST KPNSSTPASP PGTASGRNSG AWETKSPPPA APSPLPRAGK
       260        270        280        290        300
KPTTPLKTTP VASQQNASSV CEEKPIPAER HRGSSHRQEA VQSPVFPPAQ
       310        320        330        340        350
KQIHQKPIPL PRFTEGGNPT VDGPLPSFSS NSTISEQEAG VLCKPWYAGA
       360        370        380        390        400
CDRKSAEEAL HRSNKDGSFL IRKSSGHDSK QPYTLVVFFN KRVYNIPVRF
       410        420        430        440        450
IEATKQYALG RKKNGEEYFG SVAEIIRNHQ HSPLVLIDSQ NNTKDSTRLK

YAVKVS
```

Figure 11: Amino acid sequence of SLP65. The SLP65 sequence (UniProtKB - Q8WV28) is rich in prolines. The previously known proline-rich motifs PRM1, PRM4, PRM5 and PRM6 are underscored. Furthermore, the three potential motifs PRM2, PRM3 and PRM* are shaded in grey. PRM* is located between PRM4 and PRM5 and very close to PRM4. Prolines are colored in blue.

As a first approach to identify new, additional PRMs, SLP65's secondary structure was investigated to identify potential new binding sites [173]. The xP pockets of SH3 domains recognize their ligands in a polyproline II conformation [174, 175]. Although binding by the polyproline II conformation seems to be predominant within the SH3 domain family, the secondary structure of the ligand can also adapt a non-polyproline II conformation depending on the type of motif [175]. The secondary structure propensity of SLP65's IDRs were predicted from chemical shifts by the program δ2D [161] (Figure 12). In prolines, the amide does not carry a hydrogen and therefore amide proton based assignment is not possible there. The missing chemical shifts of proline hinder resonance assignment and leave gaps in the secondary structure analysis (white areas in Fig. 12). The proline-rich IDR from a.a. 40-330 showed mainly random coil conformation (~65%) and polyproline II conformation (~25%), while no striking feature around the known binding motifs PRM1, PRM4, PRM5 and PRM6 was revealed. Next, potential new binding sites were accessed according to sequence similarity (Table 9) and based on paramagnetic relaxation data [116]. Three more motifs are likely to be recognized by CIN85, termed PRM2, PRM3 and PRM*.

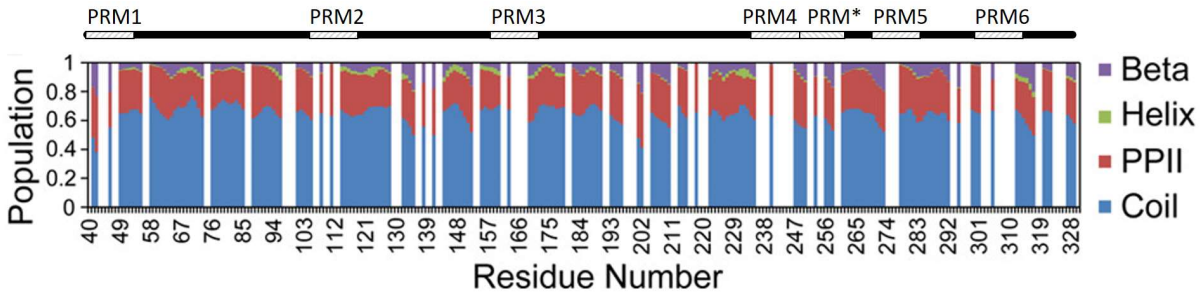

Figure 12: Predicted secondary structure propensity of SLP65$_{40–330}$. The predicted secondary structure propensity of the intrinsically disordered region of SLP65 indicated random coil and polyproline II conformations. The populations of ordered α-helical or β-strand structures were relatively low [173]. Secondary structure propensity was determined by δ2D [161]. The missing chemical shifts of the unassigned residues, in most cases due to the lack of a proline amid proton, result in gaps in the secondary structure analysis. Gaps are marked as white bars. [Reprinted with permission from J. Am. Chem. Soc. 2018, 140(10), 3518–3522. Copyright 2021 American Chemical Society].

3.1.2 The range of binding affinities reveals the strong interaction of SH3B domain to PRM4

SLP65 constitutively binds CIN85 [131] by many, promiscuous interactions between SLP65-PRMs and CIN85's three SH3 domains [116]. The phase separation relies on promiscuous interactions of PRMs with SH3 domains and is required for proper Ca^{2+} signaling during B cell activation. The aim is to capture the sequence-determinants of phase separation by a detailed inspection of the binding modules (SH3 domain and PRMs) on a residue-specific level.

In order to receive residue-specific insights by NMR, the chemical shifts were assigned to the amino acid residues of each the SH3A, SH3B and SH3C domain. NMR spectroscopy is capable to cover a wide range of dissociation constants (K_D) between nM to mM [176]. The chemical shift assignments of SH3A, SH3B and SH3C domain were available from my colleague L. Wong, however the assignment of a few peaks in the SH3C domain required to be curated. So, the assignment of all three SH3 domains was checked again. NMR triple resonance assignment experiments, which were previously recorded by my colleague L. Wong, were used, including the triple resonance experiments HNCACB and CBCA(CO)NH for assignment of SH3A domain and SH3C domain, and HNCA for the assignment of the SH3B domain. The SH3 domains were assigned with the software Cara using the script AutoLink_II v.0.84-alpha, followed by a non-automated assignment for curation. The assignment of SH3A and SH3C were converted to NMR-STAR format (Appendix B). The resonance assignment obtained at 25 °C was transferred to the peaks of the titration spectra recorded at 37 °C. Therefore, another ^{15}N-HSQC spectra was acquired at 30 °C in order to follow the chemical shifts with increasing temperature.

The first goal is to determine the binding affinities of isolated SH3 domains with isolated peptides derived from the PRM sequences and obtain an atomistic view from the perspective of the SH3 domain using NMR spectroscopy with ^{15}N-labeled SH3 domains. We extend our work also to CIN85 derived peptides, since inter-/intramolecular interactions of CIN85's SH3 domains have been proposed before [177]. The SH3A domain and the SH3B domain are proposed to bind to a proline-rich region. A closer investigation of this region identified the two motifs CIN85-PRM2 and CIN85-PRM3, which will be described later in this thesis.

In order to arrive at a thermodynamic description of phase separation in this system, the number and range of affinity of SH3-PRM interactions were determined by measuring monovalent receptor – monovalent ligand binding affinities. 27 combinations of three SH3 domains with nine PRMs (seven potential SLP65-PRMs and two CIN85-PRMs were investigated. Each of the three SH3 domains of CIN85 was expressed separately. In order to study the PRMs separately, the nine sequence-derived peptides, SLP65-PRM1-6 (including PRM*) and CIN85-PRM2-3, were synthesized for each PRMs (Table 12, Table 13). The length of 14 a.a. peptide was chosen to cover the complete binding motif regarding the specificity to CIN85 [137]. In literature, a similar peptide length between 13 – 18 a.a. was chosen for studies of CIN85-SH3 domain ligands [178-180], and also other members of the SH3 domain family [181].

Table 12: Overview of peptide sequences derived from SLP65 regions. The peptides were synthesized to measure monovalent binding affinities to each of the three CIN85 SH3 domains. The core motif is shaded; positively charged residues Lys and Arg are colored red; Pro is colored blue.

Motif	Sequence
SLP65-PRM1	K $_{40}$VKAPPSVPRRDYA $_{53}$
SLP65-PRM2	T$_{105}$RPVHPALPFARGE$_{118}$
SLP65-PRM3	A$_{158}$LQKPQVPPKPKGL$_{171}$
SLP65-PRM4	P$_{238}$PAAPSPLPRAGKK$_{251}$
SLP65-PRM*	A$_{248}$GKKPTTPLKTTPV$_{261}$
SLP65-PRM5	C$_{271}$EEKPIPAERHRGS$_{284}$
SLP65-PRM6	I$_{303}$HQKPIPLPRFTEG$_{316}$
Motif	PxxxPR/K

SLP65-PRM peptides were titrated to each ^{15}N-labeled SH3A, SH3B or SH3C. The titration was monitored by ^{15}N-HSQC spectra. A representative titration series shows that most peaks of the titration spectra were in fast exchange (Figure 13). The spectra of both titrations of SLP65-PRM4 to ^{15}N-labeled SH3C domain (Figure 14) and to ^{15}N-labeled SH3B domain (Figure 15) showed peaks in fast and intermediate exchange. An increase in intensity of the peaks R101, R102, E133,

G134 and E154 was observed, which could be explained by a ligand-induced change of an exchange process.

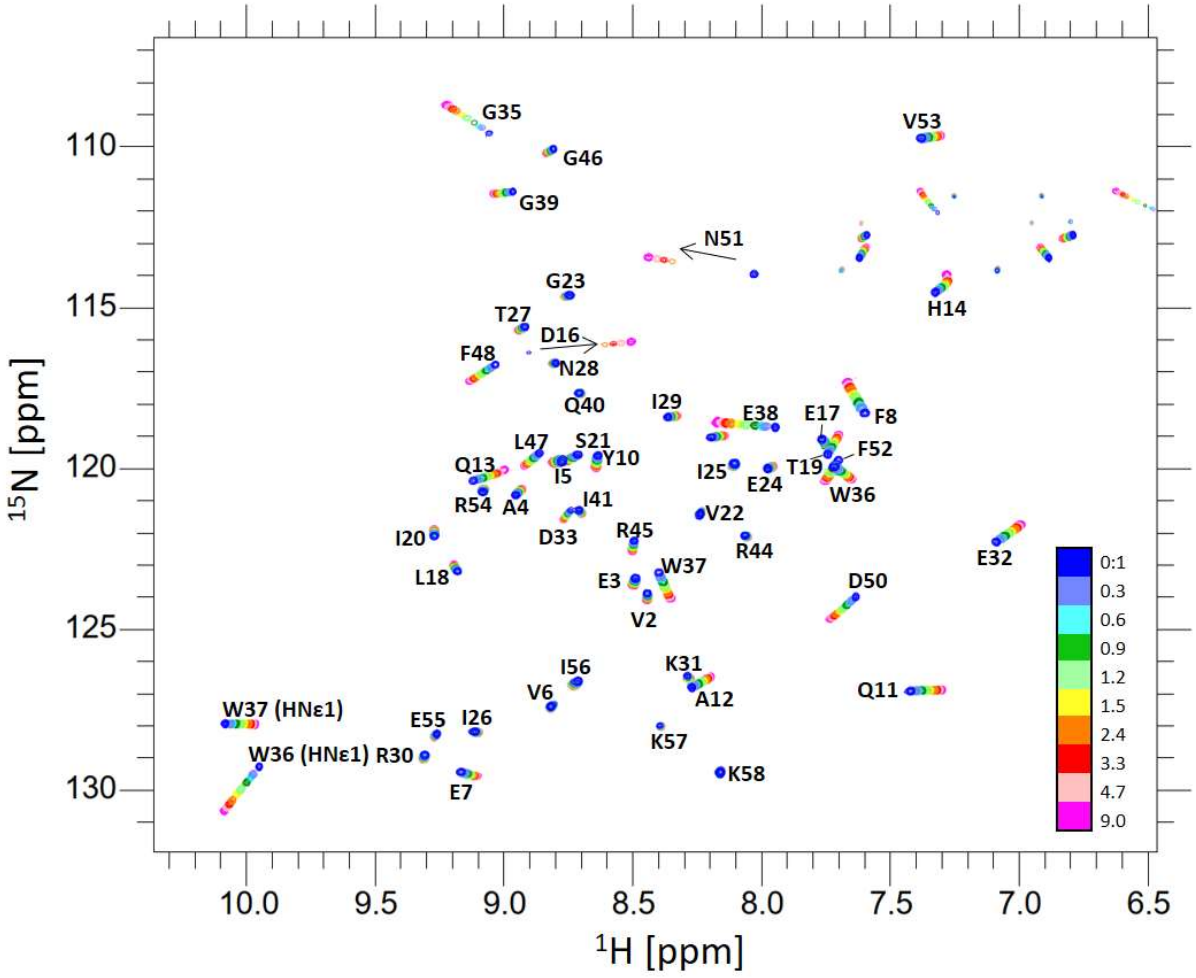

Figure 13: Representative NMR titration spectra for an interaction in fast exchange. Overlaid spectra of the titration of SLP65-PRM6 with the ^{15}N-labelded SH3A domain show that all peaks are in fast exchange, except of D16 and N51, which indicate an intermediate exchange process (marked by arrows). They have the largest difference in resonance frequency between bound and unbound such that this is compatible with the fast exchange of the other resonances which show smaller chemical shift changes between the unbound and bound states. ^{15}N-HSQC spectra were recorded at 800 MHz at 37°C and an initial SH3 domain concentration of 200 µM (0:1 ligand:protein ratio). Titration spectra are colored according to the ligand to protein ratio.

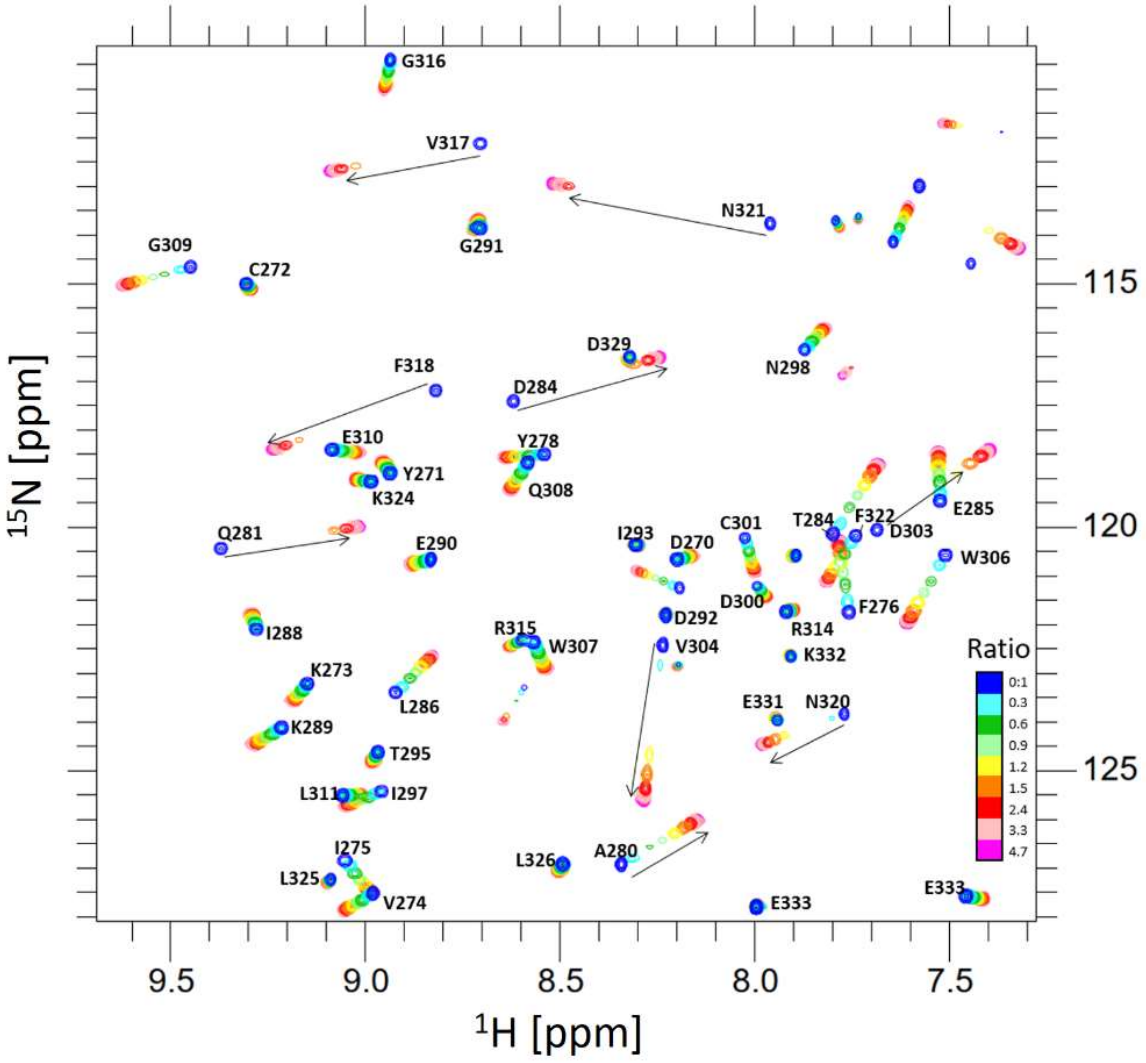

Figure 14: Representative NMR titration spectra for the intermediate exchange regime. Overlaid spectra of SLP65-PRM4 titration with the ^{15}N-labeled SH3C domain show peaks in the intermediate exchange regime (e.g. V317, F318 or F322) and peaks in fast exchange (e.g. G316, N298, L286 or K289). ^{15}N-HSQC spectra were recorded at 800 MHz at 37°C.

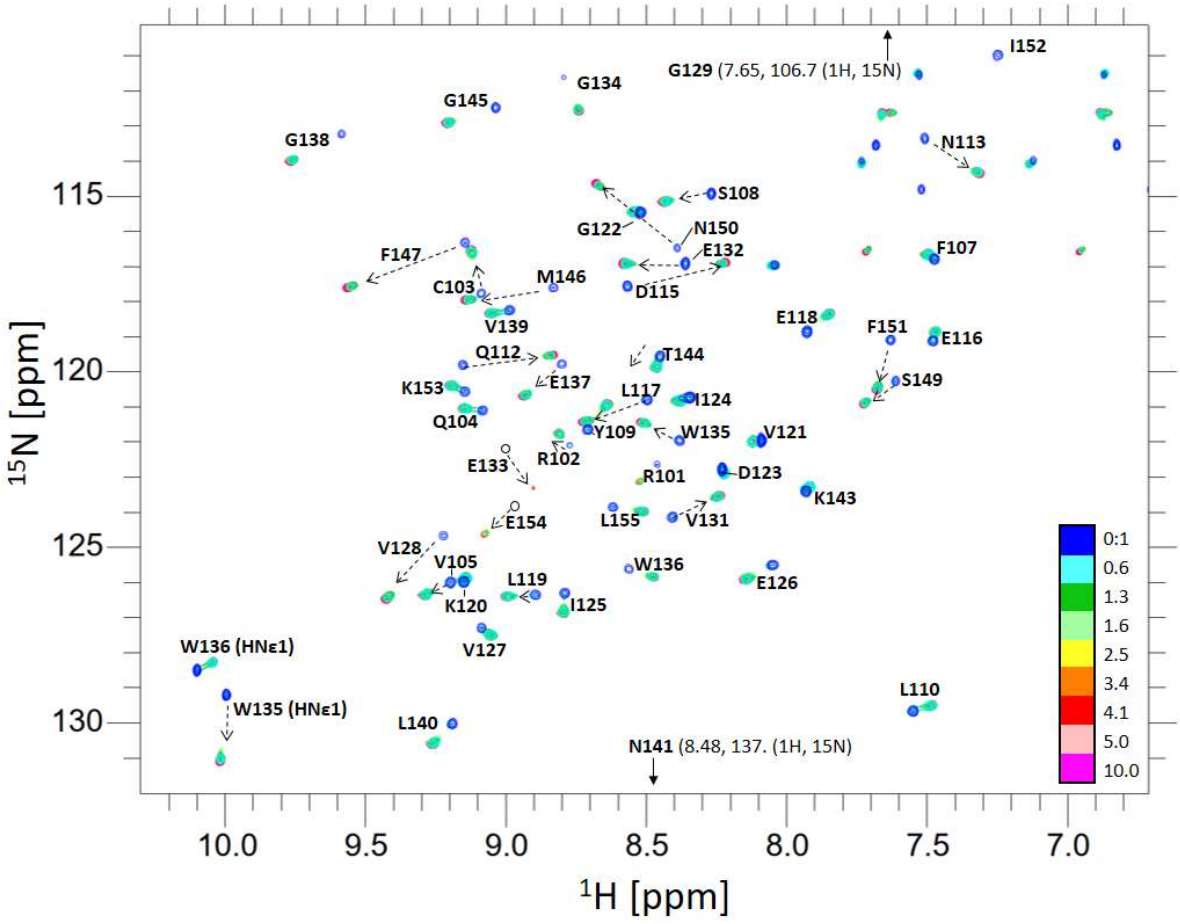

Figure 15: HSQC spectra of the titration of SLP65-PRM4 to SH3B. Overlaid NMR titration spectra with nearly all peaks in slow exchange. ^{15}N-HSQC spectra were recorded at 800 MHz at 37°C. For assignment, the chemical shifts were transferred from the unbound SH3B domain to the peptide-SH3 domain complex based on small chemical shift changes during the titration and comparison of the chemical shift direction. The chemical shift direction was compared between this titration and the titrations of SLP65-PRM5 and SLP65-PRM6 to the SH3B domain. In the spectra without ligand, peaks of E133 and E154 are below the contour level, and are indicated by circles. The intensities of peaks R101, R102, E133, G144 and E154 increase during the titration.

Also, the proline-rich sequence CIN85$_{366-425}$, including potential SH3 binding sites, was investigated. Two sequences harboring potential PRMs were synthesized and titrated to 3SH3 (Figure Appendix C). The NMR titration of CIN85$_{366-389}$ to 3SH3 did not indicate any binding, since no significant chemical shift was observed. The NMR titration of CIN85$_{390-425}$ to 3SH3 detected a binding. CIN85$_{390-425}$ was further split and the two peptides CIN85-PRM2 and CIN85-PRM3 (Table 10) were synthesized and titrated to each ^{15}N-SH3A, SH3B and SH3C.

Table 13: Overview of peptide sequences derived from the proline-rich sequence of CIN85. The peptides were synthesized to measure monovalent binding affinities to each of the three CIN85 SH3 domains. PRMs are shaded; positively charged residues Lys and Arg are colored red; Pro is colored blue.

Motif	Sequence
CIN85-PRM2	L_{390}QKPSVPAIPPKKPRPPKTNS$_{410}$
CIN85-PRM3	L_{411}SRPGALPPRRPERP$_{425}$
Motif	PxxxPR

The binding of a ligand changes the chemical environment of a nucleus and causes a chemical shift perturbation (CSP) measured in ppm, which was analyzed to study individual residues of the SH3 domains. The ^{15}N CSP was weighted by 1/10 and combined with ^{1}H CSP, such that the combined CSP was analyzed for each residue. The CSP profiles of the nine peptide titrations to each of the SH3 domains were analyzed (Figure 16; Figure 17; Figure 18). In the SH3 domain family, the RT-loop, the N-Src loop, the β3 strand, the β5 strand and the 3_{10} helix are the common secondary structure elements that are involved in SH3 ligand recognition [136, 175, 182]. The common binding pocket consists of two xP pockets, which are formed by the aromatic amino acids Y or F (F8 and F276 of CIN85 SH3A and SH3C domain, respectively) of the RT-loop, as well as the W of the β3-strand (W36/135/306 of CIN85), the P of the β4-strand (P49/148/319 of CIN85) and an aromatic residue (F52/151/322 of CIN85) form the two xP pockets. In the titrations of SH3A, SH3B and SH3C, the peptides SLP65-PRM1, -3, -4, -*, -5 and -6, as well as CIN85-PRM2-3 show large CSPs for the above mentioned xP pocket forming residues, except for W306 of the SH3C domain, which instead involves V304. Another exception is the low CS of W36 in the interaction of SLP65-PRM2 – SH3A [175]. The specificity is mainly transferred by residues of the RT- and N-Src loops [175] forming a specificity zone, where a negatively charged amino acid, D or E, is conserved. The residues D16, D115 and D284 of the RT loops of SH3A, SH3B and SH3C, respectively, have large CSPs and thus are the conserved residues of binding specificity. A different binding mechanism of SLP65-PRM3 to SH3A is apparent due to small chemical shifts of D16 and W36, which are below the average CSPs. Focusing on the conserved WWEG sequence in the N-src loop, it appears that SH3B, but also SH3C involve WWEG in the binding to the majority of the PRM-derived peptides, whereas SH3A does only involve the two tryptophan residues.

In titrations with the SH3A domain (Figure 16), SLP65-PRM3 has a similar CSP pattern compared to the other 8 peptides, but does not show large CSPs for the residues $Q_{11}AQHDD_{16}$ of the RT-loop. SLP65-PRM3 could bind to the binding site in two directions (N-term -> C-term or C-term → N-term) as it has been proposed for other SH3 ligands [183, 184]. Also, the interaction SLP65-PRM2 with SH3A shows a slightly different CSP profile, where the CSPs of the N-Src loop and the β4-strand are smaller compared to the CSPs of SLP-PRM1, 4 and 6, and CIN85-PRM2-3.

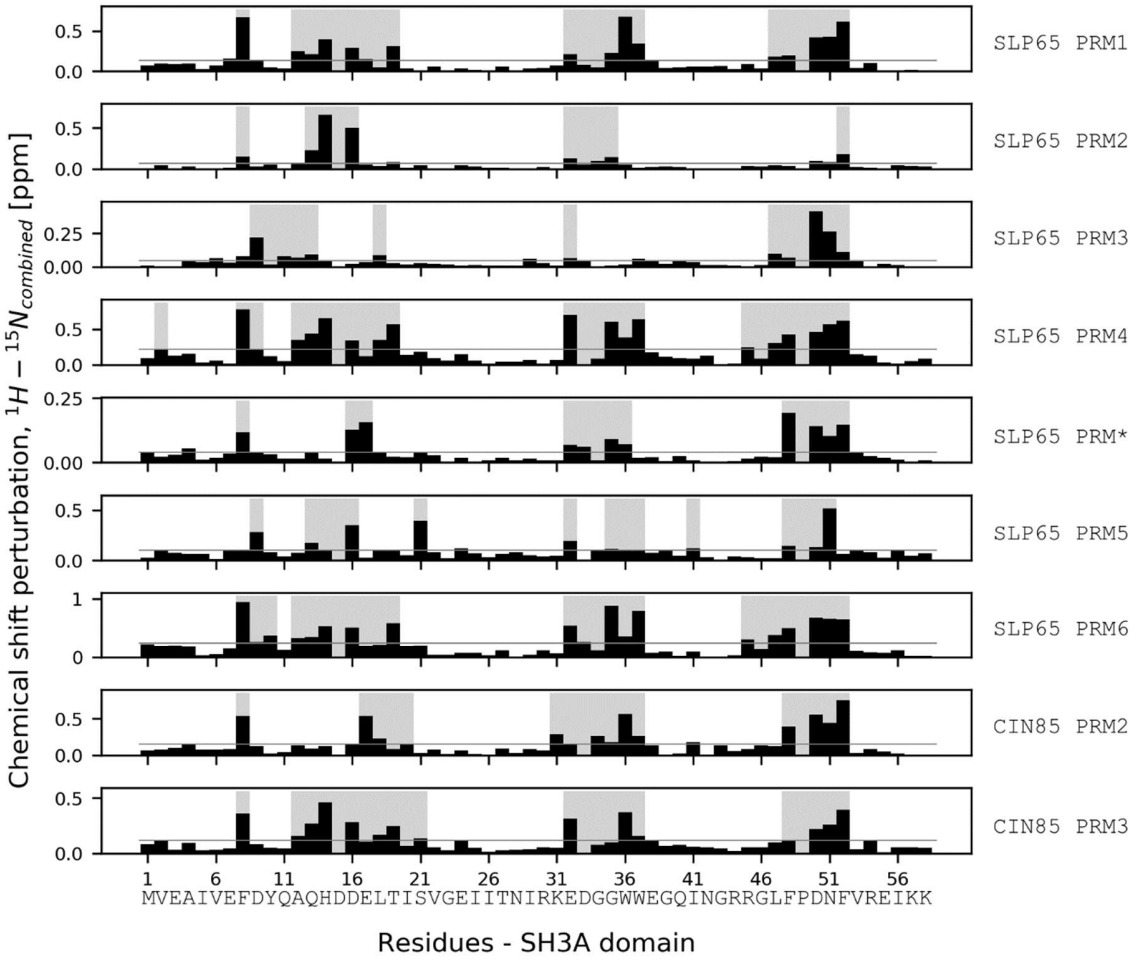

Figure 16: Combined chemical shift perturbations of peptide titrations to the SH3A domains. CSP was combined according to: ^{1}H CSP + 0.1 * ^{15}N CSP. Average CSP of each titration is indicated as grey line. The grey shaded boxes highlight regions with large CSP, which were in particular the RT-loop, N-src loop and β4-strand). Each SH3 domain has a similar CSP profile indicating a single, common binding site. The CSP are reported for the titration endpoints at a ligand/receptor ratio of 3.3, 4.7, 4.3, 10.7, 4.7, 9.0, 9.0, 9.9 and 6.8 for SLP65-PRM1, 2, 3, 4, *, 5, 6 and CIN85-PRM2 and -3, respectively.

For SH3B, all nine peptides display a similar recognition pattern involving residues Cys103 of the β1-strand, the RT-loop, Val128 of the β2-strand (except PRM3) and the 3_{10}-helix (Figure 17). All peptides recognize as well a region comprised of the N-Src loop, the β3-strand and the β4-strand in a similar way, but with distinct differences. PRM3 recognition is restricted to $V_{131}EEGWW_{136}$, while the other peptides show also CSP for E_{137} and G_{138}.

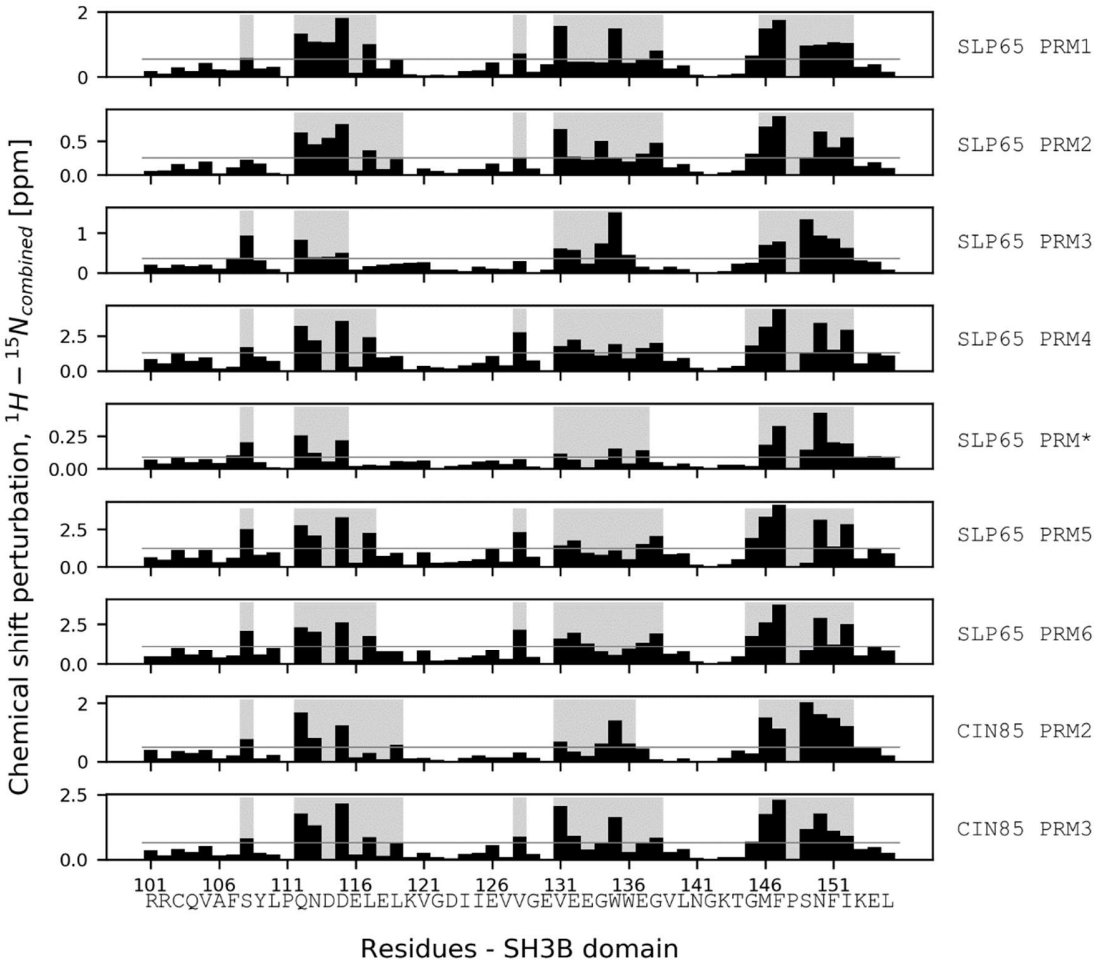

Figure 17: Combined chemical shift perturbations of peptide titrations to the SH3B domains. CSP was combined according to: ^{1}H CSP + 0.1 * ^{15}N CSP. Average CSP of each titration is indicated as grey line. The grey shaded boxes highlight regions with large CSP, which were in particular the RT-loop, the N-src loop, β4-strand and the 3_{10}-helix). Each SH3 domain has a similar CSP profile indicating a single, comemon binding site. The CSP are reported for the titration endpoints at a ligand/receptor ratio of 4.0, 10.0, 5.6, 10.0, 11.6, 8.0, 4.7, 11.2 and 6.6 for SLP65-PRM1, 2, 3, 4, *, 5, 6 and CIN85-PRM2 and -3, respectively.

For the titrations with the SH3C domain, the CSPs pattern of all nine peptides are similar, yet PRM3 involves furthermore R315 from the distal loop (Figure 18).

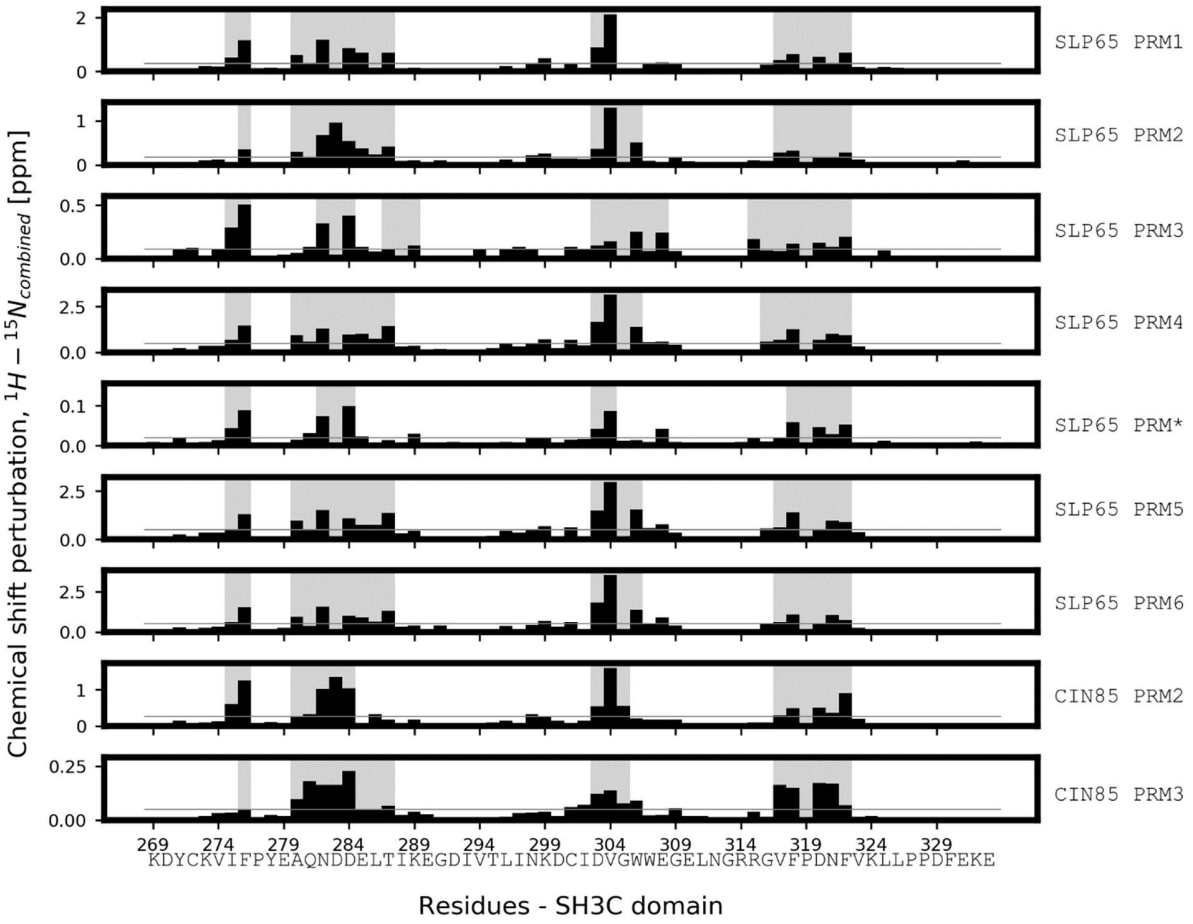

Figure 18: Combined chemical shift perturbations of peptide titrations to the SH3C domain. CSP was combined according to: ^{1}H CSP + 0.1 * ^{15}N CSP. Average CSP of each titration is indicated as grey line. The grey shaded boxes highlight regions with large CSP, which were in particular the RT-loop, the N-src loop, β4-straned and the 3_{10}-helix. The SH3C domain has a similar CSP profile for all 9 peptides, indicating a single, common binding site. The CSP are reported for the endpoints of the titration at a ligand/receptor ratio of 9.0, 12.8, 9.0, 9.0, 9.0, 9.0, 9.0, 9.8 and 9.8 for SLP65-PRM1, 2, 3, 4, *, 5, 6 and CIN85-PRM2 and -3, respectively.

In order to visualize the binding site, the normalized CSP of the titrations of SLP65-PRM1-6 with the SH3 domains SH3A, SHB and SH3C, were mapped on the crystal structures of the SH3 domains (Figure 19) [178, 179, 185]. The mapping on SH3A reveals a similar pattern for all titrated peptides

(PRM*, CIN85-PRM2 and CIN85-PRM3 not shown). The mapping on SH3B and SH3C display a similar profile as well. In order to clarify whether the profile resembles a single binding site, a crystal structure of SH3A-PxxxPR complex was taken as reference. The SH3A crystal structure originates from the SH3A-Cbl-b peptide complex, where Cbl-b peptide occupies a single binding site by its core sequence PKPRPR [179]. The main residues of the SH3A-Cbl-b interaction Q13, D16, G35, D50, N51 and F52 are identical to residues with large CSP. This indicates that SLP65-PRMs share a single binding site (Figure Appendix D).

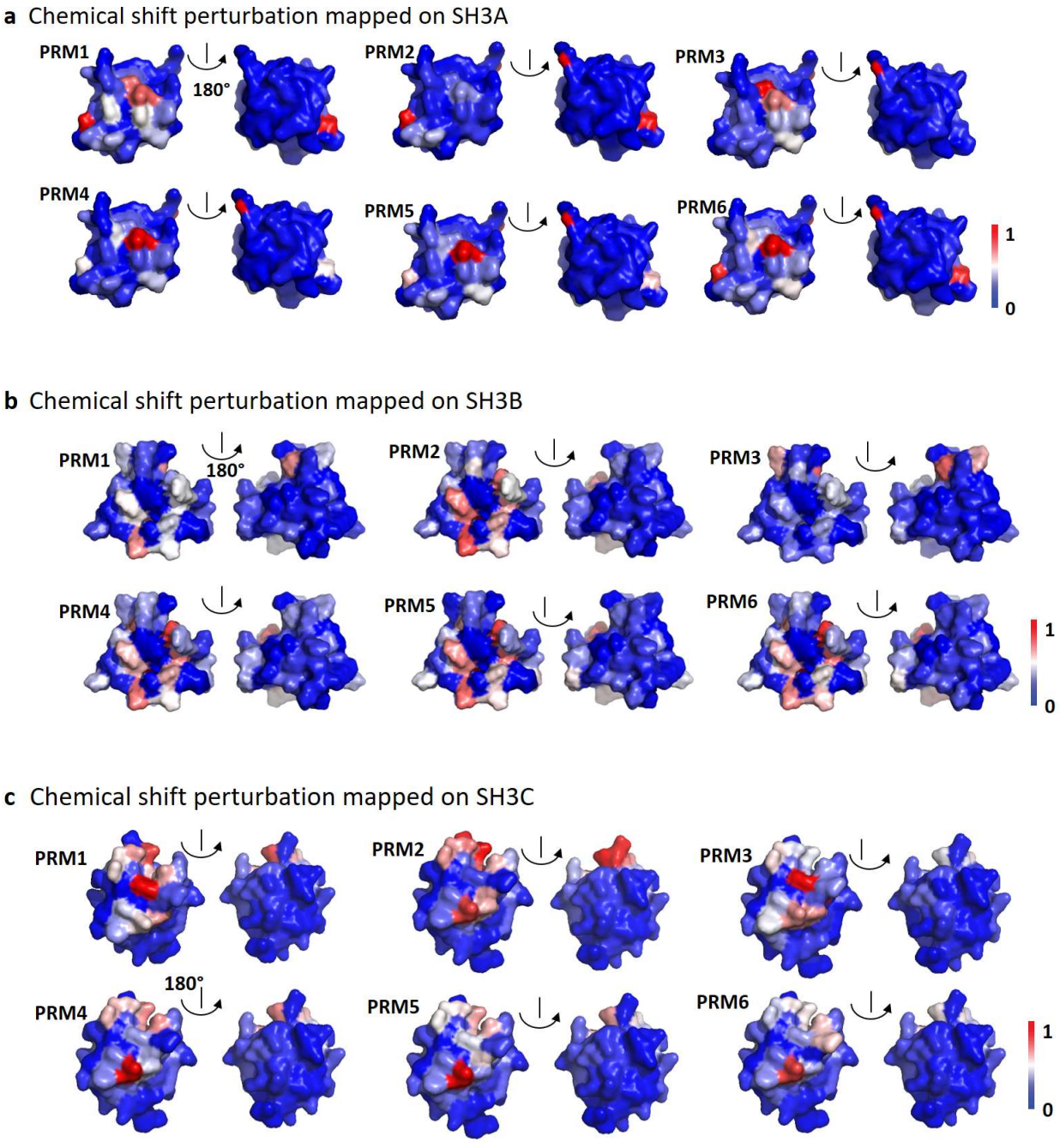

Figure 19: CSP of peptide-SH3 interactions mapped on the SH3 domains. Normalized combined chemical shifts of titrations of SLP65-PRM derived peptides to SH3A (a), SH3B (b), and SH3C domain (c) are mapped on SH3 domain crystal structures (pdb: 2bz8 [179], 2o2o [178], 2ydl [185], respectively). PRM derived peptides are recognized at a single binding site by a very similar pattern of residues.

In order to elucidate the range of binding affinities, the dissociation constants of monovalent interactions of SH3 domains to PRM derived peptides were determined applying a single-site binding model (Figure 20). The dissociation constants of SH3 domain-PRM titrations were determined by 1-dimensional chemical shift analysis (Figure 21).

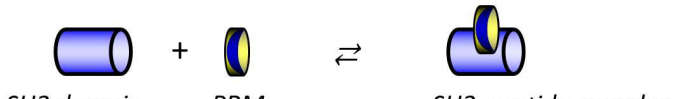

$$[\text{Receptor}] + [\text{Ligand}] \rightleftarrows [\text{Receptor}_1\text{Ligand}_1]$$

Figure 20: Single-site binding model for the interaction of CIN85-SH3 domains with PRM sequence-derived peptides. The PRM ligand is interacting with the receptor SH3 domain.

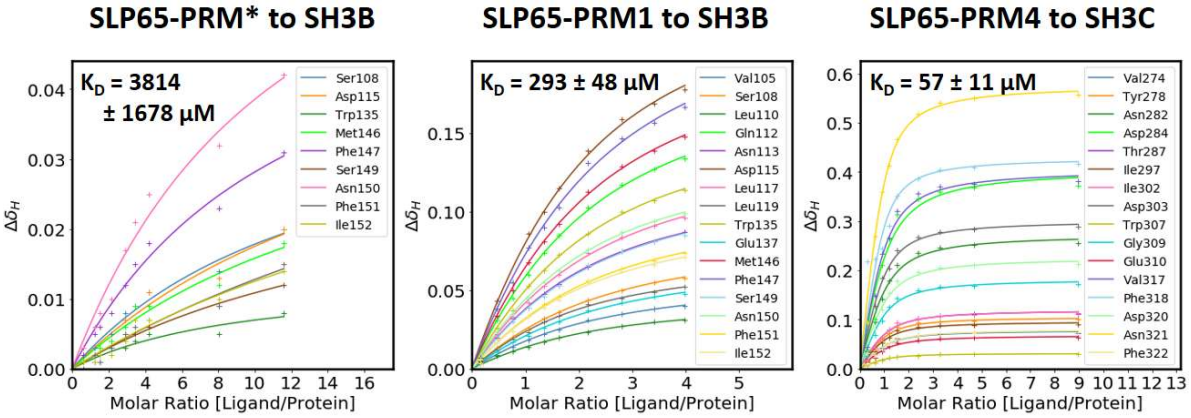

Figure 21: Representative binding isotherms of SLP65-PRMs titrated to either SH3A, B or SH3C. The dissociation constants of SH3 domain-PRM titrations were determined by 1-dimensional chemical shift analysis. Representative binding isotherms of titrations of SLP65-PRM* and SLP65-PRM1 to the SH3B domain and SLP65-PRM4 to the SH3C domain are shown (See Appendix F for all 27 binding isotherms).

During NMR titration, several resonances were observed in the intermediate and slow exchange regime, in particular the interaction of the PRM4-peptide with the SH3B domain and the SH3C domain (Figure 13, Figure 14). Binding affinities of resonances in intermediate exchange cannot be determined by 1D CS analysis or intensity analysis. Thus binding affinities were obtained by

2D lineshape analysis using the software TITAN [160] (Figure 22). If possible, dissociation constants were determined by both methods, which agreed well within the standard error (or within 2x the standard error for the SH3-peptide interactions SH3A-PRM3, SH3A-PRM4, SH3C-PRM4, SH3C-PRM5, SH3C-PRM6, SH3C-CIN85-PRM3, Figure 23). The 1D ^{1}H- and ^{15}N-CS analysis of the titrations of SLP65-PRM2 to the SH3A domain and SLP65-PRM2/PRM3/PRM* to the SH3C domain were omitted due to a large standard error (see gaps in Figure 23).

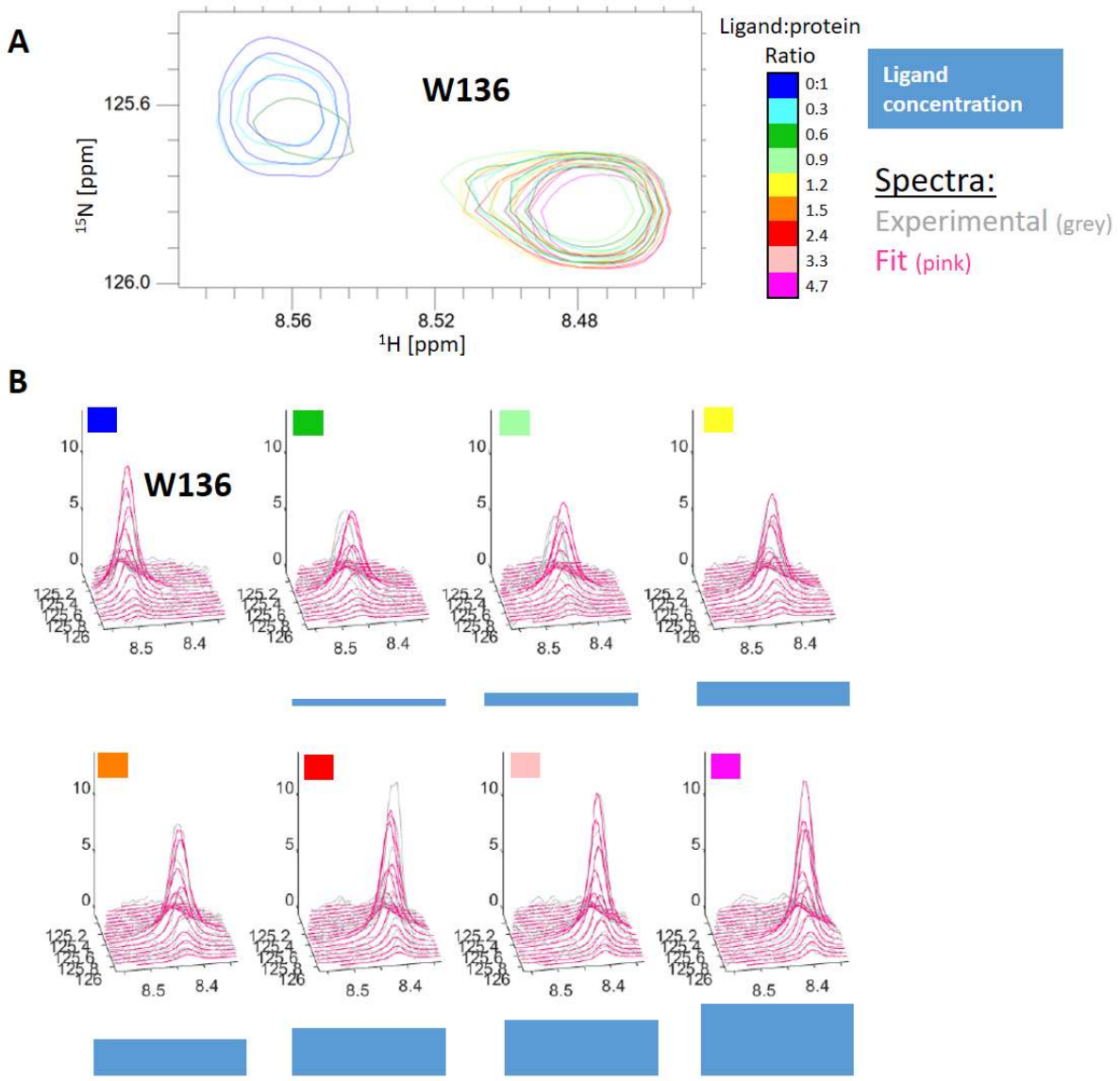

Figure 22: 2D lineshape analysis of peaks in slow exchange or the intermediate regime. A representative fitting procedure is shown for W136 of the SLP65-PRM4 to SH3B titration A) Contour plots of overlaid ^{15}N-HSQC spectra of SLP65-PRM4 titration to the SH3B domain displays the peak W136. B) 3D plots of

experimental and fitted spectra of the titration series for the different concentrations represented with colors at the left top of the peaks. The CS and the lineshape of region of interest of the experimental ^{15}N-HSQC spectrum (color coded in grey) was fitted simultaneously (color coded in pink) using a single-site binding model in the software TITAN [160]. Global fit K_D = 6.3 ± 0.1 µM. Fit of residue W136: K_D = 17.9 ± 0.4 µM, koff = 27.0 ± 0.5 s^{-1}, Chemical shifts of ligand bound state: 8.4 ± 0.0 ppm (^{1}H), 125.8 ± 0.0 ppm (^{15}N), relaxation rates: 33.9 ± 0.5 Hz (^{1}H), 12.3 ± 0.3 Hz(^{15}N).

The range of binding affinities of monovalent interactions of SH3 domains and SLP65 sequence-derived peptides revealed one particularly strong binding motif, PRM4, with dissociation constants of 6 µM and 35 µM for SH3B and SH3C, respectively. Also, SLP65-PRM6 has relatively small K_Ds of 149 ± 13 µM, 96 ± 7 µM, 89 ± 42 µM with SH3A, SH3B and SH3C, respectively. Both SLP65-PRM4 and SLP65-PRM6 include a 3rd proline in the atypical PxPxPR motifs, which are reported to bind constitutively to CIN85's SH3 domains [186], which could explain the larger K_Ds.

SLP65-PRM1 and CIN85-PRM2 are atypical PxxxPR motifs, reported to bind to CIN85's SH3 domains. Their affinity to CIN85's SH3 domains ranges from 175 ± 74 µM – 791 ± 351 µM.

SLP65-PRM3, SLP65-PRM5 and CIN85-PRM3 have a wide range of affinities and their motifs are similar to the atypical PxxxPR motifs with difference of a lysine (PxxxPK), a glutamic acid (PxxxER) or by the fourth a.a. residues leading to a 7 a.a. long PxxxxPR motif, respectively. The remaining two motifs, SLP65-PRM2 and SLP65-PRM*, have rather weak affinity for CIN85's SH3 domains with K_Ds > 1 mM. SLP65-PRM* differs from a classical PxxPxR by its lysine instead of an arginine. The SLP65-PRM2 RPxxPxxPxxR differs from a classical k2 motif (PxxPxR) by its two a.a. separating C-terminal P and R, and differs from a classical 1k motif (RxxPxxP) by an additional P after the N-terminal R[137].

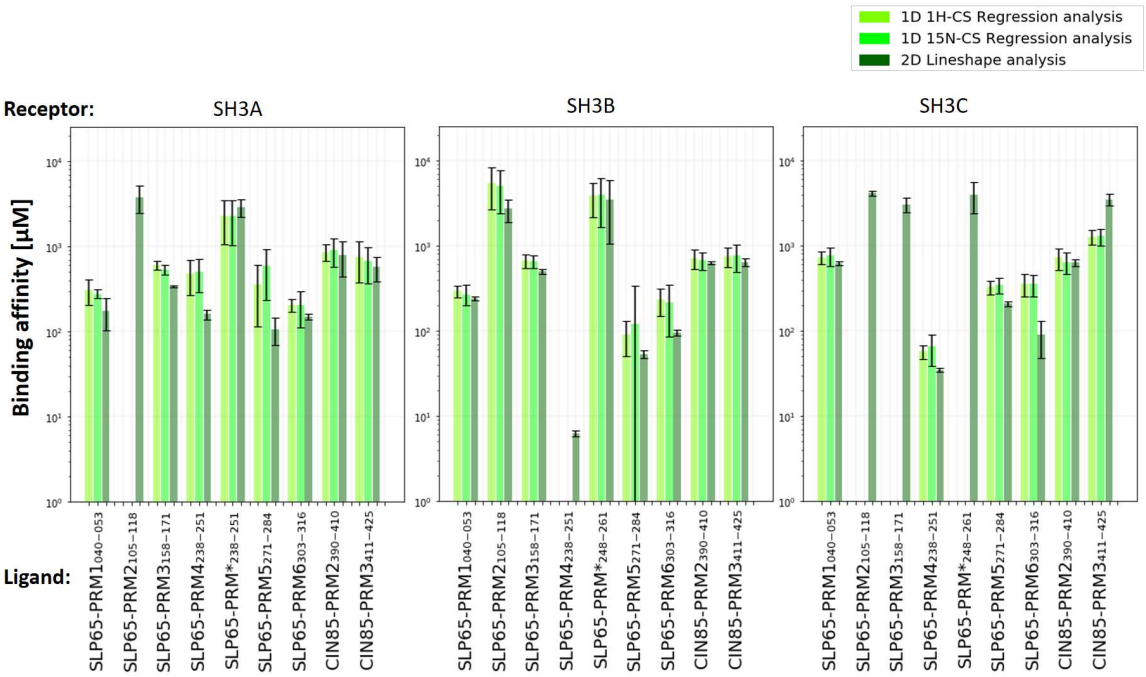

Figure 23: Binding affinities of PRM-derived peptides to CIN85's SH3A, SH3B or SH3C domain. Three K_Ds are reported for each interaction, since the NMR titrations were analyzed by both 1D regression analysis and 2D lineshape analysis of the peptide-SH3 titrations. K_Ds were within the error range in 16 out of 27 titrations. No 1D analysis was possible in 5 out of 27 titrations due to a high K_D > 3 mM or slow exchange. In 6 out of 27 titrations the determined K_Ds differed by less than ~4x SE. 2D lineshape analysis was needed to determine K_D of the interaction of SH3B to the PRM4-peptide.

In summary, the particularly strong SLP65-PRM4 was identified. Furthermore, the promiscuous interaction comprises six medium affine binding motifs SLP65-PRM1, -3, -5 and -6 and CIN85-PRM2-3 with dissociation constants in the range of ~60 µM to 1 mM, and two weak binding motifs PRM2 and PRM* with dissociation constants above 1 mM.

The intramolecular binding of CIN85 [177] was elucidated under the light of the binding affinities determined by 2D lineshape analysis (Figure 23). The K_Ds of CIN85-PRM2-3 are in the range of 550 µM to 950 µM, for SH3A and SH3B, and in the range of 600 µM to 2500 µM for SH3C (Figure 23). The CIN85-PRM2 peptide bind to all three SH3 domains with a similar K_D (Figure 20, K_D = 792 ± 352 µM, 636 ± 59 µM and 643 ± 68 µM for the interaction of the SH3A, SH3B and SH3C domain, respectively). The CIN85-PRM3 peptide prefers binding to the SH3A domain and the SH3B domain over the SH3C domain (K_D = 628 ± 28 µM, 568 ± 178 µM and 3497 ± 549 µM for the interaction

of the SH3A, the SH3B and the SH3C domain[187][187], respectively (Figure 23). Previous findings from immunoprecipitation pull-downs of either GST-SH3A, GST-SH3B or GST-SH3C with a $CIN85_{328-665}$ constructs comprising both CIN85-PRM2-3, demonstrate a preferred binding of the SH3A domain over the SH3B domain and no binding of the SH3 C domain (Figure 3B in Tibaldi *et al.* [187]. It remains unexplained why SH3A and SH3B show similar K_Ds, but show a different binding in the immuno-blots.

In order to assess the relevance of CIN85-PRM2-3 in the SLP65-bound complex, the K_Ds of SLP65-peptides and CIN85-peptides were compared. CIN85-PRMs and SLP65-PRMs bind to the same binding site on the SH3 domains (Figures 16-18), and SLP65's and CIN85's PRMs compete for CIN85's SH3 domains. 13 strong interactions of SLP65-PRMs (mainly PRM4, PRM5 and PRM6) are found while CIN85 PRM2-3 showed only six weak interactions to the CIN85 SH3 domains. Two interactions with SH3C (PRM1 and PRM3) have similar K_Ds. Three interactions of SLP65 (SH3A-PRM2, SH3C-PRM2/PRM3) and the PRM* show weaker K_Ds. In total, this indicates that SLP65 could outcompete intra-/or intermolecular interactions of CIN85.

The high affinity PRM4 and weak affinity PRM* are neighboring motifs. Residues outside of the 6 a.a. long motif can increase the affinity [188, 189]. In order to check for synergy of PRM4 and PRM*, the K_D of an extended motif PRM4*, comprising both motifs, was compared to the K_D of PRM4. The PRM4 sequence was validated considering an enhanced-affinity effect from the neighboring PRM* motif, taking an extended binding motif into consideration. The K_D of PRM4* to the SH3B domain was measured by ITC (Table 11). The K_D of PRM4* is within the standard error similar to the affinity of PRM4. The binding ratio of 1.68:1 (ligand:receptor / 1.68 PRM4* ligand to one SH3B domain) indicates that a higher PRM4 module concentration is needed for saturating the SH3B domain. The binding enthalpy ΔH is similar within 2x the standard error. The PRM* will be disregarded in further considerations, since the affinity with or without the PRM* module is similar.

Table 14: ITC titration of PRM4, PRM4-R247A and extended motif PRM4* to SH3B. The 24-aa long peptide PRM4* comprising both neighboring motifs PRM4 and PRM* binds to SH3B with similar affinity as the 14-aa long peptide PRM4. No synergy from neighboring, weak binding PRM* (K_D between 3 - 10 mM) was observed. To control for the inactivation of PRM4 by the single point mutation R-A, the K_D of PRM4-R247A to was determined. No binding was observed for single point mutation PRM4-R247A.

Titrant:	Replicates	n	K_D [µM]	ΔH [kcal/mol]	ΔS [kcal/mol]
PRM4	3	1,00 ± 0	8,98 ± 0,31	-12,78 ± 0,15	-5,61
PRM4-R247A	2	-	-	-	-
PRM4*	3	1,68 ± 0,01	9,17 ± 0,24	-12,33 ± 0,14	-5,18

ITC was used as an orthogonal technique to confirm the measured dissociation constants of SLP65-PRM1-6. Curve fitting of ITC data of a weak interaction is not possible unless the n-value is fixed [190]. For the analysis of weak SH3-PRM interactions by ITC, the n-value was set to 1, since the CSP indicated a single binding site (Figure 19: **CSP of peptide-SH3 interactions mapped on the SH3 domains.** Normalized combined chemical shifts of titrations of SLP65-PRM derived peptides to SH3A (a), SH3B (b), and SH3C domain (c) are mapped on SH3 domain crystal structures (pdb: 2bz8 [179], 2o2o [178], 2ydl [185], respectively). PRM derived peptides are recognized at a single binding site by a very similar pattern of residues.. Both techniques reported K_D values following the trend: PRM4 << PRM5 ~ PRM6 < PRM1 < PRM3 < PRM2 (Figure 24). The weak interactions of PRM2 with SH3A, SH3B and SH3C and PRM3 with SH3C interaction could not be detected by ITC, since the heat evolutions during titration were too small. Remarkably, the K_Ds of the SH3B-PRM4 (K_D = 9 µM) and SH3C-PRM4 (15 µM) interactions differed only by a factor of 1.7 as measured by ITC, in contrast to NMR lineshape analysis (SH3B-PRM4 - K_D = 6 µM; SH3C-PRM4 K_D = 35µM) were the difference was by a factor of 5.8.

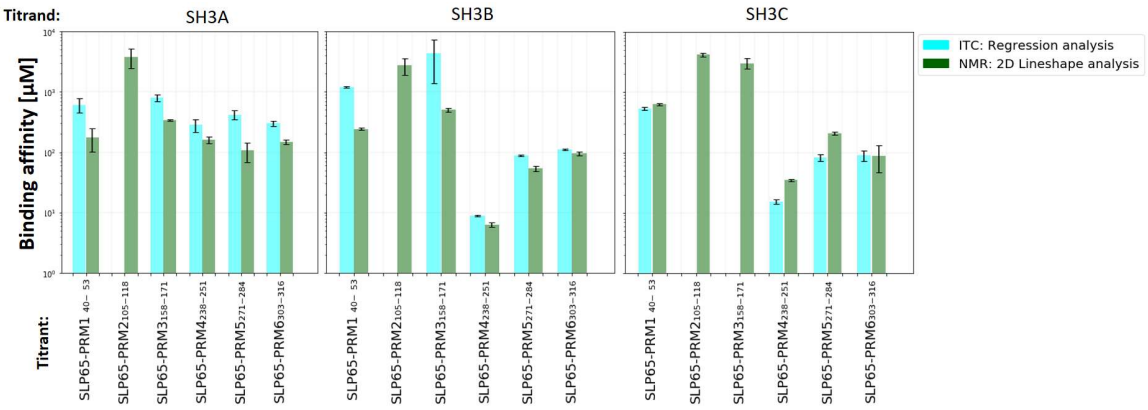

Figure 24: Comparison of dissociation constants measured by ITC and NMR. SLP65-derived peptides were titrated to isolated SH3A, SH3B and SH3C domains. 18 dissociation constants from interactions of 3 SH3 domains to 6 PRM-peptides are shown. K_Ds determined by ITC are color-coded cyan, K_Ds determined by NMR are color-coded green. The strongest interaction is PRM4-peptide to SH3B with a K_D of 6 µM (NMR) / 10 µM (ITC).

3.1.3 High affinity of PRM4 peptide-SH3B interaction is corrobated by NMR slow exchange

The measurement of the K_D by ITC and NMR deviated for the SH3C-PRM4 interaction (Figure 24, K_D = 35 µM determined by NMR lineshape analysis *vs* K_D = 15 µM determined by ITC). The NMR data was further inspected under the aspect of the binding regime. Slow exchange is observed for the PRM4-SH3B interaction (Figure 25A, K_D = 6 µM as determined by NMR). In contrast, fast and intermediate (a.a. D303) exchange is observed for the PRM4-SH3C interaction (Figure 25 B, K_D = 35 µM as determined by NMR). The residue-specific NMR analysis is more direct measurement technique compared to ITC. It cannot be concluded which technique is more accurate, however the high affinity of PRM4-SH3B is corroborated by the slow-exchange binding mode.

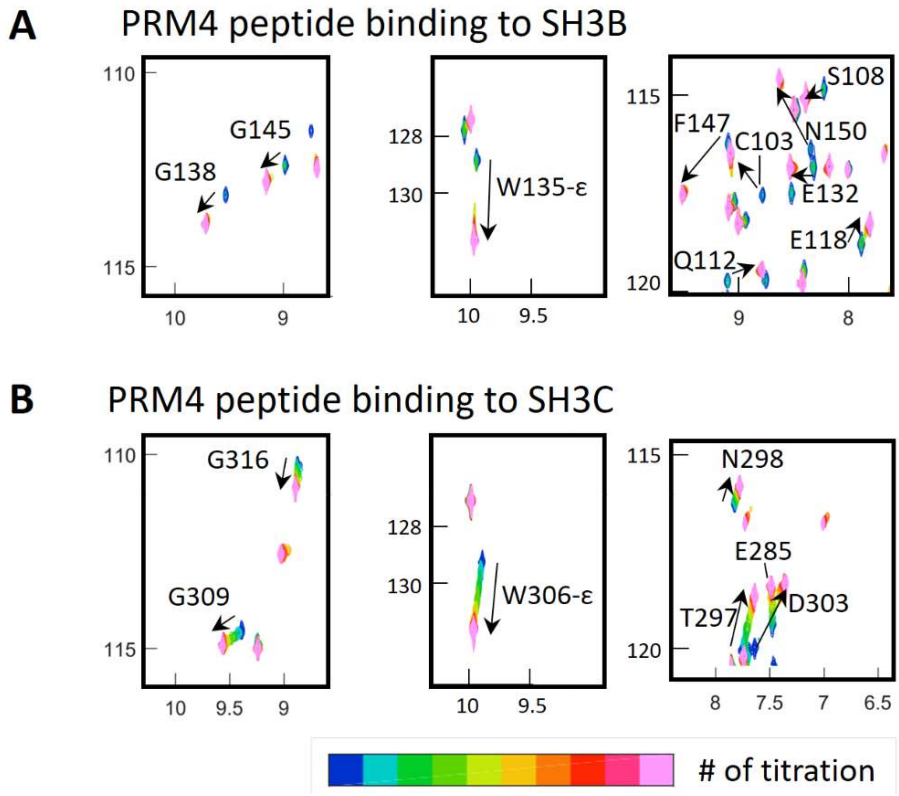

Figure 25: SH3B forms a tighter complex with PRM4-peptide compared to SH3C. Overlapped NMR spectra of PRM4-peptide titrated to a) ^{15}N-labeled SH3B indicates slow-exchange and b) ^{15}N-labeled SH3C showing intermediate/fast-exchange. In the slow exchange regime, two peaks at the bound and the unbound chemical shift are observed during titration series (peaks of slow exchange processes: e.g. G138, G145, W135-NεHε, E132). In the fast exchange regime, a single peak is observed in each spectrum from the titration series (G309, G316, W306-NεHε, E285). Selected spectral regions are shown. Each spectrum within the titration series is color-coded, indicating an increasing ligand concentration from zero (blue) to the maximum (pink). Spectra were recorded at a 800 MHz spectrometer and plotted with TITAN as shown in Figure 22. The ligand:receptor ratios were 0:1, 0.6, 1.3, 1.6, 2.5, 3.4, 4.1, 5.0, 10.0 for PRM4:SH3B and 0:1, 0.3 , 0.6, 0.9 , 1.2 , 1.5, 2.4, 3.3, 4.7, 9.0 for PRM4:SH3C, respectively.

3.2 Classification of phase-separation properties conferred by PRM4, SH3B and vesicle binding

In order to understand phase separation of adapter proteins on a modular level, constructs were designed, in which the modules were replaced or inactivated. The SH3B-PRM4 interaction has turned out to have a remarkably high affinity within the promiscuous interactions. The next goal was to assess the impact of the PRM4 or the SH3B domain on the phase separation properties. Therefore, mutation constructs were designed to have weaker and stronger binding affinities, and the critical concentration of the designed mutants was measured.

Therefore, a single point R247A mutation was introduced into the $SLP65_{1-330}$ construct to obtain the presumably weak binding construct SLP65-R247A. The R-to-A mutation disrupts the binding of PRM4. To obtain the presumably strong binding construct SLP65-3xPRM4, the two medium affine binding motifs PRM5 and PRM6 were replaced by two PRM4. Also, a strong binding version of 3SH3 was designed, referred as 3SH3B, by replacing both SH3A and SH3C by SH3B aiming to access the impact of the SH3B domain.

3.2.1 Single point mutation for PRM4-inactivation

First, a control for abolished binding of the R-to-A mutation within the PRM4-peptide was done. The PRM4-R247A peptide $PPAAPSPLPA_{247}AGKK$ was synthesized and binding was accessed by ITC and NMR titration. The titration of the PRM4-R247A peptide to SH3B did not evolve any significant heat indicating no binding (Table 11). Abolished binding was confirmed by NMR titration (Appendix F).

3.2.2 PRM4 is a key motif for SLP65-CIN85 interaction

Before evaluating the phase separation properties of the binding elements PRM4 and SH3B, the designed constructs were checked for an increase or decrease of affinity. The SLP65 constructs SLP65-R247A, *wildtype*-like $SLP65_{1-330}$ and SLP65-PRM4 were titrated to 3SH3 constructs and

measured by ITC. The released heat of the 1st injection of different titrations were compared. The enthalpy of SLP65-3xPRM4 (-23.4 kcal/mol) more negative than the enthalpy of *wildtype*-like $SLP65_{1-330}$ (-15.8 kcal/mol; Figure 26 A, B). For titrations with 3SH3B the receptor concentration had to be reduced, because this construct is supposedly forming higher-order complexes at concentrations close to the critical concentration of phase separation (Critical concentration of 3SH3B together with SLP65-3xPRM4 between 10 – 20 µM will be shown later in this thesis in Figure 27) A lower 3SH3B receptor concentration was required, concomitantly the absolute heat release was decreased. The enthalpy of the 1st injection $SLP65_{1-330}$ to 3SH3B (-4.0 kcal/mol) was smaller than the enthalpy of the titration with SLP65-3xPRM4 (Figure 26 C, D). In both titrations, the strong binding construct SLP65-3xPRM4 evolved more heat.

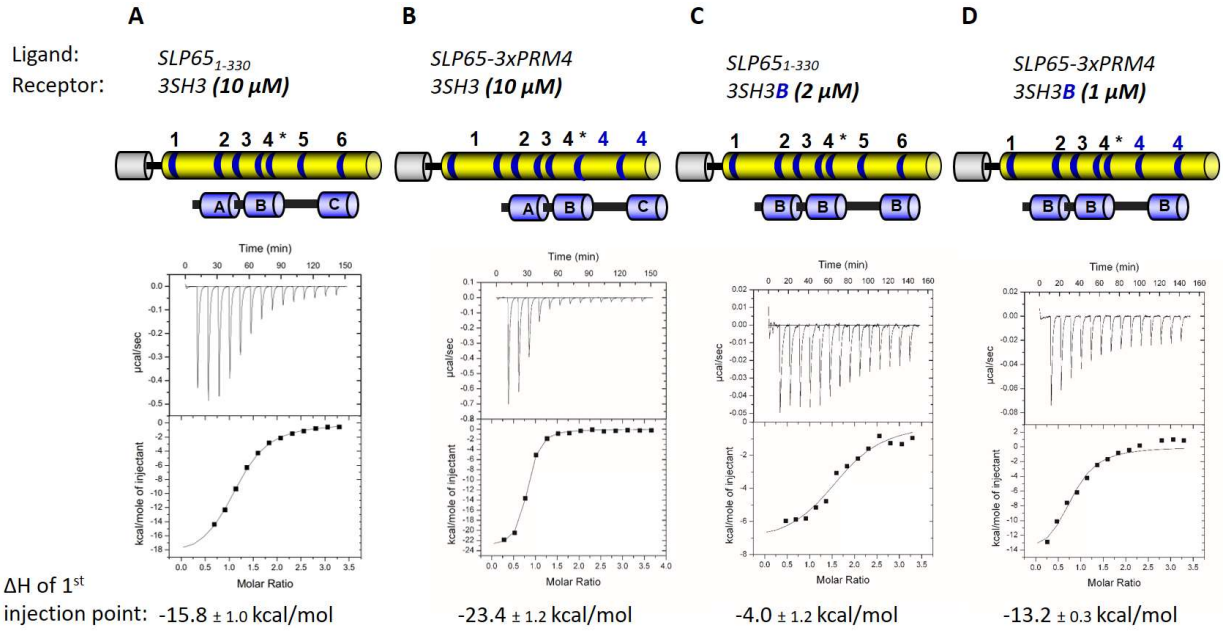

Figure 26: ITC titrations confirm the design of strong binding mutants of SLP65-3xPRM4 and CIN85-3SH3B.

Representative binding isotherm demonstrate that the 1st injection of $SLP65_{1-330}$ to 3SH3 **(A)** releases less heat than SLP65-3xPRM4 to 3SH3 **(B)**. The same trend is seen using 3SH3B. 1st injection of $SLP65_{1-330}$ to 3SH3B **(C)** releases less heat than SLP65-3xPRM4 to 3SH3B **(D)**. Receptor concentrations are 10 µM for 3SH3 titrations and were reduced to 2 µM and 1 µM for 3SH3B titrations due to higher phase separation propensity of the 3SH3B construct which interferes with the ITC measurement. The binding isotherm of the strong binding SLP65-3xPRM4 have a steeper increase than the *wildtype*-like $SLP65_{1-330}$ indicating an apparently larger binding cooperativity.

The apparent dissociation constants were obtained assuming a one-site binding model (Table 12) due to the lack of complete data set for global analysis [162, 163]. This analysis does not allow to disentangle the K_D, the n-value, the enthalpic and the entropic contributions of individual modules, but gives an average picture of the binding event. In the case of promiscuous binding with undefined stoichiometry, the n-value is regarded as the apparent number of binding sites, or number of contact sites in the context of multivalent interactions. First, the effect of the PRM4 inactivation was analyzed. No heat evolution was observed in the titration of SLP65-R247A construct to either 3SH3 or 3SH3B, indicating that PRM4 is a key motif for the SLP65-CIN85 interaction (data not shown). Next, the strong binding effect of SLP65-3xPRM4 relative to $SLP65_{1-330}$ was studied (Table 15). The titration of $SLP65_{1-330}$ to 3SH3 results in an n-value = 1.12, which indicates a binding ratio of 1.12 3SH3 to one $SLP65_{1-330}$, thus more ligand is required to saturate 3SH3. The titration of SLP65-3xPRM4 to 3SH3 results in an n-value = 0.75, which indicates a binding ratio of one 3SH3 to 1.33 SLP65-3xPRM4, thus less ligand is required to saturate 3SH3. The stronger binding by SLP65-3xPRM4 ligand is also evident by a 6x reduced K_D value and by the more negative enthalpy and entropy. Next, the titrations of either $SLP65_{1-330}$ or SLP65-3xPRM4 to 3SH3B were analyzed. The titration of $SLP65_{1-330}$ to 3SH3B results in an n-value = 1.69, which indicates a binding ratio of 1.69 $SLP65_{1-330}$ to one 3SH3B. More ligand is required to saturate 3SH3B. The titration of SLP65-3xPRM4 to 3SH3B results in an n-value = 0.78, which indicates a binding ratio of one SLP65-3xPRM4 to 1.28 3SH3B, where less ligand is required to saturate 3SH3B. The stronger binding by SLP65-3xPRM4 ligand is also evident by a 2.6x reduced K_D (K_D of titration $SLP65_{1-330}$:3SH3B over K_D of SLP65-3PRM:3SH3B) which can be explained by the decrease in both enthalpy and entropy, as described above for the comparison of $SLP65_{1-330}$ with SLP65-3PRM in the titrations with 3SH3. In summary, the absence of binding in the SLP65-R247A construct and the increased affinity and functional valence in the SLP65-3xPRM4 construct confirm a stronger binding due to replacement of two PRMs by two times PRM4. Next, the titrations were compared with respect to the 3SH3 *vs* 3SH3B. The K_D is reduced by a factor of 4.0 between the titration of $SLP65_{1-330}$ to 3SH3B *vs* $SLP65_{1-330}$ to 3SH3 and by a factor of 1.7 between the titrations of SLP65-3xPRM4 to 3SH3B *vs* SLP65-3xPRM4 to 3SH3. However the values of entropy and enthalpy are larger for the titrations with 3SH3, which could be explained by a

concentration dependence of ΔH and ΔS in multivalent systems. Although the entropy and enthalpy were obtained by fits to a one-site binding model, the values should be considered as global values and the difference could be explained if the enthalpy or entropy concentration dependent. Nevertheless, the dissociation constants and the n-values confirm a higher affinity of the 3SH3B constructs introduced by the replacement of each SH3A and SH3C with SH3B.

Table 15: Thermodynamic parameters of ITC titrations of the 3SH3 – SLP65 constructs. ITC was measured for the interactions of $SLP65_{1-330}$, SLP65-R247A or SLP65-3xPRM4 to either CIN85-3SH3 or CIN85-3SH3B. No binding was observed for SLP65-R247A which has an inactivated PRM4. SLP65-3xPRM4 and CIN85-3SH3B were designed as strong binding constructs and a lower apparent dissociation constant is observed. The apparent number of contact sites is reduced by 3xPRM4 constructs and increased for 3SH3B constructs. ITC data were analyzed using the one-site binding model due to the lack of complete data set for global analysis [162, 163]. Errors are given as standard deviation, except for the titration of SLP_{1-330} to 3SH3B without replicate, which reports the error of the fit.

ITC titration: [Titrant	to titrand]	# Replicates	n	Apparent K_D [μM]	ΔH [kcal/mol]	-TΔS [kcal/mol]
SLP65-R247A	to 3SH3	-	-	-	-	-
$SLP65_{1-330}$	to 3SH3	3	1.12 ± 0.02	1.49 ± 0.13	-20.30 ± 0.65	-12.03
SLP65-3xPRM4	to 3SH3	3	0.75 ± 0.01	0.24 ± 0.01	-24.66 ± 0.20	-15.29
SLP65-R247A	to 3SH3B	-	-	-	-	-
$SLP65_{1-330}$	to 3SH3B	1	1.69 ± 0.10	0.37 ± 0.13	-7.39 ± 4.66	-1.74
SLP65-3xPRM4	to 3SH3B	2	0.78 ± 0.08	0.14 ± 0.06	-15.68 ± 2.08	-5.99

3.2.3 Dissecting bimolecular condensate to identify drivers for phase separation

Affinity is a critical-determinant of properties of biocondensates [191]. An increase in affinity can influence liquid-liquid phase separation positively by promoting network interactions or negatively by restricting the mobility leading to solidification. After confirming a decrease and increase in affinity of the designed weak and strong binding constructs, respectively, we were interested in the phase separation properties of the designed constructs, checking whether an increase in affinity would lead to lower critical concentration for phase separation and decrease in a higher critical concentration. Fluorescence microscopy assays are commonly used to study

the phase separation behavior of purified proteins by measuring the critical concentration of phase separation [192].

The aim was to classify the binding entities 3xPRM4, 3SH3B and SUVs according to the contributions to phase separation. Therefore, different mixtures of atto-labeled SLP65, SLP65 and CIN85 constructs together with or without vesicles were prepared. In the confocal fluorescence microscopy assay, the protein concentrations were varied in order to determine the critical concentration ϕ. In the assays, an equimolar concentration was used such that the sum of the atto-labeled SLP65 and unlabeled SLP65 concentrations was equal to the concentration of the CIN85 construct.

In a first step, critical concentrations were measured for a set of mixtures including SUVs, 3SH3 constructs, SLP65 constructs and the respective atto430LS-SLP65 constructs (Figure 27), then, the phase separation propensities were assessed by the ratio of the critical concentrations (Figure 28). The mixture of the SLP65-R247A construct, the 3SH3 construct and SUVs had a 17x increased critical concentration relative to the mixture, where the $SLP65_{1-330}$ construct, instead of the SLP65-R247A construct was used (Figure 27 A) and this large factor (17x) demonstrates the significance of PRM4. Regarding the incomplete mixture of SUVs and 3SH3, the addition of a SLP65 construct promotes phase separation. A reduced critical concentration was expected, when the strong binding SLP65-3xPRM4 construct, instead of the $SLP65_{1-330}$ construct, was added to the mixture of 3SH3 and SUVs. Surprisingly no difference of the critical concentration was observed.

The same trend was observed in the set of experiments for which the 3SH3B construct, instead of the 3SH3 construct, was used (Figure 27 B). In these mixtures, the weakly binding SLP65-R247A construct showed a less pronounced effect by increasing the critical concentration by a factor of 2x, and the strongly binding SLP65-3xPRM4 construct resulted in the same critical concentration as the $SLP65_{1-330}$ construct. Although SLP65-3xPRM4's strong affinity had been confirmed previously (Figure 27), both $SLP65_{1-330}$ and SLP65-3xPRM4 resulted in equal critical concentrations (2 µM for mixtures with 3SH3, 0.5 µM for mixtures with 3SH3B) in the presence of SUVs. Since hexavalent SLP65 constructs and trivalent CIN85 constructs were mixed at

equimolar concentration, the increased affinity via PRMs could be irrelevant, if SH3 domains are already saturated. On the other hand, a large shift in the critical concentration was observed for the strong binding construct 3SH3B. Regarding mixtures including SUVs and the weak binding SLP65-R247A construct, the addition of 3SH3 *vs* 3SH3B resulted in a shift of the critical concentration from 35 µM to 1 µM.

In the next sets of experiment, the mixtures were prepared without SUVs (Figure 27 C, D) and the same combination of mixtures of SLP65 constructs (weak, *wildtype*-like and strong binding SLP65 versions) with either *wildtype*-like 3SH3 construct or strong binding 3SH3B construct were investigated. The mixture of 3SH3 and SLP65-R247A sparsely showed droplets at highest available equimolar protein concentrations, thus, no phase separation was observed for concentrations up to 320 µM. The mixture of strong binding SLP65-3xPRM4 and 3SH3 reduced phase separation as expected relative to the mixture of $SLP65_{1-330}$ by a factor of 5 (Figure 27 C). We note as an interim summary that the binding entity of 3xPRM4 (mediated by two PRM4 with a monovalent K_D = 6 µM to SH3B) has no effect in presence of SUVs and does not reduce the critical concentration from 2 µM to a lower value. Contrarily, in absence of SUV, the binding entity of the SLP65-3xPRM4 construct promote phase separation by reducing ϕ from 100 µM to 20 µM. The mixtures including the 3SH3B construct instead of the 3SH3 construct showed the same tendency, but less pronounced effect that SLP65-3xPRM *vs* $SLP65_{1-330}$ reduces phase separation by a factor of 2 (Figure 27 D). In mixtures including 3SH3B, the addition of $SLP65_{1-330}$ *vs* SLP65-R247A reduced ϕ by 2.5x. Also, the addition of SLP65-3xPRM4 reduced ϕ by 2x relative to the critical concentration of the mixture of 3SH3 and $SLP65_{1-330}$ (Figure 27 D).

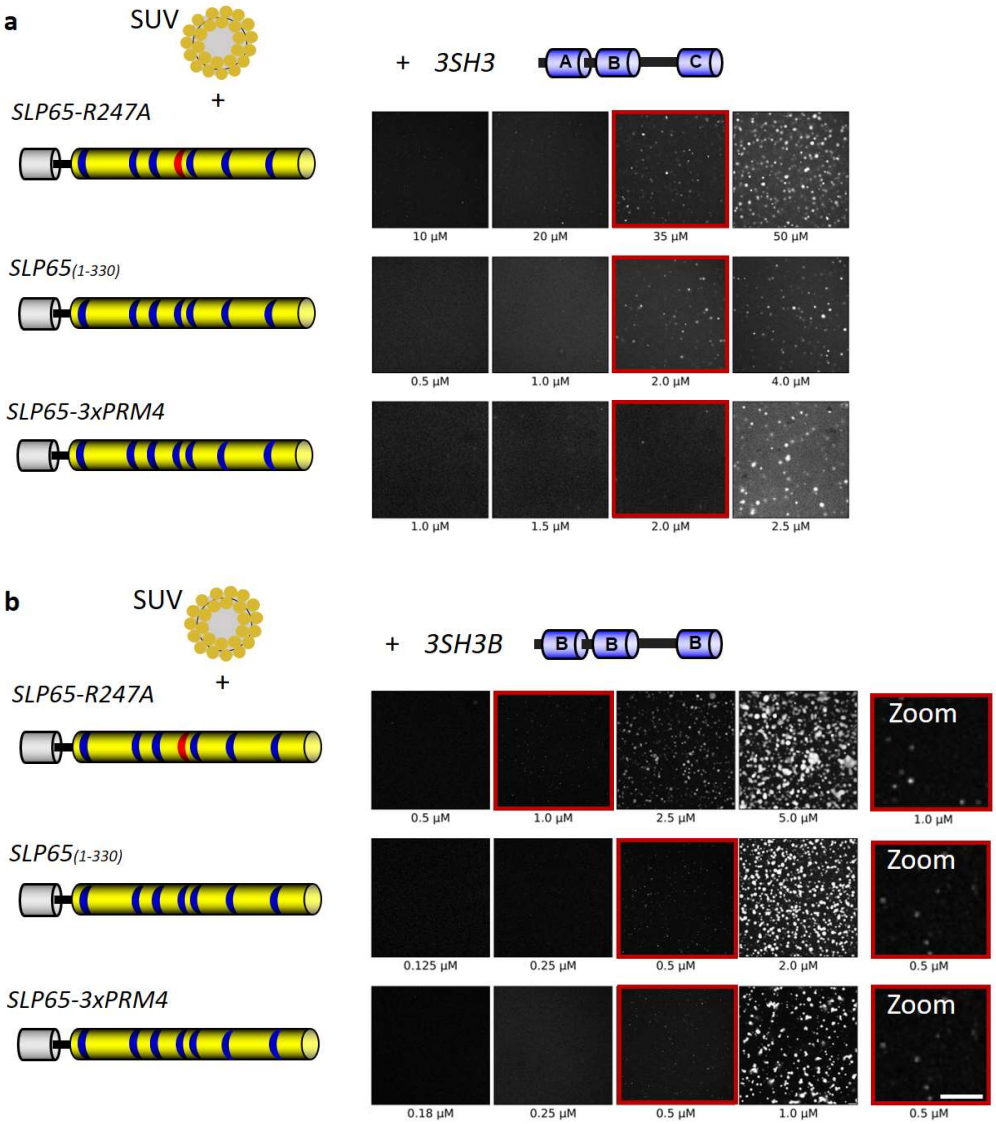

Figure 27: Measurement of critical concentrations of SLP65-CIN85 condensates by confocal fluorescence microscopy: Mixtures of protein constructs of increasing equimolar concentrations were imaged. The schematic illustrations of SLP65 *(left)* and CIN85 *(top)* indicate which constructs were mixed. The image yielding the critical concentration is highlighted *(red box)*. **A)** Mixtures of SUVs, SLP65 constructs and 3SH3 construct. **B)** Mixtures of SUVs, SLP65 constructs and 3SH3B construct. **C)** Mixtures of SLP65 constructs and 3SH3 construct without SUVs. **D)** Mixtures of SLP65 constructs and 3SH3B construct without SUVs.

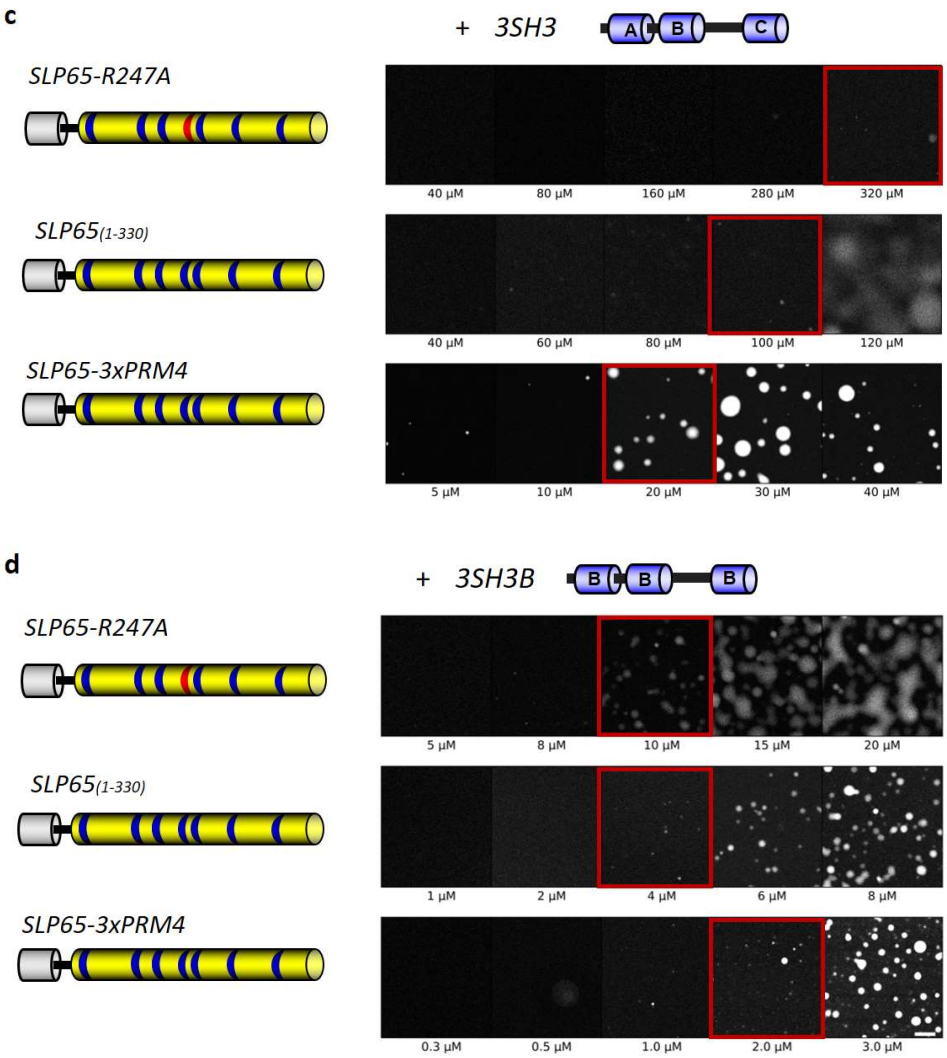

Figure 27. Continued from previous page.

We were interested how the designer constructs influence phase separation, and we noted that the weak or strong binding construct lead to a range of factors depending on the phase separation properties of other interacting components in the solution. As a next step, the range of factors was further analyzed. If vesicles were absent, the mixture of the 3SH3 construct with the SLP65 construct SLP65-R247, $SLP65_{1-330}$ or SLP65-3xPRM4 had critical concentrations at above 320 µM, 100 µM and 20 µM, respectively. In the presence of SUVs, the 3SH3 construct mixed with the SLP65 construct SLP65-R247, $SLP65_{1-330}$ or SLP65-3xPRM4 phase separated at 35 µM, 2 µM and 2 µM, respectively. The associated factors of conditions with and without SUVs, were ~9, 50 and 10, respectively. The factors were 10, 8 and 4, respectively, if the 3SH3B

construct, instead of the 3SH3 construct, was used (see also the yellow box in Figure 28). Altogether the factors range from 4 - 50, indicating a large effect of SUVs.

The contribution of the 3SH3B binding entity was analyzed from two-, and three-component mixtures (±SUVs). The associated factors of three-component mixtures either with the 3SH3 construct or the 3SH3B construct were 35, 4 and 4 for mixtures with SLP65-R247, $SLP65_{1-330}$ or SLP65-3xPRM4, respectively. The associated factors of two-component mixtures either with the 3SH3 construct or the 3SH3B construct were >32, 25 and 10 for mixtures with SLP65-R247, $SLP65_{1-330}$ or SLP65-3xPRM4, respectively (see also the blue box in Figure 28). The factors range from 4 – 35, indicating a strong effect of the 3SH3B entity. In summary, the factors reporting about 3xPRM4 range from 1 – 5, indicated a small effect (see Figure 28, ratios of critical concentrations of $SLP65_{1-330}$ *vs* SLP65-3xPRM4). The factors reporting about PRM4 range from 2 – 17.5 (see Figure 28, ratios of critical concentrations of SLP65-R247A *vs* $SLP65_{1-330}$), indicated a medium effect and the presence of the binding entity 3SH3B upon addition of SUVs promoted phase separation by the largest effect.

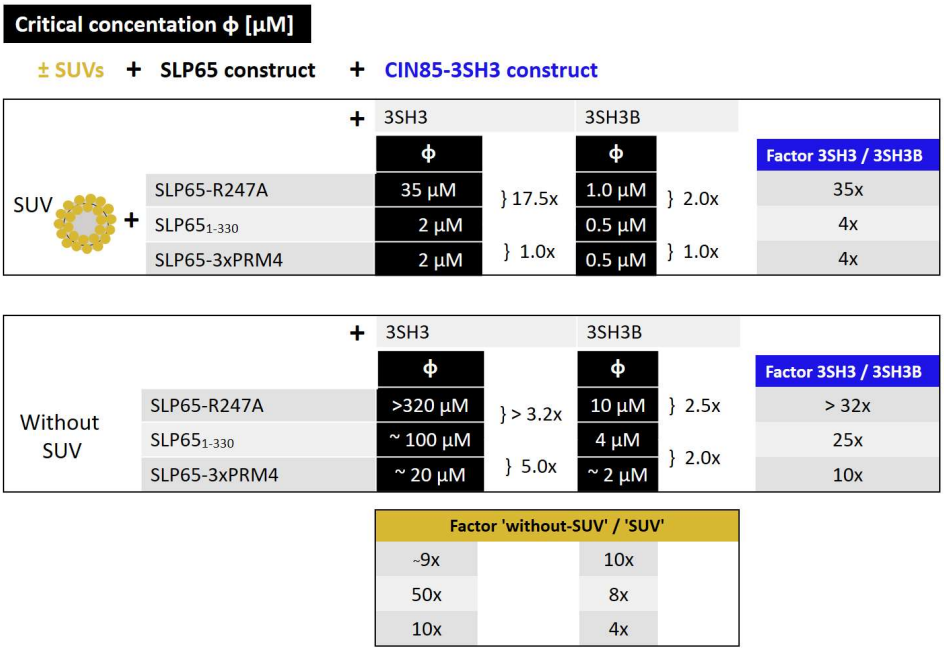

Figure 28: Critical concentrations of phase separation for mixtures of SLP65 and CIN85 constructs and the associated phase separation factors. The critical concentrations of phase separation are highlighted in black boxes. Factors were taken as the ratio of two critical concentrations. In order to compare the binding entity of 3SH3B, the phase separation factors from ratios 3SH3 over 3SH3B is shown (below blue box). In order to compare the contribution of vesicles, the factors are the ratio of conditions without vesicles over mixtures with vesicles (below yellow box).

3.2.4 SUVs and SH3B domains are classified as the main drivers for phase separation

The fluorescence microscopy assay was not sensitive to show the effect of the SLP65-3xPRM4 construct in mixtures with critical concentration of ~2 µM or below, however a different critical concentration between SLP65-3xPRM4 and $SLP65_{1-330}$ was distinguishable at higher critical concentrations. In order to classify the binding entities according to the reduction in phase separation *vs* critical concentration, the range of the factors were represented in a graph (Figure **29**).

As described above, the critical concentration ϕ was measured for different combinations of designer constructs, either with or without SUVs. The phase separation reduction factors were obtained by the ratio of $\phi_{without\text{-}binding\text{-}entity}/\phi_{with\text{-}binding\text{-}entity}$ regarding the binding entities PRM4,

3xPRM4, 3SH3B and SUVs (Figure 28). Note that a range of phase separation reduction factors is associated to a particular binding entity, e.g. the effect of a particular binding entity is strong if the reference concentration $\phi_{\text{without-binding-entity}}$ is high, *vice versa* the effect is weak, if the reference concentration is low. In order to compare two different binding entities, the phase separation reduction factors of the same reference needs to be considered. Thus, the binding entities were classified accordingly to the reduction in phase separation (Figure 29, y-axis: phase separation reduction factors, x-axis: reference critical concentration of phase separation $\phi_{\text{without-binding-entity}}$). In conclusion, the phase separation reduction factors $\phi_{SLP65^{1-330}}/\phi_{SLP65\text{-}3xPRM4}$ disclosed the weak effect of the 3xPRM4 binding entity. The factors $\phi_{SLP65\text{-}R247A}/\phi_{SLP65^{1-330}}$ revealed the medium effect of a functional PRM4. The factors ϕ_{3SH3}/ϕ_{3SH3B} and $\phi_{\text{without SUV}}/\phi_{SUV}$ disclosed the strong effects of the 3SH3B binding entity and SUVs, respectively.

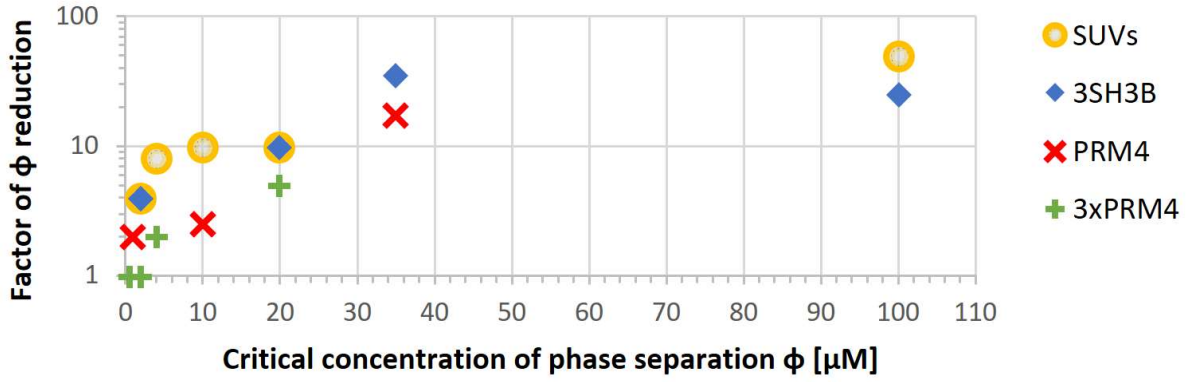

Figure 29: Comparison of binding entity's contribution to phase separation. A particular binding entity (SUVs, 3SH3B, PRM4 or 3xPRM4) promotes phase separation and reduces the critical concentration. The effect of the R247A mutation can be regarded as the effect of the functional PRM4. SUVs have the strongest effect and 3xPRM4 has the weakest effect. The contribution to phase separation is classified in the following order starting with the strongest effect: SUVs, 3SH3B, PRM4 and 3xPRM4.

3.3 Condensed SUVs are an integral part of SUVs

As demonstrated in the previous section, the binding to vesicles has a large contribution in reducing the critical concentration to physiological relevant protein concentrations. The binding

of SLP65's N-terminus to vesicles and its impact on phase separation has been reported previously, however the structural aspect of a vesicle-containing droplet remained unclear [116, 121]. Vesicles could serve as a seed, centered in the droplet surrounded by phase separating proteins. Alternatively, vesicles could distribute all around the droplet and participate in network formation. To investigate this question, cryo-electron tomograms of droplets were acquired from a mixture of 1 µM SLP65, 1 µM CIN85Δ57 and vesicles (lipid concentration 1 mM). 1/4th of the droplet was segmented for 3D-visualization and overlaid with the tomogram (Figure 30). The SUVs are highly concentrated in the droplet. The SUVs accumulated within the droplet and were less concentrated at the edge. This indicated that vesicles are a substantially part of the condensed phase and can shape the morphology on a mesoscale.

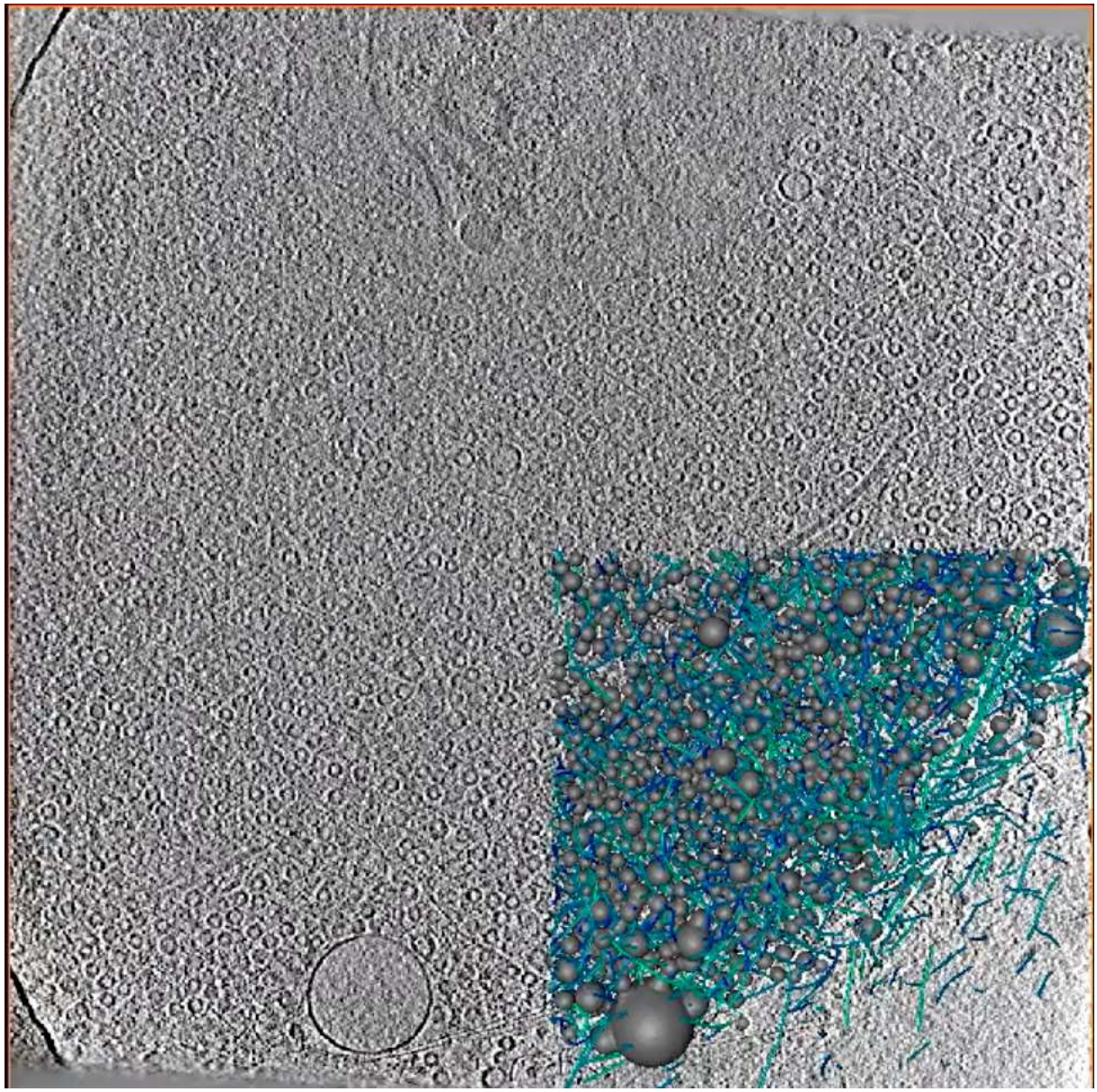

Figure 30: Vesicle distribution inside SLP65/CIN85Δ57/SUV droplets visualized by cryo-electron tomography. Approximately a quarter of the cross-section was segmented and colored. Vesicles are depicted in grey, and fibers by a blue-green colorscale color-coding the orientation. A mixture of 1 µM SLP65, 1 µM of CIN85Δ57 and vesicles (lipid concentration 1 mM) was incubated for 45 min and plunge-frozen. The vesicles accumulate within the droplet and are less concentrated at the edge, distinguishing two separate phases.

3.4 High-affine interaction counteracts fusion

The mechanism of liquid-like phase separation drive the formation of liquid- or gel-like biocondensates, which can have a biological function, quite in contrast to aggregates, which are a clump of mis-folded, dysfunctional proteins. The principles of liquid liquid phase separation and its functional consequences are reviewed by Hyman *et al.* [193]. The protein FUS is an example for an aggregation of a liquid like droplets. Phase separation of FUS is maintained by transient, weak interactions. It is speculated that more affine interaction could drive aggregation, which could lead to disease [29, 37, 194].

In this thesis, mixtures including a different combination of SLP65 and CIN85 constructs of different affinity were investigated. For the measurement of the critical concentration of phase separation, mixtures of increasing equimolecular concentrations were prepared. The mixture was incubated for 1 hour and observed by fluorescence microscopy, after the droplets had settled to the surface of the microscope slide. The droplets of almost any combination underwent liquid-liquid phase separation showing Ostwald ripening, *i.e.* the merging of smaller droplets to larger ones. Figure 31 A shows spherical droplets at the surface of the slide, which is a representative image of tripartite phase separation (SUVs + weak, *wildtype*-like or strong SLP65 constructs + 3SH3 or 3SH3B constructs), except for the two mixtures of SLP651-330/SLP65-3xPRM4, SUV and 3SH3B. Concentration dependent morphological changes were observed in these droplets. A stack of images was recorded from the surface to 10 µm above (Figure 31 A). At 5 µM concentration of the $SLP65_{1-330}$ containing mixtures, the droplets did not fuse into a confluent layer, but resembled more the shape of bubbly walls. This is not observed at a concentration of 2 µM $SLP65_{1-330}$, where the droplets settled to the surface completely as visualized in the z-stack image at 6 µm. More clearly, droplets containing the strong binding SLP65-3xPRM4 construct did not form a confluent layer on the bottom and stacks of phase separated matter extended 10 µM above the surface (Figure 31 B). The observations indicate that additional interactions, introduced either by the larger affinity (SLP65-**3xPRM4** + 3SH3**B** + SUVs) or by higher concentration and the larger affinity of 3SH3B ($SLP65_{1-330}$ + 3SH3**B** + SUVs), could change the fusion properties of SLP65-CIN85-vesicle droplets.

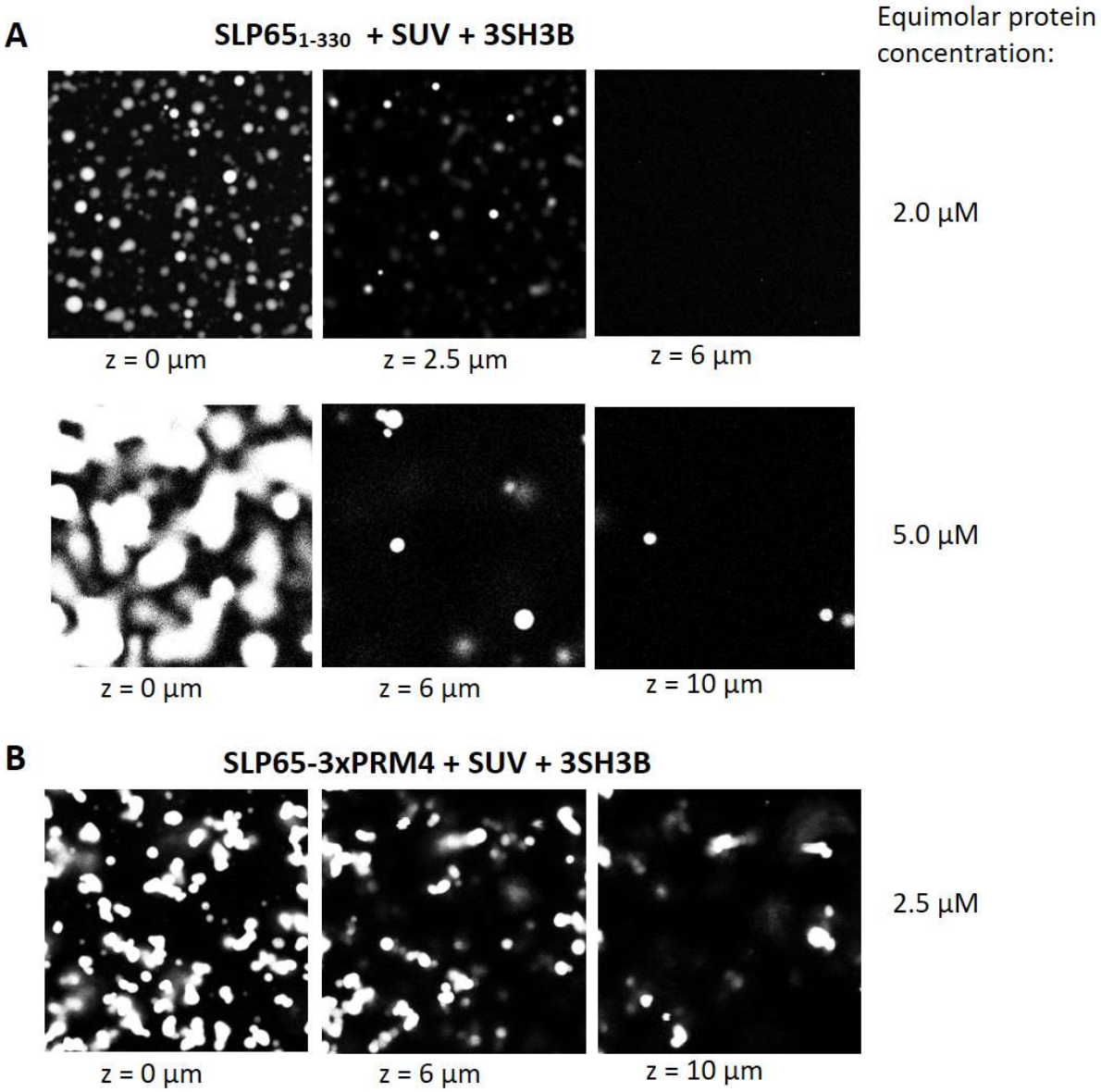

Figure 31: Strong binding constructs impede fusion. After incubation and before imaging, droplets sank down and fused on the bottom of the slide. A) Upper panel: Reconstituted droplets containing SUVs, 3SH3B and *wildtype* SLP65$_{1-330}$ at 2 µM equimolar protein concentration fused into larger spheres. With increasing equimolar concentration the spherical shape is distorted, while droplets tended to form a monophase layer. Lower panel: Reconstituted droplets containing SUVs, 3SH3B and *wildtype* SLP65$_{1-330}$ at 5 µM equimolar protein concentration attach to strings that extend to 10 µM above the surface B) SLP65-3xPRM4 reconstituted droplets have compromised fusion and do not produce a monophase layer. Z-stacks were acquired between 0 – 10 µm above the bottom of the slide (scalebar = 10 µm).

3.5 LASSI Monte Carlo simulation of phase separation/ Biocondensate visualization using LASSI

In the previous section, phase separation-relevant binding modules have been identified. Although the SH3B domain and PRM4 have a significant role within the promiscuous interactions, a model for describing the SLP65-CIN85 condensate is missing. Here, the goal was to parameterize a lattice-based sticker-spacer model, which is capable to match simulated with experimental critical concentrations using the program LASSI [103]. The cytosolic vesicles binding to SLP65's N-terminus were reconstituted *in vitro* by SUVs [116]. Since the molecular architecture of vesicles is not straightforwardly designed in LASSI, SUVs were excluded in the following experiments and we focus on the promiscuous binding between SH3 domains and PRMs,

The set-up of the protein architecture consisted of six stickers for SLP65 (6 x PRMs, exluding the weak binding PRM*; Figure 23), three stickers for 3SH3 (3x SH3 domain) and inert spacers linking the motifs/domains (Figure 32**: Molecular architecture and linker length scaling of SLP65 and CIN85.** The sticker-spacer structures of SLP65 and 3SH3 were designed according to Figure 9. The scaling factors (4/6, 3/6, 2/6, 1/6, 1/8, 1/9, 1/11) convert the number of amino acids in the linkers to the number of beads in the linkers by multiplication. Varying linker length were used to parameterize a model, where the ratios of simulated and experimental critical concentrations are in agreement.). The pairwise interaction energy matrices were derived from experimentally determined binding affinities of the monovalent SH3-PRM interactions (Figure **10**). The simulation set-up of strong and weak binding constructs of SLP65 and CINI85-3SH3 differed in the interaction energy terms according to the mutated modules. The choice of the simulation parameters for the number of molecules and the move sets was guided by the comments in the publication of LASSI [103].

SLP65's linker length scaling on the lattice:

PRM: 1 2 3 4 5 6

60 45 74 27 26 [a.a.]

	Linker 1,	-2	Linker 3	Linker 4	Linker 5
4/6	40	32	48	20	16
3/6	30	24	36	15	12
2/6	20	16	24	10	8
1/6	10	8	12	5	4
1/8	8	6	9	3	3
1/9	7	5	8	3	3
1/11	5	4	7	2	2

3SH3's linker length scaling on the lattice:

42 a.a. 108 a.a.

	SH3A - **Linker 1** - SH3B - **Linker 2** - SH3C	
4/6	28	72
3/6	21	54
2/6	14	36
1/6	7	18
1/8	5	14
1/9	4	12
1/11	4	10

Figure 32: Molecular architecture and linker length scaling of SLP65 and CIN85. The sticker-spacer structures of SLP65 and 3SH3 were designed according to Figure 9. The scaling factors (4/6, 3/6, 2/6, 1/6, 1/8, 1/9, 1/11) convert the number of amino acids in the linkers to the number of beads in the linkers by multiplication. Varying linker length were used to parameterize a model, where the ratios of simulated and experimental critical concentrations are in agreement.

For illustration, the course of a simulation of $SLP65_{1\text{-}330}$ – 3SH3B is shown in Figure 33, highlighting the network before phase separation (Figure 33 A) and after phase separation (Figure 33 B). The phase separated state is indicated by the second peak of the radial pair distribution function (PDF, Figure 33 C). A reference simulation with all anisotropic interaction terms set to zero results in a homogeneous distribution of the molecules in the simulation box.

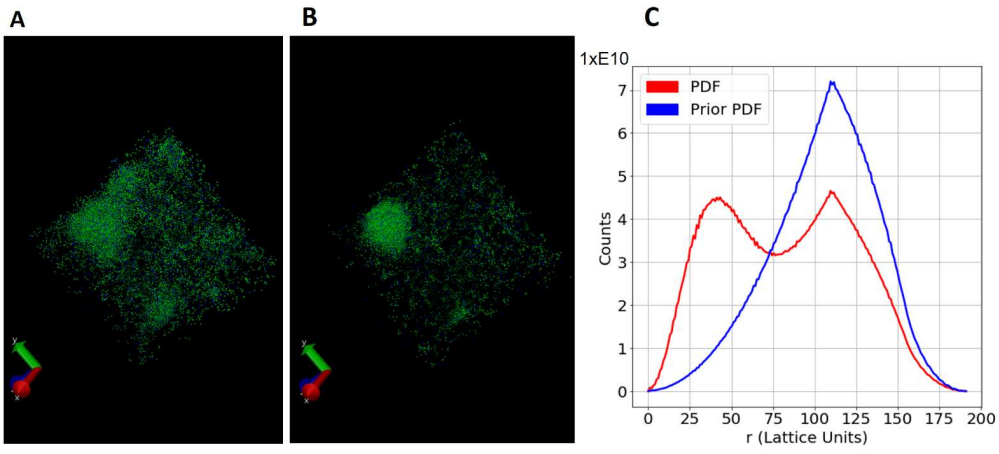

Figure 33: Representative illustration for simulating phase separation with LASSI [103]. A) The visual representation shows the distribution of molecules in an extended clustered network before phase

separation. B) The visual representation of phase separation shows a large cluster after phase separation. The binding modules SLP65-PRMs and 3SH3 are color coded green and blue, respectively. C) Two simulations were run with negative anisotropic interaction energy terms or terms set to zero in order to obtain the radial pair density distribution function and a reference, respectively. The prior radial pair density distribution (PDF) is the reference. The additional peak of the PDF *vs* the prior PDF indicates phase separation. The prior PDF was obtained by simulation with anisotropic interaction energy terms = 0, which means that there is no interaction within any of the stickers.

In order to simulate the critical concentration, the box size was varied. This was done for each combination of SLP65 – 3SH3 constructs. Furthermore, the linker length was scaled obtaining seven sets of simulations. The scaling by 1/6 were rationalized as described in the methods section. Furthermore, the linker length was increased by scaling with the factors 2/3, 1/2 and 1/3 to explore larger linkers. Harmon *et al.* show that the cooperative binding effect disappears if the linkers are too large (Figure 8 a in Harmon *et al.* [102]), so the linker length were also reduced by scaling with 1/8, 1/9 and 1/11. Thus, the critical concentrations were obtained for seven sets of simulations with scalings by 2/3, 1/2, 1/3, 1/6, 1/8, 1/9 and 1/11

The critical concentration of phase separation of simulations with either 3SH3 or 3SH3B did not differ more than a factor of 3 in all simulations regardless of the linker length scaling (Table 16), in contrast to experimental observation, where the factors range from 10 – 25 (Figure 28). Consequently, the simulated and experimental phase separation factors did not agree well (Table **17**).

Table 16: Critical concentration simulated for six SLP65 – 3SH3 combinations for seven different linker lengths. In order to determine the critical concentration [molecules / voxel], the box size was varied in steps of 10 both for each linker length and for each combination of the strong/*wildtype*-like 3SH3 construct with the strong/*wildtype*-like/weak SLP65 construct.

	Critical concentration [molecules / voxel]						
Linker length scaling:	**4/6**	**3/6**	**2/6**	**1/6**	**1/8**	**1/9**	**1/11**
SLP65-R247A & 3SH3	3.6E-05	3.1E-05	1.9E-05	1.6E-05	1.6E-05	2.7E-05	2.9E-05
$SLP65_{1-330}$ & 3SH3	1.8E-05	1.3E-05	8.0E-06	1.1E-05	2.2E-05	3.6E-05	5.1E-05
SLP65-3xPRM4 & 3SH3	1.1E-05	8.0E-06	6.0E-06	8.0E-06	1.7E-05	2.5E-05	3.9E-05
SLP65-R247A & **3SH3B**	2.9E-05	2.7E-05	1.6E-05	1.1E-05	1.6E-05	2.1E-05	2.7E-05
$SLP65_{1-330}$ & **3SH3B**	1.1E-05	8.0E-06	5.0E-06	1.0E-05	1.8E-05	3.4E-05	4.3E-05
SLP65-3xPRM4 & **3SH3B**	4.0E-06	3.0E-06	3.0E-06	1.1E-05	3.1E-05	6.7E-05	1.0E-04

Table 17: Phase separation factors of simulations with varying linker length using the 3SH3 design. The ratio of critical concentrations of two mixtures were taken in order to compare the phase separation factors to the one of the experiment (Table 17). The phase separation factors from ratios 3SH3 vs 3SH3B differed by ~10 x between simulation and experiment.

	Phase separation factors (Simulation)						
Linker length scaling:	**4/6**	**3/6**	**2/6**	**1/6**	**1/8**	**1/9**	**1/11**
Model with 3SH3:							
SLP65-R247A & 3SH3 *vs* $SLP65_{1-330}$ & 3SH3	2.0	2.5	2.4	1.5	0.7	0.7	0.6
$SLP65_{1-330}$ & 3SH3 *vs* SLP65-3xPRM4 & 3SH3	1.6	1.6	1.4	1.4	1.3	1.4	1.3
SLP65-R247A & **3SH3B** *vs* $SLP65_{1-330}$ & **3SH3B**	2.7	3.4	3.0	1.1	0.9	0.6	0.6
$SLP65_{1-330}$ & **3SH3B** *vs* SLP65-3xPRM4 & **3SH3B**	2.5	2.3	1.6	0.9	0.6	0.5	0.4
SLP65-R247A & 3SH3 *vs* SLP65-R247A & **3SH3B**	1.3	1.2	1.2	1.5	1.0	1.3	1.1
$SLP65_{1-330}$ & 3SH3 *vs* $SLP65_{1-330}$ & **3SH3B**	1.7	1.6	1.5	1.1	1.2	1.1	1.2
SLP65-3xPRM4 & 3SH3 *vs* SLP65-3xPRM4 & **3SH3B**	2.6	2.3	1.7	0.7	0.5	0.4	0.4

There is experimental evidence of intramolecular binding of SH3C to the linker region between SH3B and SH3C [195]. Additional supporting experiments demonstrate that the K_Ds of the interactions of CIN85-PRM1 to SH3A or SH3B are significantly larger compared to the K_D of the SH3C (unpublished results from my colleague D. Sieme). The modeling the 3SH3 construct with defining three SH3 domains could be incorrect, if the SH3C domain is occupied due to the intramolecular interactions. Since intramolecular interactions cannot be modeled in LASSI the 2SH3 virtual construct was designed (Figure 34), where the anisotropic pairwise interaction energy matrices of the SH3C terms were set to 0, assuming complete occupation of SH3C by the CIN85-PRM1, such that the SH3C sticker were still present, but modeled as non-interacting beads.

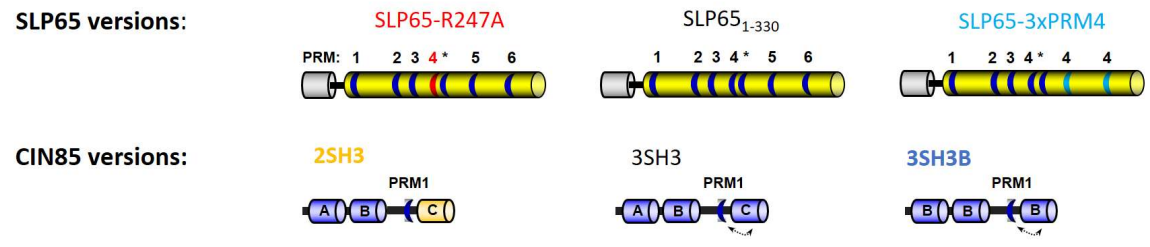

Figure 34: Schematic representation of SLP65 and CIN85. The intramolecular interaction cannot be modeled in LASSI. To take into account the interaction of SH3C with CIN85-PRM1, the energy terms of the stickers representing SH3C were set to 0 in the design of the 2SH3, such that the SH3C sticker is still present as a bead, but does not interact with other stickers.

The critical concentration of simulations with the 2SH3 design (Table 19) improved the prediction of critical concentrations for phase separation. The experimental and simulated phase separation factors of 2SH3 *vs* 3SH3B matched with deviation less than factors of 3 (Experimentally determined factors: Table 18; simulated factors:

Table **20**). This result indicates that the valency of the 3SH3 construct is reduced, i.e. that SH3C does not participate in binding to the PRMs of SLP65 because it is engaged in binding CIN85-PRM1. Note that the ordering of the experiments is the same in table 18 and 19 and therefore the phase separation factors, i.e. the factors of the critical concentrations for phase separation for the two conditions can be directly compared between experiment (Table 18) and LASSI simulations (Table 20).

Table 18: Recapitulating the phase separation factors of Table 17. Phase separation factors are given as the ratios of the experimentally determined critical concentrations of two mixtures. The critical concentration could not be determined for the SLP65-R247A & 3SH3 mixture, thus the minimal factor is given (grey shaded boxes).

Mixture of constructs:	**Phase separation factors (Experiment)**
SLP65-R247A & 3SH3 *vs* $SLP65_{1-330}$ & 3SH3	>3.2
$SLP65_{1-330}$ & 3SH3 *vs* SLP65-3xPRM4 & 3SH3	5
SLP65-R247A & **3SH3B** *vs* $SLP65_{1-330}$ & **3SH3B**	2,50
$SLP65_{1-330}$ & **3SH3B** *vs* SLP65-3xPRM4 & **3SH3B**	2
SLP65-R247A & 3SH3 *vs* SLP65-R247A & **3SH3B**	>32
$SLP65_{1-330}$ & 3SH3 *vs* $SLP65_{1-330}$ & **3SH3B**	25
SLP65-3xPRM4 & 3SH3 *vs* SLP65-3xPRM4 & **3SH3B**	10

Table 19: Critical concentration simulated for six SLP65 – 3SH3 combinations for seven different linker lengths. In order to determine the critical concentration[molecules / voxel], the box size was varied in steps of 10 both for each linker length and for each combination of the strong/*wildtype*-like 3SH3 construct with the strong/*wildtype*-like/weak SLP65 construct. Simulations that result in percolation, and not PS are shaded in the color grey.

	Critical concentration [molecules / voxel]						
Linker length scaling:	**4/6**	**3/6**	**2/6**	**1/6**	**1/8**	**1/9**	**1/11**
SLP65-R247A & 2SH3	3.6E-05	3.1E-05	1.9E-05	1.6E-05	1.6E-05	2.7E-05	2.9E-05
$SLP65_{1-330}$ & 2SH3	1.8E-05	1.3E-05	8.0E-06	1.1E-05	2.2E-05	3.6E-05	5.1E-05
SLP65-3xPRM4 & 2SH3	1.1E-05	8.0E-06	6.0E-06	8.0E-06	1.7E-05	2.5E-05	3.9E-05
SLP65-R247A & 3SH3B	2.9E-05	2.7E-05	1.6E-05	1.1E-05	1.6E-05	2.1E-05	2.7E-05
$SLP65_{1-330}$ & 3SH3B	1.1E-05	8.0E-06	5.0E-06	1.0E-05	1.8E-05	3.4E-05	4.3E-05
SLP65-3xPRM4 & 3SH3B	4.0E-06	3.0E-06	3.0E-06	1.1E-05	3.1E-05	6.7E-05	1.0E-04

Table 20: Phase separation factors of simulations with varying linker length using the 2SH3 design. SLP65's and CIN85's linkers were scaled to define the linker length in the LASSI simulation. The Varying the linker length resulted in concentrations of two mixtures were taken in order to compare the phase separation factors from the experiment (Table 18) with the simulated ones. The phase separation factors from ratios 2SH3 vs 3SH3B were in the same order in the simulation and the experiment.

	Phase separation factors (Simulation)						
Linker length scaling:	**4/6**	**3/6**	**2/6**	**1/6**	**1/8**	**1/9**	**1/11**
Model with 2SH3:							
SLP65-R247A & 2SH3 *vs* $SLP65_{1-330}$ & 2SH3	2.1	2.1	3.2	1.0	0.6	0.5	0.7
$SLP65_{1-330}$ & 2SH3 *vs* SLP65-3xPRM4 & 2SH3	1.2	1.2	1.4	1.8	2.4	1.4	1.0
SLP65-R247A & 3SH3B *vs* $SLP65_{1-330}$ & 3SH3B	2.7	3.4	3.0	1.1	0.9	0.6	0.6
$SLP65_{1-330}$ & 3SH3B *vs* SLP65-3xPRM4 & 3SH3B	2.5	2.3	1.6	0.9	0.6	0.5	0.4
SLP65-R247A & 2SH3 *vs* SLP65-R247A & 3SH3B	7.4	8.0	13.5	17.4	45.6	73.1	74.1
$SLP65_{1-330}$ & 2SH3 *vs* $SLP65_{1-330}$ & 3SH3B	9.4	12.7	12.5	19.3	64.0	81.4	64.0
SLP65-3xPRM4 & 2SH3 *vs* SLP65-3xPRM4 & 3SH3B	18.7	23.4	14.3	9.4	15.6	29.8	27.0

The simulation trajectories of all nine 3SH3 – SLP65 combinations were visualized in VMD (Figure **35**). Separated clusters are seen in simulations of 3SH3 and 3SH3B. Simulations with 3SH3B always resulted in phase separation as indicated by a global density inhomogeneity parameter >

0.025. Simulations with 2SH3 resulted in phase separation as well as percolation, which manifested itself as a steep transition from a low percolation value to a percolation value > 0.2. The distinction of percolation and phase separation is reported in table 21. The error factors (equation 23) measures the deviation of the simulated critical concentrations from the experiment within a set of simulations of a defined linker length (Table 22). The simulations with linkers scaled by 2/3 or 1/2 have acceptable error factors (2.2 and 2.1, respectively) in order to explain the large experimental factors of the 3SH3 construct (with intramolecular inhibition of SH3C by CIN85-PRM1) *vs* the 3SH3B construct (10x and 25x, Table 18), however the linker length settings could be outside the optimal range (Figure 8 a in Harmon et al. [102]). Thus, linker length were further reduced. Simulations with linker lengths in the range of 8 - 36 (scaling by 1/3) lead to good agreement of simulation and experiment (Error factor 1.9, Table 22). Further reducing the linker length to a range with lengths 4 – 18 (scaling 1/6), or even shorter, leads to a disagreement of the factor SLP65-R247A & 3SH3B *vs* SLP651-330 & 3SH3B and of SLP651-330 & 3SH3B *vs* SLP65-3xPRM4 & 3SH3B, although the factor of $SLP65_{1-330}$ & 2SH3 *vs* $SLP65_{1-330}$ & 3SH3B and of SLP65-3xPRM4 & 2SH3 vs SLP65-3xPRM4 & 3SH3B maintain a good agreement. All sets of simulations of the 2SH3 have a smaller error factor than the sets of simulations including the 3SH3 construct. The main surprising observation, namely that replacement of 3SH3 by 3SH3B causes large reduction of the critical concentration for phase separation, while replacement of SLP65 by SLP65-3PRM4 did not, is reproduced in all simulations irrespective of the linker length scaling. Thus, LASSI reproduces the experimental finding quantitatively for scaling the linker length by a factor between 1/3 and 1/6 and qualitatively for all scalings of the linker lengths.

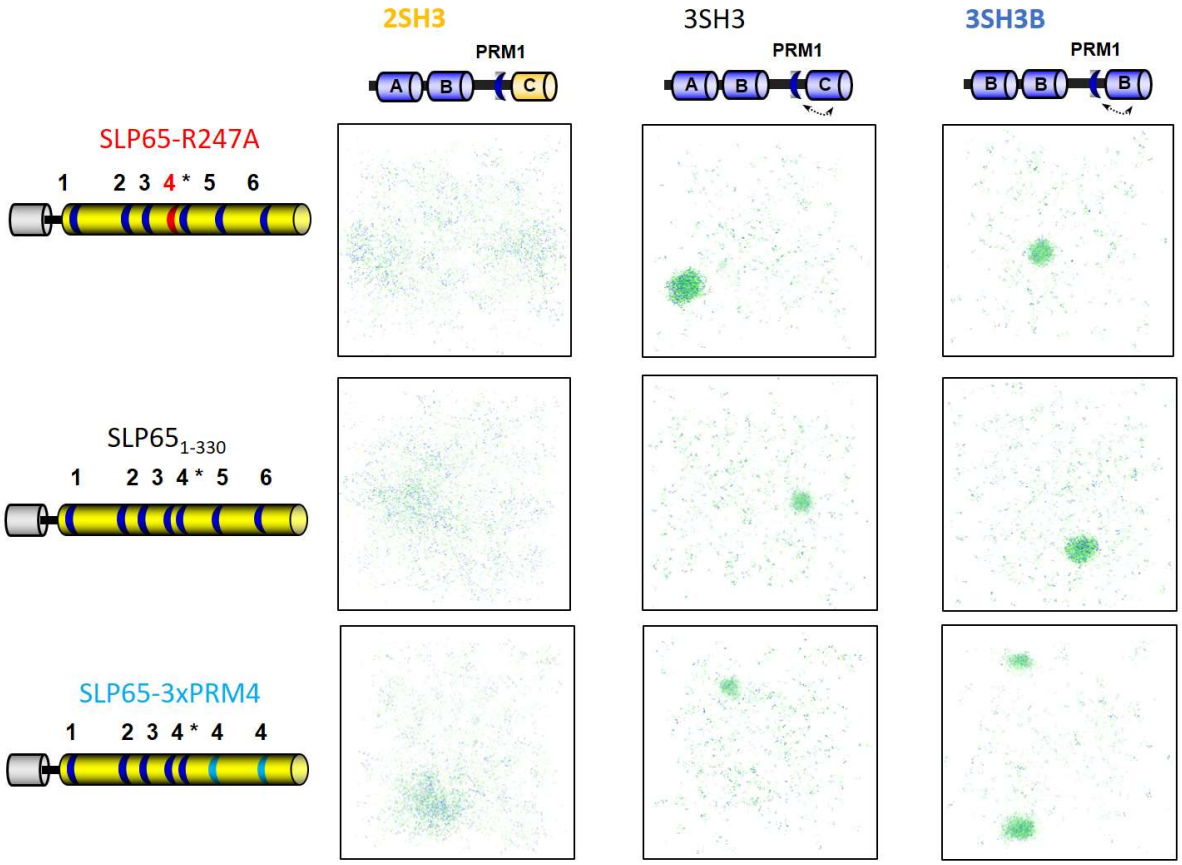

Figure 35: Simulation trajectories of all nine 3SH3 – SLP65 combinations. Single frame of a simulation trajectory were visualized in VMD. Phase separated clusters are seen in simulations of 3SH3 and 3SH3B. Simulations with 2SH3 resulted in a transition to a percolation, where separate large clusters are formed. Representative set of simulations with a linker length scaling of 1/8.

Table 21: LASSI box size from which the threshold concentration was determined. In order to determine the critical concentration, the box size was varied in steps of 10 both for each linker length and for each combination of the strong/*wildtype*-like 3SH3 construct with the strong/*wildtype*-like/weak SLP65 construct. The "critical box size" denotes the simulation with the specified box size at which a separated cluster is observed. Note that increasing the box size decreases the concentration, which results in a homogeneous phase. Sharp transitions from a homogeneous to a phase separated distribution were observed for most combinations of designed constructs, except for simulations with SLP65-R247A & 2SH3, SLP651-330 & 2SH3 and SLP65-3xPRM4 & 2SH3 (shaded in grey boxes).

Linker length scaling:	**4/6**	**3/6**	**2/6**	**1/6**	**1/8**	**1/9**	**1/11**
SLP65-R247A & 2SH3	210*	210*	210*	220*	140*	110*	100*
$SLP65_{1-330}$ & 2SH3	270*	270*	310*	220*	120*	90*	90*
SLP65-3xPRM4 & 2SH3	290	290	350	270	160	100*	90*
SLP65-R247A & 3SH3	380	400	470	500	500	420	410
$SLP65_{1-330}$ & 3SH3	480	540	630	570	450	380	340
SLP65-3xPRM4 & 3SH3	560	630	710	630	490	430	370
SLP65-R247A & 3SH3B	410	420	500	570	500	460	420
$SLP65_{1-330}$ & 3SH3B	570	630	720	590	480	390	360
SLP65-3xPRM4 & 3SH3B	770	830	850	570	400	310	270

Error factors (simulation *vs* experiment)

Linker length scaling:	**4/6**	**3/6**	**2/6**	**1/6**	**1/8**	**1/9**	**1/11**
Simulation set of 3SH3 (Table 17)	4.8	5.1	5.7	8.8	9.8	12.3	11.9
Simulation set of 2SH3 (Table **20**)	2.2	2.1	1.9	1.9	2.5	3.6	3.8

Table 22: Mean deviation of the experimentally determined factors of the critical concentrations from the simulated factors. The error factor measures the deviation of the critical concentration ratios of the simulation *vs* the ones of the experiment (eq. 23).

3.6 *Ex vivo* calcium signaling correlates with binding affinities

Pioneering studies of the T cell receptor signaling highlighted the functional relevance of phase separation in transmembrane signaling [87]. The downstream signaling proteins Linker for activation of T cells (LAT), Nck and N-WASP are adapter proteins involved in actin polymerization after T cell activation [196]. Both proteins colocalize in cytosolic clusters and their stoichiometry can regulates functional activity [197]. Moreover, Su *et al.* demonstrates the valency-dependent clustering of phosphorylated LAT by correlating experiments performed *in vitro* and in *ex vivo* cells [53].

The *in vitro* results of the preceding sections of this thesis can be correlated to *ex vivo* observations in order to get a better understanding of the SLP65-3SH3 binding in a living cell. We shift the view towards previous *ex vivo* studies, where mutant SLP65 versions were reconstituted in SLP65-deficient cells [131]. Oellerich *et al.* designed PRM-inactivated SLP65 versions by single point mutations of PRM1, PRM4 and PRM6. Transfection of the PRM-inactivated SLP65 mutants into $SLP65^{-/-}$ B cells revealed that the Ca^{2+} response was reduced as measured by a ratiofluorometric INDO-1 assay. Either PRM1, PRM4 or PRM6 was deactivated in the SLP65 mutant, reducing the signal to 81%, 36% or 57%, respectively (Figure 36). For comparison of the *in vitro* measured K_D (2D lineshape analysis) with the Ca^{2+} signal capability of the single point mutants of PRM1, PRM4 and PRM6, the three monovalent dissociation constants of SH3A, SH3B and SH3C (Figure 23) were averaged for either PRM1, PRM4 or PRM6, obtaining a K_D of 349, 67 or 111 µM, respectively. The Ca^{2+} mobilization relative to the *wildtype*-SLP65 was correlated to the averaged K_Ds with a Pearson correlation coefficient of R = 0.94. The Ca^{2+} mobilization experiments indicate that individual PRMs are not redundant but rather act cooperatively, which is corroborated by the correlation with the binding affinities measured *in vitro*. The pre-signaling cluster formation relies on promiscuous interaction of the two medium affinity motifs PRM1 and PRM6 and also the high affinity motif PRM4.

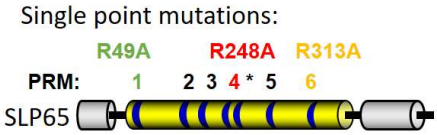

	Peak intensity of **Ca^{2+} signal*** [Relative fluorescence intensity]	**Average K_D [µM]****
PRM1 (40-53)	81%	349
PRM4 (238-251)	36%	67
PRM6 (303-316)	57%	111
Pearson correlation coefficient **R = 0.94**		

Figure 36: Binding affinities of monovalent PRM-SH3 interactions are linked to and correlate with *ex vivo* Ca^{2+} signaling. Previous studies* recorded the Ca^{2+} response in $SLP65^{-/-}$ cells reconstituted with SLP65 single point mutants by a ratiofluorometric INDO-1 assay. The R to A single-point mutations in SLP65-R49A, SLP65-R247A and SLP65-R313A mutants deactivated PRM1, PRM4 and PRM6, respectively. The reduced Ca^{2+} response is reported relative to the 100% peak intensity of the *wildtype*-SLP65 control. The average K_Ds of the PRM-SH3A, PRM-SH3B and PRM-SH3C interactions for PRM1, PRM4 and PRM6 were correlated to the Ca^{2+} signaling capabilities. (*Oellerich *et al.,* The B-cell antigen receptor signals through a preformed transducer module of SLP65 and CIN85. EMBO J, 2011, **K_D of PRM-SH3 interactions determined by 2D lineshape analysis, see figure 23).

In further ratiofluorometric Ca^{2+} mobilization assays, the SLP65-3xPRM4, *wildtype*-SLP65 or vesicle-binding deficient ΔN-SLP65 constructs were introduced in $SLP65^{-/-}$ DT40 cells by retroviral transfection (Figure 31 in Bhatt [198]). The SLP65-3xPRM4 construct is not expected to promote phase separation at physiological protein concentrations and cause more droplets compared to the *wildtype* SLP65 construct, because the binding entity 3xPRM4 did not reduce phase separation at concentrations of 0.5 µM and up to 2 µM, which are close to the physiological protein concentrations of both proteins of ~0.5 µM [116] (Figure 29). In vivo, a reduced number of droplets and a reduced Ca^{2+} mobilization was observed (Figure 37 A, B). When comparing *wildtype* SLP65 with SLP65-3xPRM4, the reduction of droplet formation *in vivo* compared to similar droplet formation *in vitro* could be due to other cellular PRM-recognizing interaction partners that could interact with SLP65 and thus also influence the Ca^{2+} mobilization. Indeed, no change of droplets would have been expected, since *in vitro* the triplication of PRM4 had a medium or vanishing effect in promoting phase separation (Figure 29). As reported in previous studies [121], the ΔN-SLP65 had showed no droplets and the lowest Ca^{2+} mobilization of 14% compared to the *wildtype* SLP65 construct (Figure 37 B), while the SLP65-R247A had the second lowest Ca^{2+} mobilization. So, the contribution of vesicles is larger than the contribution of the PRM4, which is in agreement with the *in vitro* effect (Figure 29).

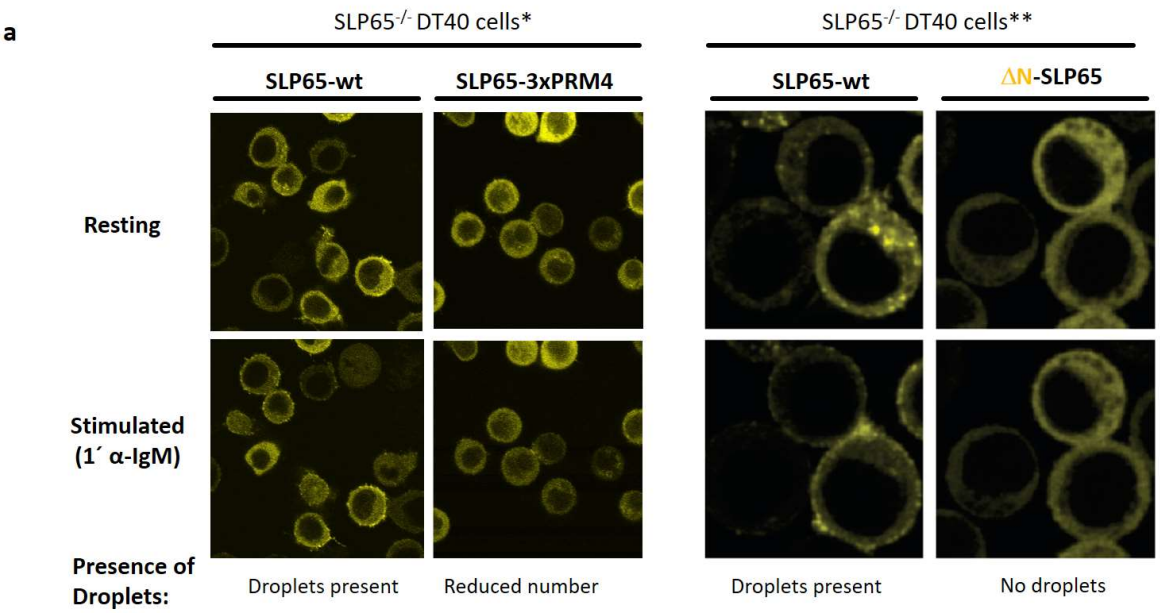

b

	SLP65-wt	SLP65-3xPRM4	ΔN-SLP65	SLP65-R247A
Relative Ca^{2+} signal:	100%	62%*	14%**	36%***

* Provided by A. Bhatt
** Engelke *et al.* 2014
*** Oellerich *et al.* 2011

Figure 37 : Previous ex vivo studies of SLP65 mutants are in line with in vitro phase separation propensities. SLP65-3xPRM4, ΔN-SLP65 of SLP65-R47A were transfected into SLP65-deficient DT40 cells. A) Pre-signaling cluster are present in the resting state, if cells are transfected with *wt*-SLP65. The number of droplets is reduced for transfection with SLP65-3xPRM4 or ΔN-SLP65. B) In the mutant SLP65-version experiments, the Ca^{2+} mobilization is reduced in a way correlating with the phase separation propensity of the *in vitro* experiments (Figure 29). From [Engelke *et al.*, Macromolecular assembly of the adaptor SLP-65 at intracellular vesicles in resting B cells. Sci Signal, 2014. 7(339): p. ra79]. Reprinted with permission from AAAS.

3.7 Actin-associated profilin-1 is not a direct binding partner of SLP65

BCR signaling is coordinated by the cytoskeleton [199]. Therefore we checked whether the actin regulator profilin which contains an SH3 like domain could be recruited as a client protein in signaling clusters to the proline-rich motifs of SLP65. SLP65 could be related to actin organization, since a SLP65 pull-down identified profilin as a potential interaction partner [131, 200].

The profilin family has four members PFN1-4 [201]. PFN2 has been shown to bind to retinoic acid receptors α (RARα) via an PRM sequence that has a 53% sequence identity to SLP65 sequence

237 – 251 which comprises PRM4 (Table 23) [202]. In our lab, the PFN1, but not the PFN2, was available. The binding of SLP65 to human profilin-1 (PFN1) was tested *in vitro* by NMR titration spectroscopy. PFN1 was titrated to 15N-SLP65$_{1-330}$, and the chemical shifts of SLP65 were monitored. No chemical shift changes were observed during titration, and the direct binding of SLP65's IDR to PFN1 was not confirmed (Appendix G).

	Sequence
RARα	**PSPPSPPPLPRIYKP**
SLP65$_{237-251}$	**PPPAAPSPLPRAGKK**
	*** * * **** ***

Table 23: Sequence alignment of RARα with SLP65-PRM4. The two motifs share a high sequence similarity. While profilin-2 binds to RARα, profiling-1 does not bind to SLP65, and thus not to PRM4.

Discussion

4.1 The effect of affinity and multivalency on phase separation

I found that the affinity of the monovalent SH3-PRM interaction ranges from 6 µM to above 3 mM (Figure 24). The SH3A and SH3C domains mediate interactions with medium and low affinity, while the SH3B domain also mediates the strong interaction with PRM4. Phase separation of SLP65 and CIN85 is likely mediated by all 21 interactions (3 SH3 domains x 7 PRMs). Although very weak and transient, the seven, locally up-concentrated PRMs could contribute to the overall specificity in a crowded cellular environment required for spatio-temporal organization. The individual contribution of weak and strong interaction sites differs depending on the effective affinity, which is related to the affinity and the effective concentration [203, 204]. The effective concentration is a function of the linker length-dependent diffusion volume [205]. For example, the connection of SLP65 and CIN85 increases the effective concentration of both SLP65-PRM3 and CIN85-SH3A due to the interaction of SLP65-PRM4 and SH3B (Figure 38).

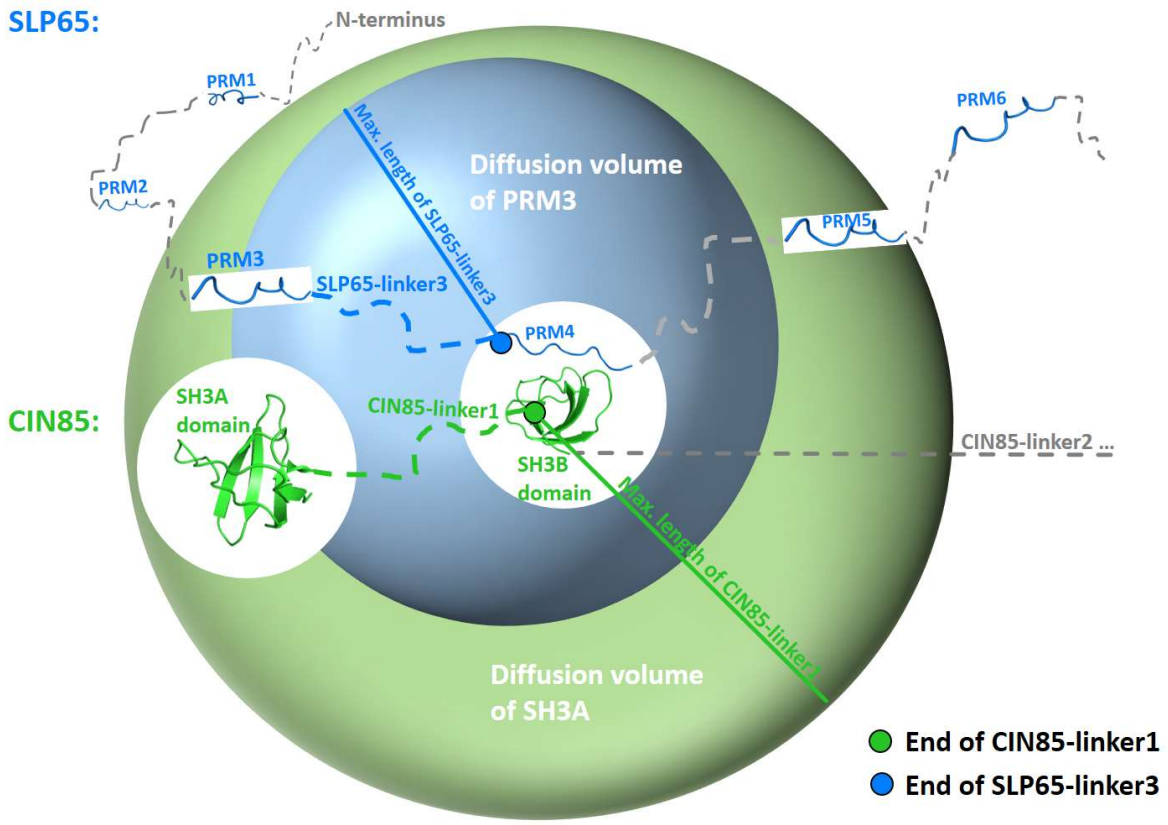

Figure 38: Diffusion volume of SLP65-PRM5 and CIN85-SH3C when CIN85-SH3B is bound to SLP65-PRM4. CIN85's SH3 domains and SLP65's PRMs are connected by flexible linkers. The diffusion of SH3A and SH3C as well as PRM3, PRM4, PRM1 and PRM6 is limited, when SH3B is bound to PRM4. Diffusion volume of PRM3 and SH3A (color coded blue and green, respectively) is defined by the CIN85-linker1 and SLP65-linker3, which determines the effective concentration. Figure adapted from Sørensen *et* Kjaergaarda [205], protein structure pdb 2bz8 [179].

I focused on the strongest interaction of PRM4 with SH3B (K_D = 6 µM) by designing 3 constructs with different affinity: The weak binding SLP65-PRM4-R247A construct, where the PRM4 is deactivated by a single point R to A mutation, the strong binding SLP65-3xPRM4 construct, where each PRM5 and PRM6 are replaced by PRM4 and the 3SH3B construct, where both SH3A and SH3C are replaced each by SH3B.

No phase separation was observed for the PRM4-inactivated SLP65-R247A construct mixed with CIN85-3SH3 at equimolar protein concentrations up to 320 µM (Figure 27 A). The absence of droplets is indicating that at least one high affinity interaction is needed for phase separation.

However, the addition of vesicles reduces the critical concentration to 35 µM protein concentration (Figure 27 B), thus by the addition of a third multivalent component phase separation occurs even in the absence of PRM4. The phase separation threshold seems to be related to the strongest interaction, which may act as seed. In the 'SUV + SLP65-R247A + CIN85-3SH3' mixture, the strongest monovalent SH3-PRM interaction K_D is ~60 µM. Hence, the critical concentration remains at the same order of the strongest monovalent interaction.

Besides affinity, phase separation is also governed by valency. Wu *et al.* reported the critical concentration, the valency and the module's binding affinity of seven systems. E.g. for an ASC PYD filament, phase separation is mediated by six interfaces, each with a K_D > mM, resulting in a critical concentration < 2 µM. Another example is Nup100, where phase separation is mediated by ~43 short motifs resulting in a critical concentration of 0.2 µM [39, 74]. Li *et al.* determined the phase separation thresholds of $SH3_n$ and PRM_n proteins [46], where the multimodular protein constructs were engineered with the same PRM or SH3 domain. The binding affinity of this SH3-PRM pair is 350 µM. No phase separation was reported for $SH3_3$-PRM_3 up to 133 µM equimolar protein concentration. The $SH3_4$-PRM_4 mixture phase separated at 50 µM equimolar protein concentration, and $SH3_5$-PRM_5 phase separated at 20 µM equimolar protein concentration, so the valency is also reducing the critical concentration of phase separation. In the SLP65-3SH3 system, the critical concentration is reduced close to physiological protein concentrations (~0.5 µM) by addition of SUVs, while the $SH3_5$-PRM_5 system is reported with critical concentration of 4 µM [46], which is on the same order as 0.5 µM.

The change of affinity of the SLP65-R247A construct can be pinned down to a single amino acid mutation. In contrast, the constructs of SLP65-3xPRM4 and 3SH3B are designed by mutations replacing two 14 a.a. long motifs or even two complete SH3 domains, respectively. $SLP65_{1-330}$ is an IDP and the replacements of the two motifs could have an impact on the secondary structural propensity. The mutation of the 3SH3 construct to 3SH3B alters ~1/3 of the a.a. sequence. This drastic change in a.a. composition affects the physico-chemical properties, which could interfere with SH3 domain stability or binding function. To validate the integrity of both the SLP65-3xPRM4 construct, as well as 3SH3B construct, the chemical shift difference of *wildtype*-like and mutant constructs could be analyzed by NMR spectroscopy. Although small but relevant changes in

affinity cannot be excluded, the ITC measurements confirm the predicted increase or decrease in binding affinity for the strong or weak binding mutant constructs, respectively (Figure 26). Thus, the mutations seem to have no unexpected impact on the function *in vitro*, although small, but relevant changes in affinity cannot be excluded.

The measured affinities allow us to make assumptions on the effect of the multivalency of SLP65 and CIN85 in B cells. The *ex vivo* Ca^{2+} signaling capability and droplet formation of $SLP65_{1-456}$-PRM4, $\Delta SLP65_{1-456}$ and $SLP65_{1-456}$-R247A were correlated with the phase separation propensities of the respective *in vitro* constructs SLP65-PRM4 and SLP65-R247A (Figure 29, Figure 37). The $SLP65_{1-456}$-3xPRM4 construct is partly active *in vivo* as demonstrated by a reduced Ca^{2+} mobilization and reduced SLP65-phosphorylation state 10 minutes after B cell activation [198]. It cannot be excluded, that the replacement of two motifs alters the binding preference to SH3-containing B cell proteins and changes the SLP65-CIN85 droplet composition. An alternative explanation is based on morphological changes as observed in *in vitro* reconstituted droplets composed of the strong binding mutant SLP65-3xPRM4 constructed mixed with SUVs and the strong binding, trivalent 3SH3B construct (Figure 31), which had decreased fusion propensity. The change of the dynamic state of a condensate could have physiological impact, so the fusion characteristics of a droplet may be of interest. The dynamics of several IDPs have been studied by Lin *et al.* revealing a maturation to less dynamic states over time [206]. Wu *et al.* relates the material state of several phase separation systems to the critical concentration, the valency and the module's binding affinity [74]. In the context of B-cell pre-signaling clusters, an additional crosslinking component with high affinity might change the dynamic state, and the CIN85 homolog CD2AP, which is bound to SLP65 in resting B-cells [131, 207], is such a candidate to change properties of pre-signaling clusters by an additional strong interaction within the promiscuous interactions.

4.2 The SH3 – PRM interaction

It is unknown how members of the SH3 domain family structurally encode specificity for their target PRMs, and specificity determinants are not well understood to explain the variety in PRM

recognition, such that the target PRMs cannot be predicted from the SH3 domain sequence [137]. The SH3 recognition was studied for 27 SH3-PRM interactions. In the following, remarkable details are discussed:

I conducted a residue-specific analysis by NMR spectroscopy by measuring the chemical shift perturbations (CSP) of SH3 – PRM interactions, which revealed a similar binding site for all three SH3 domains (Figure 16 (SH3A), Figure 17 (SH3B), Figure 18 (SH3C), Figure 19 (CSP mapped on crystal structures). Residues of the conserved binding site, but also non-conserved residues have large CSP (selected residues shown in Table 24). Apart from the conserved residues of the SH3 domain family F8 and F276 , which forms part of the xP pocket, D16, D115 and D284 as part of the specificity zone, and W36/135/306, P49/148/319 and F52/151/322 as part of the xP pocket [136, 175, 182], G35 of SH3A, V128 of SH3B or D303-V304-G305 of SH3C seem to be CIN85's intrinsic a.a. conferring specificity to the PxxxPR motif (PRM1, -4, -6 and CIN85-PRM2) or sequences slightly different from th PxxxPR motifs like RPxxxPPRxPxR of CIN85-PRM3, PxPxxR of PRM5, KPxxPXK of PRM* and RPxxPxxPxxR of SLP65-PRM2. Among all nine peptides, SLP65-PRM3, with a KPxxPPKPK sequence, shows the most different CSP profiles, which could indicate a different binding mechanism.

Although there is no crystal structure of a SH3 domain bound to a SLP65-PRM, we can expect based on the solved crystal structure of CIN85's SH3 domain (e.g. SH3A-Cbl-b, Appendix D) that the Arg of the PxxxPR motif is likely binding to the negatively charged Asp or Gln at D16, Q112/D115 or Q281 for SH3A, SH3B or SH3C, respectively (Table 24). For further studies, the Asp and Gln could be targeted by a single point mutation to obtain binding deficient SH3 domains, which would allow to study phase separation properties of mutant versions of the 3SH3 construct. Other studies targeted the Trp of the binding site to disrupt binding [208, 209].

Table 24: SH3A, SH3B and SH3C domains have common binding residues to recognize PRMs. The Arg within the motif is likely to be recognized by QD16, D115 or D284.

Domain:	Residues with large CSP upon PRM binding:										
SH3A	D9	Q13	**D16**		G35/W36		F48	D50	N51	F52	
SH3B	S108	**Q112**	**D115**	V128	E135/G138	M146	F147		N150	F151	I152
SH3C		**Q281**	D284	D303	V304/G305/W306	V317	F318		D320	F321	

The K_Ds of the monovalent binding affinities have been measured for both SLP65-PRMs and the PRMs of the CIN85 PRR (Figure 23), and not for CIN85-PRM1, which was identified recently (unpublished results, D. Sieme). SLP65 has more PRMs with higher affinity, compared to CIN85. In presence of SLP65, the SLP65-PRMs could outcompete the CIN85-PRMs. In absence of SLP65, CIN85 forms a trimer (or a heterotrimer with CD2AP) via the C-terminal coiled coil domain, where CIN85's PRMs and SH3 domains interact promiscuously [122, 177]. An intermolecular CIN85-CIN85 interaction could establish a network and have a positive effect on phase separation. However, an intramolecular interaction could have a negative effect by competing for SH3 domain binding sites. We note, that the CIN85Δ57 construct, where the 57 a.a. long PRR of CIN85 is deleted [116], phase separated on its own at high concentrations (> 80 µM, data not shown), however the high concentrations are physiological irrelevant, and this effect was not further studies.

4.3 Specific *vs* promiscuous interactions – are both relevant?

The SLP65-CIN85 assembly or disassembly is based on the three SH3 domains interacting with 7 PRMs (Figure 23). The stability of the network could be based on the availability of a sufficient number of interactions. The significant effects of PRM4 (Figures 24, 36) could be an important requirement for the pre-signaling cluster stability, making it more important than the weak binding PRMs. So, PRM4 could be the point of action in regulating the SLP65-CIN85 complex e.g. by post translational modifications. Biocondensates can be dissolved by a monovalent peptide [210]. In the cellular context, one PRM4-specific regulator could disturb the integrity of the biocondensate. On the other hand, promiscuous interactions of at least 4 PRMs are significant, as demonstrated by the effect of PRM1 (Figure 36, [131]), since the relatively weak PRM1 has on average larger K_Ds to the three SH3 domains than PRM4, 5, and 6 (Figures 24), whereas it still has a measurable effect on the Ca^{2+} mobilization (Figure 24, 36). It cannot be ruled out, that the single-point mutation of PRM1 has an unknown side-effect, nevertheless it is likely that it contributes to SLP65-CIN85 complex formation *in vivo*. This finding supports the relevance of many, weak interactions in mediating phase separation. The integrity of the pre-signaling cluster

could rely on the participation of certain SLP65-CIN85 interactions out of all possible SLP65-CIN85 interaction. The promiscuity could provide the basis for an adjustable signaling system.

4.4 Aspects of stoichiometry

The ITC experiments were performed at concentrations close to and below the critical concentration. The number of contact of the $SLP65_{1-330}$-3SH3 complex is 1.12 (Table 15), indicating a stoichiometry of ~1:1. The *in vitro* phase separation studies were performed at equimolar concentrations of both proteins (Figure 27). Further investigations of the phase separation at different stoichiometry could give a hint, if nature has evolved the interaction of $SLP65_{1-330}$ with $CIN85_{1-333}$ (3SH3) to be optimized for a ~1:1 stoichiometry, or if the complex has excess PRMs available to saturate all 3SH3 domains of CIN85. We note, that the weak SLP65-3PRM4 effect indicates that additional binding transferred by PRMs could perish due to pre-saturated SH3 domains. Since the modular concentration of PRMs is higher, abundant PRMs could recruit more SH3-containing components in SLP65-CIN85 condensates (e.g. CD2AP [122] or CARMIL proteins [211]). The composition of biocondensates can be regulated based on the availability of binding sites [54], so the splice variants of CIN85 could be a regulatory element [187, 212].

4.5 Profilin - a potential client protein of the immune signaling clusters

The occupancy of SH3 domains or PRMs in the cellular environment is not known, and it is possible that free binding sites of SLP65 and CIN85 are occupied by other interaction partners. Profilin-1 was detected in the SLP65 interactome of DT40 cells [131], however the direct interaction of profilin-1 with SLP65 could not be confirmed in this thesis (Figure Appendix G). Thus, the interaction is mediated indirectly. In the SLP65 pull-down assay, SLP65 could capture profilin-1 based on three indirect interactions (Figure: **39**): First, the SLP65 interaction with CD2AP/CIN85, secondly, the CD2AP/CIN85 interaction with Cbl-b and finally, Cbl-b's interaction with profilin-1. CIN85 and the homolog CD2AP, both interaction partners of SLP65, are reported

to bind Cbl-b [207, 213, 214]. Cbl-b was detected in the CIN85 interactome [122]. Cbl-b assumingly binds profilin, because Cbl-b has two Pro_6 and two Pro_4 stretches and proline stretches are generally bound by profilin [215, 216].

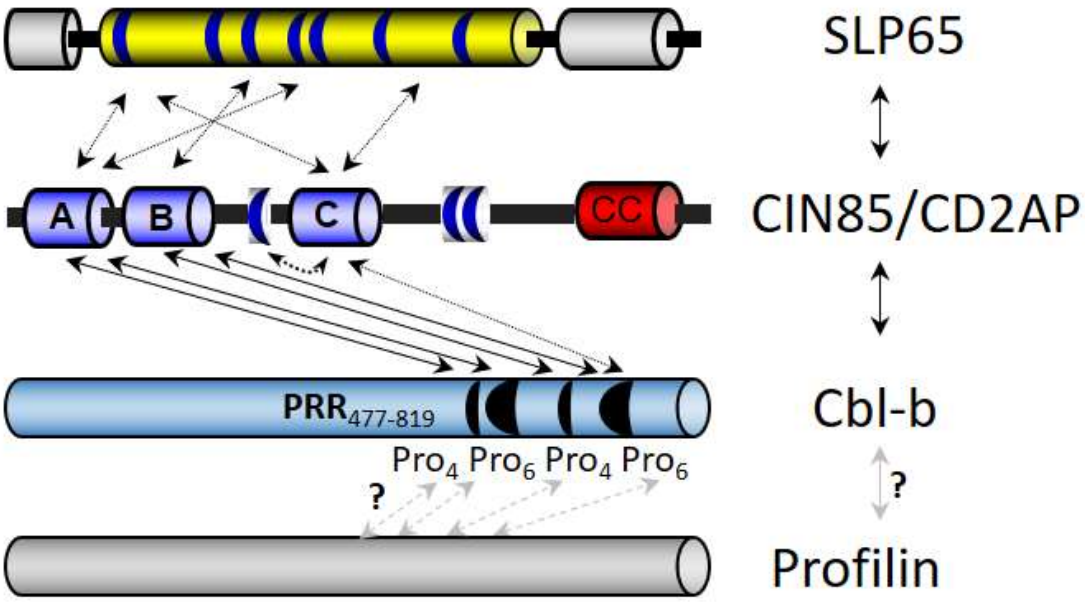

Figure: 39 Hypothetical binding interactions resulting in an indirect SLP65-profilin interaction. The illustration shows that SLP65 can be linked to profilin by CIN85/CD2AP binding to Cbl-b by SH3-PRM interactions and yet not verified interactions of Cbl-b with profilin by Cbl-b's Pro stretches.

4.6 Modeling of phase separation of SLP65 and CIN85

Phase separation is driven by many, weak interactions, e.g. in the protein FUS, where more than 20 tyrosine-containing repeats mediate phase separation/hydrogel formation [57, 214], or also in phenylalanine and glycine containing nucleoproteins (FG Nups), which contain more than 30 repeats of the FG motif [39]. It is unfeasible to dissect a set of >20 times >20 weak interactions in its individual components, whereas the SLP65-3SH3 system can be studied by each binding

module individually, such that it is feasible to tackle the question how phase separation emerges from single binding modules.

The LASSI engine is well-suited to investigate the molecular architecture of a phase-separating system of IDPs but also of multivalent proteins [103]. This thesis aimed to find LASSI parameter sets, which could serve as starting points to develop a model for phase separation of two multivalent, immune signaling proteins. The study of Bremer *et al.* [217] demonstrates that LASSI can be applied to model phase separation of IDPs. In LASSI, each amino acid can be represented by a single bead, either a sticker or spacer. The predictive model [217] does not require an accurate size representation of the volume of the amino acids. For example, the size of glycine and tryptophan differ. Although all amino acids are defined with the same size in LASSI, the 1:1 (amino acid:bead) representation resulted in the latter mentioned predictive model, that can explain the phase separation behavior of low complexity domains [104, 217]. It seems that for a predictive model, factors such as concentration, interaction strength, temperature or excluded volumes (taken into account by the isotropic interaction energy terms) are more relevant than an accurate volumetric size representation. For other proteins than IDPs, the molecular design cannot represent a 1:1 ratio of beads and binding elements. In case of a multivalent protein with folded domains connected by flexible polypeptide linkers, the defined molecular architecture inevitably deviates regarding the volume and length of a folded domain *vs* a polypeptide linker from the real volumes or distances. Linker lengths and natural lengths do not match. The quality and predictive power of a LASSI model of multivalent proteins may therefore be difficult to realize. LASSI implements a coarse grained lattice with the requirement that any sticker occupies only one lattice unit of length 1, and the stickers are so called single beads. The excluded volume of different type of stickers, e.g. folded domains, can only be considered by a repulsive energy term in the isotropic interaction matrix.

In the lattice simulation set up of this thesis, the volume of the folded domain is disregarded by setting the energy terms of the isotropic interactions to 0. For the purpose of defining the order of interaction strength of the sticker-sticker interactions, the pairwise anisotropic interaction energy matrix were derived from experimentally determined monovalent binding affinities between CIN85 SH3 domains and the PRMs in SLP65 and CIN85. This thermodynamic

parameterization can approximate the multivalent SH3-PRM interactions of a natural system. As a drawback, the LASSI engine does not work with intramolecular interactions. So, the computational model of 2SH3, 3SH3, and 3SH3B disregards any potential intramolecular interactions of CIN85. In fact, I needed to make a 3SH3 construct with an inert SH3C, the so called 2SH3 construct, to simulate the strong interaction of SH3C with CIN85-PRM1. I parameterized the LASSI model of the SLP65-3SH3 system, including the design of both *wildtype* and mutant representations, and simulated phase separation. As already mentioned above, I changed energy terms of the sticker representing the SH3C domain in order to consider the intramolecular binding of SH3C to a PRM within the linker region close to SH3C [195] (unpublished results from D. Sieme). By comparing the ratios of phase separation of the strong, *wildtype* and weak affinity constructs, I found that the simulated ratios were on the same order relative to the experimental ratios. The simulations could explain the > 10x difference in critical concentration between the 3SH3 and 3SH3B construct (Figure 28) but only when I included the binding of CIN85's SH3C domain to CIN85-PRM1 reducing the multivalency of 3x SH3 to 2x SH3. Only then the ratios of critical concentrations found experimentally could be reproduced in the LASSI simulations. I simulated only the 3SH3 construct ($CIN85_{1\text{-}333}$) and did not include the trimerization of CIN85's CC domain [122], which are expectedly irrelevant for the SH3C's interaction to CIN85-PRM1. In a B cell, the SLP65-CIN85 complex of trimeric CIN85, could recruit other proteins e.g. endophilin [218] or CRK [122], which would be translocated to the plasma membrane concomitantly after B cell stimulation. Also, the intramolecular interaction of CIN85's proline-rich motifs CIN85-PRM2 and CIN85-PRM3 [177] have very low affinity (Figure 23). Indeed, I measured the K_Ds of 27 PRM-SH3 domain interactions from which I conclude that CIN85's auto-inhibition with CIN85-PRM2 and CIN85-PRM3 is outcompeted by SLP65, since the intramolecular interactions of CIN85-PRM2 and CIN85-PRM3 to CIN85's SH3 domains are weaker compared to the interactions of SLP65-PRMs (Figure 23) and the linkers connecting the SH3 domains to CIN85-PRM2 and CIN85-PRM3 are much longer than the linker between SH3C and CIN85-PRM1. The latter is the interaction that is not outcompeted by SLP65. Yet, the role of CIN85-PRM1 could be clarified to fully engage SH3C in an intramolecular interaction preventing it from interacting with SLP65-PRMs (Table 22 and unpublished findings of my colleague D. Sieme). The vesicles are not

included as a third molecular species in the LASSI model, because the complexity of SLP65-3SH3 system is already challenging. Thus their contribution to phase separation mediated by the binding of SLP65's N-terminus to SUVs [121] is not considered. However, since the experimental critical concentrations of tripartite phase separation have been determined as well (Figure 28), including vesicles in a further advanced model would offer another way to compare the simulations with experimental data. To approach this issue, the question arises, how vesicles could be represented on a lattice. One could include vesicles as additional multivalent molecule species disregarding their geometry, leading us to the question, what is the maximum number of SLP65 molecules clustering around a SUV? So, modeling of SUVs could be investigated in further studies.

The phase separation threshold concentrations has been determined for the SLP65 and 3SH3 constructs, in order to find a relationship of the factors of critical concentration of phase separation of different constructs in the simulation and the *in vitro* experiments. The Monte Carlo simulation temperature value was set to 1, on the same order as in previous simulations [102, 103], which resulted in phase separation in the $SLP65_{1\text{-}330}$-3SH3 system. Also, the lattice units can only be roughly estimated by considering the size of an SH3 domain (~14 Å) and the PRMs at the interaction site (~6 a.a.), which results in a distance residue length of ~2.3 Å. The distance between two amides of consecutive residues in a planar peptide in *trans* configuration is ~3.8 Å [209]. The translation in a α-helix is 1.5 Å [210]. So the estimate is within the range between 1.5 Å to 3.8 Å, if linkers are scaled by 1/6. The effect of the linker length is a major determinant for network formation, as shown by Harmon *et al.* [102]. In the LASSI set-up of this thesis, the linkers are assumed to have no attractive or repulsive interactions, so they are treated as Flory-random coils (FRC) [102]. The simulated phase separated clusters have similar appearance compared with the $SH3_7$:PRM_7 system reported by Harmon *et al.* [102] (Figure 35) as seen by the visualization of the simulation trajectories. The implicit linkers do not occupy a point on the lattice and behave as phantom linkers by the distance restraint [103]. This could influence phase separation due to the lack of the exclusion volume of the linkers. Also, long linker length could lead to ineffective distance restraints of the linkers resulting percolation due to a loss of cooperativity (Figure 8 a in Harmon *et al.* [102]). Yet, irrespective of the linker length scaling, the simulations considering the

inhibition of SH3C by an intramolecular interaction using the 2SH3 design resulted in better agreement with the experimental data compared to the 3SH3 design (Table 22). Thus, the model captures the main features originating from a reduction in multivalency from 3 to 2 independently from the linker length. It remains to be investigated, if the herein described thermodynamic model yield insights into the structural of SLP65-3SH3 droplets obtained from the radial pair distribution function. The distance distribution could be studied experimentally by paramagnetic resonance spectroscopy and compared to simulations, if the paramagnetic tag is introduced close to a binding site.

Summary

In this thesis, I investigated and modeled the B cell relevant process of tripartite phase separation of *in vitro* reconstituted pre-signaling clusters composed of small unilamellar vesicles (SUVs) and two construct of the adapter proteins SLP65 and CIN85. The promiscuous interactions of both SLP65's N-terminus to SUVs and SLP65's PRMs to three SH3 domains of CIN85 mediate phase separation of the three component mixture composed of SUVs, SLP65- and CIN85-3SH3 constructs. First, I characterized the thermodynamics of the monovalent PRM-SH3 interactions of seven SLP65-PRM-derived peptides with each of the three CIN85-SH3 domain (in total 21). The range of affinities of the monovalent interactions of the seven PRMs of SLP65 to SH3A, B and C comprises one interaction with the dissociation constant K_D of 6 µM, one interaction with the K_D of 35 µM, 12 interactions with K_Ds between 80 – 600 µM and 7 interactions with K_Ds larger than 1 mM. Thus, I identified the relatively strong interaction of SLP65-PRM4 to CIN85-SH3B and confirmed weak interactions of three PRMs (SLP65-PRM2, 3, *) to any of the CIN85-SH3 domains (A, B, C). Based on the known monovalent binding affinities, we designed strong binding constructs of both proteins replacing weak SH3 domains/PRMs by strong ones. We also expressed a weak binding construct of SLP65. I measured critical concentration of phase separation of the designer constructs and classified the binding entities ('PRM4', SUVs, '1xPRM4 - 1xPRM5 - 1xPRM6 --> 3xPRM4' and 'SH3-ABC --> 3xSH3B') according to the contribution to phase separation and could identify that SUVs are largely contributing to phase separation. Moreover, I could obtain a cryo-ET structure of *in vitro* condensates highlighting the distribution of vesicles in the dense phase. Finally, I applied the established program LASSI to parameterize a thermodynamic lattice model with the experimentally determined monovalent SH3-PRM affinities in order to understand phase separation emerging from single components. The *in silico* critical concentrations of phase separation reproduced satisfactorily the experimental critical concentrations, even when the linker lengths were varied dramatically. Regarding the physiological relevance of phase separation, I found a correlation of B cell Ca^{2+} signaling assays to binding affinities (K_Ds of individual SLP65-PRM-derived peptides to each individual SH3 domain of CIN85), which supports the physiological relevance of phase separation for B cell receptor signaling.

Abbreviations:

a. a.	Amino acid
BCR	B-cell receptor
BLNK	B cell linker protein, alternative name of SLP65
bp	Base pair
CC	Coiled coil
CD2AP	CD2-associated protein
CIN85	Cbl-interacting protein of 85 kDa
Cit	Citrine
CRK	Adapter molecule crk
CSP	Chemical shift perturbation
C-term	Carboxy-terminus
D_2O	Deuterium oxide
DAG	Diacylglycerol
DIC	Differential interference contrast
DOPC	1,2-dioleoyl-sn-glycero-3-phosphocholine
DOPE	1,2-dioleoyl-sn-glycero-3-phosphoethanolamine
DOPS	1,2-dioleoyl-sn-glycero-3-phospho-L-serine
DLS	Dynamic light scattering
DNA	Deoxyribonucleic acid
DSS	Sodium trimethylsilylpropanesulfonate
EDTA	Ethylenediaminetetraacetic acid
EGTA	Ethylene glycol-bis(β-aminoethyl ether)-N,N,N’,N’-tetraacetic acid
FID	Free induction decay
forw.	foreward - Primer direction in PCR
FUS	RNA-binding protein FUS (Fused in Sarcoma)
GRB2	Growth factor receptor-bound protein 2
GDIP	Global density inhomogeneity parameter
GST	Glutathione-S-transferase

HEPES 4-(2-hydroxyethyl)-1-piperazineethanesulfonic acid

His7 Polyhistidin-tag

HSQC Heteronuclear single quantum coherence

IDP Intrinsically disordered protein

IDR Intrinsically disordered region

INEPT Insensitive nuclei enhancement by polarization transfer

IP3 Inositol-1,4,5-trisphosphate

IPTG Isopropyl-β-D-thiogalactopyranoside

ITAM Immunoreceptor tyrosine-based activation motif

ITC Isothermal titration calorimetry

kDa Kilodalton

LASSI LAttice simulation engine for Sticker and Spacer Interactions

LAT Linker for activation of T cells

LCI Live cell imaging

M Molar

MD Molecular dynamics

N-term Amino-terminus

N-WASP Neural Wiskott-Aldrich syndrome protein

Nck Non-catalytic region of tyrosine kinase adaptor protein 1

NMR Nuclear magnetic resonance spectroscopy

Nups FG nucleoproteins

PDF (Radial) pair density distribution function

PI3K Phosphoinositide 3'-kinase

PIP_2 Phosphatidylinositol-4,5-bisphosphate

PLCγ2 Phospholipase C γ2

PLD Prion-like domain

PTFE Polytetrafluoroethylene

RARα Retinoic acid receptors α

rev. reverse - Primer direction in PCR

RNA	Ribonucleic acid
Sec	Seconds
SH3	Src-homology 3
SLiM	Short linear motifs
SLP65	SH2 domain-containing leukocyte adaptor protein of 65 kDa
Syk	Spleen tyrosine kinase
TCEP	Tris(2-carboxyethyl)phosphine
Tris	Tris(hydroxymethyl)aminomethan
TFA	Trifluoroacetic acid
UV	Ultraviolet
Wt	wild-type
%w/w	Percentage by weight
Δ	deletion/truncation

Amino acid 3-letter and 1 letter code

Name	**3 / 1 Letter code**	
Alanine	Ala	A
Arginine	Arg	R
Asparagine	Asn	N
Aspartic Acid	Asp	D
Cysteine	Cys	C
Glutamic Acid	Glu	E
Glutamine	Gln	Q
Glycine	Gly	G
Histidine	His	H
Isoleucine	Ile	I
Leucine	Leu	L
Lysine	Lys	K
Methionine	Met	M

Phenylalanine	Phe	F
Proline	Pro	P
Serine	Ser	S
Threonine	Thr	T
Tryptophan	Trp	W
Tyrosine	Tyr	Y
Valine	Val	V

References

1. Mecznikoff, C., *Ueber die Entwicklung der Cecidomyienlarve aus dem Pseudovum.* Arch. Naturgeschichte, 1865. **B**: p. 304-310.
2. Walter, H. and D.E. Brooks, *Phase separation in cytoplasm, due to macromolecular crowding, is the basis for microcompartmentation.* FEBS Letters, 1995. **361**(2-3): p. 135-139.
3. Cajal, S.R., *El núcleo de las células piramidales del cerebro humano y de algunos mamíferos*. 1910.
4. Spector, D.L., *SnapShot: Cellular bodies.* Cell, 2006. **127**(5): p. 1071.
5. Bernstein, R.M., et al., *Diversity of autoantibodies in primary biliary cirrhosis and chronic active hepatitis.* Clin Exp Immunol, 1984. **55**(3): p. 553-60.
6. Maul, G.G., et al., *Review: properties and assembly mechanisms of ND10, PML bodies, or PODs.* J Struct Biol, 2000. **129**(2-3): p. 278-87.
7. Brangwynne, C.P., et al., *Germline P granules are liquid droplets that localize by controlled dissolution/condensation.* Science, 2009. **324**.
8. Kedersha, N.L., et al., *RNA-binding Proteins TIA-1 and TIAR Link the Phosphorylation of eIF-2a to the Assembly of Mammalian Stress Granules.* JCB, 1999. **147**(7).
9. Jones, N., et al., *Nck adaptor proteins link nephrin to the actin cytoskeleton of kidney podocytes.* Nature, 2006. **440**(7085): p. 818-23.
10. Platani, M., et al., *In vivo analysis of Cajal body movement, separation, and joining in live human cells.* JCB, 2000. **151**(7): p. 1561–1574.
11. Purcell, E.M., *Life at low Reynolds number.* American Journal of Physics, 1977. **45**(1): p. 3-11.
12. Mao, Y.S., et al., *Direct visualization of the co-transcriptional assembly of a nuclear body by noncoding RNAs.* Nat Cell Biol, 2011. **13**(1): p. 95-101.
13. D., P.R. and M. T., *High mobility of proteins in the mammalian cell nucleus.* Nature, 2000. **404**: p. 604-609.
14. Wiesmeijer, K., et al., *Mobile foci of Sp100 do not contain PML: PML bodies are immobile but PML and Sp100 proteins are not.* J Struct Biol., 2002. **140**.
15. Bernardi, R. and P.P. Pandolfi, *Structure, dynamics and functions of promyelocytic leukaemia nuclear bodies.* Nat Rev Mol Cell Biol, 2007. **8**(12): p. 1006-16.
16. Kaiser, T.E., R.V. Intine, and M. Dundr, *De Novo Formation of a Subnuclear Body.* Science, 2008. **322**(5908): p. 1713-1717.
17. Andrei, M.A., et al., *A role for eIF4E and eIF4E-transporter in targeting mRNPs to mammalian processing bodies.* RNA, 2005. **11**(5): p. 717-27.
18. Aizer, A., et al., *The dynamics of mammalian P body transport, assembly, and disassembly in vivo.* Mol Biol Cell, 2008. **19**(10): p. 4154-66.
19. Kedersha, N., et al., *Stress granules and processing bodies are dynamically linked sites of mRNP remodeling.* J Cell Biol, 2005. **169**(6): p. 871-84.
20. Mollet, S., et al., *Translationally repressed mRNA transiently cycles through stress granules during stress.* Mol Biol Cell, 2008. **19**(10): p. 4469-79.
21. Brangwynne, C.P., T.J. Mitchison, and A.A. Hyman, *Active liquid-like behavior of nucleoli determines their size and shape in Xenopus laevis oocytes.* Proc Natl Acad Sci U S A, 2011. **108**(11): p. 4334-9.
22. Wilson, E.B., *The structure of protoplasm.* Science, 1899. **10**(237): p. 33-45.
23. Hyman, A.A. and C.P. Brangwynne, *Beyond Stereospecificity: Liquids and Mesoscale Organization of Cytoplasm.* Developmental Cell, 2011. **21**(1): p. 14-16.

24. Banani, S.F., et al., *Biomolecular condensates: organizers of cellular biochemistry.* Nat Rev Mol Cell Biol, 2017. **18**(5): p. 285-298.
25. Schwarz-Romond, T., et al., *The Wnt signalling effector Dishevelled forms dynamic protein assemblies rather than stable associations with cytoplasmic vesicles.* J Cell Sci, 2005. **118**(Pt 22): p. 5269-77.
26. Boeynaems, S., et al., *Protein Phase Separation: A New Phase in Cell Biology.* Trends Cell Biol, 2018. **28**(6): p. 420-435.
27. Bartolini, A., et al., *Liquid-liquid phase separation of polymeric microdomains with tunable inner morphology: Mechanistic insights and applications.* J Colloid Interface Sci, 2019. **556**: p. 74-82.
28. Wang, J., et al., *A Molecular Grammar Governing the Driving Forces for Phase Separation of Prion-like RNA Binding Proteins.* Cell, 2018. **174**(3): p. 688-699 e16.
29. Patel, A., et al., *A Liquid-to-Solid Phase Transition of the ALS Protein FUS Accelerated by Disease Mutation.* Cell, 2015. **162**(5): p. 1066-77.
30. Lafontaine, D.L.J., et al., *The nucleolus as a multiphase liquid condensate.* Nat Rev Mol Cell Biol, 2020.
31. Nott, T.J., et al., *Phase transition of a disordered nuage protein generates environmentally responsive membraneless organelles.* Mol Cell, 2015. **57**(5): p. 936-947.
32. Rebane, A.A., et al., *Liquid-liquid phase separation of the Golgi matrix protein GM130.* FEBS Lett, 2020. **594**(7): p. 1132-1144.
33. Rothman, J.E., *Jim's View: Is the Golgi stack a phase-separated liquid crystal?* FEBS Lett, 2019. **593**(19): p. 2701-2705.
34. Mackinder, L.C., et al., *A repeat protein links Rubisco to form the eukaryotic carbon-concentrating organelle.* Proc Natl Acad Sci U S A, 2016. **113**(21): p. 5958-63.
35. Prouteau, M. and R. Loewith, *Regulation of Cellular Metabolism through Phase Separation of Enzymes.* Biomolecules, 2018. **8**(4).
36. Wippich, F., et al., *Dual specificity kinase DYRK3 couples stress granule condensation/dissolution to mTORC1 signaling.* Cell, 2013. **152**(4): p. 791-805.
37. Molliex, A., et al., *Phase separation by low complexity domains promotes stress granule assembly and drives pathological fibrillization.* Cell, 2015. **163**(1): p. 123-33.
38. King, C., et al., *ER membranes exhibit phase behavior at sites of organelle contact.* Proc Natl Acad Sci U S A, 2020. **117**(13): p. 7225-7235.
39. Schmidt, H.B. and D. Gorlich, *Nup98 FG domains from diverse species spontaneously phase-separate into particles with nuclear pore-like permselectivity.* Elife, 2015. **4**.
40. Hubstenberger, A., et al., *Translation repressors, an RNA helicase, and developmental cues control RNP phase transitions during early development.* Dev Cell, 2013. **27**(2): p. 161-173.
41. Chiu, Y.P., et al., *Liquid-liquid phase separation and extracellular multivalent interactions in the tale of galectin-3.* Nat Commun, 2020. **11**(1): p. 1229.
42. Aggarwal, S., et al., *Myelin membrane assembly is driven by a phase transition of myelin basic proteins into a cohesive protein meshwork.* PLoS Biol, 2013. **11**(6): p. e1001577.
43. Alberti, S. and D. Dormann, *Liquid-Liquid Phase Separation in Disease.* Annu Rev Genet, 2019. **53**: p. 171-194.
44. Morimoto, M. and C.F. Boerkoel, *The role of nuclear bodies in gene expression and disease.* Biology (Basel), 2013. **2**(3): p. 976-1033.
45. Decker, C.J. and R. Parker, *P-bodies and stress granules: possible roles in the control of translation and mRNA degradation.* Cold Spring Harb Perspect Biol, 2012. **4**(9): p. a012286.
46. Li, P., et al., *Phase transitions in the assembly of multivalent signalling proteins.* Nature, 2012. **483**(7389): p. 336-40.

47. Wu, H., *Higher-order assemblies in a new paradigm of signal transduction.* Cell, 2013. **153**(2): p. 287-92.
48. Larson, A.G. and G.J. Narlikar, *The Role of Phase Separation in Heterochromatin Formation, Function, and Regulation.* Biochemistry, 2018. **57**(17): p. 2540-2548.
49. Raff, J.W., *Phase Separation and the Centrosome: A Fait Accompli?* Trends Cell Biol, 2019. **29**(8): p. 612-622.
50. Yasuda, S., et al., *Stress- and ubiquitylation-dependent phase separation of the proteasome.* Nature, 2020. **578**(7794): p. 296-300.
51. O'Flynn, B.G. and T. Mittag, *The role of liquid-liquid phase separation in regulating enzyme activity.* Curr Opin Cell Biol, 2021. **69**: p. 70-79.
52. Holehouse, A.S. and R.V. Pappu, *Functional Implications of Intracellular Phase Transitions.* Biochemistry, 2018. **57**(17): p. 2415-2423.
53. Su, X., et al., *Phase separation of signaling molecules promotes T cell receptor signal transduction.* Science, 2016. **352**(6285): p. 595-9.
54. Banani, S.F., et al., *Compositional Control of Phase-Separated Cellular Bodies.* Cell, 2016. **166**(3): p. 651-663.
55. Feric, M., et al., *Coexisting Liquid Phases Underlie Nucleolar Subcompartments.* Cell, 2016. **165**(7): p. 1686-1697.
56. Shin, Y. and C.P. Brangwynne, *Liquid phase condensation in cell physiology and disease.* Science, 2017. **357**(6357).
57. Kato, M., et al., *Cell-free formation of RNA granules: low complexity sequence domains form dynamic fibers within hydrogels.* Cell, 2012. **149**(4): p. 753-67.
58. Murakami, T., et al., *ALS/FTD Mutation-Induced Phase Transition of FUS Liquid Droplets and Reversible Hydrogels into Irreversible Hydrogels Impairs RNP Granule Function.* Neuron, 2015. **88**(4): p. 678-90.
59. Forman-Kay, J.D. and T. Mittag, *From sequence and forces to structure, function, and evolution of intrinsically disordered proteins.* Structure, 2013. **21**(9): p. 1492-9.
60. Donau, C., et al., *Active coacervate droplets as a model for membraneless organelles and protocells.* Nat Commun, 2020. **11**(1): p. 5167.
61. Tena-Solsona, M., et al., *Self-selection of dissipative assemblies driven by primitive chemical reaction networks.* Nat Commun, 2018. **9**(1): p. 2044.
62. Drobot, B., et al., *Compartmentalised RNA catalysis in membrane-free coacervate protocells.* Nat Commun, 2018. **9**(1): p. 3643.
63. Mitrea, D.M. and R.W. Kriwacki, *Phase separation in biology; functional organization of a higher order.* Cell Commun Signal, 2016. **14**: p. 1.
64. Milovanovic, D., et al., *A liquid phase of synapsin and lipid vesicles.* Science, 2018. **361**(6402): p. 604-607.
65. Aumiller, W.M., M. Uchida, and T. Douglas, *Protein cage assembly across multiple length scales.* Chem Soc Rev, 2018. **47**(10): p. 3433-3469.
66. Lin, Y.-H., et al., *Charge pattern matching as a 'fuzzy' mode of molecular recognition for the functional phase separations of intrinsically disordered proteins.* New Journal of Physics, 2017. **19**(11): p. 115003.
67. Updike, D.L., et al., *P granules extend the nuclear pore complex environment in the C. elegans germ line.* J Cell Biol, 2011. **192**(6): p. 939-48.
68. Pak, C.W., et al., *Sequence Determinants of Intracellular Phase Separation by Complex Coacervation of a Disordered Protein.* Mol Cell, 2016. **63**(1): p. 72-85.
69. Urry, D.W., et al., *Hydrophobicity scale for proteins based on inverse temperature transitions.* Biopolymers, 1992. **32**(9): p. 1243-50.

70. Vernon, R.M., et al., *Pi-Pi contacts are an overlooked protein feature relevant to phase separation.* Elife, 2018. **7**.
71. Fasting, C., et al., *Multivalency as a chemical organization and action principle.* Angew Chem Int Ed Engl, 2012. **51**(42): p. 10472-98.
72. Han, T.W., et al., *Cell-free formation of RNA granules: bound RNAs identify features and components of cellular assemblies.* Cell, 2012. **149**(4): p. 768-79.
73. Pierce, W.K., et al., *Multiple Weak Linear Motifs Enhance Recruitment and Processivity in SPOP-Mediated Substrate Ubiquitination.* J Mol Biol, 2016. **428**(6): p. 1256-1271.
74. Wu, H. and M. Fuxreiter, *The Structure and Dynamics of Higher-Order Assemblies: Amyloids, Signalosomes, and Granules.* Cell, 2016. **165**(5): p. 1055-1066.
75. Mittag, T. and R. Parker, *Multiple Modes of Protein-Protein Interactions Promote RNP Granule Assembly.* J Mol Biol, 2018. **430**(23): p. 4636-4649.
76. Uversky, V.N., *Recent Developments in the Field of Intrinsically Disordered Proteins: Intrinsic Disorder-Based Emergence in Cellular Biology in Light of the Physiological and Pathological Liquid-Liquid Phase Transitions.* Annu Rev Biophys, 2021.
77. Jonas, S. and E. Izaurralde, *The role of disordered protein regions in the assembly of decapping complexes and RNP granules.* Genes Dev, 2013. **27**(24): p. 2628-41.
78. Van Treeck, B. and R. Parker, *Emerging Roles for Intermolecular RNA-RNA Interactions in RNP Assemblies.* Cell, 2018. **174**(4): p. 791-802.
79. Hughes, M.P., et al., *Atomic structures of low-complexity protein segments reveal kinked beta sheets that assemble networks.* Science, 2018. **359**(6376): p. 698-701.
80. Li, Y.R., et al., *Stress granules as crucibles of ALS pathogenesis.* J Cell Biol, 2013. **201**(3): p. 361-72.
81. Zhang, H., et al., *RNA Controls PolyQ Protein Phase Transitions.* Mol Cell, 2015. **60**(2): p. 220-30.
82. Lee, K.H., et al., *C9orf72 Dipeptide Repeats Impair the Assembly, Dynamics, and Function of Membrane-Less Organelles.* Cell, 2016. **167**(3): p. 774-788 e17.
83. Chong, P.A., R.M. Vernon, and J.D. Forman-Kay, *RGG/RG Motif Regions in RNA Binding and Phase Separation.* J Mol Biol, 2018. **430**(23): p. 4650-4665.
84. van der Lee, R., et al., *Classification of intrinsically disordered regions and proteins.* Chem Rev, 2014. **114**(13): p. 6589-631.
85. Peran, I. and T. Mittag, *Molecular structure in biomolecular condensates.* Curr Opin Struct Biol, 2020. **60**: p. 17-26.
86. Larson, A.G., et al., *Liquid droplet formation by HP1alpha suggests a role for phase separation in heterochromatin.* Nature, 2017. **547**(7662): p. 236-240.
87. Case, L.B., J.A. Ditlev, and M.K. Rosen, *Regulation of Transmembrane Signaling by Phase Separation.* Annu Rev Biophys, 2019. **48**: p. 465-494.
88. Weber, C.A., et al., *Physics of active emulsions.* Rep Prog Phys, 2019. **82**(6): p. 064601.
89. Lin, Y.H., J.D. Forman-Kay, and H.S. Chan, *Theories for Sequence-Dependent Phase Behaviors of Biomolecular Condensates.* Biochemistry, 2018. **57**(17): p. 2499-2508.
90. Koningsveld, R. and A.J. Staverman, *Liquid-liquid phase separation in multicomponent polymer solutions.* Kolloid-Zeitschrift und Zeitschrift für Polymere, 1967. **218**(2): p. 114-124.
91. Ranganathan, S. and E. Shakhnovich, *Liquid-liquid microphase separation leads to formation of membraneless organelles.* bioRxiv, 2019: p. 2019.12.18.881565.
92. Bari, K.J. and D.D. Prakashchand, *Fundamental Challenges and Outlook in Simulating Liquid-Liquid Phase Separation of Intrinsically Disordered Proteins.* J Phys Chem Lett, 2021. **12**(6): p. 1644-1656.
93. Dignon, G.L., et al., *Sequence determinants of protein phase behavior from a coarse-grained model.* PLoS Comput Biol, 2018. **14**(1): p. e1005941.
94. Dutagaci, B., et al., *Charge-driven condensation of RNA and proteins suggests broad role of phase separation in cytoplasmic environments.* eLife, 2021. **10**: p. e64004.

95. Zheng, W., et al., *Molecular Details of Protein Condensates Probed by Microsecond Long Atomistic Simulations.* J Phys Chem B, 2020. **124**(51): p. 11671-11679.
96. Espinosa, J.R., et al., *Liquid network connectivity regulates the stability and composition of biomolecular condensates with many components.* Proc Natl Acad Sci U S A, 2020. **117**(24): p. 13238-13247.
97. Statt, A., et al., *Model for disordered proteins with strongly sequence-dependent liquid phase behavior.* J Chem Phys, 2020. **152**(7): p. 075101.
98. Benayad, Z., et al., *Simulation of FUS Protein Condensates with an Adapted Coarse-Grained Model.* J Chem Theory Comput, 2021. **17**(1): p. 525-537.
99. Zumbro, E. and A. Alexander-Katz, *Multivalent polymers can control phase boundary, dynamics, and organization of liquid-liquid phase separation.* bioRxiv, 2020: p. 2020.12.31.424934.
100. Agudo-Canalejo, J. and R. Golestanian, *Active Phase Separation in Mixtures of Chemically Interacting Particles.* Phys Rev Lett, 2019. **123**(1): p. 018101.
101. Ghosh, A., K. Mazarakos, and H.X. Zhou, *Three archetypical classes of macromolecular regulators of protein liquid-liquid phase separation.* Proc Natl Acad Sci U S A, 2019. **116**(39): p. 19474-19483.
102. Harmon, T.S., et al., *Intrinsically disordered linkers determine the interplay between phase separation and gelation in multivalent proteins.* Elife, 2017. **6**.
103. Choi, J.M., F. Dar, and R.V. Pappu, *LASSI: A lattice model for simulating phase transitions of multivalent proteins.* PLoS Comput Biol, 2019. **15**(10): p. e1007028.
104. Martin, E.W., et al., *Valence and patterning of aromatic residues determine the phase behavior of prion-like domains.* Science, 2020. **367**(6478): p. 694-699.
105. Janeway, C.J., P. Travers, and M. Walport, *Immunobiology: The Immune System in Health and Disease.* 5th edition, Garland Science, 2001.
106. Kwak, K., M. Akkaya, and S.K. Pierce, *B cell signaling in context.* Nat Immunol, 2019. **20**(8): p. 963-969.
107. Kumar, B.V., T.J. Connors, and D.L. Farber, *Human T Cell Development, Localization, and Function throughout Life.* Immunity, 2018. **48**(2): p. 202-213.
108. LeBien, T.W. and T.F. Tedder, *B lymphocytes: how they develop and function.* Blood, 2008. **112**(5): p. 1570-80.
109. Kurosaki, T. and J. Wienands, *B Cell Receptor Signaling*. 1 ed. Current Topics in Microbiology and Immunology. Vol. 393. 2016: Springer, Cham.
110. Tonegawa, S., *Somatic generation of antibody diversity.* Nature, 1983. **302**(5909): p. 575-81.
111. Gellert, M., *Molecular analysis of V(D)J recombination.* Annu Rev Genet, 1992. **26**: p. 425-46.
112. Wienands, J., et al., *SLP-65: a new signaling component in B lymphocytes which requires expression of the antigen receptor for phosphorylation.* J Exp Med, 1998. **188**(4): p. 791-5.
113. Liu, S.K., et al., *The hematopoietic-specific adaptor protein gads functions in T-cell signaling via interactions with the SLP-76 and LAT adaptors.* Curr Biol, 1999. **9**(2): p. 67-75.
114. Pawson, T. and J.D. Scott, *Signaling through scaffold, anchoring, and adaptor proteins.* Science, 1997. **278**(5346): p. 2075-80.
115. Borowicz, P., et al., *Adaptor proteins: Flexible and dynamic modulators of immune cell signalling.* Scandinavian Journal of Immunology, 2020. **92**(5): p. e12951.
116. Wong, L.E., et al., *Tripartite phase separation of two signal effectors with vesicles priming B cell responsiveness.* Nat Commun, 2020. **11**(1): p. 848.
117. Pappu, R., et al., *Requirement for B cell linker protein (BLNK) in B cell development.* Science, 1999. **286**(5446): p. 1949-54.
118. Minegishi, Y., et al., *An essential role for BLNK in human B cell development.* Science, 1999. **286**(5446): p. 1954-7.

119. Keller, B., et al., *Germline deletion of CIN85 in humans with X chromosome-linked antibody deficiency.* J Exp Med, 2018. **215**(5): p. 1327-1336.
120. Chong, P.A. and J.D. Forman-Kay, *Liquid-liquid phase separation in cellular signaling systems.* Curr Opin Struct Biol, 2016. **41**: p. 180-186.
121. Engelke, M., et al., *Macromolecular assembly of the adaptor SLP-65 at intracellular vesicles in resting B cells.* Sci Signal, 2014. **7**(339): p. ra79.
122. Kühn, J., et al., *The adaptor protein CIN85 assembles intracellular signaling clusters for B cell activation.* Sci Signal, 2016. **9**(434): p. ra66.
123. Gold, M.R. and M.G. Reth, *Antigen Receptor Function in the Context of the Nanoscale Organization of the B Cell Membrane.* Annu Rev Immunol, 2019. **37**: p. 97-123.
124. Gold, M.R., et al., *Tyrosine phosphorylation of components of the B-cell antigen receptors following receptor crosslinking.* Proc Natl Acad Sci U S A, 1991. **88**(8): p. 3436-40.
125. Luisiri, P., et al., *Cooperativity and segregation of function within the Ig-alpha/beta heterodimer of the B cell antigen receptor complex.* J Biol Chem, 1996. **271**(9): p. 5158-63.
126. Kurosaki, T., et al., *Syk activation by the Src-family tyrosine kinase in the B cell receptor signaling.* J Exp Med, 1994. **179**(5): p. 1725-9.
127. Flaswinkel, H. and M. Reth, *Dual role of the tyrosine activation motif of the Ig-alpha protein during signal transduction via the B cell antigen receptor.* Embo j, 1994. **13**(1): p. 83-9.
128. Rowley, R.B., et al., *Syk protein-tyrosine kinase is regulated by tyrosine-phosphorylated Ig alpha/Ig beta immunoreceptor tyrosine activation motif binding and autophosphorylation.* J Biol Chem, 1995. **270**(19): p. 11590-4.
129. Dal Porto, J.M., et al., *B cell antigen receptor signaling 101.* Mol Immunol, 2004. **41**(6-7): p. 599-613.
130. Kulathu, Y., et al., *The kinase Syk as an adaptor controlling sustained calcium signalling and B-cell development.* EMBO J, 2008. **27**(9): p. 1333-44.
131. Oellerich, T., et al., *The B-cell antigen receptor signals through a preformed transducer module of SLP65 and CIN85.* EMBO J, 2011. **30**(17): p. 3620-34.
132. Fu, C., et al., *BLNK: a central linker protein in B cell activation.* Immunity, 1998. **9**(1): p. 93-103.
133. Hashimoto, S., et al., *Identification of the SH2 domain binding protein of Bruton's tyrosine kinase as BLNK--functional significance of Btk-SH2 domain in B-cell antigen receptor-coupled calcium signaling.* Blood, 1999. **94**(7): p. 2357-64.
134. Ishiai, M., et al., *BLNK required for coupling Syk to PLC gamma 2 and Rac1-JNK in B cells.* Immunity, 1999. **10**(1): p. 117-25.
135. Kärkkäinen, S., et al., *Identification of preferred protein interactions by phage-display of the human Src homology-3 proteome.* EMBO Rep, 2006. **7**(2): p. 186-91.
136. Li, S.S., *Specificity and versatility of SH3 and other proline-recognition domains: structural basis and implications for cellular signal transduction.* Biochem J, 2005. **390**(Pt 3): p. 641-53.
137. Carducci, M., et al., *The protein interaction network mediated by human SH3 domains.* Biotechnol Adv, 2012. **30**(1): p. 4-15.
138. Cavanagh, J., et al., *Protein NMR Spectroscopy: Principles and Practice*, in *Protein NMR Spectroscopy (Second Edition)*, J. Cavanagh, et al., Editors. 2007, Academic Press: Burlington.
139. Levitt, M.H., *Spin Dynamics: Basics of Nuclear Magnetic Resonance.* Wiley, 2008: p. xxiv+686 pp.
140. Zeeman, P., *XXXII. On the influence of magnetism on the nature of the light emitted by a substance.* The London, Edinburgh, and Dublin Philosophical Magazine and Journal of Science, 1897. **43**(262): p. 226-239.
141. Gerlach, W. and O. Stern, *Der experimentelle Nachweis des magnetischen Moments des Silberatoms.* Zeitschrift für Physik, 1922. **8**(1): p. 110-111.

142. Gerlach, W. and O. Stern, *Der experimentelle Nachweis der Richtungsquantelung im Magnetfeld.* Zeitschrift für Physik, 1922. **9**(1): p. 349-352.
143. Gerlach, W. and O. Stern, *Das magnetische Moment des Silberatoms.* Zeitschrift für Physik, 1922. **9**(1): p. 353-355.
144. Rabi, I.I., et al., *A New Method of Measuring Nuclear Magnetic Moment.* Physical Review, 1938. **53**(4): p. 318-318.
145. Bloch, F., *Nuclear Induction.* Physical Review, 1946. **70**(7-8): p. 460-474.
146. Purcell, E.M., H.C. Torrey, and R.V. Pound, *Resonance Absorption by Nuclear Magnetic Moments in a Solid.* Physical Review, 1946. **69**(1-2): p. 37-38.
147. Ernst, R.R. and W.A. Anderson, *Application of Fourier Transform Spectroscopy to Magnetic Resonance.* Review of Scientific Instruments, 1966. **37**(1): p. 93-102.
148. Sørensen, O.W., et al., *Product operator formalism for the description of NMR pulse experiments.* Progress in Nuclear Magnetic Resonance Spectroscopy, 1984. **16**: p. 163-192.
149. Goldenberg, D.P., *The Product Operator Formalism: A Physical and Graphical Interpretation.* Concepts in magnetic resonance. Part A, Bridging education and research, 2010. **36A**(2): p. 49-83.
150. Morris, G.A. and R. Freeman, *Enhancement of nuclear magnetic resonance signals by polarization transfer.* Journal of the American Chemical Society, 1979. **101**(3): p. 760-762.
151. Williamson, M.P., *Chemical Shift Perturbation*, in *Modern Magnetic Resonance*. 2017. p. 1-19.
152. Pierce, M.M., C.S. Raman, and B.T. Nall, *Isothermal titration calorimetry of protein-protein interactions.* Methods, 1999. **19**(2): p. 213-21.
153. Lin, K. and G. Wu, *Isothermal Titration Calorimetry Assays to Measure Binding Affinities In Vitro.* Methods Mol Biol, 2019. **1893**: p. 257-272.
154. Matsuda, T. and C.L. Cepko, *Electroporation and RNA interference in the rodent retina in vivo and in vitro.* Proc Natl Acad Sci U S A, 2004. **101**(1): p. 16-22.
155. LaVallie, E.R., et al., *A thioredoxin gene fusion expression system that circumvents inclusion body formation in the E. coli cytoplasm.* Biotechnology (N Y), 1993. **11**(2): p. 187-93.
156. Keller, R.L.J., *The Computer Aided Resonance Assignment Tutorial*. 1st Edition ed. 2004.
157. Vranken, W.F., et al., *The CCPN data model for NMR spectroscopy: development of a software pipeline.* Proteins, 2005. **59**(4): p. 687-96.
158. Madeira, F., et al., *The EMBL-EBI search and sequence analysis tools APIs in 2019.* Nucleic Acids Res, 2019. **47**(W1): p. W636-W641.
159. Humphrey, W., A. Dalke, and K. Schulten, *VMD: visual molecular dynamics.* J Mol Graph, 1996. **14**(1): p. 33-8, 27-8.
160. Waudby, C.A., et al., *Two-Dimensional NMR Lineshape Analysis.* Scientific Reports, 2016. **6**(1): p. 24826.
161. Camilloni, C., et al., *Determination of Secondary Structure Populations in Disordered States of Proteins Using Nuclear Magnetic Resonance Chemical Shifts.* Biochemistry, 2012. **51**(11): p. 2224-2231.
162. Zhao, H., G. Piszczek, and P. Schuck, *SEDPHAT--a platform for global ITC analysis and global multi-method analysis of molecular interactions.* Methods, 2015. **76**: p. 137-148.
163. Houtman, J.C., et al., *Studying multisite binary and ternary protein interactions by global analysis of isothermal titration calorimetry data in SEDPHAT: application to adaptor protein complexes in cell signaling.* Protein Sci, 2007. **16**(1): p. 30-42.
164. *M9 Bacterial Minimal Medium*, in *Encyclopedia of Genetics, Genomics, Proteomics and Informatics*. 2008, Springer Netherlands: Dordrecht. p. 1135-1135.
165. Wittekind, M. and L. Mueller, *HNCACB, a High-Sensitivity 3D NMR Experiment to Correlate Amide-Proton and Nitrogen Resonances with the Alpha- and Beta-Carbon Resonances in Proteins.* Journal of Magnetic Resonance, Series B, 1993. **101**(2): p. 201-205.

166. Muhandiram, D.R. and L.E. Kay, *Gradient-Enhanced Triple-Resonance Three-Dimensional NMR Experiments with Improved Sensitivity.* Journal of Magnetic Resonance, Series B, 1994. **103**(3): p. 203-216.
167. Grzesiek, S. and A. Bax, *Amino acid type determination in the sequential assignment procedure of uniformly 13C/15N-enriched proteins.* Journal of Biomolecular NMR, 1993. **3**(2): p. 185-204.
168. Grzesiek, S. and A. Bax, *Improved 3D triple-resonance NMR techniques applied to a 31 kDa protein.* Journal of Magnetic Resonance (1969), 1992. **96**(2): p. 432-440.
169. Sattler, M., et al., *A simultaneous (15)N, (1)H- and (13)C, (1)H-HSQC with sensitivity enhancement and a heteronuclear gradient echo.* J Biomol NMR, 1995. **5**(1): p. 97-102.
170. Kay, L.E., G.Y. Xu, and T. Yamazaki, *Enhanced-Sensitivity Triple-Resonance Spectroscopy with Minimal H2O Saturation.* Journal of Magnetic Resonance, Series A, 1994. **109**(1): p. 129-133.
171. Mikes, J. and K. Dusek, *Simulation of polymer network formation by the Monte Carlo method.* Macromolecules, 1982. **15**(1): p. 93-99.
172. Marsh, J.A., et al., *Sensitivity of secondary structure propensities to sequence differences between alpha- and gamma-synuclein: implications for fibrillation.* Protein Sci, 2006. **15**(12): p. 2795-804.
173. Wong, L.E., et al., *Sensitivity-Enhanced Four-Dimensional Amide-Amide Correlation NMR Experiments for Sequential Assignment of Proline-Rich Disordered Proteins.* J Am Chem Soc, 2018. **140**(10): p. 3518-3522.
174. Cobos, E.S., et al., *A miniprotein scaffold used to assemble the polyproline II binding epitope recognized by SH3 domains.* J Mol Biol, 2004. **342**(1): p. 355-65.
175. Saksela, K. and P. Permi, *SH3 domain ligand binding: What's the consensus and where's the specificity?* FEBS Lett, 2012. **586**(17): p. 2609-14.
176. Skinner, A.L. and J.S. Laurence, *High-field solution NMR spectroscopy as a tool for assessing protein interactions with small molecule ligands.* J Pharm Sci, 2008. **97**(11): p. 4670-95.
177. Havrylov, S., M.J. Redowicz, and V.L. Buchman, *Emerging roles of Ruk/CIN85 in vesicle-mediated transport, adhesion, migration and malignancy.* Traffic, 2010. **11**(6): p. 721-31.
178. Ababou, A., M. Pfuhl, and J.E. Ladbury, *Novel insights into the mechanisms of CIN85 SH3 domains binding to Cbl proteins: solution-based investigations and in vivo implications.* J Mol Biol, 2009. **387**(5): p. 1120-36.
179. Jozic, D., et al., *Cbl promotes clustering of endocytic adaptor proteins.* Nat Struct Mol Biol, 2005. **12**(11): p. 972-9.
180. Ceregido, M.A., et al., *Multimeric and differential binding of CIN85/CD2AP with two atypical proline-rich sequences from CD2 and Cbl-b*.* FEBS J, 2013. **280**(14): p. 3399-415.
181. Kazlauskas, A., et al., *Large-Scale Screening of Preferred Interactions of Human Src Homology-3 (SH3) Domains Using Native Target Proteins as Affinity Ligands.* Mol Cell Proteomics, 2016. **15**(10): p. 3270-3281.
182. Kurochkina, N. and U. Guha, *SH3 domains: modules of protein-protein interactions.* Biophys Rev, 2013. **5**(1): p. 29-39.
183. Zarrinpar, A., R.P. Bhattacharyya, and W.A. Lim, *The structure and function of proline recognition domains.* Sci STKE, 2003. **2003**(179): p. Re8.
184. Zarrinpar, A. and W.A. Lim, *Converging on proline: the mechanism of WW domain peptide recognition.* Nat Struct Biol, 2000. **7**(8): p. 611-3.
185. Ortega Roldan, J.L., et al., *Distinct ubiquitin binding modes exhibited by SH3 domains: molecular determinants and functional implications.* PLoS One, 2013. **8**(9): p. e73018.
186. Kowanetz, K., et al., *Identification of a novel proline-arginine motif involved in CIN85-dependent clustering of Cbl and down-regulation of epidermal growth factor receptors.* J Biol Chem, 2003. **278**(41): p. 39735-46.

187. Tibaldi, E.V. and E.L. Reinherz, *CD2BP3, CIN85 and the structurally related adaptor protein CMS bind to the same CD2 cytoplasmic segment, but elicit divergent functional activities.* Int Immunol, 2003. **15**(3): p. 313-29.
188. Bartelt, R.R., et al., *Regions outside of conserved PxxPxR motifs drive the high affinity interaction of GRB2 with SH3 domain ligands.* Biochim Biophys Acta, 2015. **1853**(10 Pt A): p. 2560-9.
189. Stollar, E.J., et al., *Structural, functional, and bioinformatic studies demonstrate the crucial role of an extended peptide binding site for the SH3 domain of yeast Abp1p.* J Biol Chem, 2009. **284**(39): p. 26918-27.
190. Turnbull, W.B. and A.H. Daranas, *On the value of c: can low affinity systems be studied by isothermal titration calorimetry?* J Am Chem Soc, 2003. **125**(48): p. 14859-66.
191. Schmit, J.D., M. Feric, and M. Dundr, *How Hierarchical Interactions Make Membraneless Organelles Tick Like Clockwork.* Trends in Biochemical Sciences, 2021.
192. Alberti, S., et al., *A User's Guide for Phase Separation Assays with Purified Proteins.* J Mol Biol, 2018. **430**(23): p. 4806-4820.
193. Hyman, A.A., C.A. Weber, and F. Julicher, *Liquid-liquid phase separation in biology.* Annu Rev Cell Dev Biol, 2014. **30**: p. 39-58.
194. Maharana, S., et al., *RNA buffers the phase separation behavior of prion-like RNA binding proteins.* Science, 2018. **360**(6391): p. 918-921.
195. Li, Q., et al., *Biochemical and Structural Studies of the Interaction between ARAP1 and CIN85.* Biochemistry, 2018. **57**(14): p. 2132-2139.
196. Barda-Saad, M., et al., *Dynamic molecular interactions linking the T cell antigen receptor to the actin cytoskeleton.* Nat Immunol, 2005. **6**(1): p. 80-9.
197. Case, L.B., et al., *Stoichiometry controls activity of phase-separated clusters of actin signaling proteins.* Science, 2019. **363**(6431): p. 1093-1097.
198. Bhatt, A., *Unraveling details of CIN85/CD2AP assistance to SLP65-mediated B cell activation* in *Institute of Cellular and Molecular Immunology*. 2019, Georg-August University Göttingen: eDiss - SUB Göttingen. p. 126.
199. Tolar, P., *Cytoskeletal control of B cell responses to antigens.* Nat Rev Immunol, 2017. **17**(10): p. 621-634.
200. Alkam, D., et al., *Profilin1 biology and its mutation, actin(g) in disease.* Cell Mol Life Sci, 2017. **74**(6): p. 967-981.
201. Jockusch, B.M., K. Murk, and M. Rothkegel, *The profile of profilins*, in *Reviews of Physiology, Biochemistry and Pharmacology*, S.G. Amara, et al., Editors. 2007, Springer Berlin Heidelberg: Berlin, Heidelberg. p. 131-149.
202. Andriamoratsiresy, D., et al., *PFN2a, a new partner of RARalpha in the cytoplasm.* Biochem Biophys Res Commun, 2018. **495**(1): p. 846-853.
203. Ranganathan, S. and E.I. Shakhnovich, *Dynamic metastable long-living droplets formed by sticker-spacer proteins.* Elife, 2020. **9**.
204. Errington, W.J., B. Bruncsics, and C.A. Sarkar, *Mechanisms of noncanonical binding dynamics in multivalent protein-protein interactions.* Proc Natl Acad Sci U S A, 2019. **116**(51): p. 25659-25667.
205. Sorensen, C.S. and M. Kjaergaard, *Effective concentrations enforced by intrinsically disordered linkers are governed by polymer physics.* Proc Natl Acad Sci U S A, 2019. **116**(46): p. 23124-23131.
206. Lin, Y., et al., *Formation and Maturation of Phase-Separated Liquid Droplets by RNA-Binding Proteins.* Mol Cell, 2015. **60**(2): p. 208-19.
207. Dikic, I., *CIN85/CMS family of adaptor molecules.* FEBS Lett, 2002. **529**(1): p. 110-5.
208. Li, M., et al., *The SH3 domain of Lck modulates T-cell receptor-dependent activation of extracellular signal-regulated kinase through activation of Raf-1.* Mol Cell Biol, 2008. **28**(2): p. 630-41.

209. Sokolik, C.G., N. Qassem, and J.H. Chill, *The Disordered Cellular Multi-Tasker WIP and Its Protein-Protein Interactions: A Structural View.* Biomolecules, 2020. **10**(7).
210. Banjade, S. and M.K. Rosen, *Phase transitions of multivalent proteins can promote clustering of membrane receptors.* Elife, 2014. **3**.
211. Edwards, M., et al., *Capping protein regulators fine-tune actin assembly dynamics.* Nat Rev Mol Cell Biol, 2014. **15**(10): p. 677-89.
212. Buchman, V.L., et al., *Organization of the mouse Ruk locus and expression of isoforms in mouse tissues.* Gene, 2002. **295**(1): p. 13-17.
213. Lynch, D.K., et al., *A Cortactin-CD2-associated protein (CD2AP) complex provides a novel link between epidermal growth factor receptor endocytosis and the actin cytoskeleton.* J Biol Chem, 2003. **278**(24): p. 21805-13.
214. Kirsch, K.H., et al., *The adapter type protein CMS/CD2AP binds to the proto-oncogenic protein c-Cbl through a tyrosine phosphorylation-regulated Src homology 3 domain interaction.* J Biol Chem, 2001. **276**(7): p. 4957-63.
215. Mahoney, N.M., P.A. Janmey, and S.C. Almo, *Structure of the profilin-poly-L-proline complex involved in morphogenesis and cytoskeletal regulation.* Nat Struct Biol, 1997. **4**(11): p. 953-60.
216. Perelroizen, I., et al., *Interaction of profilin with G-actin and poly(L-proline).* Biochemistry, 1994. **33**(28): p. 8472-8.
217. Bremer, A., et al., *Deciphering how naturally occurring sequence features impact the phase behaviors of disordered prion-like domains*. 2021, bioRxiv.
218. Dikic, I., *Mechanisms controlling EGF receptor endocytosis and degradation.* Biochemical Society Transactions, 2003. **31**(6): p. 1178-1181.

List of figures

List of tables

Appendices

Appendix A: HSQC pulse program

```
;hsqcetf3gpsi
;avance-version (07/04/04)
;HSQC
;2D H-1/X correlation via double inept transfer
;   using sensitivity improvement
;phase sensitive using Echo/Antiecho-TPPI gradient selection
;with decoupling during acquisition
;using trim pulses in inept transfer
;using f3 - channel
;
;A.G. Palmer III, J. Cavanagh, P.E. Wright & M. Rance, J. Magn.
;   Reson. 93, 151-170 (1991)
;L.E. Kay, P. Keifer & T. Saarinen, J. Am. Chem. Soc. 114,
;   10663-5 (1992)
;J. Schleucher, M. Schwendinger, M. Sattler, P. Schmidt, O. Schedletzky,
;   S.J. Glaser, O.W. Sorensen & C. Griesinger, J. Biomol. NMR 4,
;   301-306 (1994)
;
;$CLASS=HighRes
;$DIM=2D
;$TYPE=
;$SUBTYPE=
;$COMMENT=

#include <Avance.incl>
#include <Grad.incl>
#include <Delay.incl>

"p2=p1*2"
"p22=p21*2"
"d11=30m"
"d13=4u"
"d26=1s/(cnst4*4)"

"d0=3u"

"in0=inf1/2"

"DELTA1=d13+p16+d16+4u"

#   ifdef LABEL_CN
```

```
"DELTA=p16+d16+larger(p2,p14)+d0*2"
#   else
"DELTA=p16+d16+p2+d0*2"
#   endif /*LABEL_CN*/
1 ze
  d11 pl16:f3
2 d1 do:f3
3 (p1 ph1)
  d26 pl3:f3
  (center (p2 ph1) (p22 ph6):f3 )
  d26 UNBLKGRAD
  p28 ph1
  d13
  (p1 ph2)
  3u
  p16:gp1
  d16
  (p21 ph3):f3
  d0

#   ifdef LABEL_CN
  (center (p2 ph7) (p14:sp3 ph1):f2 )
#   else
  (p2 ph7)
#   endif /*LABEL_CN*/

  d0
  p16:gp2*EA
  d16
  (p22 ph4):f3
  DELTA
  (center (p1 ph1) (p21 ph4):f3 )
  d24
  (center (p2 ph1) (p22 ph1):f3 )
  d24
  (center (p1 ph2) (p21 ph5):f3 )
  d26
  (center (p2 ph1) (p22 ph1):f3 )
  d26
  (p1 ph1)
  DELTA1
  (p2 ph1)
  d13
  p16:gp3
  d16 pl16:f3
  4u BLKGRAD
  go=2 ph31 cpd3:f3
  d1 do:f3 mc #0 to 2
```

```
   F1EA(igrad EA & ip5*2, id0 & ip3*2 & ip6*2 & ip31*2)
exit

ph1=0
ph2=1
ph3=0 2
ph4=0 0 2 2
ph5=1 1 3 3
ph6=0
ph7=0 0 2 2
ph31=0 2 2 0

;pl1 : f1 channel - power level for pulse (default)
;pl3 : f3 channel - power level for pulse (default)
;pl16: f3 channel - power level for CPD/BB decoupling
;sp3: f2 channel - shaped pulse 180 degree (adiabatic)
;p1 : f1 channel -  90 degree high power pulse
;p2 : f1 channel - 180 degree high power pulse
;p14: f2 channel - 180 degree shaped pulse for inversion (adiabatic)
;p16: homospoil/gradient pulse                    [1 msec]
;p21: f3 channel -  90 degree high power pulse
;p22: f3 channel - 180 degree high power pulse
;p28: f1 channel - trim pulse                     [1 msec] No trim pulse used
;d0 : incremented delay (2D)                      [3 usec]
;d1 : relaxation delay; 1-5 * T1
;d11: delay for disk I/O                          [30 msec]
;d13: short delay                                 [4 usec]
;d16: delay for homospoil/gradient recovery
;d24: 1/(4J)YH for YH
;    1/(8J)YH for all multiplicities
;d26: 1/(4J(YH))
;cnst4: = J(YH)
;inf1: 1/SW(X) = 2 * DW(X)
;in0: 1/(2 * SW(X)) = DW(X)
;nd0: 2
;NS: 1 * n
;DS: >= 16
;td1: number of experiments
;FnMODE: echo-antiecho
;cpd3: decoupling according to sequence defined by cpdprg3
;pcpd3: f3 channel - 90 degree pulse for decoupling sequence

;use gradient ratio:    gp 1 : gp 2 : gp 3
;           50 :   80 : 20.1      for C-13
;           50 :   80 :  8.1      for N-15

;for z-only gradients:
;gpz1: 50%
```

```
;gpz2: 80%
;gpz3: 20.1% for C-13, 8.1% for N-15

;use gradient files:
;gpnam1: SINE.100
;gpnam2: SINE.100
;gpnam3: SINE.100

                              ;preprocessor-flags-start
;LABEL_CN: for C-13 and N-15 labeled samples start experiment with
;          option -DLABEL_CN (eda: ZGOPTNS)
                              ;preprocessor-flags-end

;$Id: hsqcetf3gpsi,v 1.4 2007/04/11 13:34:30 ber Exp $
```

Appendix B: Resonance assignment of SH3A and SH3C

SH3A assignment:

```
loop_
  _Atom_shift_assign_ID
  _Residue_seq_code
  _Residue_label
  _Atom_name
  _Atom_type
  _Chem_shift_value
  _Chem_shift_value_error
  _Chem_shift_ambiguity_code

    1   1  MET  CA   C  55.637 0.3    1
    2   1  MET  CB   C  33.347 0.3    1
    3   1  MET  H    H   8.450 0.020  1
    4   1  MET  N    N 122.214 0.3    1
    5   2  VAL  CA   C  62.662 0.3    1
    6   2  VAL  CB   C  32.657 0.3    1
    7   2  VAL  H    H   8.460 0.020  1
    8   2  VAL  N    N 124.037 0.3    1
    9   3  GLU  CA   C  54.405 0.3    1
   10   3  GLU  CB   C  34.539 0.3    1
   11   3  GLU  H    H   8.513 0.020  1
   12   3  GLU  N    N 123.332 0.3    1
   13   4  ALA  CA   C  51.561 0.3    1
   14   4  ALA  CB   C  23.759 0.3    1
   15   4  ALA  H    H   8.930 0.020  1
   16   4  ALA  N    N 120.509 0.3    1
   17   5  ILE  CA   C  58.642 0.3    1
   18   5  ILE  CB   C  41.332 0.3    1
   19   5  ILE  H    H   8.715 0.020  1
   20   5  ILE  N    N 119.558 0.3    1
   21   6  VAL  CA   C  64.766 0.3    1
   22   6  VAL  CB   C  31.972 0.3    1
   23   6  VAL  H    H   8.812 0.020  1
   24   6  VAL  N    N 127.217 0.3    1
   25   7  GLU  CA   C  57.244 0.3    1
   26   7  GLU  CB   C  32.185 0.3    1
   27   7  GLU  H    H   9.162 0.020  1
   28   7  GLU  N    N 129.306 0.3    1
   29   8  PHE  CA   C  56.792 0.3    1
   30   8  PHE  CB   C  42.959 0.3    1
   31   8  PHE  H    H   7.573 0.020  1
   32   8  PHE  N    N 118.201 0.3    1
   33   9  ASP  CA   C  55.186 0.3    1
   34   9  ASP  CB   C  42.657 0.3    1
   35   9  ASP  H    H   7.965 0.020  1
   36   9  ASP  N    N 118.576 0.3    1
   37  10  TYR  CA   C  59.360 0.3    1
   38  10  TYR  CB   C  41.552 0.3    1
   39  10  TYR  H    H   8.605 0.020  1
   40  10  TYR  N    N 119.281 0.3    1
   41  11  GLN  CA   C  54.006 0.3    1
   42  11  GLN  CB   C  29.382 0.3    1
   43  11  GLN  H    H   7.427 0.020  1
   44  11  GLN  N    N 126.724 0.3    1
   45  12  ALA  CA   C  53.747 0.3    1
   46  12  ALA  CB   C  20.688 0.3    1
   47  12  ALA  H    H   8.296 0.020  1
   48  12  ALA  N    N 126.643 0.3    1
```

```
 49  13  GLN  CA   C  55.364 0.3    1
 50  13  GLN  CB   C  30.946 0.3    1
 51  13  GLN  H    H   9.075 0.020  1
 52  13  GLN  N    N 120.084 0.3    1
 53  14  HIS  CA   C  54.449 0.3    1
 54  14  HIS  CB   C  33.355 0.3    1
 55  14  HIS  H    H   7.268 0.020  1
 56  14  HIS  N    N 113.761 0.3    1
 57  16  ASP  CA   C  53.741 0.3    1
 58  16  ASP  CB   C  39.706 0.3    1
 59  16  ASP  H    H   8.737 0.020  1
 60  16  ASP  N    N 115.831 0.3    1
 61  17  GLU  CA   C  55.409 0.3    1
 62  17  GLU  CB   C  33.210 0.3    1
 63  17  GLU  H    H   7.729 0.020  1
 64  17  GLU  N    N 119.068 0.3    1
 65  18  LEU  CA   C  53.597 0.3    1
 66  18  LEU  CB   C  46.249 0.3    1
 67  18  LEU  H    H   9.180 0.020  1
 68  18  LEU  N    N 123.384 0.3    1
 69  19  THR  CA   C  62.875 0.3    1
 70  19  THR  CB   C  70.130 0.3    1
 71  19  THR  H    H   7.782 0.020  1
 72  19  THR  N    N 119.612 0.3    1
 73  20  ILE  CA   C  60.048 0.3    1
 74  20  ILE  CB   C  40.865 0.3    1
 75  20  ILE  H    H   9.267 0.020  1
 76  20  ILE  N    N 122.029 0.3    1
 77  21  SER  CA   C  56.384 0.3    1
 78  21  SER  CB   C  65.935 0.3    1
 79  21  SER  H    H   8.687 0.020  1
 80  21  SER  N    N 119.442 0.3    1
 81  22  VAL  CA   C  65.628 0.3    1
 82  22  VAL  CB   C  32.005 0.3    1
 83  22  VAL  H    H   8.220 0.020  1
 84  22  VAL  N    N 121.211 0.3    1
 85  23  GLY  CA   C  44.832 0.3    1
 86  23  GLY  H    H   8.717 0.020  1
 87  23  GLY  N    N 114.467 0.3    1
 88  24  GLU  CA   C  57.746 0.3    1
 89  24  GLU  CB   C  30.767 0.3    1
 90  24  GLU  H    H   7.951 0.020  1
 91  24  GLU  N    N 119.836 0.3    1
 92  25  ILE  CA   C  59.602 0.3    1
 93  25  ILE  CB   C  38.726 0.3    1
 94  25  ILE  H    H   8.117 0.020  1
 95  25  ILE  N    N 119.647 0.3    1
 96  26  ILE  CA   C  59.786 0.3    1
 97  26  ILE  CB   C  39.570 0.3    1
 98  26  ILE  H    H   9.090 0.020  1
 99  26  ILE  N    N 128.023 0.3    1
100  27  THR  CA   C  60.061 0.3    1
101  27  THR  CB   C  71.836 0.3    1
102  27  THR  H    H   8.933 0.020  1
103  27  THR  N    N 115.355 0.3    1
104  28  ASN  CA   C  54.194 0.3    1
105  28  ASN  CB   C  37.616 0.3    1
106  28  ASN  H    H   8.790 0.020  1
107  28  ASN  N    N 116.465 0.3    1
108  29  ILE  CA   C  62.195 0.3    1
109  29  ILE  CB   C  38.760 0.3    1
110  29  ILE  H    H   8.365 0.020  1
111  29  ILE  N    N 118.198 0.3    1
112  30  ARG  CA   C  54.974 0.3    1
113  30  ARG  CB   C  32.646 0.3    1
114  30  ARG  H    H   9.302 0.020  1
```

115 30 ARG N N 128.916 0.3 1
116 31 LYS CA C 56.549 0.3 1
117 31 LYS CB C 32.794 0.3 1
118 31 LYS H H 8.287 0.020 1
119 31 LYS N N 126.334 0.3 1
120 32 GLU CA C 55.515 0.3 1
121 32 GLU CB C 32.956 0.3 1
122 32 GLU H H 7.046 0.020 1
123 32 GLU N N 121.853 0.3 1
124 33 ASP CA C 55.413 0.3 1
125 33 ASP CB C 41.747 0.3 1
126 33 ASP H H 8.770 0.020 1
127 33 ASP N N 121.224 0.3 1
128 34 GLY CA C 46.017 0.3 1
129 34 GLY H H 8.756 0.020 1
130 34 GLY N N 109.163 0.3 1
131 35 GLY CA C 45.068 0.3 1
132 35 GLY H H 9.124 0.020 1
133 35 GLY N N 109.636 0.3 1
134 36 TRP CA C 55.891 0.3 1
135 36 TRP CB C 31.221 0.3 1
136 36 TRP H H 7.723 0.020 1
137 36 TRP N N 119.781 0.3 1
138 37 TRP CA C 52.570 0.3 1
139 37 TRP CB C 33.867 0.3 1
140 37 TRP H H 8.378 0.020 1
141 37 TRP N N 123.089 0.3 1
142 38 GLU CA C 54.194 0.3 1
143 38 GLU CB C 34.287 0.3 1
144 38 GLU H H 8.148 0.020 1
145 38 GLU N N 118.838 0.3 1
146 39 GLY CA C 46.230 0.3 1
147 39 GLY H H 8.937 0.020 1
148 39 GLY N N 111.240 0.3 1
149 40 GLN CA C 54.005 0.3 1
150 40 GLN CB C 33.644 0.3 1
151 40 GLN H H 8.671 0.020 1
152 40 GLN N N 117.330 0.3 1
153 41 ILE CA C 60.990 0.3 1
154 41 ILE CB C 41.009 0.3 1
155 41 ILE H H 8.673 0.020 1
156 41 ILE N N 120.856 0.3 1
157 42 ASN CA C 54.651 0.3 1
158 42 ASN CB C 37.811 0.3 1
159 42 ASN H H 9.302 0.020 1
160 42 ASN N N 125.436 0.3 1
161 43 GLY CA C 45.820 0.3 1
162 43 GLY H H 8.694 0.020 1
163 43 GLY N N 104.893 0.3 1
164 44 ARG CA C 55.398 0.3 1
165 44 ARG CB C 32.424 0.3 1
166 44 ARG H H 8.029 0.020 1
167 44 ARG N N 122.003 0.3 1
168 45 ARG CA C 54.447 0.3 1
169 45 ARG CB C 33.811 0.3 1
170 45 ARG H H 8.519 0.020 1
171 45 ARG N N 122.061 0.3 1
172 46 GLY CA C 45.825 0.3 1
173 46 GLY H H 8.785 0.020 1
174 46 GLY N N 109.914 0.3 1
175 47 LEU CA C 54.420 0.3 1
176 47 LEU CB C 45.523 0.3 1
177 47 LEU H H 8.865 0.020 1
178 47 LEU N N 119.339 0.3 1
179 48 PHE CA C 55.339 0.3 1
180 48 PHE CB C 39.003 0.3 1

```
    181   48   PHE  H     H   9.023 0.020   1
    182   48   PHE  N     N 116.747 0.3     1
    183   50   ASP  CA    C  56.345 0.3     1
    184   50   ASP  CB    C  37.264 0.3     1
    185   50   ASP  H     H   7.595 0.020   1
    186   50   ASP  N     N 123.991 0.3     1
    187   51   ASN  CA    C  53.495 0.3     1
    188   51   ASN  CB    C  36.394 0.3     1
    189   51   ASN  H     H   8.029 0.020   1
    190   51   ASN  N     N 113.811 0.3     1
    191   52   PHE  CA    C  57.260 0.3     1
    192   52   PHE  CB    C  38.038 0.3     1
    193   52   PHE  H     H   7.677 0.020   1
    194   52   PHE  N     N 119.637 0.3     1
    195   53   VAL  CA    C  58.390 0.3     1
    196   53   VAL  CB    C  35.000 0.3     1
    197   53   VAL  H     H   7.358 0.020   1
    198   53   VAL  N     N 109.657 0.3     1
    199   54   ARG  CA    C  54.402 0.3     1
    200   54   ARG  CB    C  33.091 0.3     1
    201   54   ARG  H     H   9.053 0.020   1
    202   54   ARG  N     N 120.536 0.3     1
    203   55   GLU  CA    C  57.718 0.3     1
    204   55   GLU  CB    C  31.064 0.3     1
    205   55   GLU  H     H   9.305 0.020   1
    206   55   GLU  N     N 128.420 0.3     1
    207   56   ILE  CA    C  61.491 0.3     1
    208   56   ILE  CB    C  38.956 0.3     1
    209   56   ILE  H     H   8.719 0.020   1
    210   56   ILE  N     N 126.922 0.3     1
    211   57   LYS  CA    C  55.857 0.3     1
    212   57   LYS  CB    C  33.360 0.3     1
    213   57   LYS  H     H   8.446 0.020   1
    214   57   LYS  N     N 128.104 0.3     1
    215   58   LYS  CA    C  57.730 0.3     1
    216   58   LYS  CB    C  34.058 0.3     1
    217   58   LYS  H     H   8.195 0.020   1
    218   58   LYS  N     N 129.310 0.3     1
stop_
```

SH3C assignment:

```
 loop_
   _Atom_shift_assign_ID
   _Residue_seq_code
   _Residue_label
   _Atom_name
   _Atom_type
   _Chem_shift_value
   _Chem_shift_value_error
   _Chem_shift_ambiguity_code

     1   6  ARG  H     H   8.364 0.020   1
     2   6  ARG  N     N 122.542 0.3     1
     3   7  THR  CA    C  63.009 0.3     1
     4   7  THR  CB    C  70.596 0.3     1
     5   7  THR  H     H   8.140 0.020   1
     6   7  THR  N     N 114.984 0.3     1
     7   8  LYS  CA    C  57.173 0.3     1
     8   8  LYS  CB    C  33.915 0.3     1
     9   8  LYS  H     H   8.312 0.020   1
    10   8  LYS  N     N 124.007 0.3     1
    11   9  SER  CA    C  59.381 0.3     1
```

12 9 SER CB C 64.948 0.3 1
13 9 SER H H 8.342 0.020 1
14 9 SER N N 117.927 0.3 1
15 10 LYS CA C 56.758 0.3 1
16 10 LYS CB C 34.621 0.3 1
17 10 LYS H H 8.222 0.020 1
18 10 LYS N N 122.798 0.3 1
19 11 ASP CA C 54.227 0.3 1
20 11 ASP CB C 44.682 0.3 1
21 11 ASP H H 8.221 0.020 1
22 11 ASP N N 120.461 0.3 1
23 12 TYR CA C 57.471 0.3 1
24 12 TYR CB C 36.924 0.3 1
25 12 TYR H H 8.951 0.020 1
26 12 TYR N N 118.681 0.3 1
27 13 CYS CA C 56.349 0.3 1
28 13 CYS CB C 32.925 0.3 1
29 13 CYS H H 9.285 0.020 1
30 13 CYS N N 114.727 0.3 1
31 14 LYS CA C 55.275 0.3 1
32 14 LYS CB C 36.781 0.3 1
33 14 LYS H H 9.108 0.020 1
34 14 LYS N N 123.045 0.3 1
35 15 VAL CA C 65.318 0.3 1
36 15 VAL CB C 32.217 0.3 1
37 15 VAL H H 8.965 0.020 1
38 15 VAL N N 127.346 0.3 1
39 16 ILE CA C 62.074 0.3 1
40 16 ILE CB C 39.640 0.3 1
41 16 ILE H H 9.042 0.020 1
42 16 ILE N N 126.844 0.3 1
43 17 PHE CA C 55.414 0.3 1
44 17 PHE CB C 42.218 0.3 1
45 17 PHE H H 7.725 0.020 1
46 17 PHE N N 121.668 0.3 1
47 19 TYR CA C 59.858 0.3 1
48 19 TYR CB C 42.661 0.3 1
49 19 TYR H H 8.531 0.020 1
50 19 TYR N N 118.301 0.3 1
51 20 GLU CA C 55.366 0.3 1
52 20 GLU CB C 31.392 0.3 1
53 20 GLU H H 7.460 0.020 1
54 20 GLU N N 127.352 0.3 1
55 21 ALA CA C 54.376 0.3 1
56 21 ALA CB C 21.605 0.3 1
57 21 ALA H H 8.359 0.020 1
58 21 ALA N N 126.745 0.3 1
59 22 GLN CA C 56.135 0.3 1
60 22 GLN CB C 31.282 0.3 1
61 22 GLN H H 9.357 0.020 1
62 22 GLN N N 120.234 0.3 1
63 23 ASN CA C 53.111 0.3 1
64 23 ASN CB C 41.674 0.3 1
65 23 ASN H H 7.532 0.020 1
66 23 ASN N N 112.616 0.3 1
67 24 ASP CA C 57.730 0.3 1
68 24 ASP CB C 41.660 0.3 1
69 24 ASP H H 8.656 0.020 1
70 24 ASP N N 117.633 0.3 1
71 25 ASP CA C 55.559 0.3 1
72 25 ASP CB C 41.606 0.3 1
73 25 ASP H H 8.594 0.020 1
74 25 ASP N N 117.269 0.3 1
75 26 GLU CB C 34.025 0.3 1
76 26 GLU H H 7.495 0.020 1
77 26 GLU N N 119.392 0.3 1

78 27 LEU CA C 54.183 0.3 1
79 27 LEU CB C 47.135 0.3 1
80 27 LEU H H 8.914 0.020 1
81 27 LEU N N 123.505 0.3 1
82 28 THR CA C 63.839 0.3 1
83 28 THR CB C 70.434 0.3 1
84 28 THR H H 7.830 0.020 1
85 28 THR N N 120.159 0.3 1
86 29 ILE CA C 60.626 0.3 1
87 29 ILE CB C 41.985 0.3 1
88 29 ILE H H 9.275 0.020 1
89 29 ILE N N 121.973 0.3 1
90 30 LYS CA C 54.809 0.3 1
91 30 LYS CB C 35.626 0.3 1
92 30 LYS H H 9.185 0.020 1
93 30 LYS N N 124.026 0.3 1
94 31 GLU CA C 59.871 0.3 1
95 31 GLU CB C 30.121 0.3 1
96 31 GLU H H 8.795 0.020 1
97 31 GLU N N 120.512 0.3 1
98 32 GLY CA C 45.798 0.3 1
99 32 GLY H H 8.682 0.020 1
100 32 GLY N N 113.788 0.3 1
101 33 ASP CA C 56.919 0.3 1
102 33 ASP CB C 43.032 0.3 1
103 33 ASP H H 8.179 0.020 1
104 33 ASP N N 121.620 0.3 1
105 34 ILE CA C 59.945 0.3 1
106 34 ILE CB C 37.867 0.3 1
107 34 ILE H H 8.349 0.020 1
108 34 ILE N N 120.207 0.3 1
109 35 VAL CA C 62.218 0.3 1
110 35 VAL CB C 35.717 0.3 1
111 35 VAL H H 8.969 0.020 1
112 35 VAL N N 128.874 0.3 1
113 36 THR CA C 63.788 0.3 1
114 36 THR CB C 70.206 0.3 1
115 36 THR H H 8.991 0.020 1
116 36 THR N N 124.584 0.3 1
117 37 LEU CA C 56.727 0.3 1
118 37 LEU CB C 43.449 0.3 1
119 37 LEU H H 8.888 0.020 1
120 37 LEU N N 130.354 0.3 1
121 38 ILE CA C 62.239 0.3 1
122 38 ILE CB C 39.585 0.3 1
123 38 ILE H H 8.959 0.020 1
124 38 ILE N N 125.475 0.3 1
125 39 ASN CA C 54.156 0.3 1
126 39 ASN CB C 42.169 0.3 1
127 39 ASN H H 7.819 0.020 1
128 39 ASN N N 116.109 0.3 1
129 40 LYS CA C 57.120 0.3 1
130 40 LYS CB C 33.936 0.3 1
131 40 LYS H H 8.611 0.020 1
132 40 LYS N N 123.380 0.3 1
133 41 ASP CA C 54.699 0.3 1
134 41 ASP CB C 41.778 0.3 1
135 41 ASP H H 7.958 0.020 1
136 41 ASP N N 121.127 0.3 1
137 42 CYS CA C 59.648 0.3 1
138 42 CYS CB C 29.681 0.3 1
139 42 CYS H H 7.979 0.020 1
140 42 CYS N N 120.340 0.3 1
141 43 ILE CA C 64.153 0.3 1
142 43 ILE CB C 38.910 0.3 1
143 43 ILE H H 8.233 0.020 1

144 43 ILE N N 121.222 0.3 1
145 44 ASP CA C 54.156 0.3 1
146 44 ASP CB C 43.049 0.3 1
147 44 ASP H H 7.627 0.020 1
148 44 ASP N N 119.585 0.3 1
149 45 VAL CA C 65.037 0.3 1
150 45 VAL CB C 32.765 0.3 1
151 45 VAL H H 8.242 0.020 1
152 45 VAL N N 122.802 0.3 1
153 46 GLY CA C 45.743 0.3 1
154 46 GLY H H 8.734 0.020 1
155 46 GLY N N 113.844 0.3 1
156 47 TRP CA C 56.899 0.3 1
157 47 TRP CB C 31.881 0.3 1
158 47 TRP H H 7.453 0.020 1
159 47 TRP N N 120.492 0.3 1
160 48 TRP CA C 54.056 0.3 1
161 48 TRP CB C 35.219 0.3 1
162 48 TRP H H 8.561 0.020 1
163 48 TRP N N 122.013 0.3 1
164 49 GLU CA C 55.505 0.3 1
165 49 GLU H H 8.526 0.020 1
166 49 GLU N N 118.414 0.3 1
167 50 GLY CA C 46.561 0.3 1
168 50 GLY H H 9.421 0.020 1
169 50 GLY N N 114.575 0.3 1
170 51 GLU CA C 55.450 0.3 1
171 51 GLU CB C 35.086 0.3 1
172 51 GLU H H 9.063 0.020 1
173 51 GLU N N 118.180 0.3 1
174 52 LEU CB C 47.276 0.3 1
175 52 LEU H H 9.044 0.020 1
176 52 LEU N N 125.154 0.3 1
177 54 GLY CA C 46.421 0.3 1
178 54 GLY H H 8.992 0.020 1
179 54 GLY N N 104.333 0.3 1
180 55 ARG CA C 55.672 0.3 1
181 55 ARG CB C 33.130 0.3 1
182 55 ARG H H 7.877 0.020 1
183 55 ARG N N 121.526 0.3 1
184 56 ARG CA C 55.146 0.3 1
185 56 ARG CB C 34.794 0.3 1
186 56 ARG H H 8.596 0.020 1
187 56 ARG N N 121.968 0.3 1
188 57 GLY CA C 46.781 0.3 1
189 57 GLY H H 8.906 0.020 1
190 57 GLY N N 110.250 0.3 1
191 58 VAL CA C 60.582 0.3 1
192 58 VAL CB C 35.345 0.3 1
193 58 VAL H H 8.692 0.020 1
194 58 VAL N N 111.874 0.3 1
195 59 PHE CA C 55.899 0.3 1
196 59 PHE CB C 39.270 0.3 1
197 59 PHE H H 8.809 0.020 1
198 59 PHE N N 117.137 0.3 1
199 61 ASP CA C 56.953 0.3 1
200 61 ASP CB C 37.984 0.3 1
201 61 ASP H H 7.756 0.020 1
202 61 ASP N N 123.831 0.3 1
203 62 ASN CA C 53.936 0.3 1
204 62 ASN H H 7.955 0.020 1
205 62 ASN N N 113.646 0.3 1
206 63 PHE CA C 57.558 0.3 1
207 63 PHE CB C 37.819 0.3 1
208 63 PHE H H 7.717 0.020 1
209 63 PHE N N 120.169 0.3 1

```
    210  64  VAL  CA    C  59.428 0.3    1
    211  64  VAL  CB    C  37.111 0.3    1
    212  64  VAL  H     H   7.315 0.020  1
    213  64  VAL  N     N 109.043 0.3    1
    214  65  LYS  CA    C  55.213 0.3    1
    215  65  LYS  CB    C  36.814 0.3    1
    216  65  LYS  H     H   8.953 0.020  1
    217  65  LYS  N     N 118.859 0.3    1
    218  66  LEU  CA    C  57.290 0.3    1
    219  66  LEU  CB    C  43.381 0.3    1
    220  66  LEU  H     H   9.114 0.020  1
    221  66  LEU  N     N 127.058 0.3    1
    222  67  LEU  CA    C  53.771 0.3    1
    223  67  LEU  CB    C  41.674 0.3    1
    224  67  LEU  H     H   8.471 0.020  1
    225  67  LEU  N     N 126.970 0.3    1
    226  70  ASP  CA    C  54.376 0.3    1
    227  70  ASP  CB    C  40.850 0.3    1
    228  70  ASP  H     H   8.318 0.020  1
    229  70  ASP  N     N 116.326 0.3    1
    230  71  PHE  CA    C  60.204 0.3    1
    231  71  PHE  CB    C  40.465 0.3    1
    232  71  PHE  H     H   7.893 0.020  1
    233  71  PHE  N     N 120.615 0.3    1
    234  72  GLU  CA    C  56.734 0.3    1
    235  72  GLU  CB    C  31.826 0.3    1
    236  72  GLU  H     H   7.938 0.020  1
    237  72  GLU  N     N 124.078 0.3    1
    238  73  LYS  CB    C  33.977 0.3    1
    239  73  LYS  H     H   7.907 0.020  1
    240  73  LYS  N     N 122.607 0.3    1
    241  74  GLU  CA    C  59.270 0.3    1
    242  74  GLU  CB    C  31.997 0.3    1
    243  74  GLU  H     H   8.033 0.020  1
    244  74  GLU  N     N 127.821 0.3    1
stop_
```

Appendix C: The 3SH3 construct is not binding to CIN85$_{366-389}$

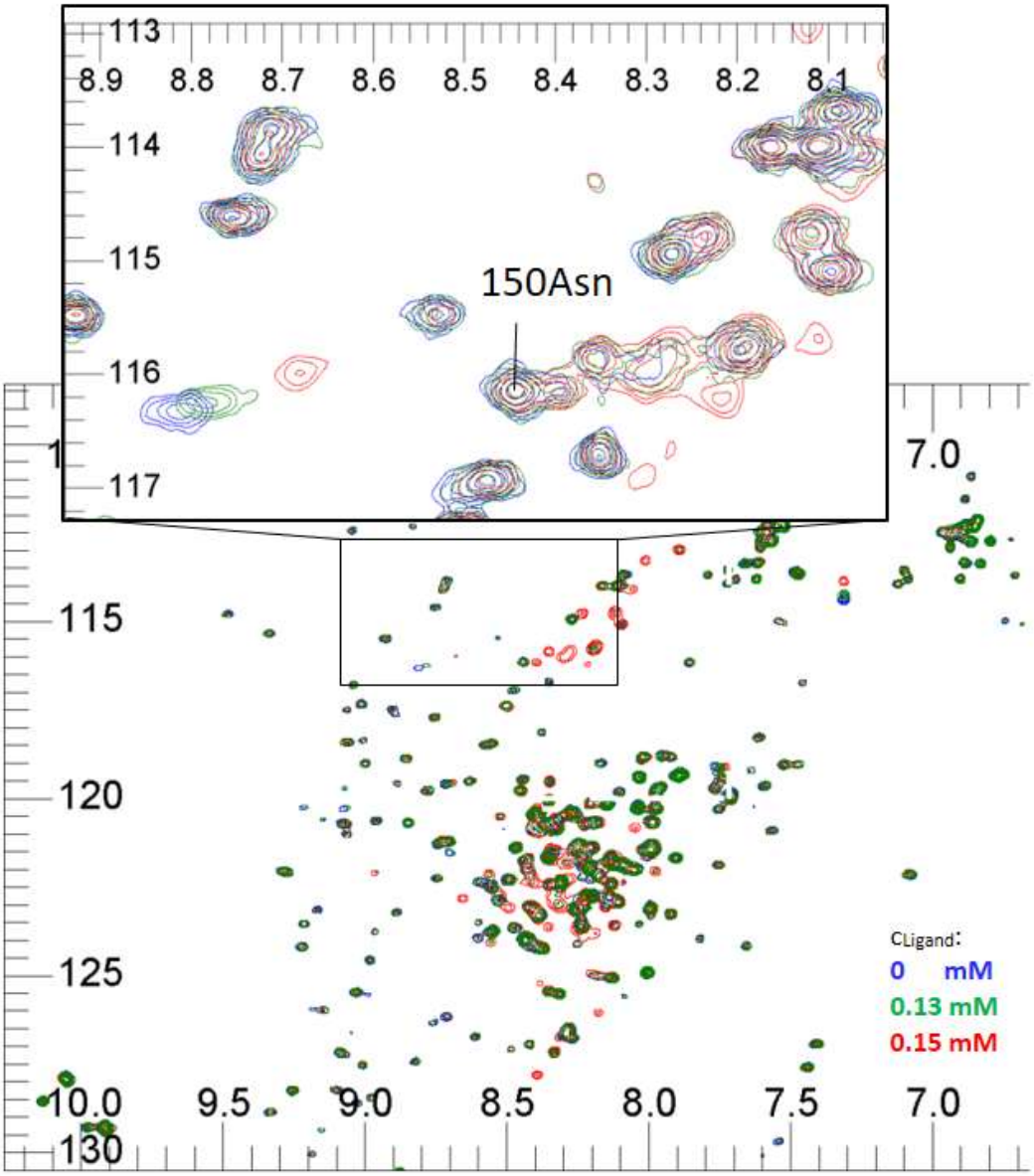

Figure Appendix C: NMR titration of CIN85$_{366-389}$ to CIN85-3SH3. The potential binding of the proline-rich region CIN85$_{366-389}$ to CIN85-3SH3 was studied to check potential intra-/ intermolecular interactions of CIN85. Overlaid ^{15}N-HSQC spectra of titration of CIN85$_{366-389}$ ERPEMLPNRTEEKERPEREPKLD to 0.1 mM 3SH3. No chemical shift change is observed for residues of the binding site (e.g. Asp150).

Appendix D: SH3A residues of the Cbl-b binding site

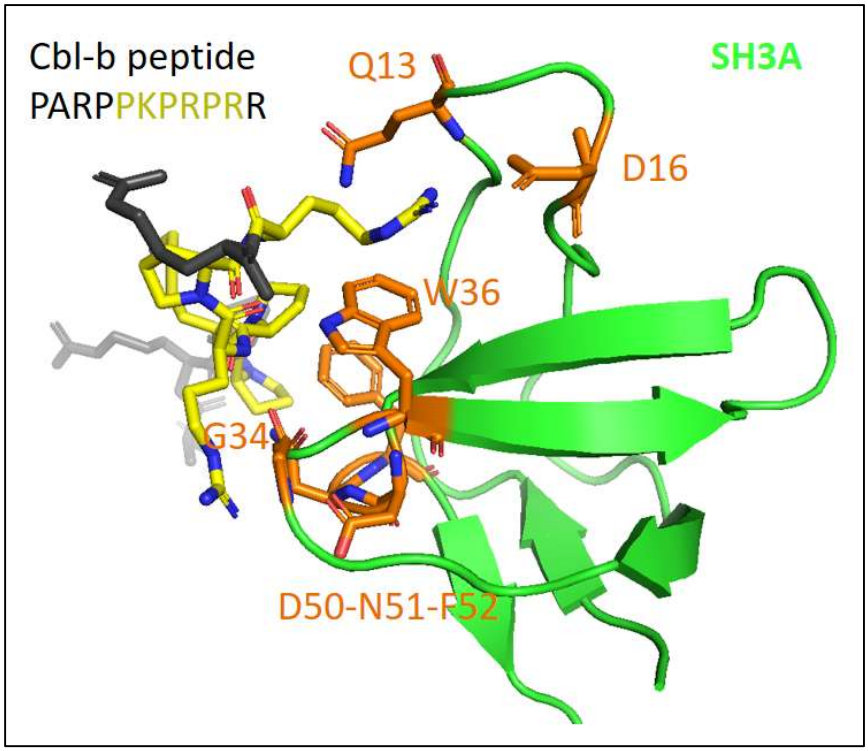

Figure Appendix D: The SH3A-Cbl-b interaction occurs at a single binding site. Crystal structure of the SH3-Cbl-b complex (pdb: 2bz8 [160]). The SH3 domain residues Q13, D16, G35, D50, N51 and F52 (colored orange) are interacting with the core motif of Cbl-b peptide (colored yellow). The SH3 domain residues which are not directly interacting are color-coded green.

Appendix E: Binding isotherms of the NMR titration of PRM-derived peptides to ^{15}N-SH3A

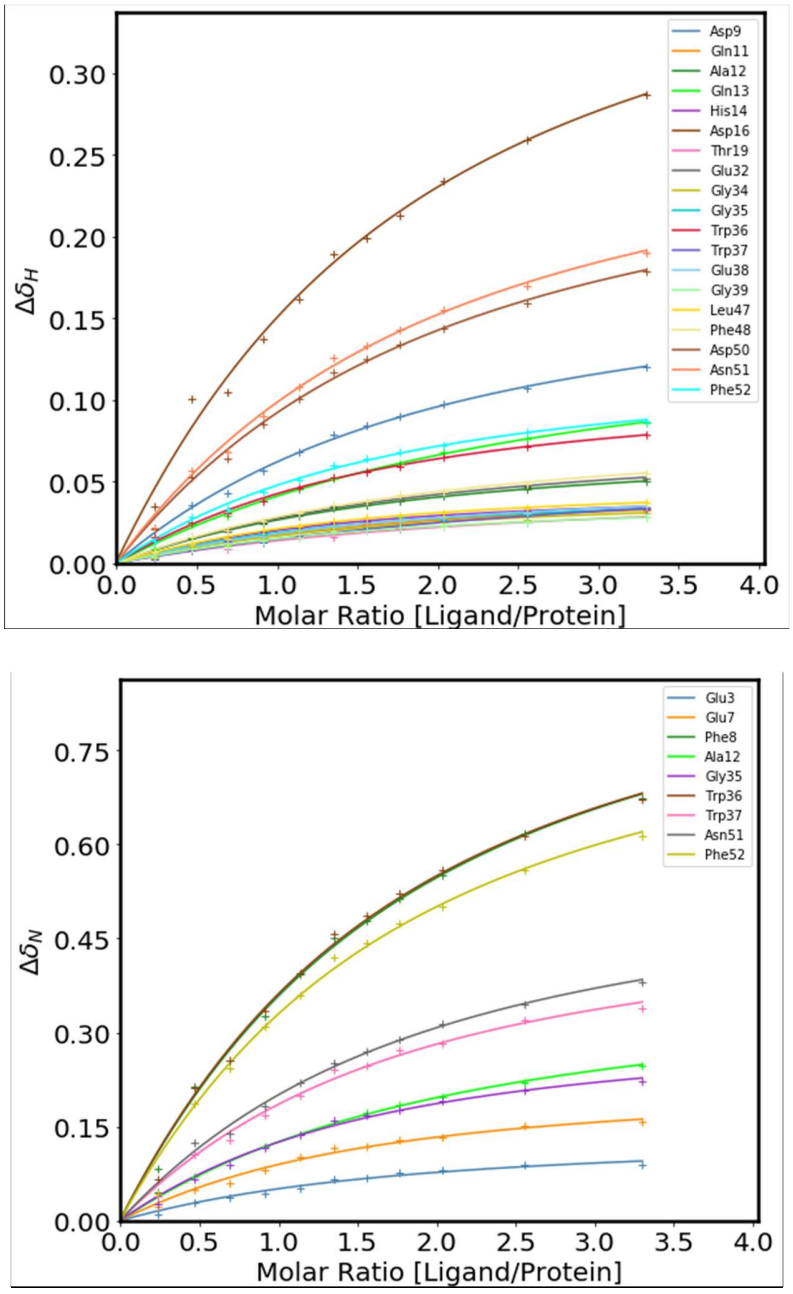

Figure Appendix-E-1: Binding isotherms of the NMR titration of SLP65-PRM1 to ^{15}N-SH3A. Individual K_Ds for both ^{1}H and ^{15}N CS were obtain by fits to equation S1. The global K_D was calculated as the mean of the individual ^{1}H and ^{15}N K_Ds. Representative isotherms for ^{1}H CSP (top) and ^{15}N CSP (bottom) are shown.

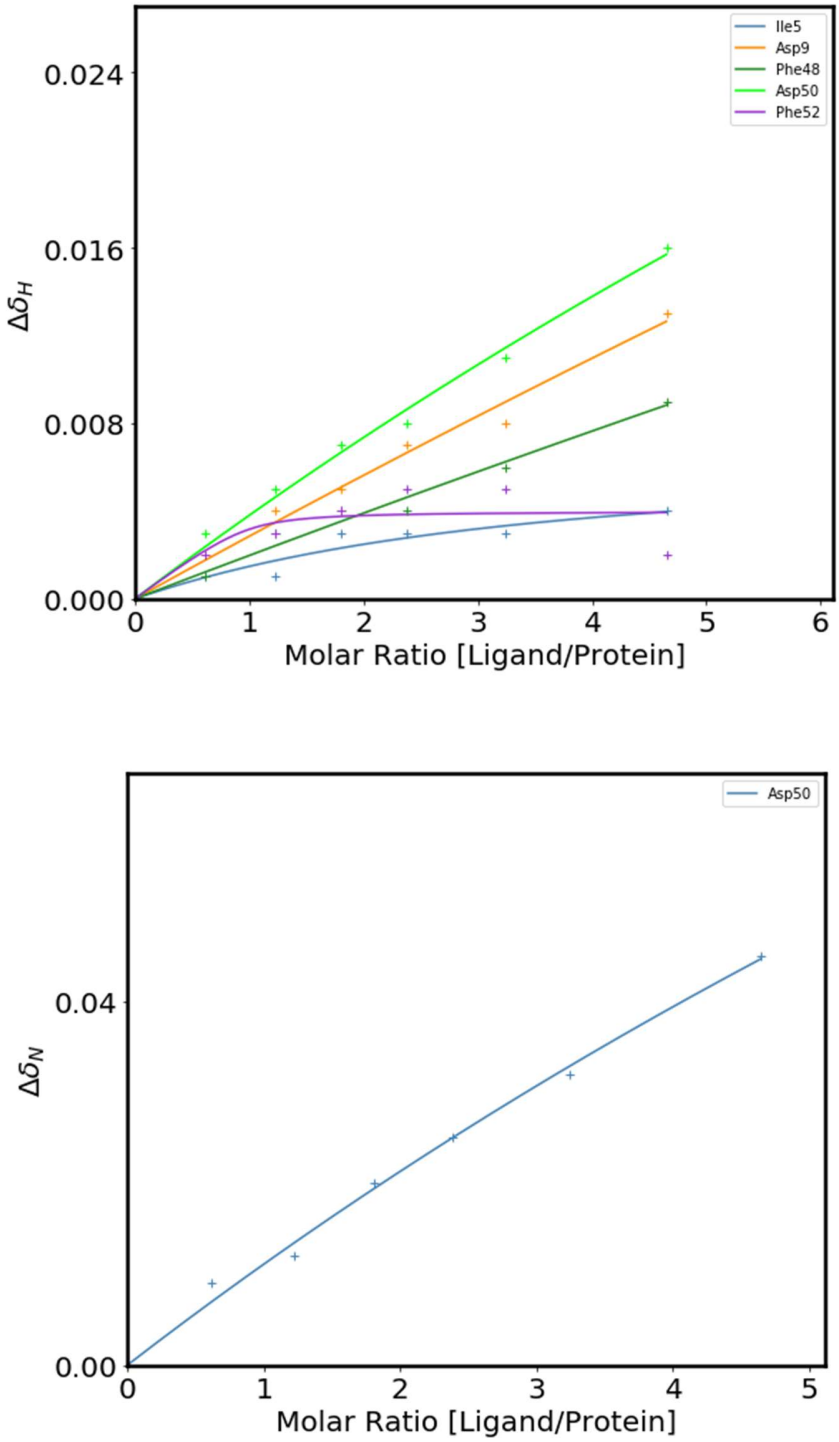

Figure Appendix-E-2: Binding isotherms of the NMR titration of SLP65-PRM2 to ^{15}N-SH3A. Binding isotherms of both ^{1}H (top) and ^{15}N (bottom) chemical shifts were fitted to equation S1. No K_D was obtained, since the fitting error was too large. ^{1}H CSPs were < 0.02 ppm (top) and ^{15}N CSP were smaller than 0.1 ppm (bottom).

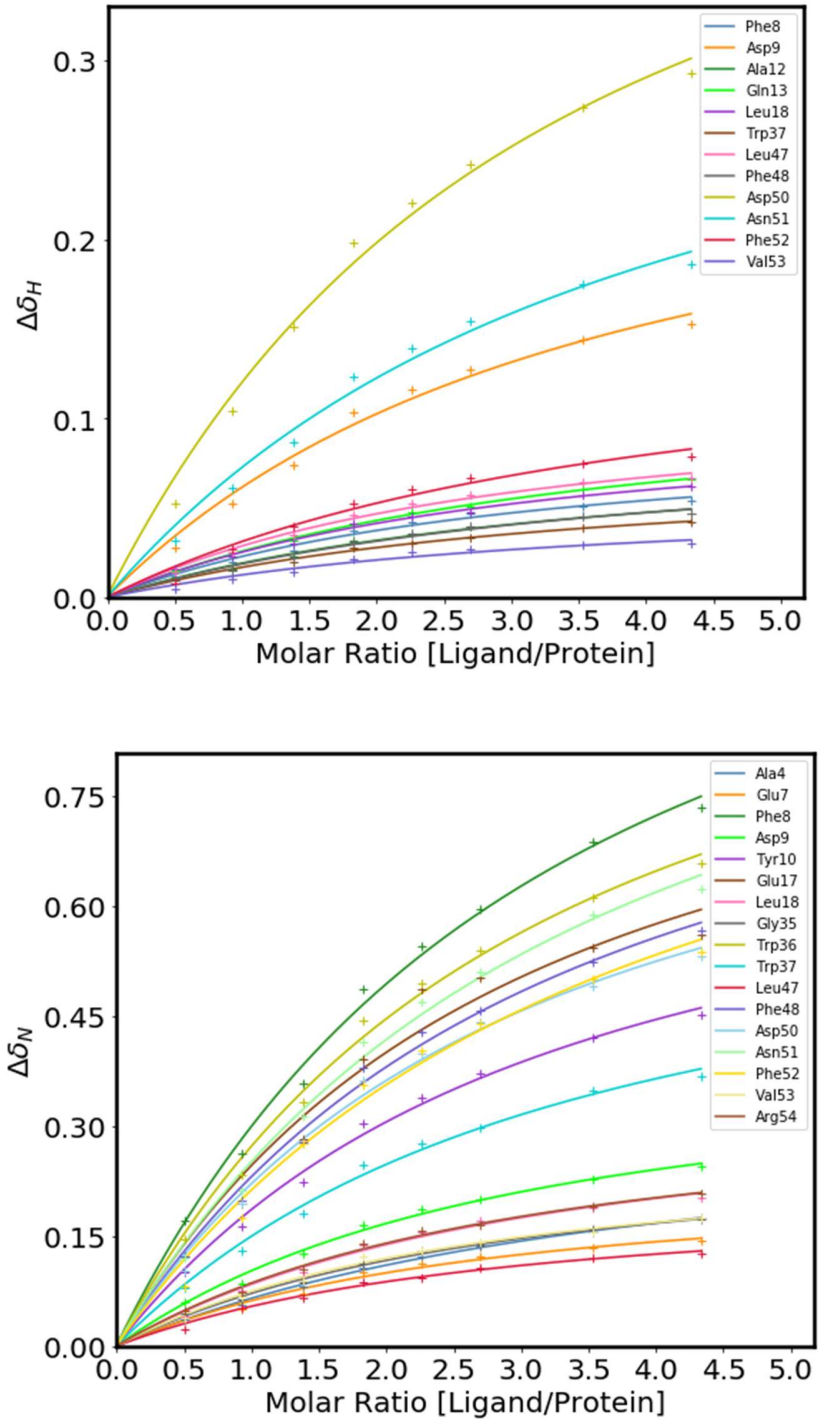

Figure Appendix-E-3: Binding isotherms of the NMR titration of SLP65-PRM3 to ^{15}N-SH3A. Individual K_Ds for both ^{1}H and ^{15}N CS were obtain by fits to equation S1. The global K_D was calculated as the mean of the individual ^{1}H and ^{15}N K_Ds. Representative isotherms for ^{1}H CSP (top) and ^{15}N CSP (bottom) are shown.

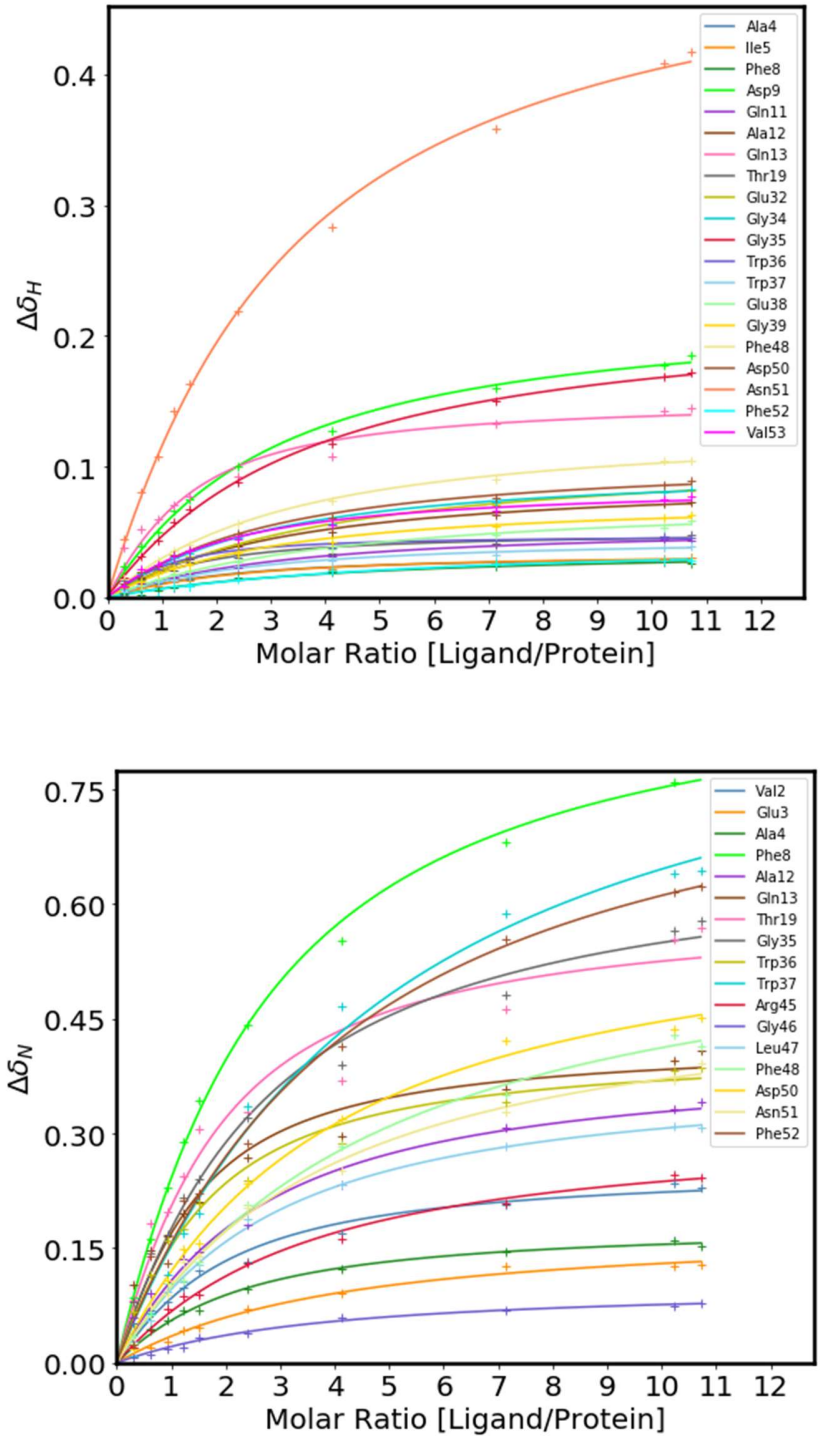

Figure Appendix-E-4: Binding isotherms of the NMR titration of SLP65-PRM4 to ^{15}N-SH3A. Individual K_Ds for both ^{1}H and ^{15}N CS were obtain by fits to equation S1. The global K_D was calculated as the mean of the individual ^{1}H and ^{15}N K_Ds. Representative isotherms for ^{1}H CSP (top) and ^{15}N CSP (bottom) are shown.

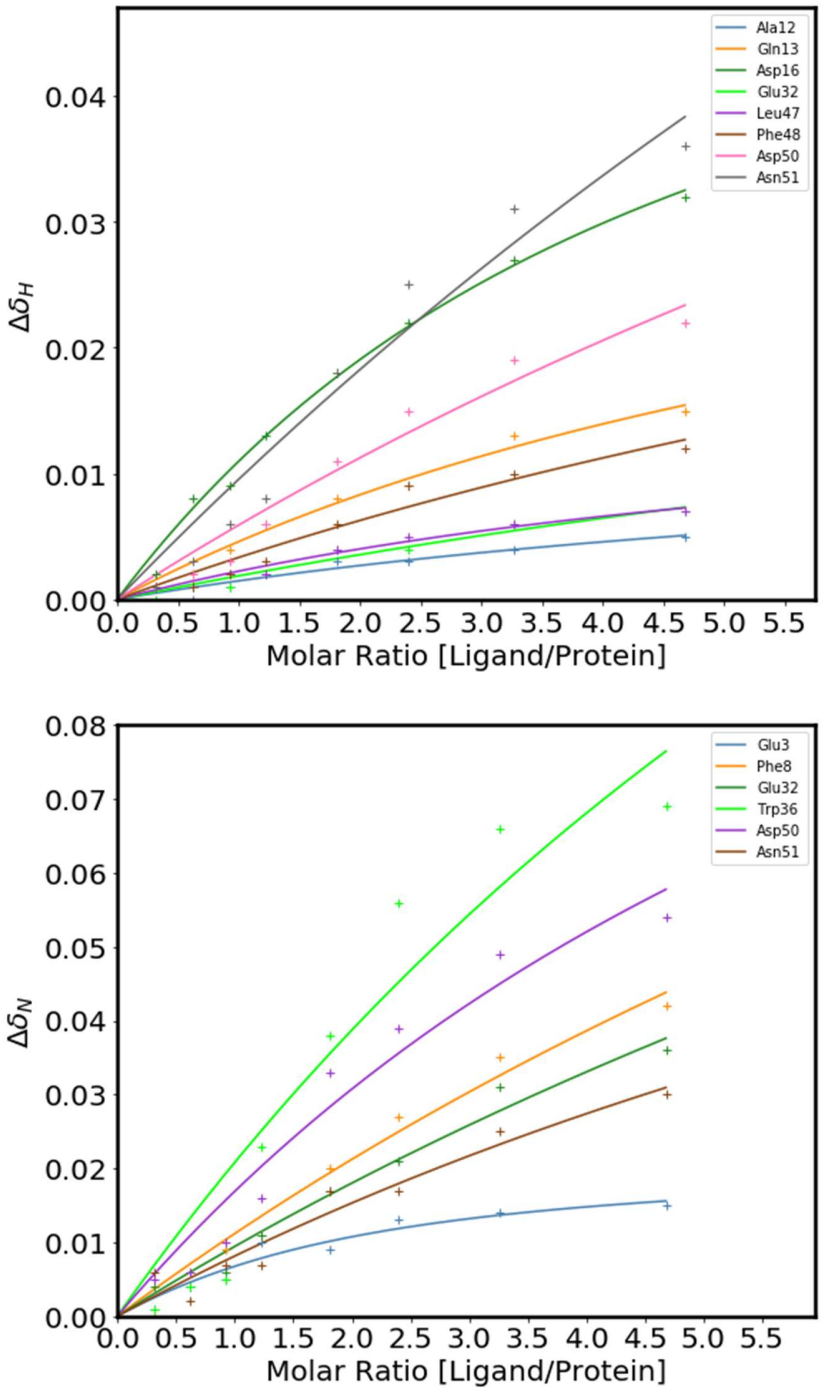

Figure Appendix-E-5: Binding isotherms of the NMR titration of SLP65-PRM* to ^{15}N-SH3A. Individual K_Ds for both ^{1}H and ^{15}N CS were obtain by fits to equation S1. The global K_D was calculated as the mean of the individual ^{1}H and ^{15}N K_Ds. Representative isotherms for ^{1}H CSP (top) and ^{15}N CSP (bottom) are shown.

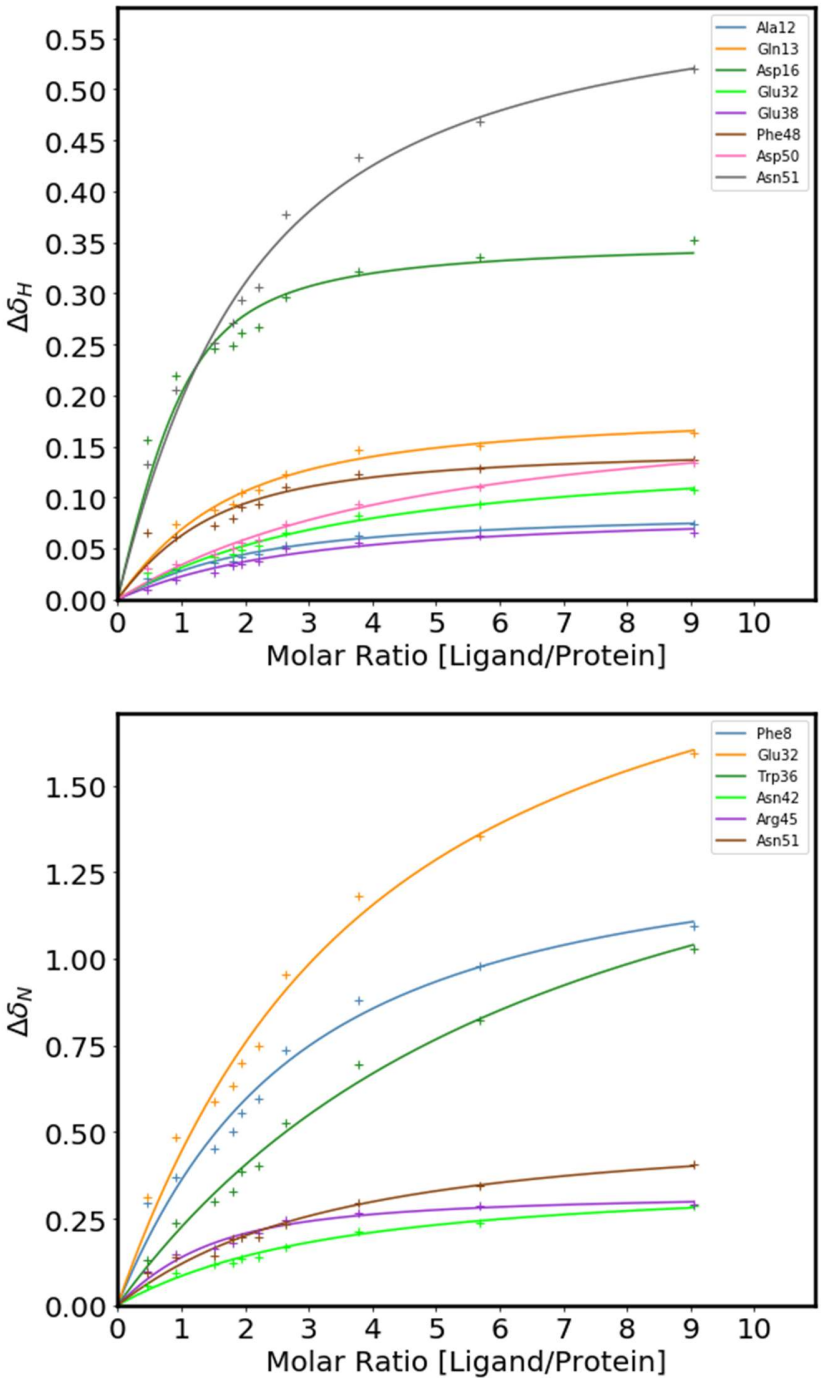

Figure Appendix-E-6: Binding isotherms of the NMR titration of SLP65-PRM5 to ^{15}N-SH3A. Individual K_Ds for both ^{1}H and ^{15}N CS were obtain by fits to equation S1. The global K_D was calculated as the mean of the individual ^{1}H and ^{15}N K_Ds. Representative isotherms for ^{1}H CSP (top) and ^{15}N CSP (bottom) are shown.

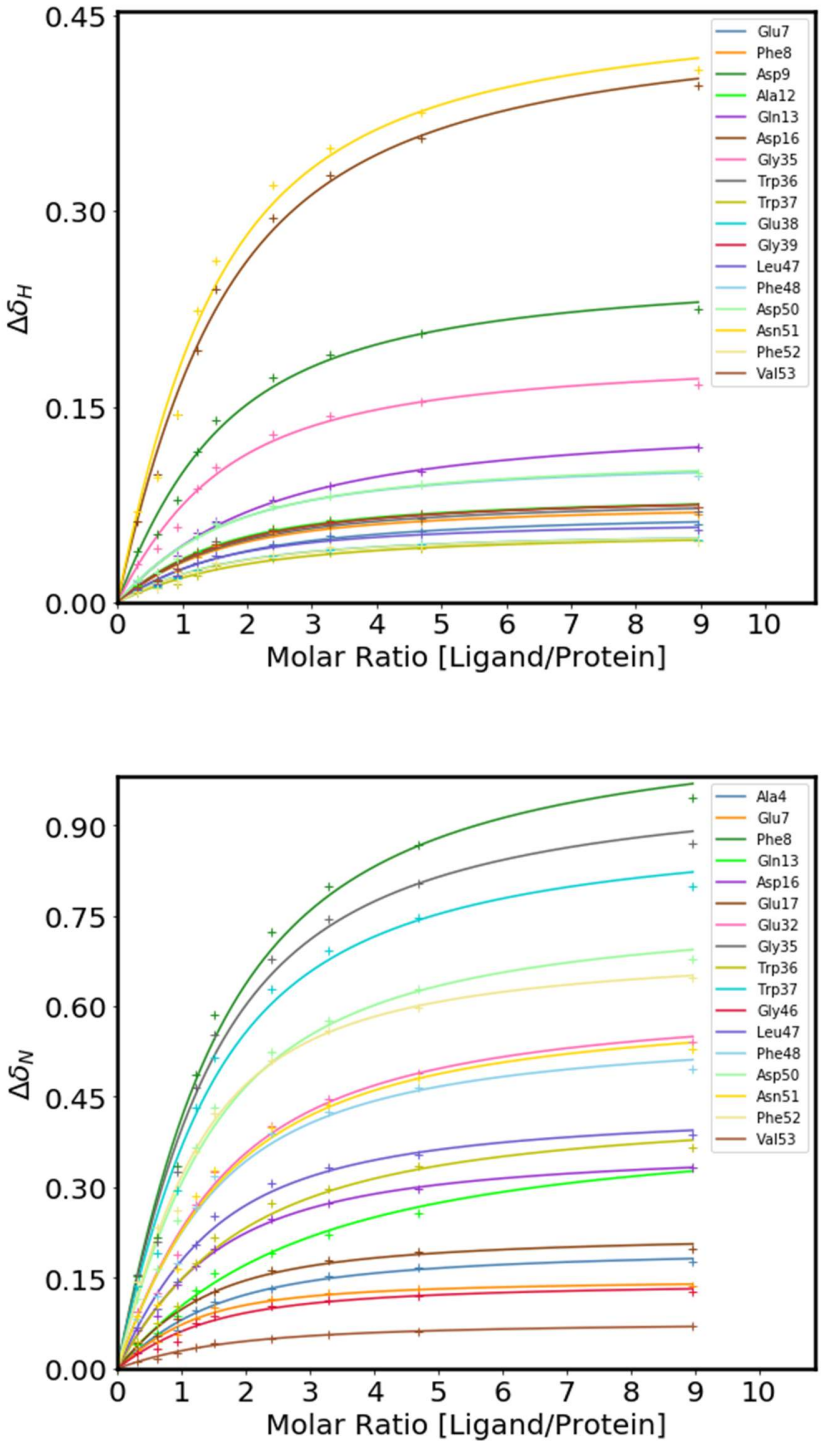

Figure Appendix-E-7: Binding isotherms of the NMR titration of SLP65-PRM6 to ^{15}N-SH3A. Individual K_Ds for both ^{1}H and ^{15}N CS were obtain by fits to equation S1. The global K_D was calculated as the mean of the individual ^{1}H and ^{15}N K_Ds. Representative isotherms for ^{1}H CSP (top) and ^{15}N CSP (bottom) are shown.

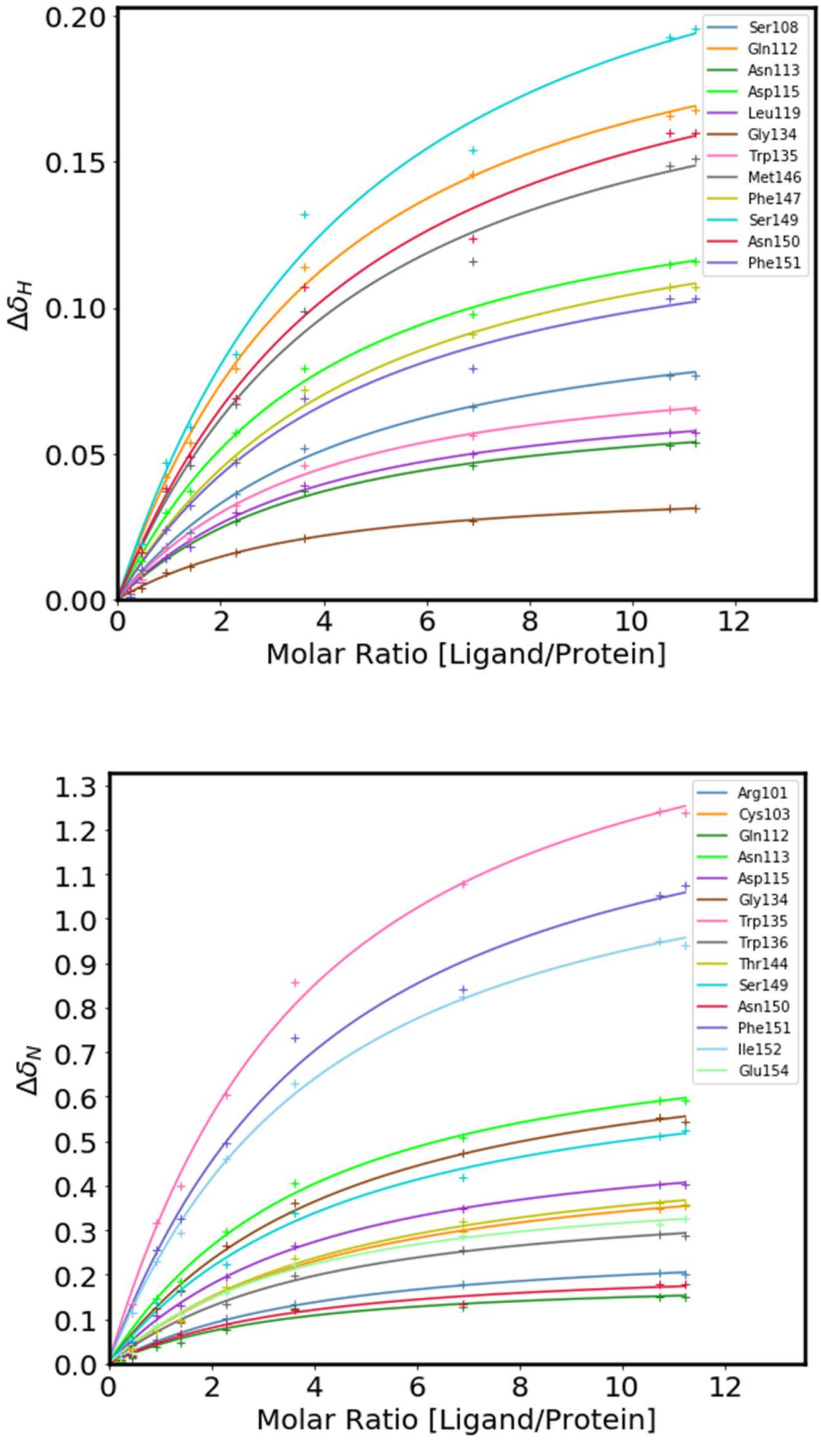

Figure Appendix-E-8: Binding isotherms of the NMR titration of CIN85-PRM2 to ^{15}N-SH3A. Individual K_Ds for both ^{1}H and ^{15}N CS were obtain by fits to equation S1. The global K_D was calculated as the mean of the individual ^{1}H and ^{15}N K_Ds. Representative isotherms for ^{1}H CSP (top) and ^{15}N CSP (bottom) are shown.

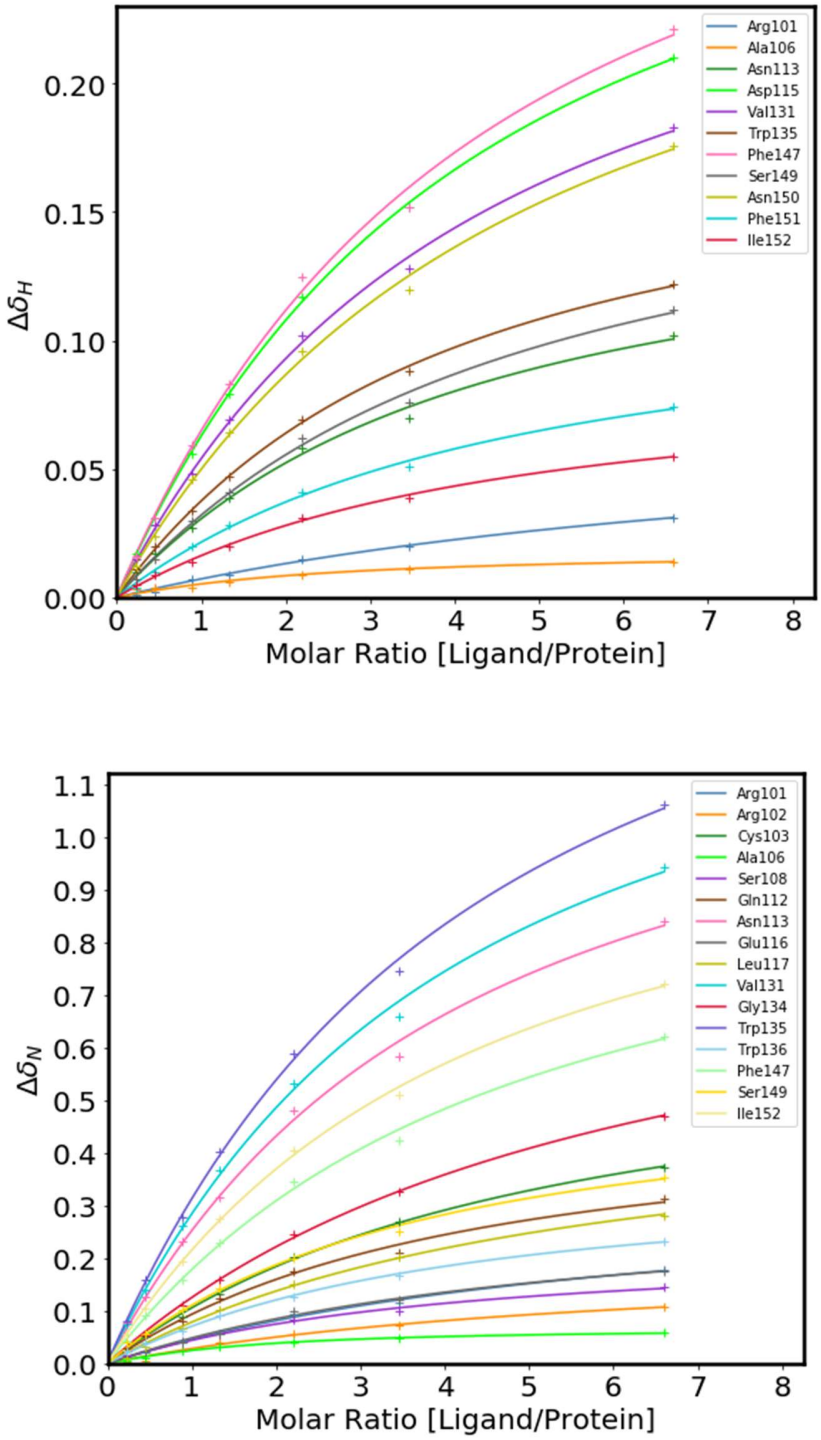

Figure Appendix-E-9: Binding isotherms of the NMR titration of CIN85-PRM3 to ^{15}N-SH3A. Individual K_Ds for both ^{1}H and ^{15}N CS were obtain by fits to equation S1. The global K_D was calculated as the mean of the individual ^{1}H and ^{15}N K_Ds. Representative isotherms for ^{1}H CSP (top) and ^{15}N CSP (bottom) are shown.

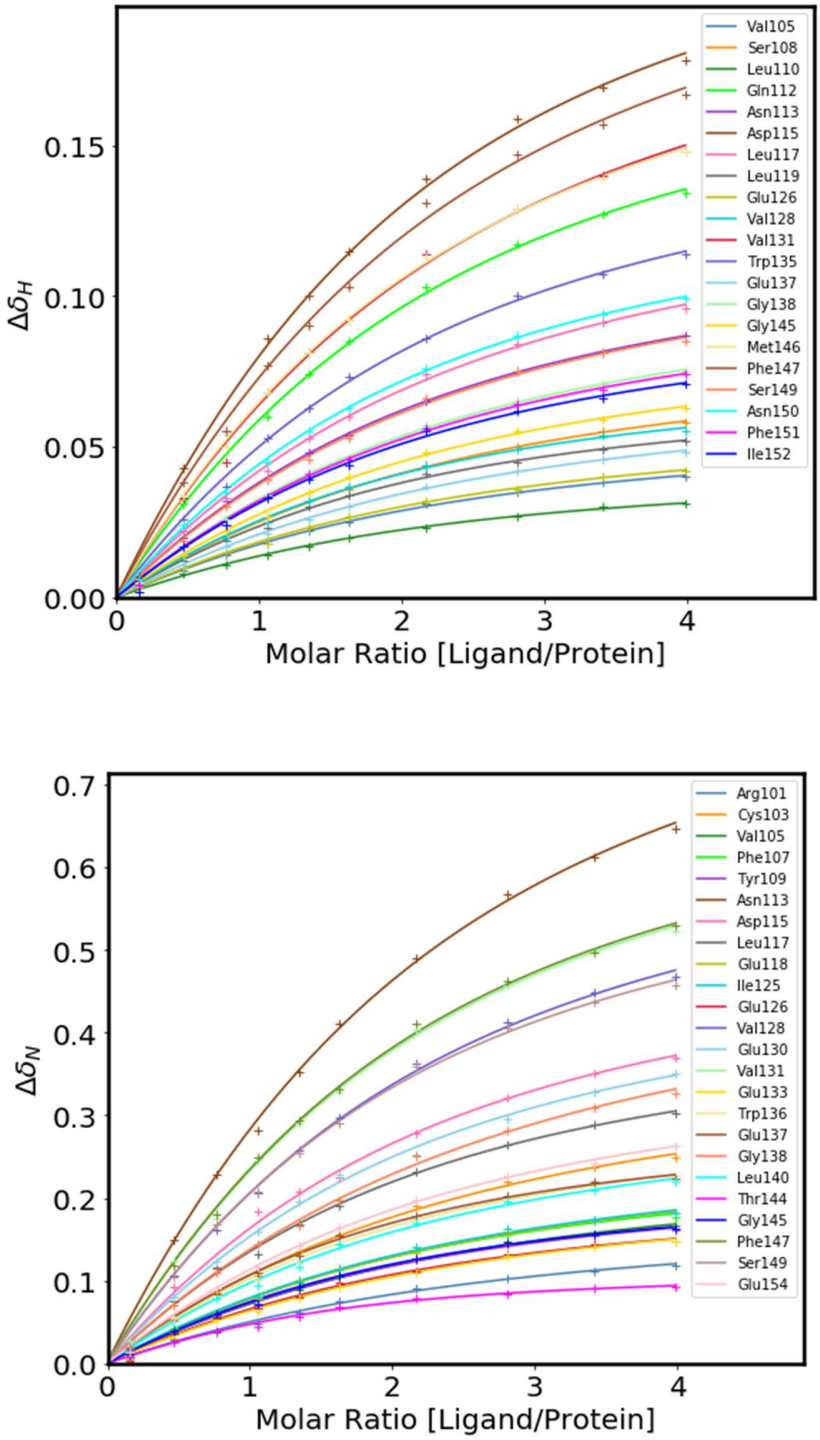

Figure Appendix-E-10: Binding isotherms of the NMR titration of SLP65-PRM1 to ^{15}N-SH3B. Individual K_Ds for both ^{1}H and ^{15}N CS were obtain by fits to equation S1. The global K_D was calculated as the mean of the individual ^{1}H and ^{15}N K_Ds. Representative isotherms for ^{1}H CSP (top) and ^{15}N CSP (bottom) are shown.

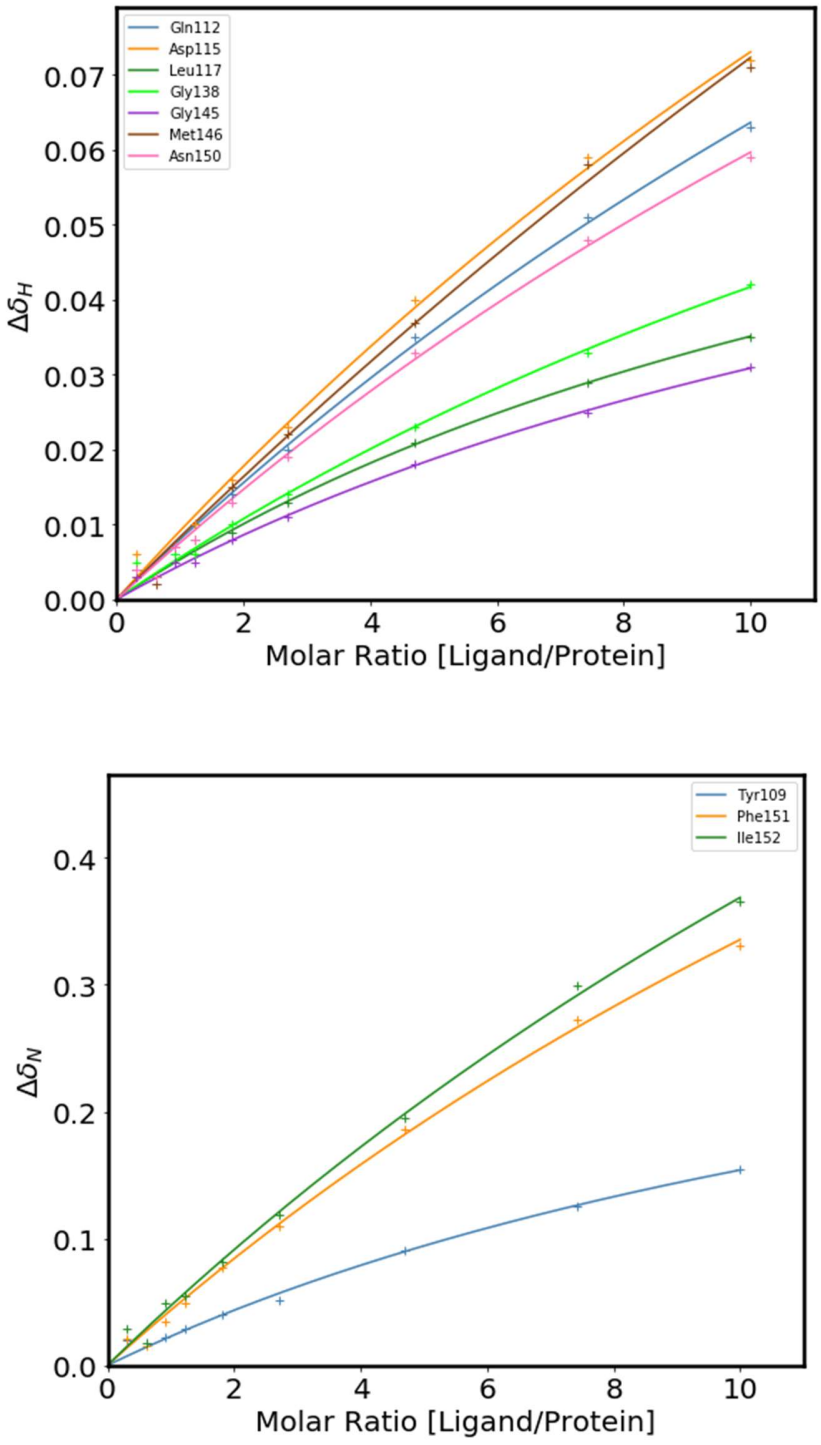

Figure Appendix-E-11: Binding isotherms of the NMR titration of SLP65-PRM2 to ^{15}N-SH3B. Individual K_Ds for both ^{1}H and ^{15}N CS were obtain by fits to equation S1. The global K_D was calculated as the mean of the individual ^{1}H and ^{15}N K_Ds. Representative isotherms for ^{1}H CSP (top) and ^{15}N CSP (bottom) are shown.

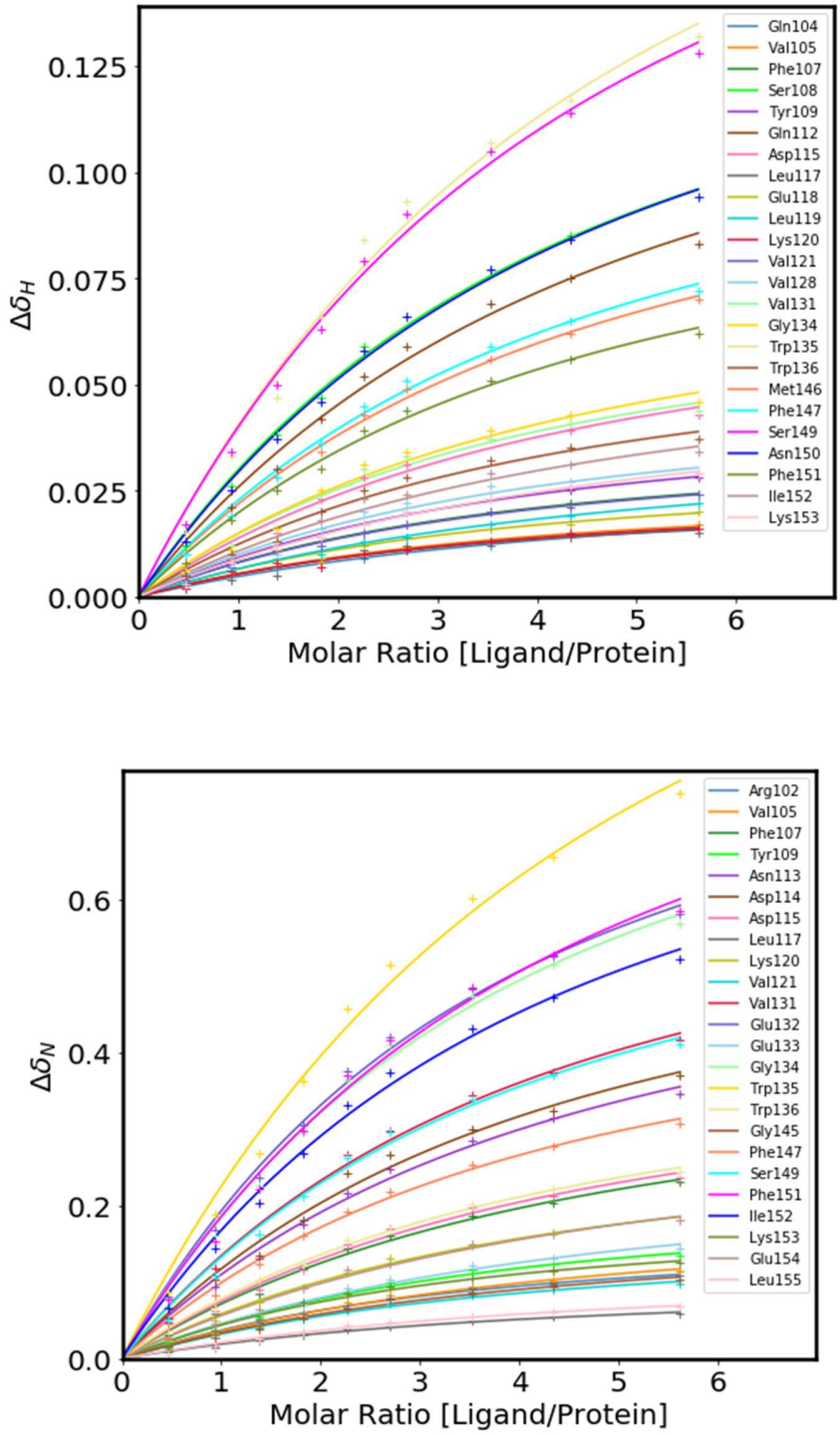

Figure Appendix-E-12: Binding isotherms of the NMR titration of SLP65-PRM3 to ^{15}N-SH3B. Individual K_Ds for both ^{1}H and ^{15}N CS were obtain by fits to equation S1. The global K_D was calculated as the mean of the individual ^{1}H and ^{15}N K_Ds. Representative isotherms for ^{1}H CSP (top) and ^{15}N CSP (bottom) are shown.

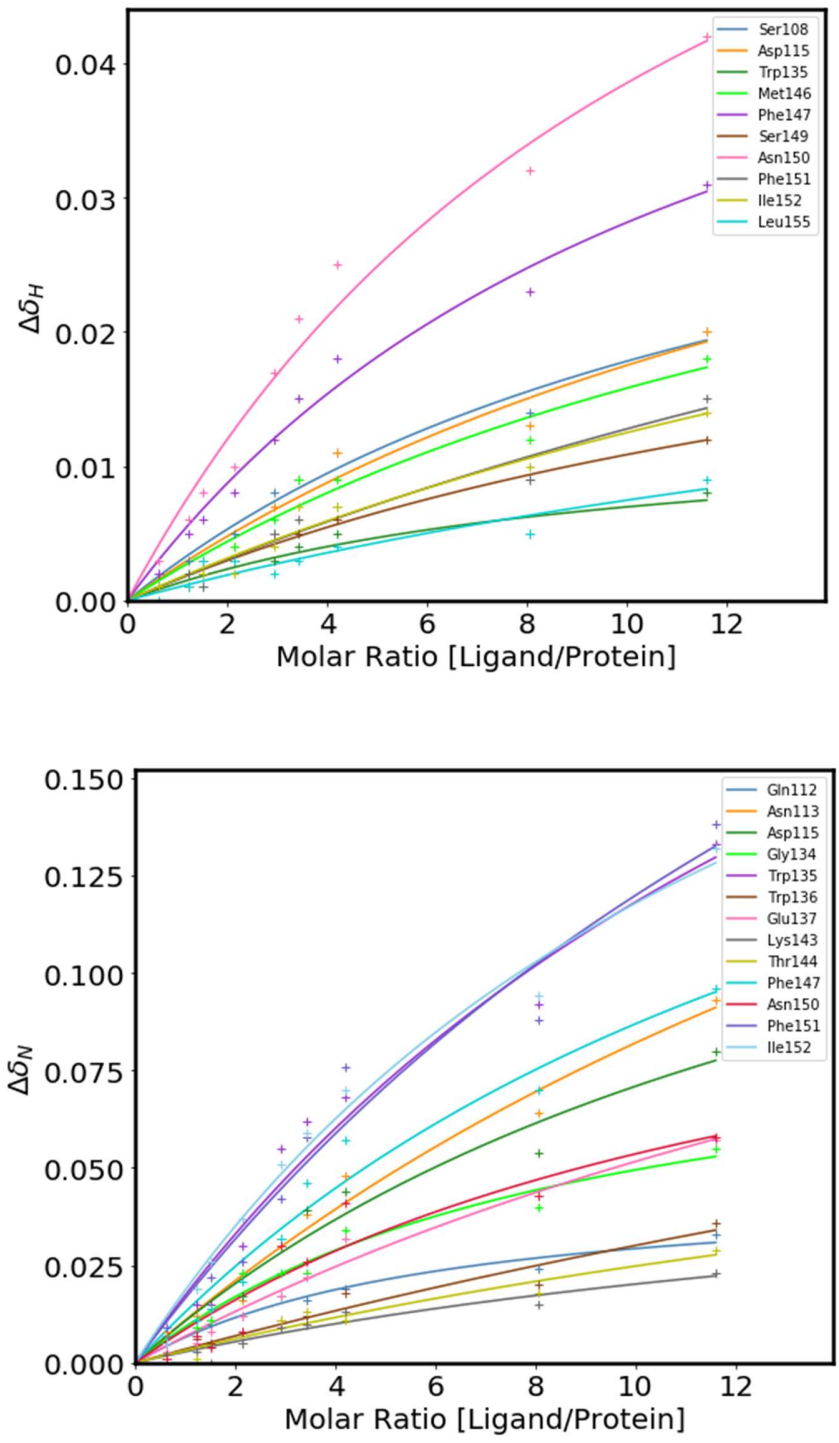

Figure Appendix-E-13: Binding isotherms of the NMR titration of SLP65-PRM* to ^{15}N-SH3B. Individual K_Ds for both ^{1}H and ^{15}N CS were obtain by fits to equation S1. The global K_D was calculated as the mean of the individual ^{1}H and ^{15}N K_Ds. Representative isotherms for ^{1}H CSP (top) and ^{15}N CSP (bottom) are shown.

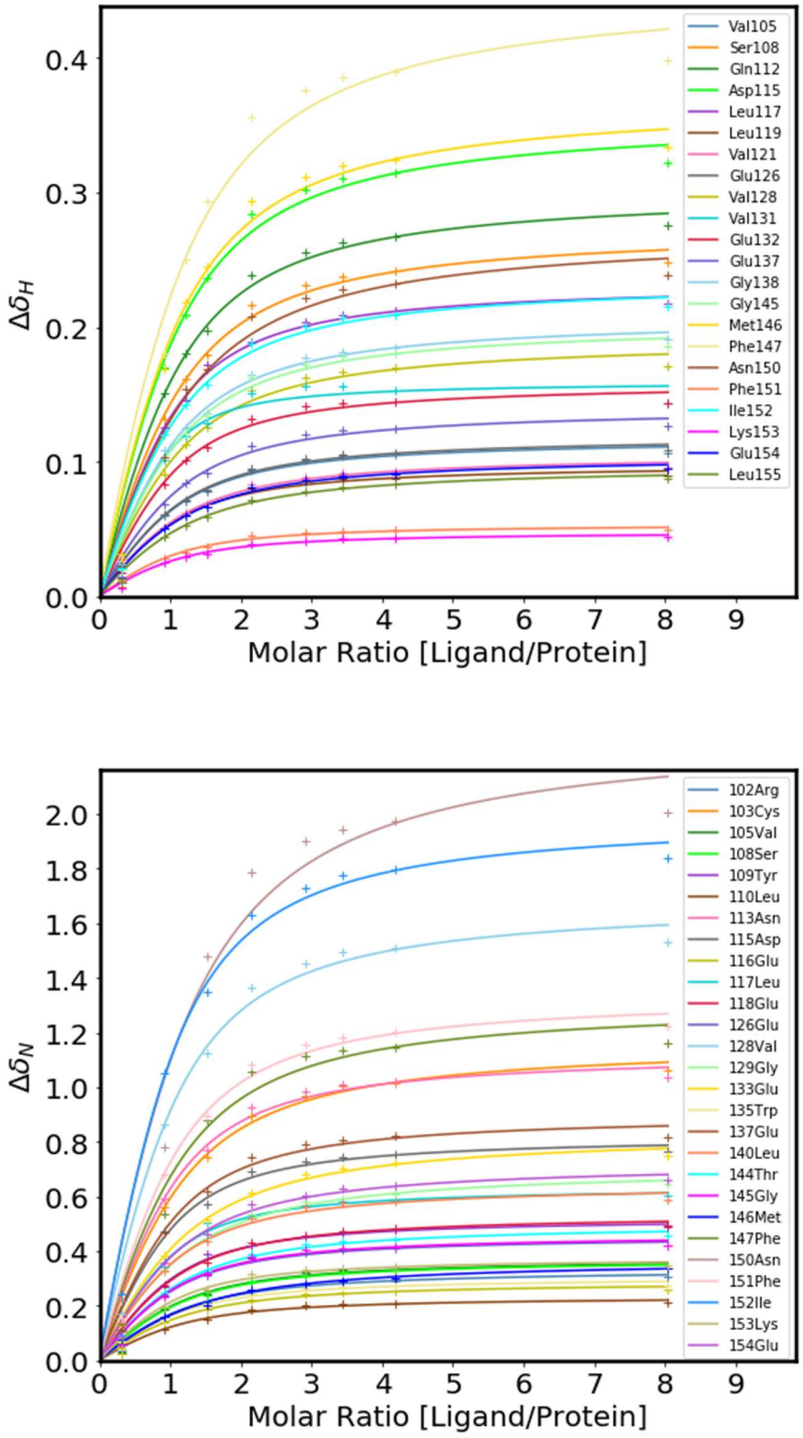

Figure Appendix-E-14: Binding isotherms of the NMR titration of SLP65-PRM5 to ^{15}N-SH3B. Individual K_Ds for both ^{1}H and ^{15}N CS were obtain by fits to equation S1. The global K_D was calculated as the mean of the individual ^{1}H and ^{15}N K_Ds. Representative isotherms for ^{1}H CSP (top) and ^{15}N CSP (bottom) are shown.

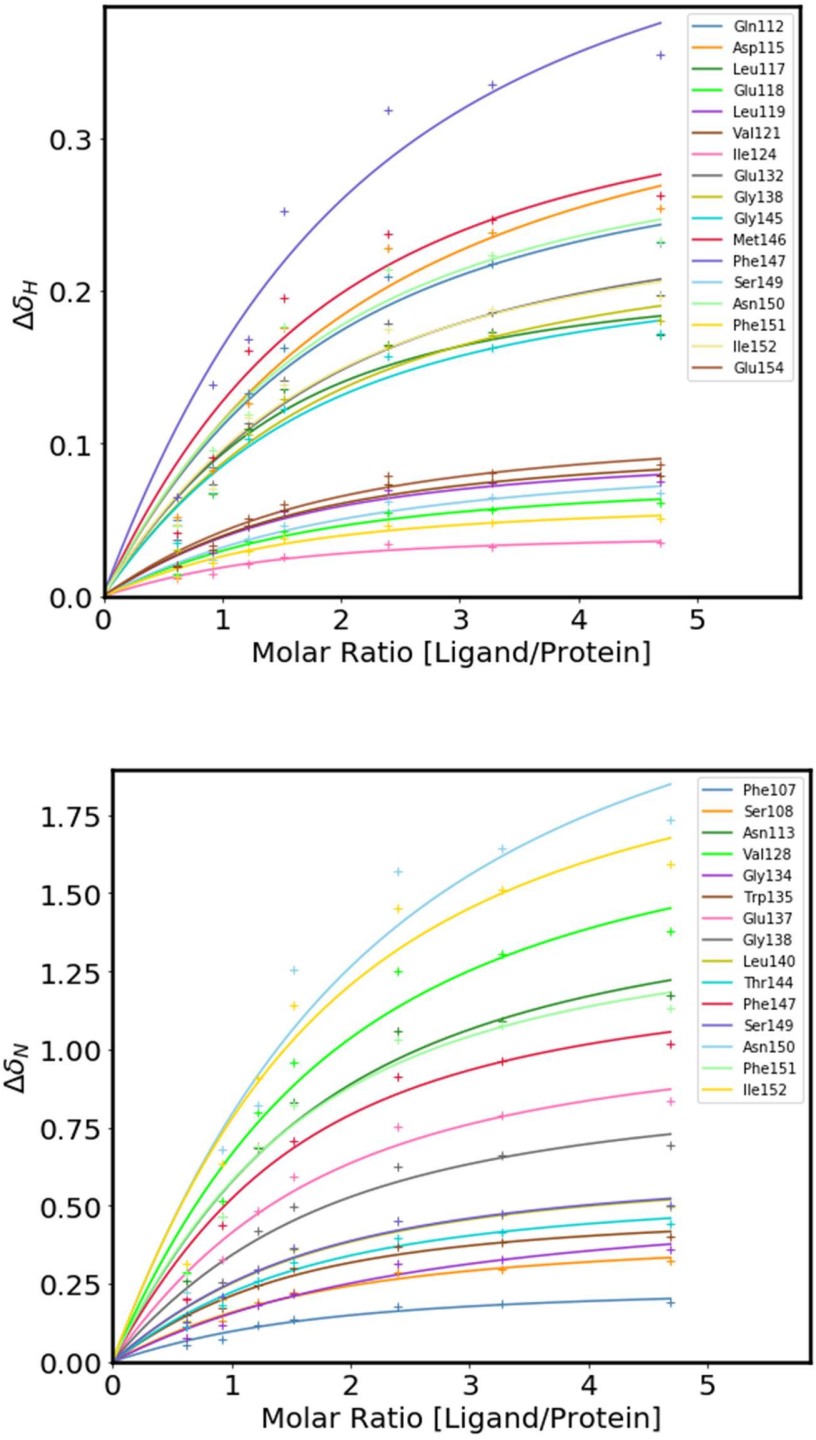

Figure Appendix-E-15: Binding isotherms of the NMR titration of SLP65-PRM6 to ^{15}N-SH3B. Individual K_Ds for both ^{1}H and ^{15}N CS were obtain by fits to equation S1. The global K_D was calculated as the mean of the individual ^{1}H and ^{15}N K_Ds. Representative isotherms for ^{1}H CSP (top) and ^{15}N CSP (bottom) are shown.

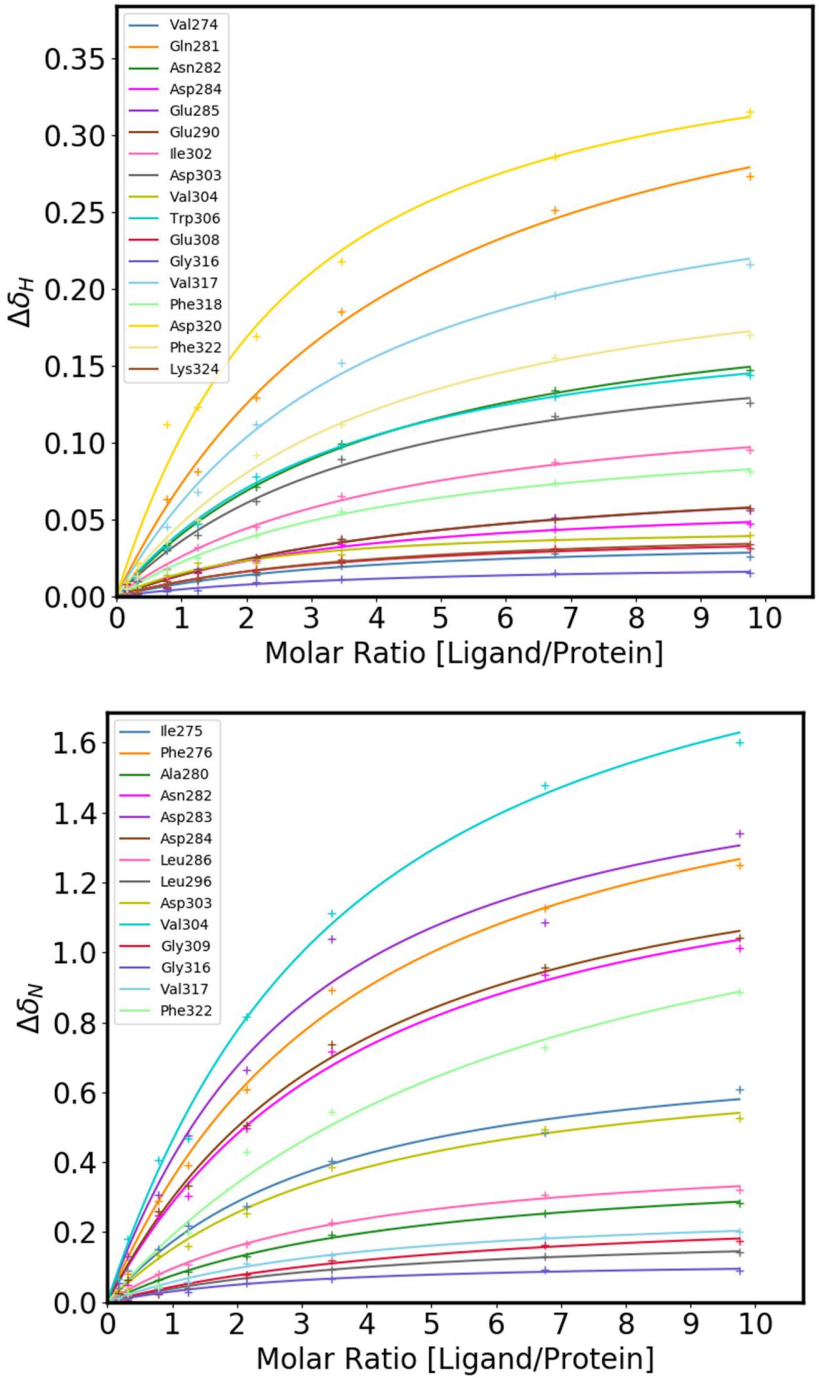

Figure Appendix-E-16: Binding isotherms of the NMR titration of CIN85-PRM2 to ^{15}N-SH3B. Individual K_Ds for both ^{1}H and ^{15}N CS were obtain by fits to equation S1. The global K_D was calculated as the mean of the individual ^{1}H and ^{15}N K_Ds. Representative isotherms for ^{1}H CSP (top) and ^{15}N CSP (bottom) are shown.

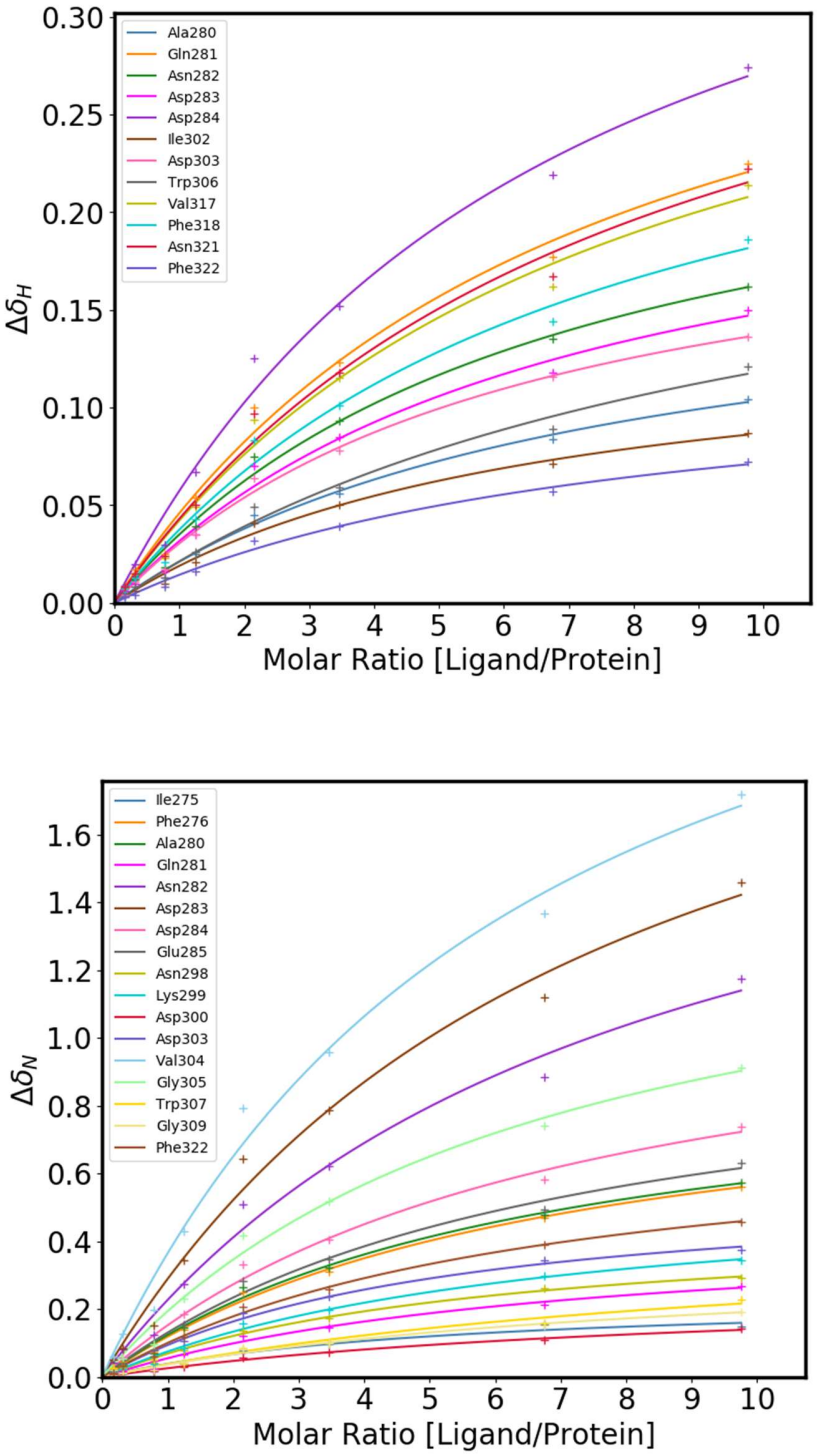

Figure Appendix-E-17: Binding isotherms of the NMR titration of CIN85-PRM3 to ^{15}N-SH3B. Individual K_Ds for both ^{1}H and ^{15}N CS were obtain by fits to equation S1. The global K_D was calculated as the mean of the individual ^{1}H and ^{15}N K_Ds. Representative isotherms for ^{1}H CSP (top) and ^{15}N CSP (bottom) are shown.

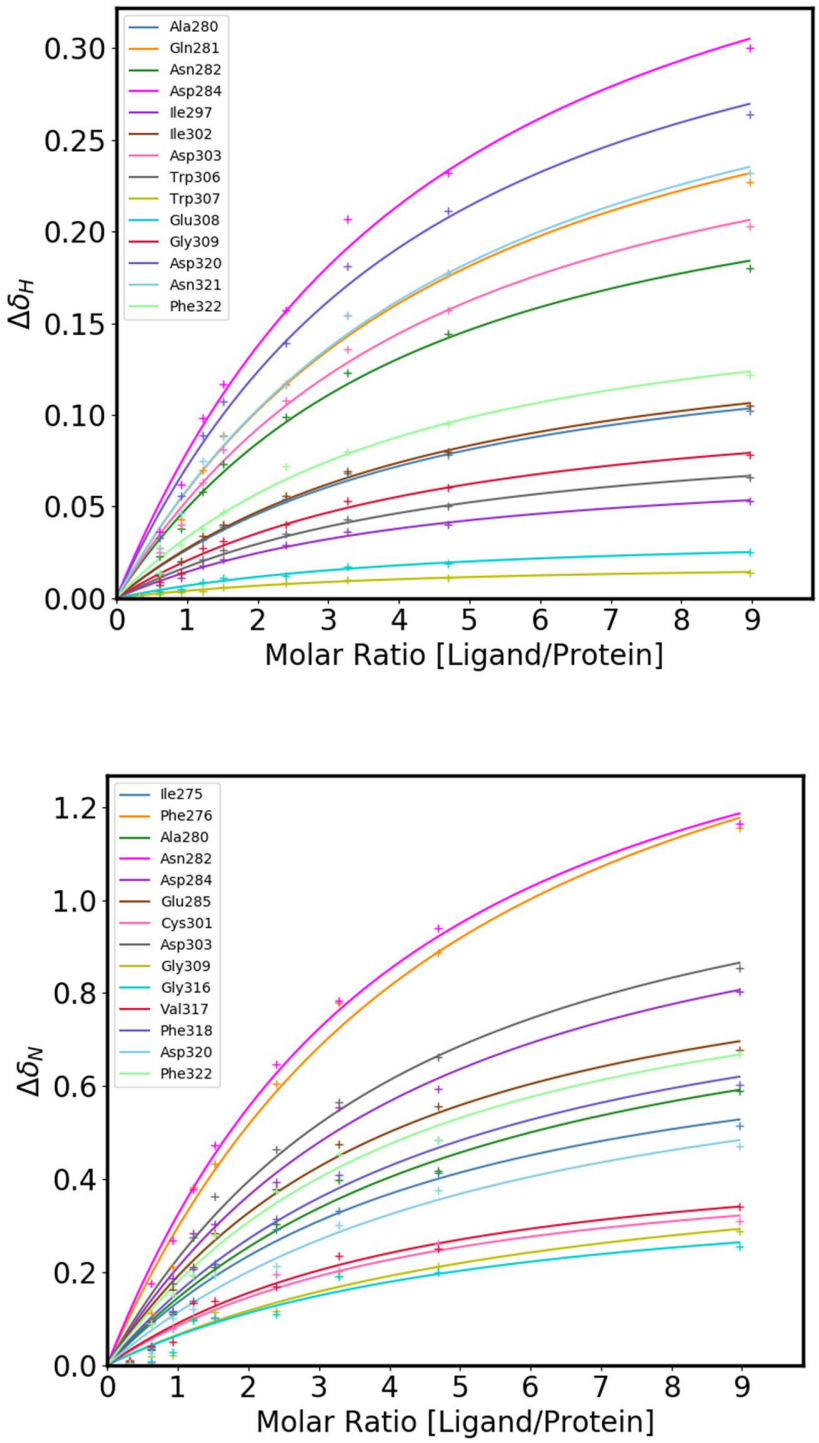

Figure Appendix-E-18: Binding isotherms of the NMR titration of SLP65-PRM1 to ^{15}N-SH3C. Individual K_Ds for both ^{1}H and ^{15}N CS were obtain by fits to equation S1. The global K_D was calculated as the mean of the individual ^{1}H and ^{15}N K_Ds. Representative isotherms for ^{1}H CSP (top) and ^{15}N CSP (bottom) are shown.

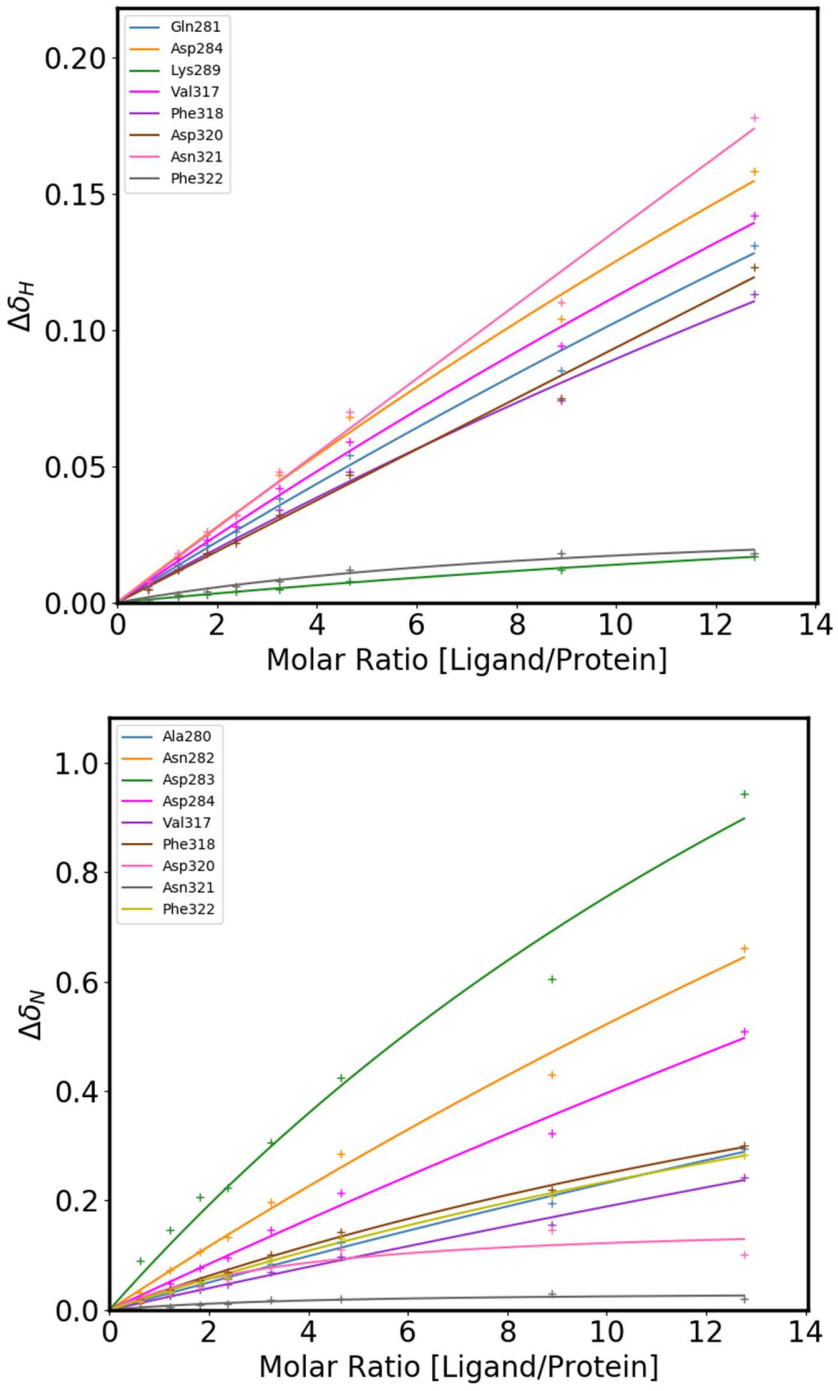

Figure Appendix-E-19: Binding isotherms of the NMR titration of SLP65-PRM2 to ^{15}N-SH3C. Binding isotherms of both ^{1}H (top) and ^{15}N (bottom) chemical shifts were fitted to equation S1. No K_D was obtained, since the fitting error was too large.

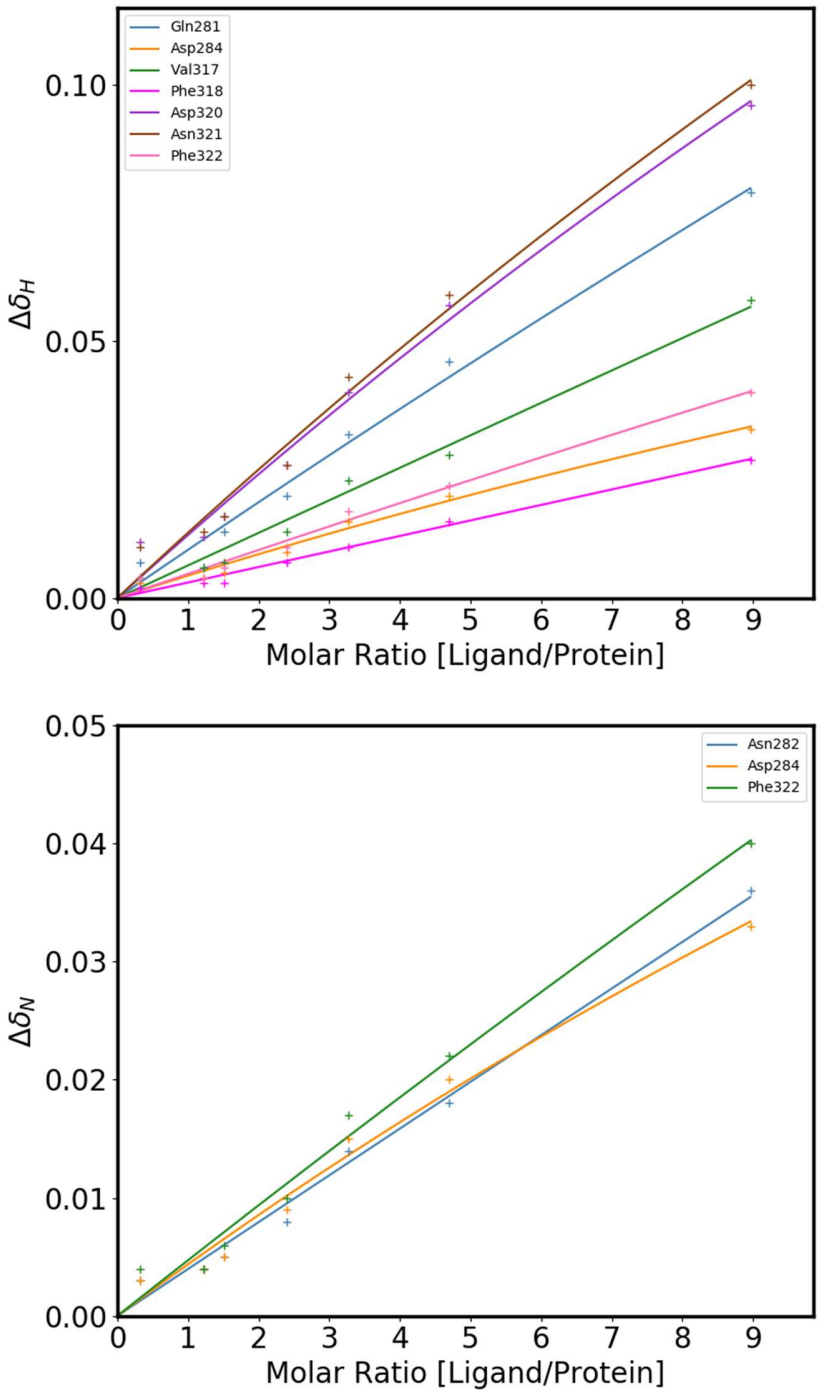

Figure Appendix-E-20: Binding isotherms of the NMR titration of SLP65-PRM3 to ^{15}N-SH3C. Binding isotherms of both ^{1}H (top) and ^{15}N (bottom) chemical shifts were fitted to equation S1. No K_D was obtained, since the fitting error was too large.

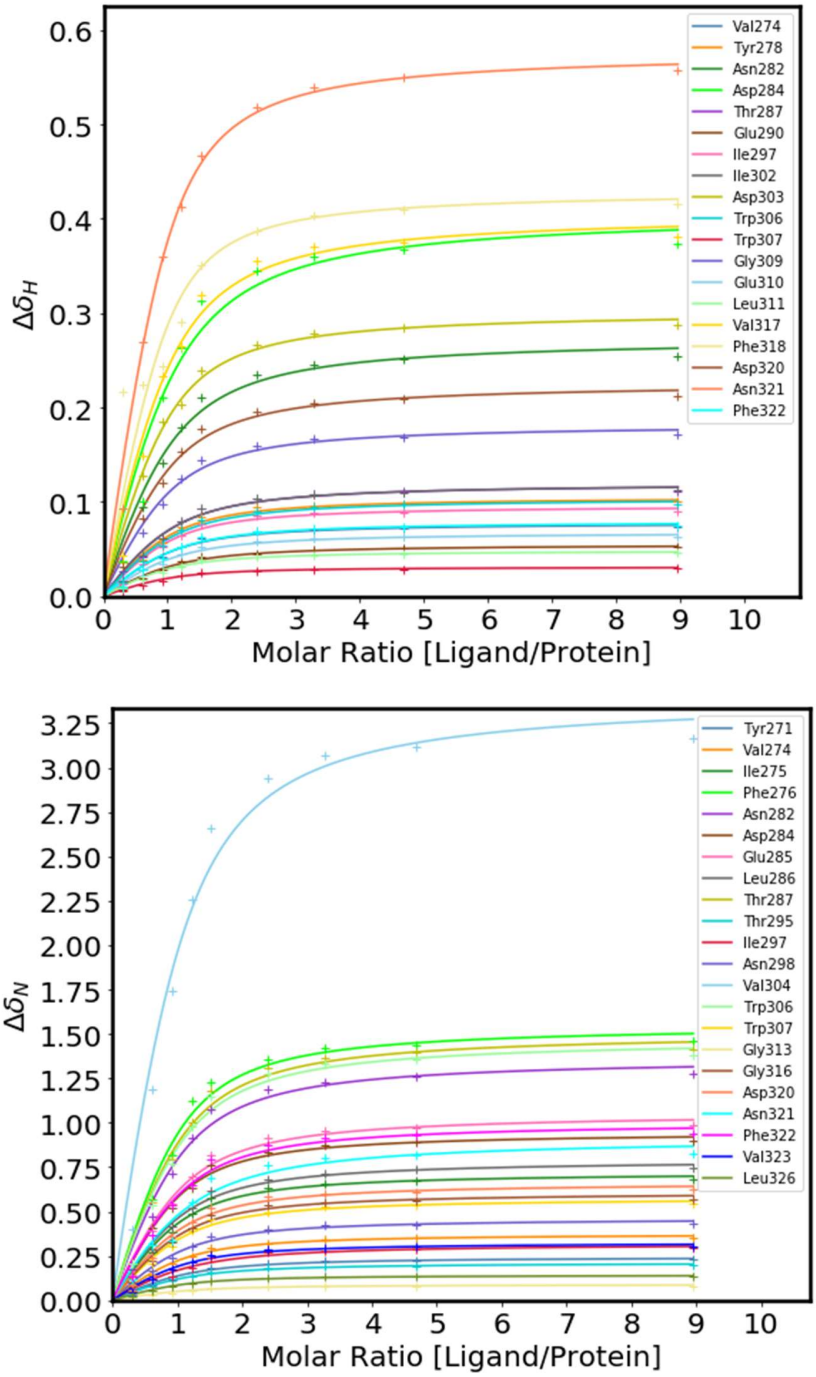

Figure Appendix-E-21: Binding isotherms of the NMR titration of SLP65-PRM4 to ^{15}N-SH3C. Individual K_Ds for both ^{1}H and ^{15}N CS were obtain by fits to equation S1. The global K_D was calculated as the mean of the individual ^{1}H and ^{15}N K_Ds. Representative isotherms for ^{1}H CSP (top) and ^{15}N CSP (bottom) are shown.

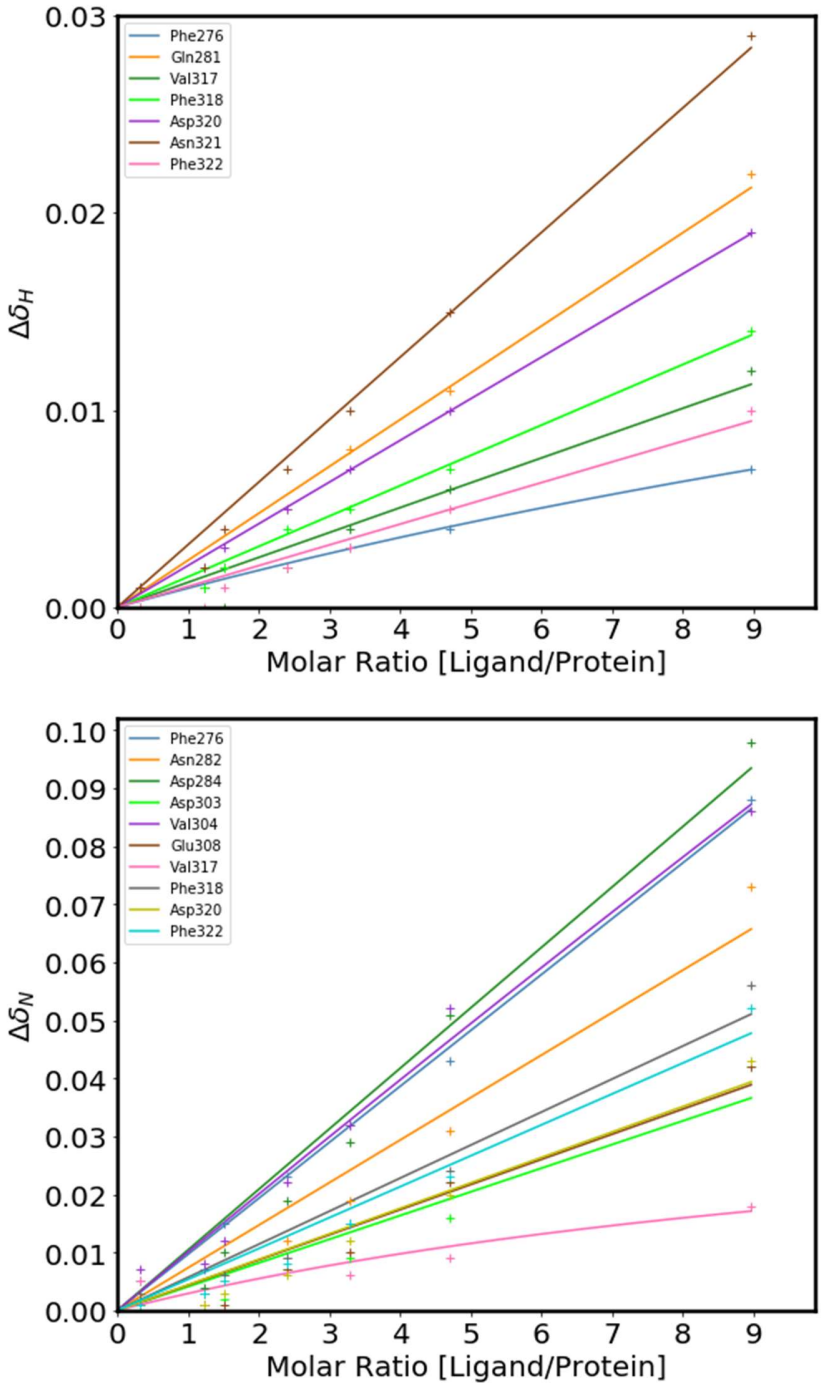

Figure Appendix-E-22: Binding isotherms of the NMR titration of SLP65-PRM* to ^{15}N-SH3C. Binding isotherms of both ^{1}H (top) and ^{15}N (bottom) chemical shifts were fitted to equation S1. No K_D was obtained, since the fitting error was too large. ^{1}H CSPs were < 0.03 ppm (top) and ^{15}N CSP were smaller than 0.1 ppm (bottom).

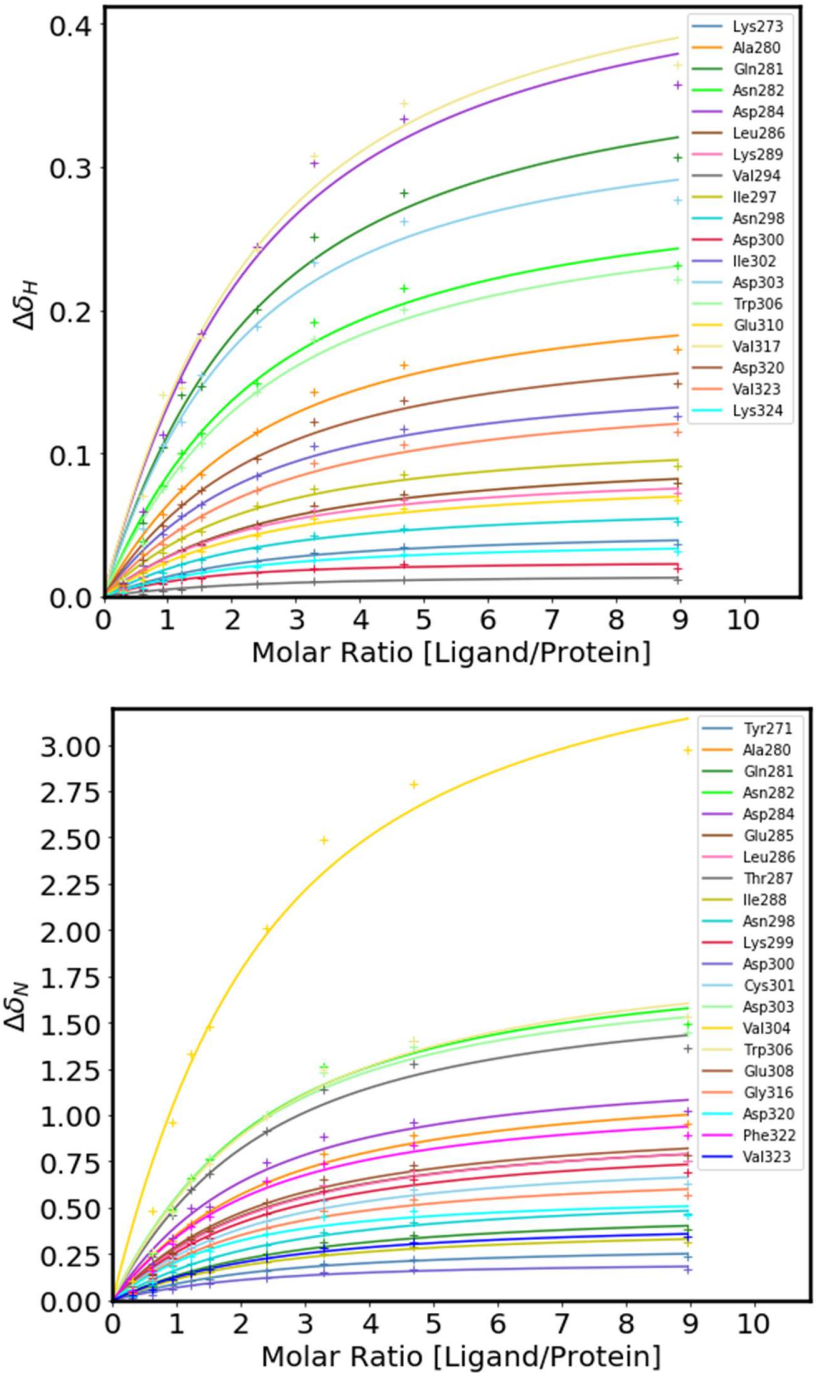

Figure Appendix-E-23: Binding isotherms of the NMR titration of SLP65-PRM5 to ^{15}N-SH3C. Individual K_Ds for both ^{1}H and ^{15}N CS were obtain by fits to equation S1. The global K_D was calculated as the mean of the individual ^{1}H and ^{15}N K_Ds. Representative isotherms for ^{1}H CSP (top) and ^{15}N CSP (bottom) are shown.

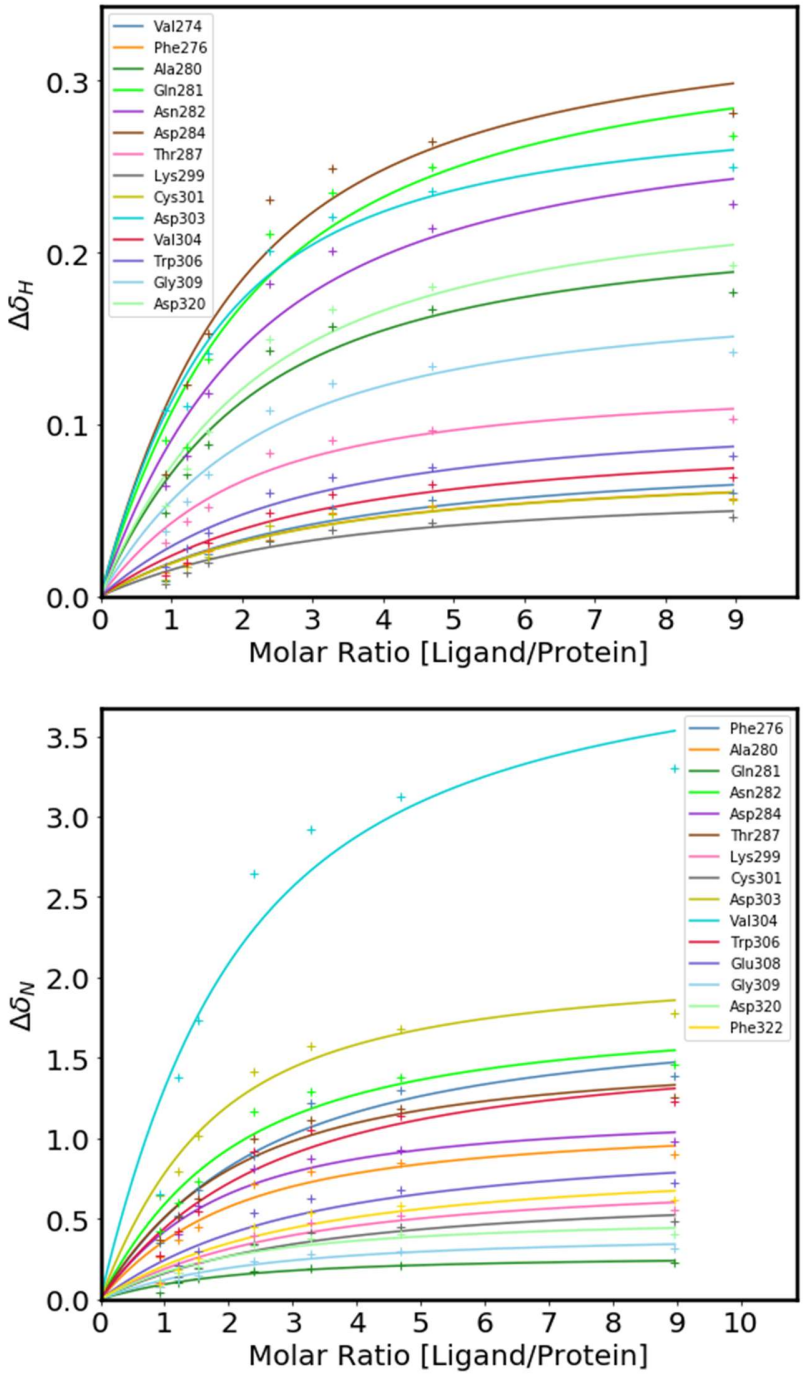

Figure Appendix-E-24: Binding isotherms of the NMR titration of SLP65-PRM6 to ^{15}N-SH3C. Individual K_Ds for both ^{1}H and ^{15}N CS were obtain by fits to equation S1. The global K_D was calculated as the mean of the individual ^{1}H and ^{15}N K_Ds. Representative isotherms for ^{1}H CSP (top) and ^{15}N CSP (bottom) are shown.

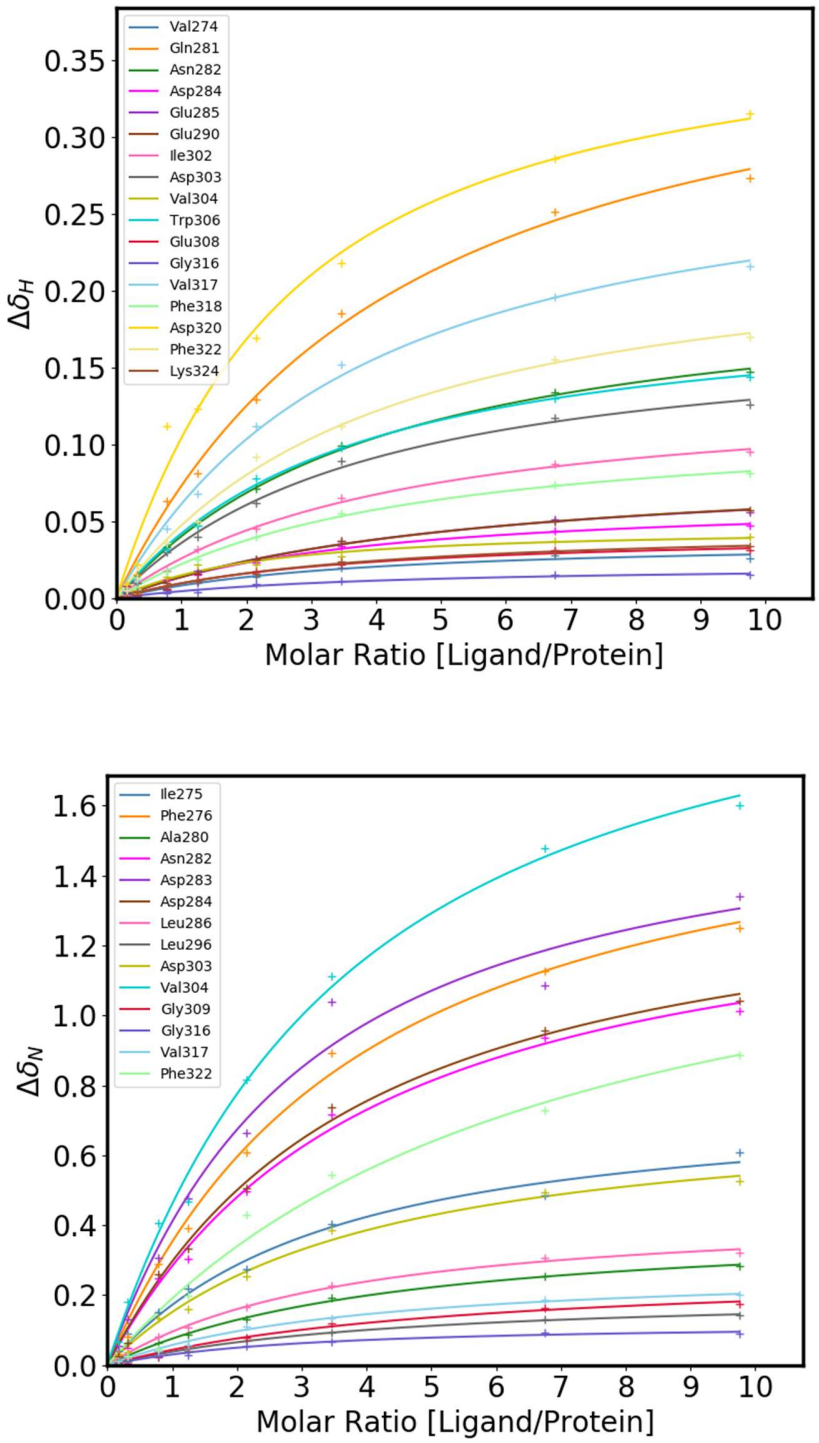

Figure Appendix-E-25: Binding isotherms of the NMR titration of CIN85-PRM2 to ^{15}N-SH3C. Individual K_Ds for both ^{1}H and ^{15}N CS were obtain by fits to equation S1. The global K_D was calculated as the mean of the individual ^{1}H and ^{15}N K_Ds. Representative isotherms for ^{1}H CSP (top) and ^{15}N CSP (bottom) are shown.

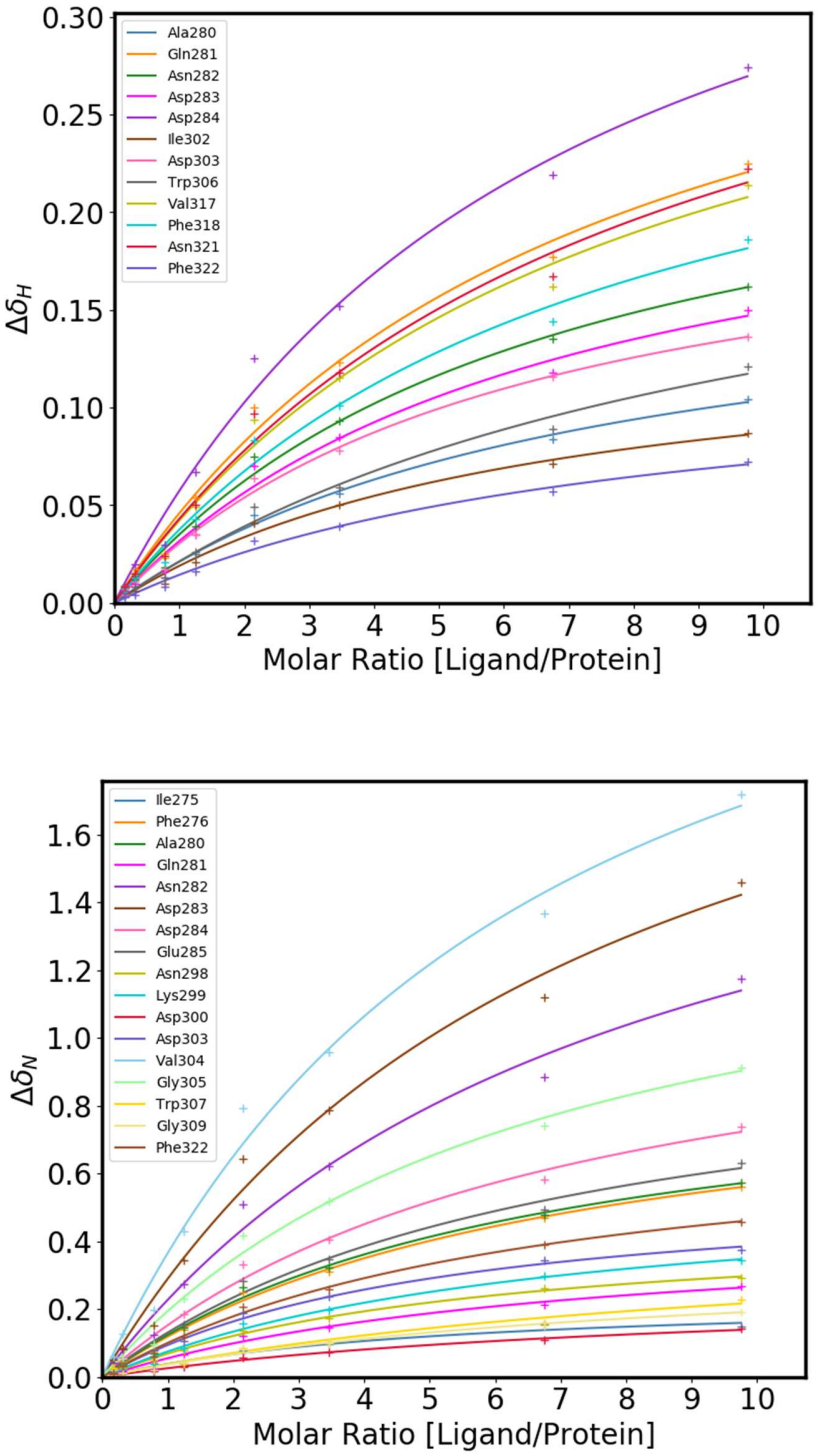

Figure Appendix-E-26: Binding isotherms of the NMR titration of CIN85-PRM3 to ^{15}N-SH3C. Individual K_Ds for both ^{1}H and ^{15}N CS were obtain by fits to equation S1. The global K_D was calculated as the mean of the individual ^{1}H and ^{15}N K_Ds. Representative isotherms for ^{1}H CSP (top) and ^{15}N CSP (bottom) are shown.

Appendix F: PRM4-R247 mutation drastically reduces affinity for SH3B

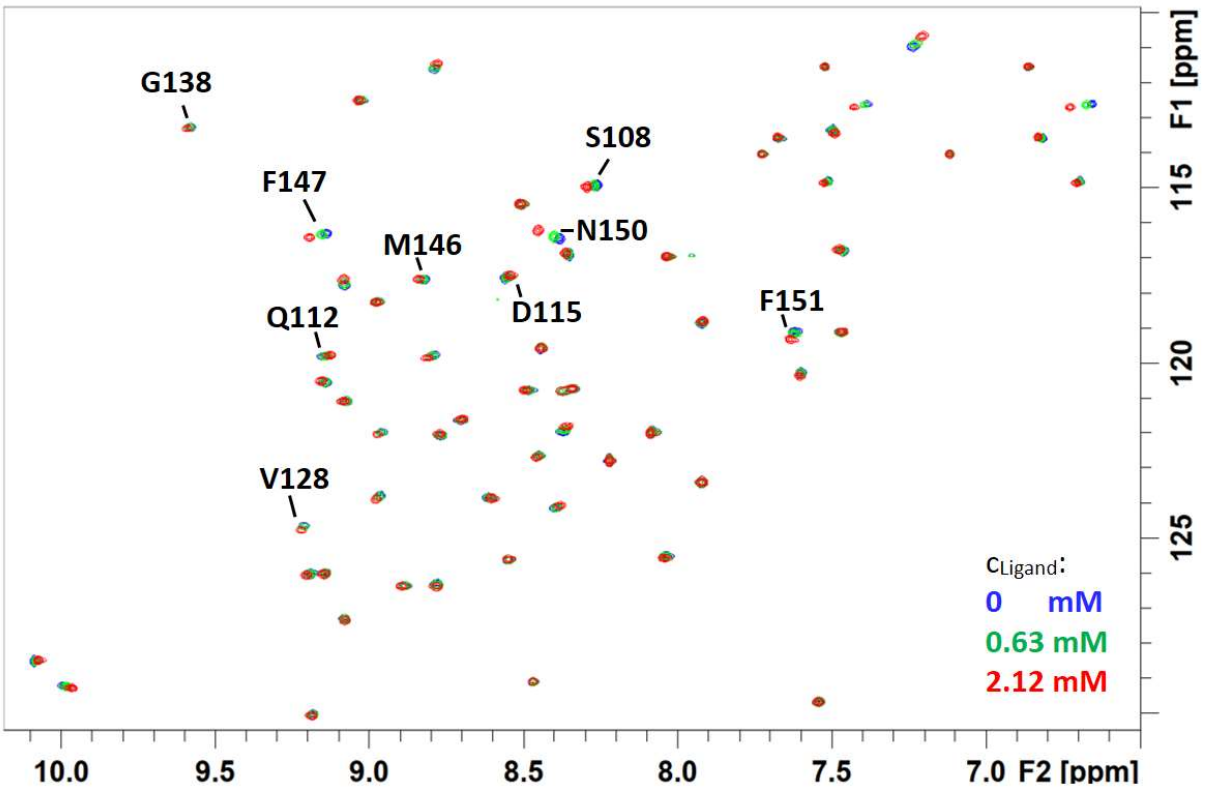

Figure Appendix-F: Overlaid ^{15}N-HSQC spectra of titrations of SLP65-PRM4-R247A peptide to ^{15}N-SH3B. The CSP of the titration were too small for an accurate fitting with a K_D > 10 mM. The dissociation constant K_D = 7 µM of the interaction of SLP65-PRM4 with SH3B was determined previously (Figure 23). The binding is almost completely abolished by the R247A mutation in PRM4.

Appendix G: Test binding of SLP65 to profilin-1

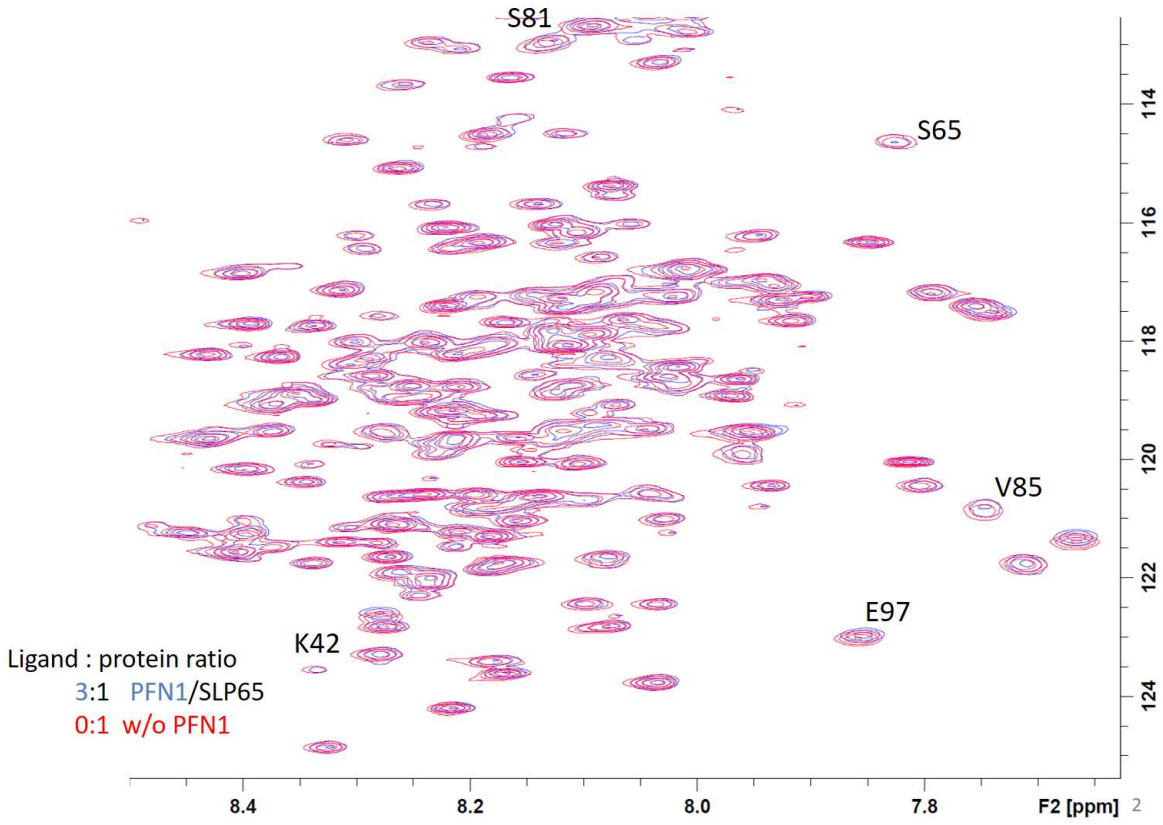

Figure Appendix-G: The titration of PFN1 to ^{15}N-labeld SLP65$_{40\text{-}330}$ was monitored by HSQC spectra. The potential binding of actin regulator PFN1 with SLP65 was checked by an NMR titration experiment. HSQC titration spectra of ^{15}N-labeld SLP65$_{40\text{-}330}$ without ligand (red) and with 3:1 PFN1/^{15}N- SLP65$_{40\text{-}330}$ (blue) are overlaid. No significant change of chemical shift was observed, which indicates that the PFN1 is not binding to SLP65's disordered region a.a. 40 – 330.

Appendix H: 1D chemical shift *vs* 2D lineshape analysis

^{1}H and ^{15}N chemical shifts were fitted to equation:

$$\Delta CS_{obs} = \Delta CS_{max} * \frac{(R_t + L_t + K_D) - \sqrt{(L_t + R_t + K_D)^2 - (4 * R_t * L_t)}}{2 * R_t} \qquad \text{(eq. S1)}$$

CS_{obs} = change of observed chemical shift from the free state
CS_{max} = maximum chemical shift change on saturation
R_t = total receptor concentration
L_t = total ligand concentration
K_D = dissociation constant

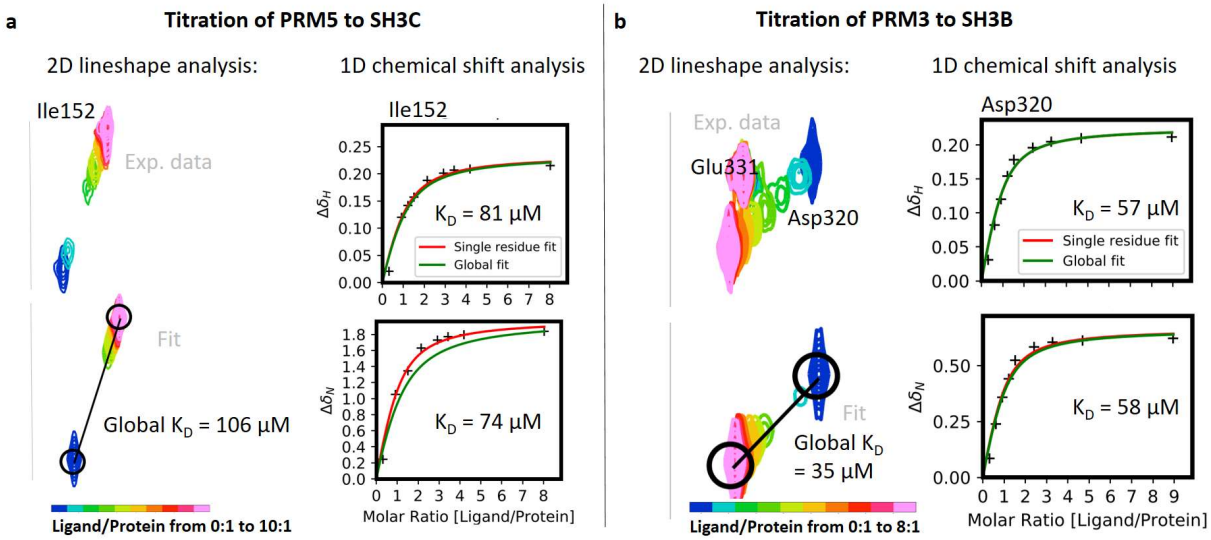

Figure Appendix H: Comparision of 1D CS analysis and 2D lineshape analysis to determine binding affinities. NMR titration spectra of experimental data (top) and fitted spectrum (bottom) and 1D chemical shift analysis (1H or 15N chemical shift binding isotherm fitted to equation S1; Color-coding of the titration ratio 0:1 to 10:1) **a)** Analysis of Ile152 from the NMR titration of PRM5 to SH3C. **b)** Analysis of Asp320 from the NMR titration of PRM3 to SH3B. Spectra were plotted with TITAN.

Appendix I: Plots of SLP65-3SH3 interaction binding isotherms

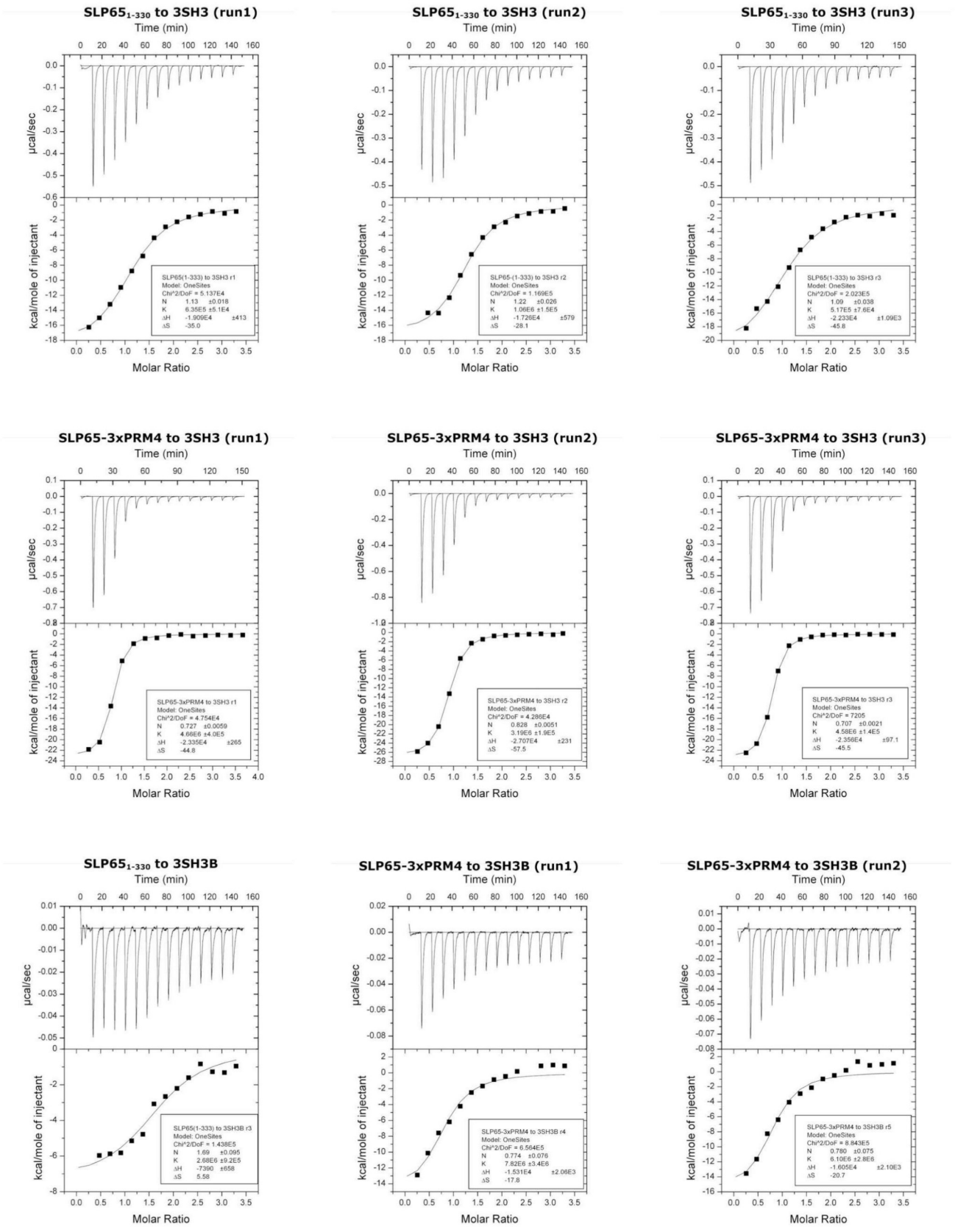

Figure A8: Plots of binding isotherms from ITC titrations of SLP651-330 or SLP65-3xPRM4 to SH3 or SH3B.

Appendix J: ITC binding isotherms of monovalent PRM-SH3 domain interactions

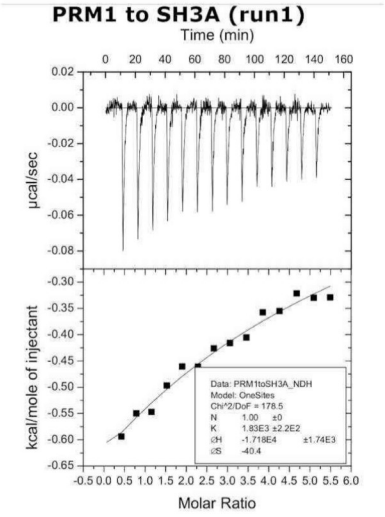

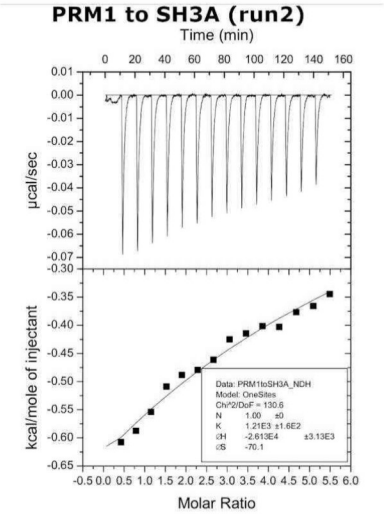

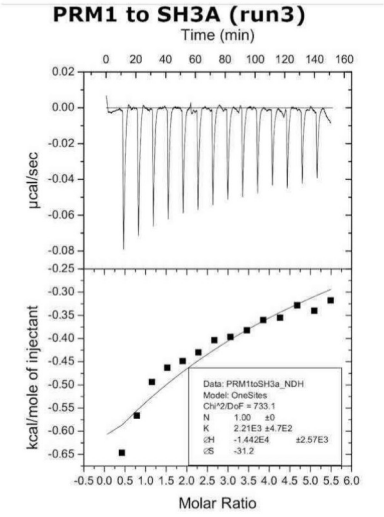

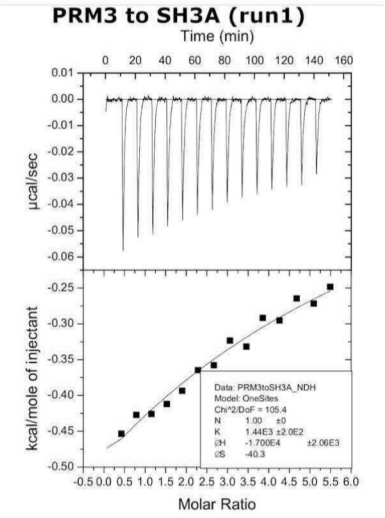

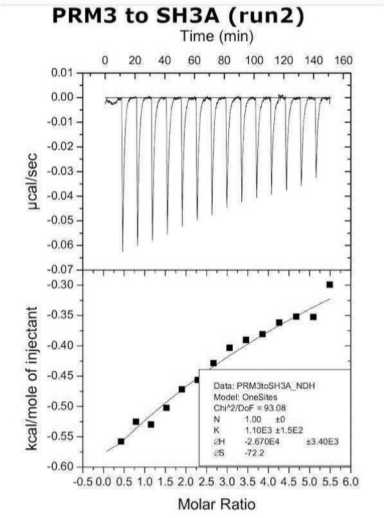

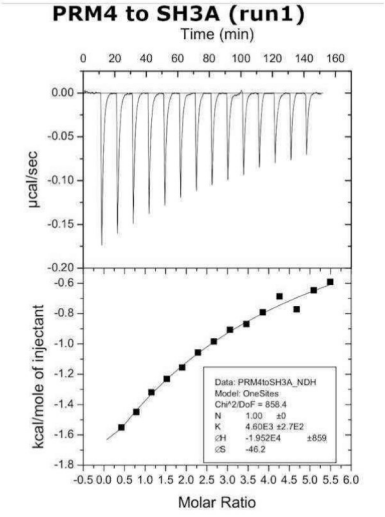

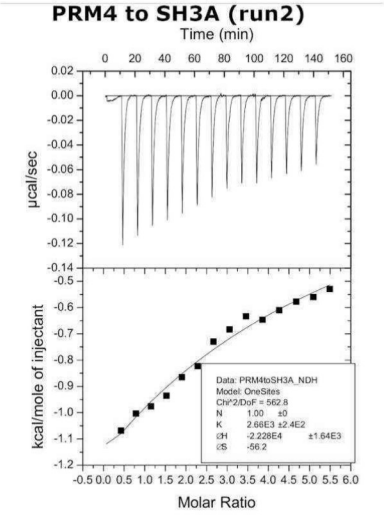

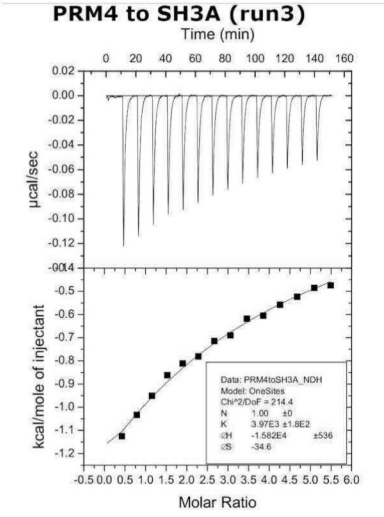

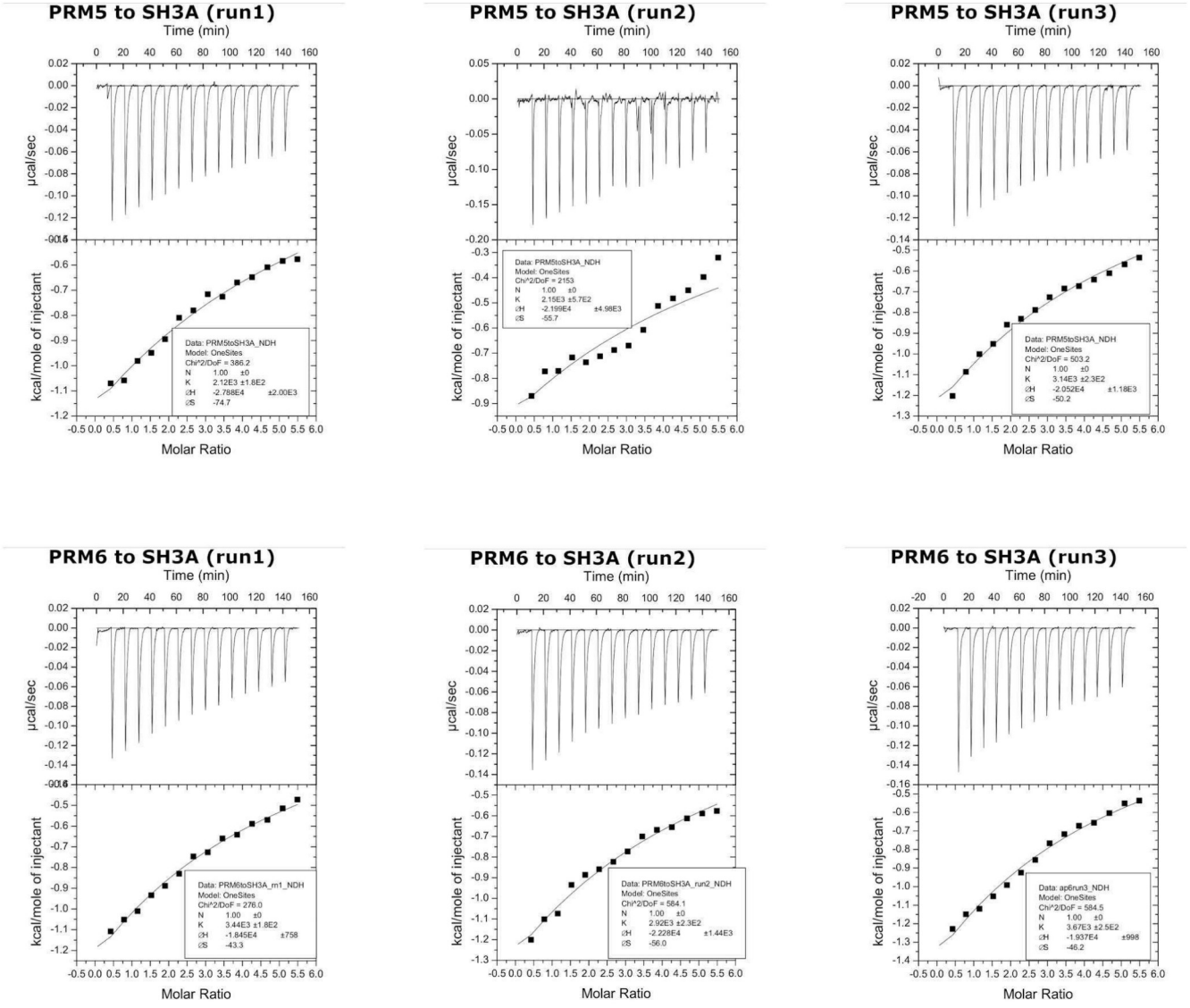

Figure A7-1: ITC titrations of PRM1 - PRM6 to SH3A

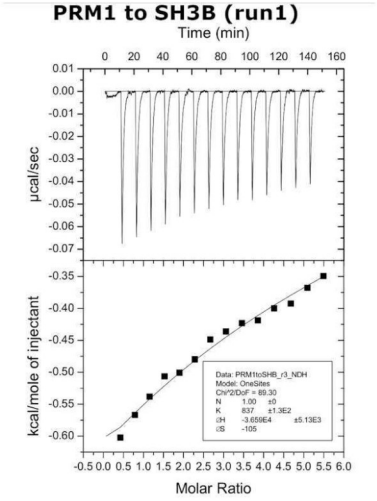
PRM1 to SH3B (run1)
Time (min)
µcal/sec
kcal/mole of injectant
Molar Ratio
Data: PRM1toSH3B_r3_NDH
Model: OneSites
Chi^2/DoF = 89.30
N 1.00 ±0
K 837 ±1.3E2
∅H -3.659E4 ±5.13E3
∅S -105

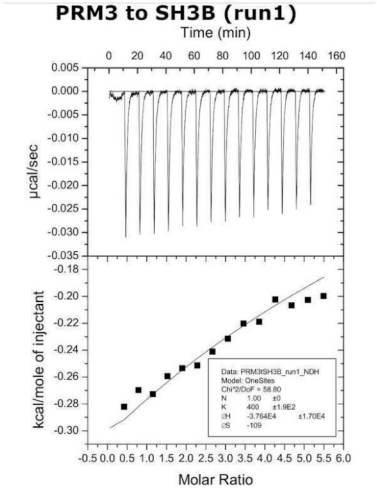
PRM3 to SH3B (run1)
Time (min)
µcal/sec
kcal/mole of injectant
Molar Ratio
Data: PRM3tSH3B_run1_NDH
Model: OneSites
Chi^2/DoF = 58.80
N 1.00 ±0
K 400 ±1.9E2
∅H -3.764E4 ±1.70E4
∅S -109

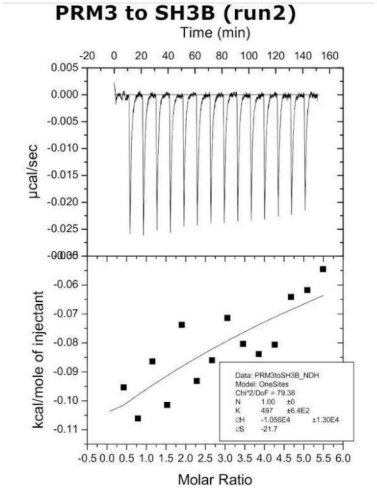
PRM3 to SH3B (run2)
Time (min)
µcal/sec
kcal/mole of injectant
Molar Ratio
Data: PRM3toSH3B_NDH
Model: OneSites
Chi^2/DoF = 79.38
N 1.00 ±0
K 497 ±6.4E2
∅H -1.056E4 ±1.30E4
∅S -21.7

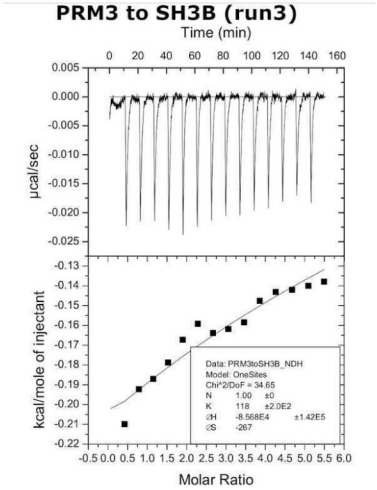
PRM3 to SH3B (run3)
Time (min)
µcal/sec
kcal/mole of injectant
Molar Ratio
Data: PRM3toSH3B_NDH
Model: OneSites
Chi^2/DoF = 34.65
N 1.00 ±0
K 118 ±2.0E2
∅H -8.568E4 ±1.42E5
∅S -267

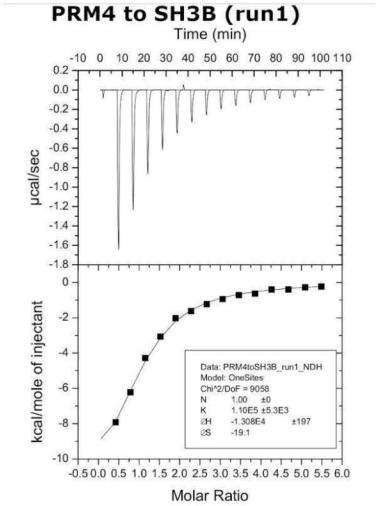
PRM4 to SH3B (run1)
Time (min)
µcal/sec
kcal/mole of injectant
Molar Ratio
Data: PRM4toSH3B_run1_NDH
Model: OneSites
Chi^2/DoF = 9058
N 1.00 ±0
K 1.10E5 ±5.3E3
∅H -1.308E4 ±197
∅S -19.1

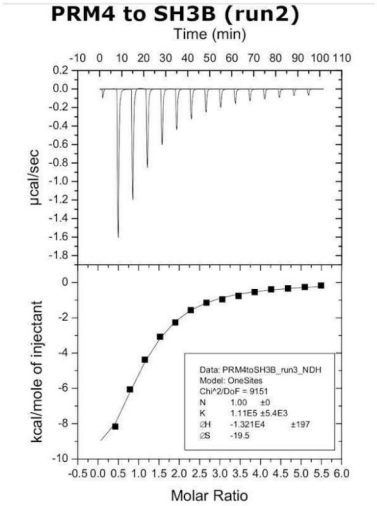
PRM4 to SH3B (run2)
Time (min)
µcal/sec
kcal/mole of injectant
Molar Ratio
Data: PRM4toSH3B_run3_NDH
Model: OneSites
Chi^2/DoF = 9151
N 1.00 ±0
K 1.11E5 ±5.4E3
∅H -1.321E4 ±197
∅S -19.5

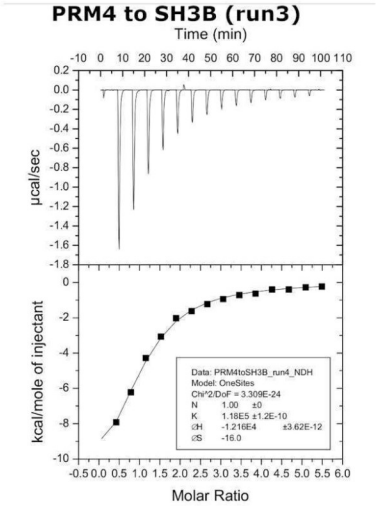
PRM4 to SH3B (run3)
Time (min)
µcal/sec
kcal/mole of injectant
Molar Ratio
Data: PRM4toSH3B_run4_NDH
Model: OneSites
Chi^2/DoF = 3.309E-24
N 1.00 ±0
K 1.18E5 ±1.2E-10
∅H -1.216E4 ±3.62E-12
∅S -16.0

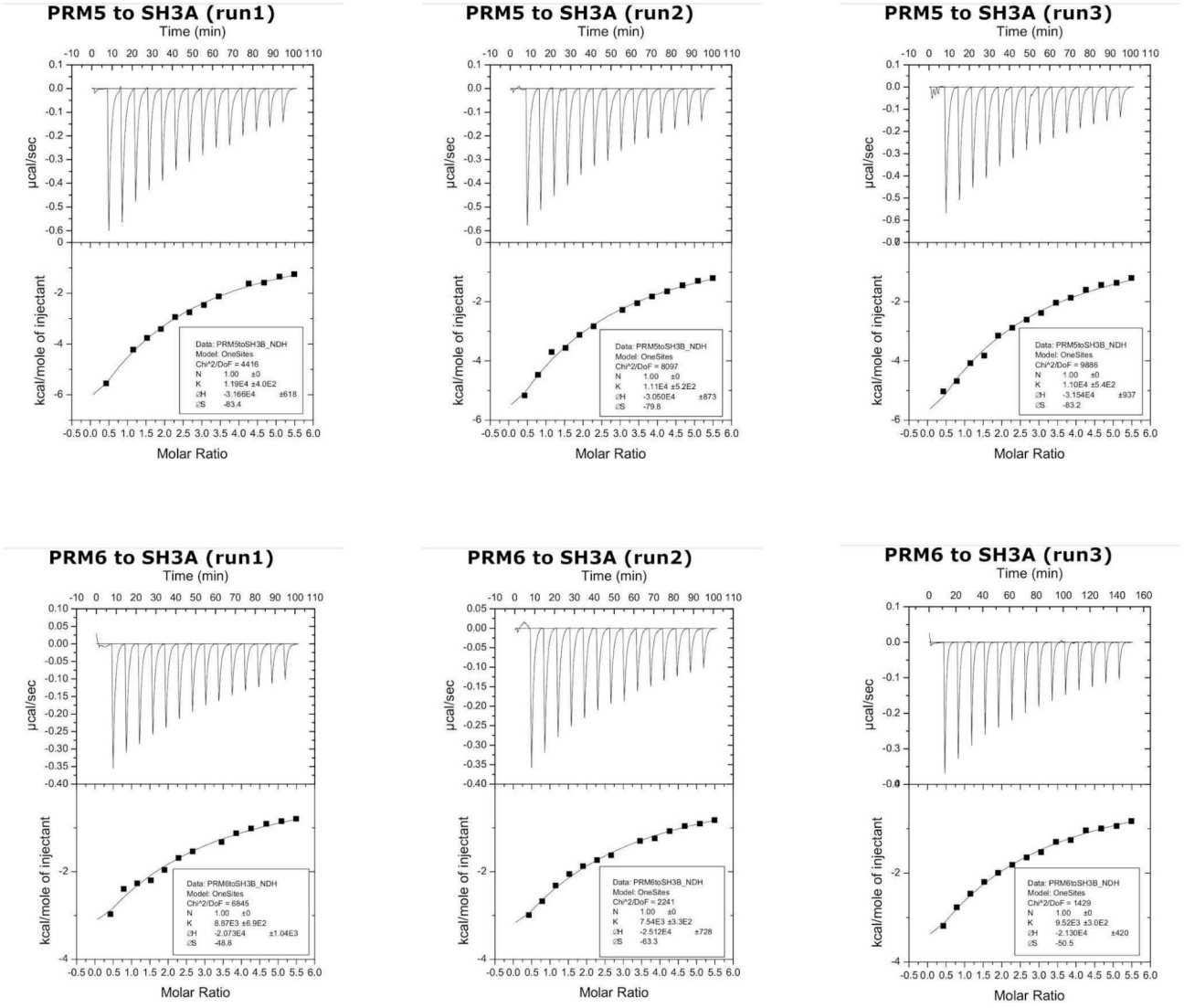

Figure A7-2: ITC titrations of PRM1 - PRM6 to SH3B

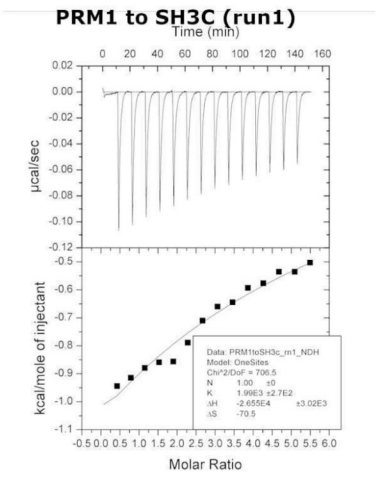
PRM1 to SH3C (run1)
Time (min)
µcal/sec
kcal/mole of injectant
Molar Ratio
Data: PRM1toSH3c_m1_NDH
Model: OneSites
Chi^2/DoF = 706.5
N 1.00 ±0
K 1.99E3 ±2.7E2
ΔH -2.655E4 ±3.02E3
ΔS -70.5

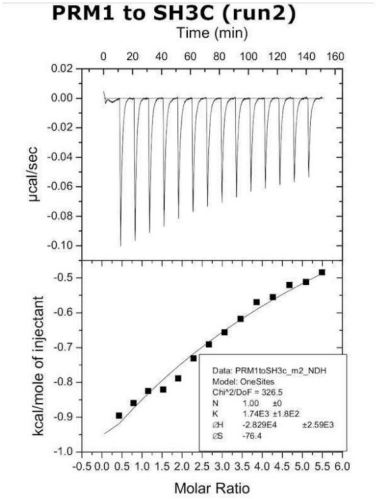
PRM1 to SH3C (run2)
Time (min)
µcal/sec
kcal/mole of injectant
Molar Ratio
Data: PRM1toSH3c_m2_NDH
Model: OneSites
Chi^2/DoF = 326.5
N 1.00 ±0
K 1.74E3 ±1.8E2
∅H -2.829E4 ±2.59E3
∅S -76.4

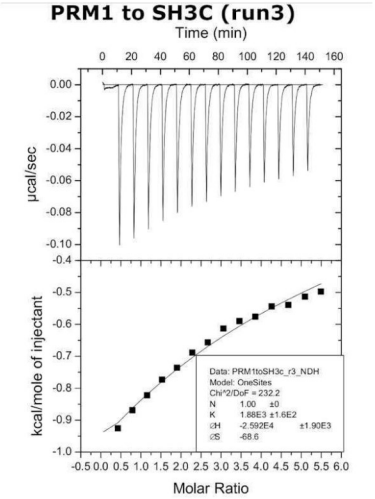
PRM1 to SH3C (run3)
Time (min)
µcal/sec
kcal/mole of injectant
Molar Ratio
Data: PRM1toSH3c_r3_NDH
Model: OneSites
Chi^2/DoF = 232.2
N 1.00 ±0
K 1.88E3 ±1.6E2
∅H -2.592E4 ±1.90E3
∅S -68.6

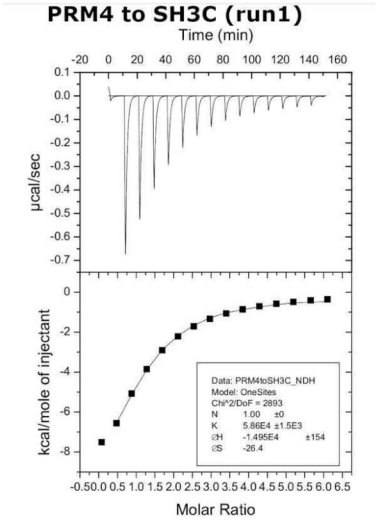
PRM4 to SH3C (run1)
Time (min)
µcal/sec
kcal/mole of injectant
Molar Ratio
Data: PRM4toSH3C_NDH
Model: OneSites
Chi^2/DoF = 2893
N 1.00 ±0
K 5.86E4 ±1.5E3
∅H -1.495E4 ±154
∅S -26.4

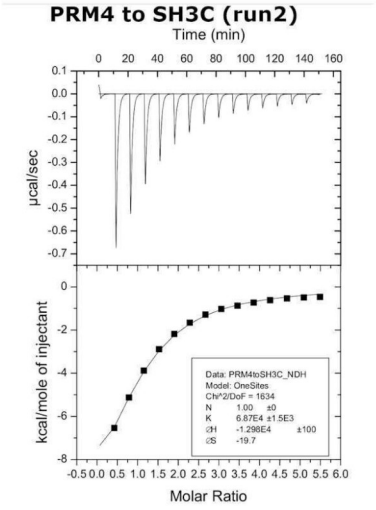
PRM4 to SH3C (run2)
Time (min)
µcal/sec
kcal/mole of injectant
Molar Ratio
Data: PRM4toSH3C_NDH
Model: OneSites
Chi^2/DoF = 1634
N 1.00 ±0
K 6.87E4 ±1.5E3
∅H -1.298E4 ±100
∅S -19.7

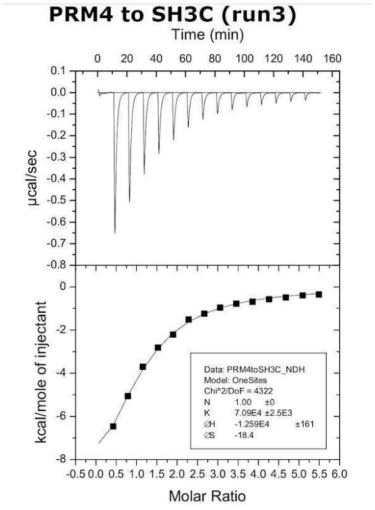
PRM4 to SH3C (run3)
Time (min)
µcal/sec
kcal/mole of injectant
Molar Ratio
Data: PRM4toSH3C_NDH
Model: OneSites
Chi^2/DoF = 4322
N 1.00 ±0
K 7.09E4 ±2.5E3
∅H -1.259E4 ±161
∅S -18.4

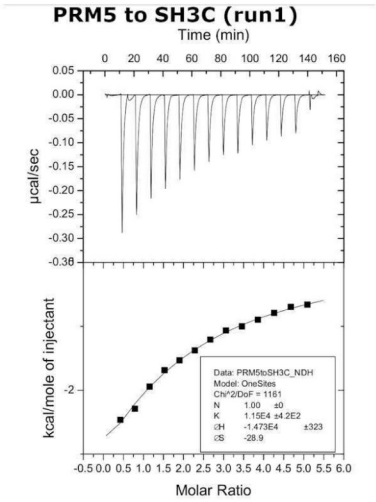
PRM5 to SH3C (run1)
Time (min)
µcal/sec
kcal/mole of injectant
Molar Ratio
Data: PRM5toSH3C_NDH
Model: OneSites
Chi^2/DoF = 1161
N 1.00 ±0
K 1.15E4 ±4.2E2
∅H -1.473E4 ±323
∅S -28.9

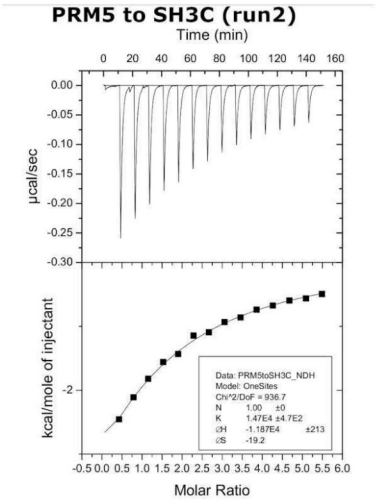
PRM5 to SH3C (run2)
Time (min)
µcal/sec
kcal/mole of injectant
Molar Ratio
Data: PRM5toSH3C_NDH
Model: OneSites
Chi^2/DoF = 936.7
N 1.00 ±0
K 1.47E4 ±4.7E2
∅H -1.187E4 ±213
∅S -19.2

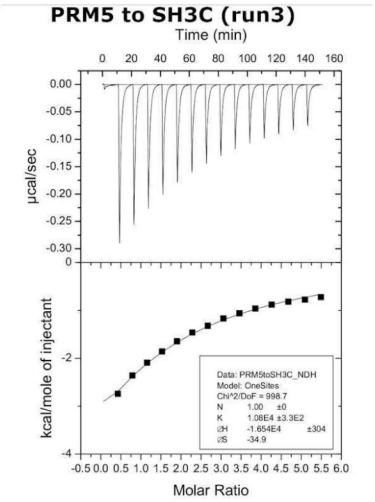
PRM5 to SH3C (run3)
Time (min)
µcal/sec
kcal/mole of injectant
Molar Ratio
Data: PRM5toSH3C_NDH
Model: OneSites
Chi^2/DoF = 998.7
N 1.00 ±0
K 1.08E4 ±3.3E2
∅H -1.654E4 ±304
∅S -34.9

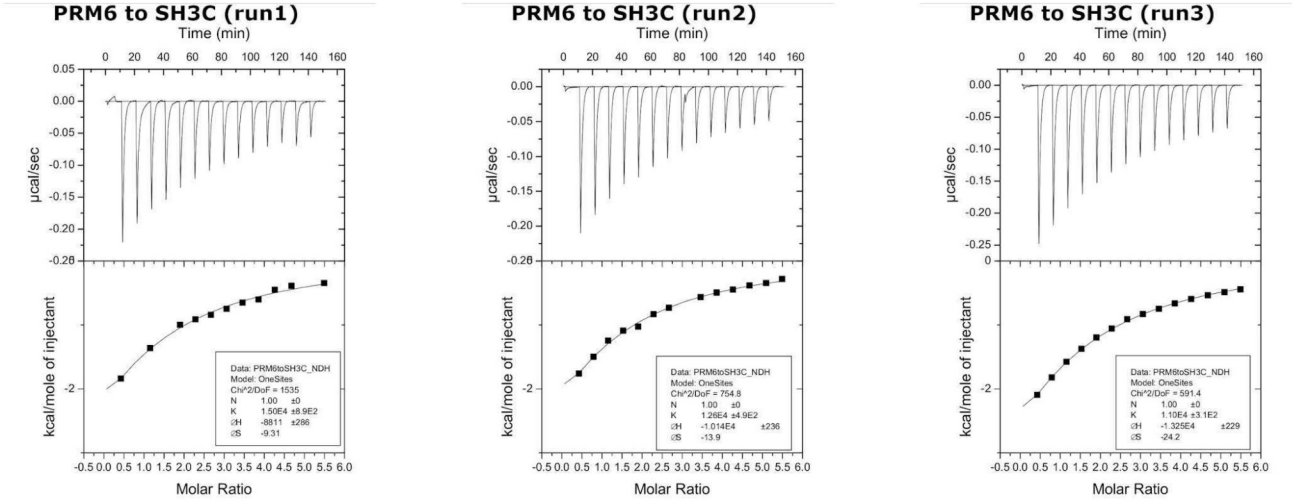

Figure A7-3: ITC titrations of PRM1 - PRM6 to SH3C